



DCU

**DESIGN AND OPTIMIZATION OF
MAGNETOSTRICTIVE ACTUATOR**

Student: Artur Grunwald

August 2007

Supervisor

Dr Abdul Ghani Olabi

School of Mechanical and Manufacturing

Engineering

Declaration

I hereby declare that all work produced in this thesis is entirely my own work, except where otherwise stated, and has not been submitted in whole or in part to any other University.

Artur Grunwald

Artur Grunwald, ID: 54149941, Date: 28th August 2007

DCU

**DESIGN AND OPTIMIZATION OF
MAGNETOSTRICTIVE ACTUATOR**

A Thesis submitted for the degree of PhD

Student: Artur Grunwald

ID: 54149941

August 2007

Supervisor:

Dr Abdul Ghani Olabi

**School of Mechanical and Manufacturing
Engineering**

Design and optimization of a magnetostrictive actuator

Artur Grunwald, Dublin City University, Ireland

Abstract

Magnetostrictive (“MS”) technology and Magneto-Rheological Fluid (“MRF”) technology are old “newcomers” coming to the market at high speed. Various industries including the automotive industry are full of potential MS and MRF applications. Magnetostrictive technology and Magneto-Rheological Fluid technology have been successfully employed in some low and high volume applications. A structure based on “MS”-technology might be the next generation in design for products where power density, accuracy and dynamic performance are key features. Since the introduction of active (MS) materials such as Terfenol-D, with stable characteristics over a wide range of temperatures and high magnetoelastic properties, interest in MS technology has been growing.

Additionally, for products where is a need to control fluid motion by varying the viscosity, a structure based on MRF might be an *improvement in performance*. Two aspects of this technology, direct shear mode (used in brakes and clutches) and valve mode (used in dampers) have been studied thoroughly and several applications are already present on the market. Excellent features like fast response, simple interface between electrical input and hydraulic output make MRF technology attractive for many applications.

This *dissertation* is the introduction of an actuator based on “MS”-technology. The possible control arrangement is based on “MR”-technology. The thesis is submitted for the degree of the PhD. The dissertation contains the layout definition, analytical calculations, simulations, and design verification and optimization with evaluation of experimental results for the actuator based on “MS”-technology in combination of a possible control device based on “MR”-technology.

Table of Content

Chapter	Chapter title	Page
Chapter 1	Introduction	1-5
	1.1 Introduction of magnetostrictive “MS” technology	1-3
	1.2 Introduction of magnetorheological “MR” technology	3-5
	1.3 Objectives and structure of the thesis	5
Chapter 2	Literature survey of magnetostrictive (MS) technology	6-34
	2.1 Magnetostriction Effects	6-9
	2.2 Giant Magnetostrictive Materials and Their Properties	9-11
	2.2.1 Terfenol-D Production	11-12
	2.2.2 Young's Modulus	12-13
	2.2.3 The Magnetomechanical Coupling Factor & the Magnetostrictive Coefficient	13-15
	2.2.4 Quality Factor	15
	2.2.5 Permeability	15-19
	2.2.6 Blocked Force	19-20
	2.2.7 Typical Optimization	20-23
	2.3 Applications of Terfenol-D	23-33
	2.3.1 Reaction Mass Actuator	23-24
	2.3.2 A standard Terfenol-D Actuator	24-25
	2.3.3 Linear Motor Based on Terfenol-D (Worm Motor)	25-26
	2.3.4 Terfenol-D in Sonar Transducers	26-27
	2.3.5 Terfenol-D Wireless Rotational Motor	27-28
	2.3.6 Terfenol-D Electro-Hydraulic Actuator	28-29
	2.3.7 Wireless Linear Micro-Motor	29-30
	2.3.8 Other Magnetostrictive Film Applications	30
	2.3.9 Magnetostrictive Contactless Torque Sensors	31-33
	2.4 Remarks on MS Technology	33-34
Chapter 3	Literature survey of magneto-rheological (MR) technology	35-49
	3.1 Rheological Background of the MRF Technology	35-38
	3.2 MRF Components	39-41
	3.3 MRF Operational Modes and Applications	42-48
	3.3.1 Valve Mode	42-45
	3.3.2 Direct Shear Mode	45-48

Chapter	Chapter title	Page
	3.3.3 Squeeze Mode	48-49
	3.4 Remarks on MRF Technology	49
Chapter 4	Actuator layout definition and analytical calculations	50-70
	4.1 Actuator introduction	50-53
	4.2 Basic Performance Calculations	53-54
	4.2.1 The choice of mechanical load as reference for the study	54-56
	4.2.2 Terfenol-D Shaft and MRF Capability Parameter Calculations	56-61
	4.2.3 MRF Capability Parameter Calculations	61-70
Chapter 5	Magnetic field calculations and simulations for "MS" and "MR" devices	71-116
	5.1 Electric circuit of the actuator system	71-74
	5.2 The Magnetic circuitry for the magnetostrictive actuator	74-80
	5.3 The Magnetic circuitry for the magnetorheological devices	81-88
	5.4 Electric coil for actuator and magnetorheological devices	88-92
	5.5 Magnetic Field Simulation	92-97
	5.5.1 Magnetic field simulation results from "MS"-actuator	98-107
	5.5.2 Magnetic field simulation results from "MR"-valve	107-111
	5.5.3 Magnetic field simulation results from "MR"-orifice	112-116
Chapter 6	Experimental procedures and conclusions	117-153
	6.1 Experimental rig	117-120
	6.2 Rig test equipment and tools for experimental evaluation	120-122
	6.3 Experimental evaluation of magnetostrictive actuator	122-131
	6.4 Experimental evaluation of magneto-rheological control	131-136
	6.5 Experimental evaluation of "MS"-pump	136-141
	6.6 Experimental evaluation of complete actuator assembly	141-147
	6.7 Experimental evaluation of the "MS"-pump actuator	147-153
Chapter 7	Conclusions and recommendation	154-156
	7.1 Conclusions	154-155
	7.2 Recommendation for future work	155-157
References	Reference list of used literature	158-166
Appendices	A, B, C, D, E, F, G, H with drawings, specifications, list of publications and additional test results	167-219

Table of figures in the thesis

Figure	Figure title	Page
Fig.1	Strain versus magnetic field	1
Fig.2	"MS"-effect, schematically	2
Fig.3	"MR"-effect, schematically	4
Fig.4	Magnetostrictive effects [4]	6
Fig.5	Length change versus Terfenol-D rod with strain as parameter	10
Fig.6	Young's modulus versus magnetic field	12
Fig.7	Strain versus magnetic field	14
Fig.8	Factor k_{33} and d_{33} versus applied stress [19]	14
Fig.9	Magnetization curve [22]	17
Fig.10	B-H curve for comparison	17
Fig.11	General B-H curve	18
Fig.12	Full loop of magnetization [23]	19
Fig.13	Typical optimization with magnetic bias	21
Fig.14	Typical optimization with mechanic bias [similar to 24, 25]	22
Fig.15	Reaction mass actuator [27]	24
Fig.16	Standard actuator [14]	25
Fig.17	Worm motor [15]	26
Fig.18	Sonar transducers [6]	27
Fig.19	Rotational stepping motor [28]	28
Fig.20	Electro-hydraulic actuator [29]	29
Fig.21	Magnetostrictive thin film actuator [12]	30
Fig.22	Thin film application in valves [30]	31
Fig.23	Contactless sensor application based on magnetostrictive materials [12]	32
Fig.24	Sensor applications [31]	33
Fig.25	Different types of fluids with equations [41]	36
Fig.26	Shear stress against shear rate for various fluids	37
Fig.27	Valve Mode	42
Fig.28	Functional principle of MRF damper [32-36]	44
Fig.29	Direct Shear Mode	45
Fig.30	Functional principle of MRF brake [32-36, 46]	46
Fig.31	MRF in squeeze mode	48

Fig.32	Arrangement for the study	50
Fig.33	Arrangement for the study	51
Fig.34	Actuation principle	52
Fig.35	Cross-section of the actuator used in the study	52
Fig.36	Cross-section of the “MR” control valve	53
Fig.37	Cross-section of the “MR” control orifice	53
Fig.38	Micro stepping hydraulic actuator	54
Fig.39	Axial force versus elastic deformation	54
Fig.40	Cross-section of the load arrangement used in this study	55
Fig.41	Length change versus strain	56
Fig.42	Supplier characteristic and specification for Terfenol-D shaft [15]	57
Fig.43	Axial force versus strain and Young’s modulus E as parameter	58
Fig.44	Achievable pressure versus strain	58
Fig.45	Pump volume per loop versus strain	59
Fig.46	Flow rate versus frequency with strain as parameter	60
Fig.47	Main piston displacement versus number of pump loops	61
Fig.48	Cross section of the control valve	62
Fig.49	Cross section of the control orifice	62
Fig.50	Supplier specification of reference MRF-132-AD [35 and 36]	63
Fig.51	Supplier specification of reference MRF-336-AG [35 and 36]	63
Fig.52	Pressure versus gap size with yield stress as parameter	64
Fig.53	Pressure versus gap size at various flow rates	65
Fig.54	Wall shear rate ψ [s^{-1}] in the rectangular channel	66
Fig.55	Pressure versus orifice diameter with yield stress as parameter	67
Fig.56	Pressure versus orifice diameter at various flow rates	68
Fig.57	Wall shear rate ψ [s^{-1}] in the cylindrical channel	69
Fig.58	Picture from Lee Inc. catalog, check valve [93]	70
Fig.59	Alternative voltage versus time relationships	71
Fig.60	Inductor response in AC [22]	72
Fig.61	Impedance [22]	72
Fig.62	Layout of the actuator coil	74
Fig.63	Magnetic path through the actuator	75
Fig.64	Strain versus applied magnetic field intensity (A/m) [14]	75
Fig.65	B-H diagram of Ck15 with measurement data	77

Fig.66	B-H diagram of Terfenol-D with measurement data [14]	77
Fig.67	Number of turns versus achievable magnetic field strength	80
Fig.68	Layout of the valve control arrangement	81
Fig.69	Layout of the control valve arrangement	82
Fig.70	Magnetic path through the control valve	82
Fig.71	Layout of the control orifice	83
Fig.72	Layout of the orifice assembly	83
Fig.73	Magnetic path through the control arrangement	84
Fig.74	B-H diagram of MRF132-AD [69 and 79]	84
Fig.75	B-H diagram of MRF336-AG [69 and 79]	85
Fig.76	Number of turns versus achievable magnetic field strength for the valve	87
Fig.77	Number of turns versus achievable magnetic field strength for the orifice	87
Fig.78	Air coil geometry	88
Fig.79	Current density versus wire diameter with current as parameter	91
Fig.80	Geometry and coil specification of the magnetostrictive actuator	91
Fig.81	Geometry and coil specification of the control valve	91
Fig.82	Geometry and coil specification of the control orifice	92
Fig.83	FEMM software window with user interface [48]	97
Fig.84	Meshed actuator with FEMM	98
Fig.85	FEMM Flux density B (T) in actuator	99
Fig.86	FEMM Magnetic Circuit Results for actuator	100
Fig.87	Reference figure of the actuator for plots of B (T) and H (A/m)	101
Fig.88	FEMM Flux density B (T) in the actuator	101
Fig.89	FEMM Field intensity H (A/m) in the actuator	102
Fig.90	Opera software window with user interface [49]	103
Fig.91	Meshed actuator with Opera	104
Fig.92	Opera Potential lines and flux density plot B (T) in the valve	105
Fig.93	Comparison of actuator simulation results regarding field density B (T)	106
Fig.94	Comparison of actuator simulation results regarding field intensity H (A/m)	106
Fig.95	Meshed control valve with FEMM	107
Fig.96	FEMM Magnetic flux density B (T) in the valve	108
Fig.97	FEMM Magnetic Circuit Results for valve	109
Fig.98	Reference figure of the valve for plots of B (T) and H (A/m)	110
Fig.99	FEMM Flux density B (T) in the valve	110

Fig.100	FEMM Field intensity H (A/m) in the valve, mid of MRF gap	111
Fig 101	Meshed control orifice with FEMM	112
Fig.102	FEMM Flux density B (T) in the orifice	113
Fig.103	FEMM Magnetic Circuit Results for orifice	114
Fig.104	Reference figure of the orifice for plots of B (T) and H (A/m)	115
Fig.105	FEMM Flux density B (T) in the orifice	115
Fig.106	FEMM Field intensity H (A/m) in the orifice	116
Fig 107	Picture from assembly	117
Fig.108	Picture from control valve assembly	118
Fig.109	Picture from control orifice assembly	118
Fig.110	Picture from load assembly	119
Fig.111	Picture from assembly	119
Fig.112	Test rig equipment with “MS”-actuator prototype	121
Fig.113	Test rig equipment with function generator (left) and NI I/O card (right)	121
Fig.114	Actuator assembly for performance measurements	122
Fig 115	Actuator assembly cross section for performance measurements	123
Fig.116	“MS”-performance at pre-load with 300 N	123
Fig.117	“MS”-performance at pre-load with 400 N	124
Fig.118	“MS”-performance at pre-load with 500 N	124
Fig.119	“MS”-performance at pre-load with 600 N	124
Fig.120	“MS”-performance at pre-load with 650 N	124
Fig.121	“MS”-performance at pre-load with 750 N	125
Fig.122	“MS”-performance at pre-load with 850 N	125
Fig 123	“MS”-performance at pre-load with 950 N	125
Fig.124	“MS”-performance at pre-load with 1050 N	125
Fig.125	“MS”-performance at pre-load with 1150 N	126
Fig.126	“MS”-performance at pre-load with 1250 N	126
Fig.127	“MS”-performance at pre-load with 1350 N	126
Fig.128	“MS”-performance at pre-load with 1450 N	126
Fig.129	“MS”-performance at pre-load with 1600 N	127
Fig.130	“MS”-performance at pre-load with 1650 N	127
Fig.131	“MS”-performance at pre-load with 1700 N	127
Fig.132	Optimization of achievable strain with various pre-load	128
Fig.133	Butterfly-curve at 550 N pre-load at 20 Hz with sinusoidal power	128

Fig.134	Butterfly-curve at 550 N pre-load at 30 Hz with sinusoidal power	129
Fig.135	Butterfly-curve at 550 N pre-load at 40 Hz with sinusoidal power	129
Fig.136	Butterfly-curve at 550 N pre-load at 50 Hz with sinusoidal power	129
Fig.137	Butterfly-curve at 550 N pre-load at 60 Hz with sinusoidal power	129
Fig.138	Butterfly-curve at 550 N pre-load at 70 Hz with sinusoidal power	130
Fig.139	Butterfly-curves, force versus current, at medium level	130
Fig.140	Butterfly-curves, force versus current, at medium level	131
Fig.141	Layout for experimental tests of the valve	132
Fig.142	Layout for experimental tests of the orifice	132
Fig.143	Pressure capacity of valve with MRF 132-AD	133
Fig.144	Pressure capacity of valve with MRF 132-AD (1.2 MPa @ 2 A)	133
Fig.145	Pressure capacity of valve with MRF 132-AD (1.4 MPa @ 3 A)	134
Fig.146	Pressure capacity of valve with MRF 132-AD (1.7 MPa @ 4.5 A)	134
Fig.147	Pressure capacity of valve with MRF 132-AD (1.8 MPa @ 6 A)	134
Fig.148	Pressure capacity of MRF control assemblies	135
Fig.149	"MS"-pump actuator assembly with check valves	136
Fig.150	"MS"-pump actuator assembly with check valves and CHF11S	137
Fig.151	"MS"-pump actuator assembly with check valves and MRF 132-AD	137
Fig.152	"MS"-shaft force, voltage and current from pump actuator	138
Fig.153	NI interface for actuator with "MS" and "MR" control	139
Fig.154	Current and voltage flow during the testing	140
Fig.155	"MS"-pump actuator assembly with "MR"-valves	140
Fig.156	"MS"-pump actuator assembly with two "MR" valves and MRF 132-AD	141
Fig.157	Reference assembly on test bench	142
Fig.158	Experimental tests of the load arrangements	143
Fig.159	Measurement of the reference assembly	143
Fig.160	Axial force and displacement versus pressure	144
Fig.161	Disengagement performance from 3 MPa	144
Fig.162	Disengagement performance from 2.5 MPa	145
Fig.163	Disengagement performance from 2.0 MPa	145
Fig.164	Disengagement performance from 1.7 MPa	145
Fig.165	Disengagement performance from 1.6 MPa	146
Fig.166	Disengagement performance from 1.0 MPa	146
Fig.167	Disengagement performance from 0.7 MPa	146

Fig.168	Disengagement performance from 0.5 MP	147
Fig.169	MS actuator with full MRF control	148
Fig.170	Cross section of "MS" actuator with full MRF control	148
Fig.171	Micro-pumping at low frequency (>1 Hz)	149
Fig.172	Micro-pumping at medium frequency (>15 Hz)	149
Fig.173	"MS" pump actuator with "MR" release valve	150
Fig.174	Cross section of "MS" pump actuator with "MR" release valve	150
Fig.175	Basic performance at 1 Hz	151
Fig.176	Basic performance at 10 Hz	151
Fig.177	Engagement performance at 25 Hz	152
Fig.178	Pressure release performance	152
Fig.179	Achievable pressure versus operational frequency	153
Fig.180	Actuator layout with integrated inlet valve	156
Fig.181	Actuator layout with conventional pump	157

Table of tables in the thesis

Table	Table title	Page
Tab.1	Comparison of Strain capability [14, 15]	3
Tab.2	MRF versus ERF [1, 2, 32-35]	4
Tab.3	Technology features overview [1, 2, 8, 9, 10 and 11]	8
Tab.4	Terfenol-D properties, [1, 2, 4, 5, 6, 9, 12, 14 and 16]	10-11
Tab.5	Relative permeability [22]	16
Tab.6	Typical layouts in comparison [1, 2]	23
Tab.7	MRF operational modes	38
Tab.8	MRF versus Ferrofluid [1, 2, 32-46]	41
Tab.9	Valve mode features [32-36]	44
Tab.10	Shear mode features [32-36, 46]	47
Tab.11	Rig test data and sensors	120
Tab.12	"MS"-actuator key data	154
Tab.13	"MR"-control devices key data	155

Acknowledgements

I would like to express my appreciation to my supervisor, Professor Dr. Abdul Ghani Olabi, for providing me with the unique opportunity to work in the research area of “smart materials”, for his assistance and his expert guidance throughout the dissertation.

I would like to thank GKN Driveline for the technical and financial support during the dissertation. Especially, I will wish to acknowledge my appreciation to Mr. Werner Krude who enables the company support for this dissertation. In addition to this I would like to thank colleagues from experimental department for their generous help in the experimental phase of this research.

Finally, I would like to thank my family for their love, patient and support. Without them, this work could not have been completed.

Chapter One

Introduction

1.1 Introduction of magnetostrictive (“MS”) technology

Magnetostriction (“MS”) is the change in shape of materials under the influence of an external magnetic field. The magnetostrictive effect was first described in the 19th century (1842) by an English physicist James Joule. He observed that a sample of ferromagnetic material, i.e. iron, changes its length in the presence of a magnetic field. Joule actually observed a material with negative magnetostriction, but since that time materials with positive magnetostriction have been discovered. The causes of magnetostriction are similar for both types of material. This change in length is the result of the rotation of small magnetic domains. This rotation and re-orientation causes internal strains in the material structure. The strains in the structure lead to the stretching, in the case of positive magnetostriction, of the material in the direction of the magnetic field. During this stretching process the cross-section is reduced in a way that the volume is kept nearly constant. The size of the volume change is so small that it can be neglected under normal operating conditions. Applying a stronger field leads to stronger and more re-orientation of more and more domains in the direction of magnetic field. When all the magnetic domains have become aligned with the magnetic field the saturation point has been achieved. Fig.1 shows the idealized behavior of length change versus applied magnetic field.

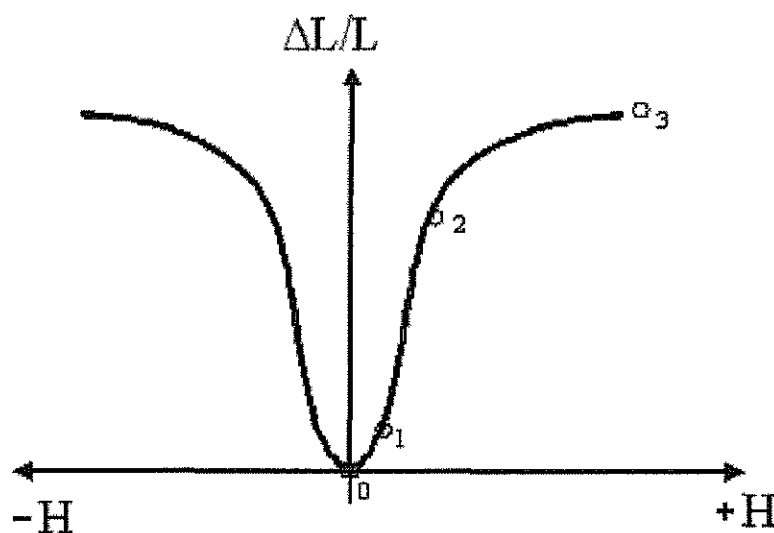


Fig.1. Strain versus magnetic field

When a magnetic field is established in the opposite direction, the field is understood to be negative, but the negative field produces the same elongation in the magnetostrictive material, as a positive field would. The shape of the curve is reminiscent of a butterfly and so the curves are referred as butterfly curves. The physical background for the re-orientation of magnetic domains is depicted with some simplification schematically in Fig. 2. In the region between 0 and 1, where the applied magnetic field is small, the magnetic domains show almost no common orientation pattern. Depending on how the material was formed there may be a small amount of a common orientation pattern, which would show itself as a permanent magnet bias. The resulting strain depends very much on how homogeneous is the base structure of the magnetostrictive material and the material formulation. In the region 1-2 ideally there should be an almost linear relationship between strain and magnetic field. Because the relationship is a simple one, it is easier to predict the behavior of the material and so most devices are designed to operate in this region. Beyond point 2, the relationship becomes non-linear again as a result of the fact that most of the magnetic domains have become aligned with the magnetic field direction. At point 3 there is a saturation effect, which prevents further strain increase.

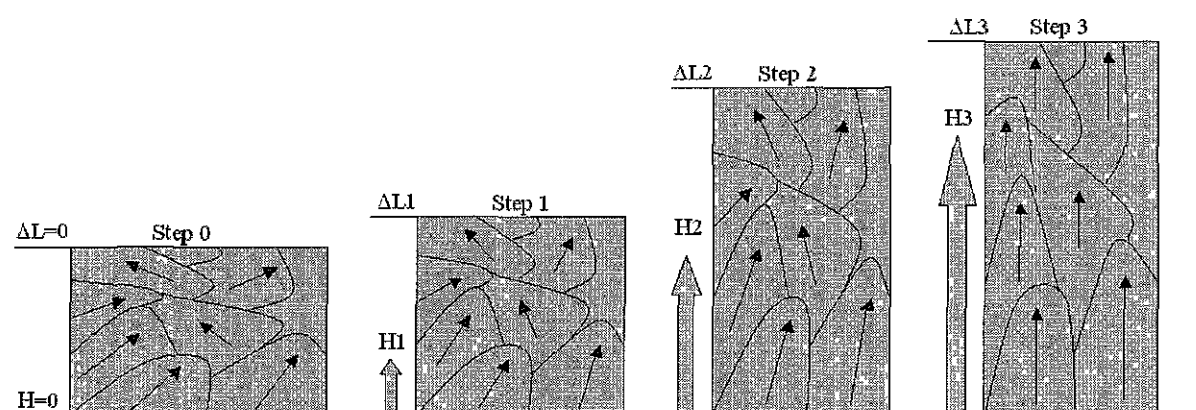


Fig. 2: "MS"-effect, schematically

With pre-stress and magnetic bias the strain capability could be optimized. The behavior of the magnetostrictive materials in various applications is complex, because the changing conditions during operation cause changes in material properties. The maximum useful magnetoelastic strain is one of the key parameters defining the resulting mechanical output in the case of a magnetostrictive actuator. In comparison with other magnetostrictive materials Terfenol-D shows a good trade-off between high strain and high Curie temperature. Magnetostriction only occurs in a material at temperatures below the Curie temperature, but

often the Curie temperature is below the temperature of the environment and this causes the magnetostriction effect to have little practical value. Development of further alternative magnetostrictive materials is ongoing [48, 51 and 61] Table 1 compares typical strains for various magnetostrictive materials.

Table 1: Comparison of strain capability [14, 15 and 62]

Material	Saturation strain in [ppm]	Curie temperature in [K]
Ni	-50	630
Fe	-14	1040
Fe ₃ O ₄	60	860
Terfenol-D	2000	650
Tb _{0.5} Zn _{0.5}	5500	180
Tb _{0.5} Dy _x Zn	5000	200

In case a shaft is made of magnetostrictive material, i.e. Terfenol-D, magnetic field along the shaft axle will cause axial elongation. The elongation of the “MS”-shaft is proportional to the applied magnetic field. A higher magnetic field leads to larger elongation. Without the magnetic field the shape of the magnetostrictive material reverses to the original. The magnetostriction is a reversible feature. This unique feature from magnetostrictive material could be used for an actuator device. The “MS”-technology offers an attractive controllability with high power density.

1.2 Introduction of magnetorheological (“MR”) technology

Magnetorheology (“MR”) is the change of rheological behavior under an external magnetic field. Magnetorheological fluid contains three components: basic fluid, ferromagnetic particles and stabilizing additives. The external magnetic field forces the ferromagnetic particles to form a chain-like structure. The chain-like structure resists the free fluid motion and the fluid behavior becomes controllable with the external magnetic field. The behavior of the magneto-rheological fluid (“MRF”) is dependent on the chemical formulation and the stability of the chain-like structure, which the fluid has to pass. The physical background for the “MR”-effect is depicted with some simplification schematically in Fig. 3.

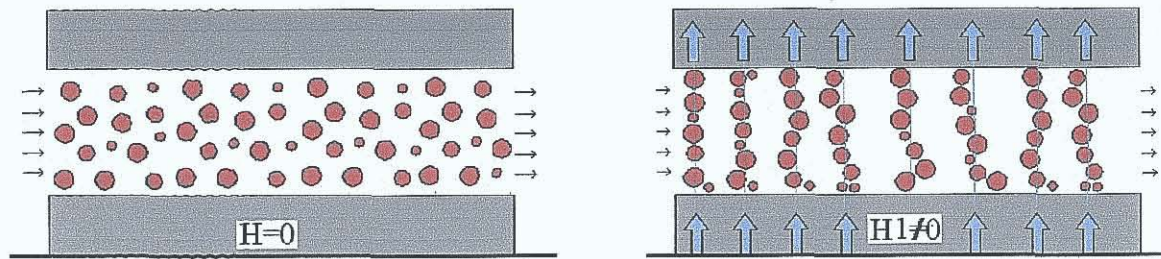


Fig. 3: "MR"-effect, schematically

Without the external magnetic field, the magnetorheological fluid behaves like Newtonian fluid. The "MR"-effect is a reversible feature and could be used in a device where fluid motion should be controlled. Ever since some industrial issues were solved, both the technical and the commercial benefits for various MRF applications have become very promising. As a result MRF development is ongoing continuously. More than sixty five years ago, in the 1940s, Jacob Rabinov discovered the MRF effect at the US National bureau of Standards. At the same time W. Wislow was working on a competitive technology called Electro-Rheological Fluid (ERF). There are some similarities between the two different technologies regarding the required power, but in the case of ERF, thousands of volts and some milli-amperes are required, and in the case of MRF, normally between 2 and 24 volts and some amperes are required. The electro-rheological (ER) effect depends on an electric field, and the magneto-rheological (MR) effect depends on a magnetic field. MRF products have between 20 and 50 times higher capacity than the equivalent ERF products. Table 2 gives an overview of the ER and MR key features.

Table 2: MRF versus ERF [1, 2, 65-68]

Representative Feature	MRF	ERF
Max. Yield Stress	50-100 kPa	2-5 kPa
Power Supply	2-24 V @ 1-2 A	2-5 kV @ 1-10 mA
Response time	some millisecond	some millisecond
Operational Field	~250 kA/m	~4 kV/mm
Energy density	0.1 J/cm ³	0.001 J/cm ³
Stability	Good for most impurities	Poor for most impurities
Operational temperature	-40°C up to +150°C	-25°C up to +125°C

d a very high level of interest to introduce
st recent couple of years. At the beginning
behaviour, such as in-use thickening,
his created some challenges for the
TRF, especially for an automotive
sedimentation and abrasive behavior have
in the USA, Europe, and Japan. Recently
e bearings have already come to the market

“smart” materials area and their features
ity and non-contact nature make them
is thesis are as follows:
nology;
MR” technology;
ic field simulations;

xperimental evaluation of an “MS”-actuator
e devices, valve and orifice, have been
for Terfenol-D shaft from the “MS”-
evaluation.

d three are summaries of “MS” and “MR”
d known applications. Chapter four
nd control device performance. Chapter
ults of magnetic field simulations for the
different software packages for magnetic
d professional Vector Fields Opera-
uator design and the “MR”-control design.
chapter six. In the last chapter conclusions
en proposed. Experimental rig drawings
of this thesis.

All these MRF technology advantages have created a very high level of interest to introduce products based on MRF technology during the most recent couple of years. At the beginning of the development work on MRF, non-predictable behaviour, such as in-use thickening, sedimentation and abrasion [67] were described. This created some challenges for the industrialization of the first application based on MRF, especially for an automotive application. During the last few years the stability, sedimentation and abrasive behavior have been studied in several universities and companies in the USA, Europe, and Japan. Recently MRF applications such as dampers, clutches, active bearings have already come to the market or are close to the start of serial production.

1.3 Objectives and structure of the thesis

Both technologies, “MS” and “MR”, belong to the “smart” materials area and their features like fast response, high power density, controllability and non-contact nature make them attractive for various applications. Objectives of this thesis are as follows:

- to define an actuator concept based on “MS” technology;
- to define a concept of a control device based on “MR” technology;
- to perform analytical calculations and the magnetic field simulations;
- to design and to build experimental rig
- and finally to confirm the basic functionality by experimental evaluation of an “MS”-actuator and “MR”-control devices Two different control devices, valve and orifice, have been evaluated in this thesis. Furthermore, the pre-load for Terfenol-D shaft from the “MS”-actuator has been optimized based on experimental evaluation.

The thesis is structured as follows. Chapter two and three are summaries of “MS” and “MR” literature surveys including technologies basics and known applications. Chapter four contains the parametrical calculations of actuator and control device performance. Chapter five handles the magnetic field calculations and results of magnetic field simulations for the “MS”-actuator and the “MR”-control devices. Two different software packages for magnetic field simulation, free available FEMM-software and professional Vector Fields Opera-software, have been used to optimize the “MS”-actuator design and the “MR”-control design. The experimental evaluation has been discussed in chapter six. In the last chapter conclusions and future work for continuing development has been proposed. Experimental rig drawings with specifications are summarized in appendixes of this thesis.

Chapter Two

Literature survey of magnetostrictive “MS” technology

2.1 Magnetostriction Effects

Crystals of ferromagnetic materials change their shape when they are placed in a magnetic field. This phenomenon is called magnetostriction. It is related to various other physical effects [1-7]. Magnetostriction is, in general, a reversible exchange of energy between the mechanical form and the magnetic form. The ability to convert an amount of energy from one form into another allows the use of magnetostrictive materials in actuator and sensor applications. Fig. 4 shows various physical effects which are related to the magnetostrictive effect.

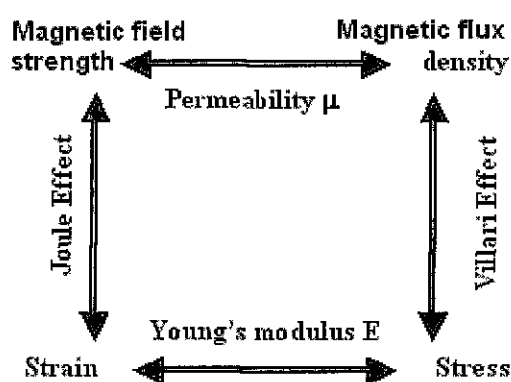


Fig 4: Magnetostrictive effects, similar to [4]

The most understood effect which is related to magnetostriction is the **Joule effect**. This is the expansion, positive magnetostriction, or contraction, negative magnetostriction, of a ferromagnetic rod in relation to a longitudinal magnetic field. This effect is mainly used in magnetostrictive actuators. Magnetostriction is a fully reversible material feature. In the absence of the magnetic field, the sample shape returns to its original dimensions. The ratio of $\Delta L/L$ in Terfenol-D is in the range of 800 ppm up to 2000 ppm, and can be up to 4000 ppm at resonance frequency. The increase in length (longitudinal strain) or the contraction of diameter (lateral strain) is proportional to the applied magnetic field and this can be used for various purposes in an actuator mechanism.

Another widely utilized effect related to magnetostriction is the **Villari Effect**. This effect is based on the fact that when a mechanical stress is imposed on a sample, there is a change in

the magnetic flux density which flows through the sample as a result of the creation of a magnetic field. The change in flux density can be detected by a pickup coil and is proportional to the level of the applied stress. The Villari effect is reversible and is used in sensor applications.

The **ΔE -Effect** is another effect related to magnetostriction. It is the change of the Young's Modulus as a result of a magnetic field. The $\Delta E/E$ in Terfenol-D is in the range of more than 5 and can be employed in tuneable vibration and broadband sonar systems [6]. Due to the change of the Young's Modulus there is a change in the velocity of sound inside magnetostrictive materials, and this can be observed.

Another effect related to magnetostriction is the **Wiedemann Effect**. The physical background to this effect is similar to that of the Joule effect, but instead of a purely tensile or compressive strain forming as a result of the magnetic field, there is a shear strain which results in a torsional displacement of the ferromagnetic sample.

The **inverse Wiedemann Effect** is called **Matteuci Effect**. Alternating current fed to a coil creates a longitudinal magnetic field in a sample, and this in turn creates a magnetic flux density in the sample. The presence of the alternating magnetic flux can be detected by another coil, a pickup coil which measures the rate of change in the magnetic flux density. Twisting the ferromagnetic sample induces a change in the magnetization of the sample, which results in a change in the rate of change of the magnetic flux density. By detecting the magnetization change using the pickup coil, the change in shear stress can be evaluated and as a result the magnitude of the applied torque can be calculated. The Matteuci effect is modified by introducing a permanent magnetic bias in the ferromagnetic sample and this is used in sensor applications.

An additional magnetostrictive effect is the **Barrett Effect** [6]. In certain extreme operational conditions the volume of the material may change in response to a magnetic field. For instance, the fraction volume change of nickel is only 10^{-7} at 80 kA/m. This volume change in response to a magnetic field is so small that it can be neglected under normal operational conditions. The inverse Barret effect, the **Nagaoka-Honda Effect**, is the change of magnetic state caused by a change in the volume of a sample as a result of hydrostatic pressure. Due to the very extreme operational conditions required to make it possible to detect these effects connected with volume change, they have not found wide use in industry.

The two most widely used magnetostrictive effects are the Joule effect and the Villari effect. They can be analyzed using the following equations. Firstly the Villari effect:

$$B = d\sigma + \mu^{\sigma} H \quad (1)$$

In the Eq. (1) B is the magnetic flux density in T, d is the magnetostrictive constant in m/A, σ [Pa] symbolizes the stress change and μ^σ [N/A²] is the permeability at constant mechanical stress. The Joule effect can be represented by a similar equation:

$$S = c^H \sigma + dH \quad (2)$$

In the Eq. (2) S is the mechanical strain, c^H [m²/N] is the compliance coefficient at constant field strength and d [m/A] is the magnetostrictive constant at constant stress.

The magnetic field strength, H , could be calculated using

$$H = \frac{IN}{l} \quad (3)$$

Where I is the current [A], N [-] number of coil turns and l [m] is length of the magnetic path. Due to the fact that the axis of a typical bar-shaped sample is usually in line with the direction of magnetization only the axial component needs to be considered.

In a magnetostrictive application the physical parameters described above do not remain constant during the operations. Table 3 presents a summary of some features of different materials and the structures where they are normally used. It is intended for use as a comparison between the main materials used in actuators and sensors.

Table 3: Technology features overview [1, 2, 8, 9, 10, 11, 58, 59 and 60]

Typical features	PZT	Terfenol-D	SMA
Actuation mechanism	Piezoelectric material	Magnetostrictive material	Shape memory alloys
Elongation	0.1%	0.2 %	5%
Energy density	2.5 kJ/m ³	20 kJ/m ³	1 kJ/m ³
Bandwidth	100 kHz	10 kHz	0.5 kHz
Hysteresis	10%	2%	30%
Costs as reference	200 \$ / cm ³	130 \$ / cm ³	200 \$ / cm ³

Similar technology overviews are summarized in several references [1], [2], [8], [9], [10], [11] and [32]. These classifications of various technologies can be used to select the optimum

technology candidates for a particular application

Other material properties, related to Terfenol-D only, are summarized in the section 2.2.

These features can only be used for rough comparisons since the properties are variable in each application. These tabled Terfenol-D features are only valid as a starting point because the manufacturing process has a great influence on the exact values for these properties. Also the level of pre-stress and level of magnetic bias can have a great influence on the properties.

2.2 Giant Magnetostrictive Materials and Their Properties

The development of giant magnetostrictive materials (GMM) was started in the 1960's by A.E. Clark and other researchers. The best trade-off giving a high magnetostrain at a relatively low magnetic field over a wide range of operating temperatures is the commercially-available alloy $Tb_{0.3}D_{0.7}Fe_{1.9}$. Terfenol is a rare earth iron alloy. The alloy formulation is known as Terfenol-D, where “Ter” is from Terbium, “Fe” is the chemical symbol for iron, “NOL” is derived from Naval Ordnance Laboratory and “D” is for Dysprosium (Ter+Fe+Nol+D). Terfenol-D was discovered by a research group led by A.E. Clark in the 1970's at the Naval Ordnance Laboratory. One of the first applications of Terfenol-D was a high-performance sonar transducer. Terfenol-D is capable of providing a positive magneto-strain of typical range of 800-2000 ppm at 50-200 kA/m in bulk materials [12] and about 4000 ppm [1, 13] at mechanical resonance frequencies and at high magnetic fields.

$$\lambda_s = \frac{(\Delta L)}{L} \quad (4)$$

$$\lambda_s = 800 - 4000 \text{ ppm} \quad (5)$$

In a typical application for a Terfenol-D rod, parts per million (ppm) values are expressed as the length change multiplied by a million divided by the length of the sample rod. Fig. 5 shows the total range of length change for a given length of Terfenol-D rod.

Elongation versus shaft length

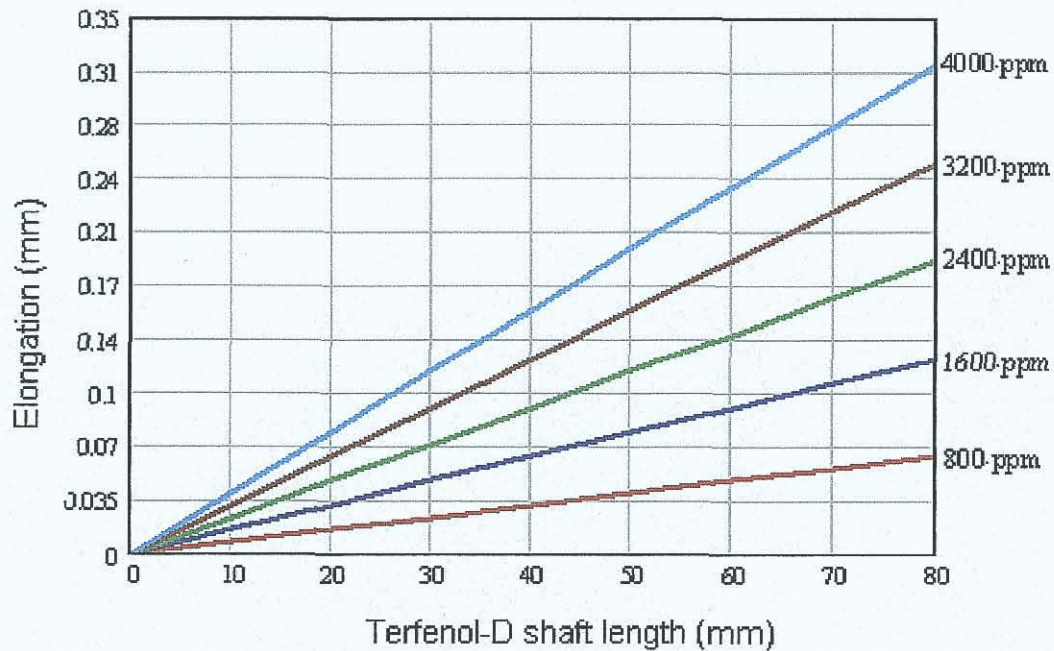


Fig. 5: Length change versus Terfenol-D rod with strain as parameter

Some devices using Terfenol D's property of expansion have been designed using magnetic and mechanical bias to have a zero point at the beginning of the linear section of the performance curve of the material. When the magnetic field is established the response of the material will be along the linear section of the curve, ensuring a response which is predictable and proportional, and in the range of a strain up to 1500 ppm at relatively low flux density of 0.3 T [43]. The delay between magnetic field and the elongation is in the range of one micro second [41 and 52]. Terfenol-D properties are summarized in Table 4.

Table 4: Terfenol-D properties, [1, 2, 4, 5, 6, 9, 12, 14, 16, 44 and 63]

Terfenol-D property	Value range	Comments
1. Nominal composition	$Tb_xD_{1-x}Fe_y$	$0.27 < x < 0.3$ & $1.9 < y < 2$
2. Density δ	9250 kg/m ³	Depending on manufacturing
3. Mechanical properties		
Compressive strength	305-880 MPa	Preferred in applications
Tensile strength	28-40 MPa	To be avoided in applications
Young's modulus E^H	10-75 GPa	At constant H

Terfenol-D property	Value range	Comments
Young's modulus E^B	30-80 GPa	At constant B
Sound speed	1640-1940 m/s	Due to ΔE -Effect
4 Thermal properties		
Coefficient of thermal expansion	12 ppm/ $^{\circ}C$	Not widely reported
Specific heat coefficient	0.35 kJ/kgK @25 $^{\circ}C$	Not widely reported
Thermal conductivity	13.5 W/mK @25 $^{\circ}C$	Not widely reported
5 Electrical properties		
Resistivity	(58-63) $10^{-8} \Omega m$	Not widely reported
6 Magnetomechanical properties		
Relative permeability μ^T/μ_0	9.0-12.0	Permeability at constant stress
Relative permeability μ^S/μ_0	3.0-5.0	Permeability at constant strain
Magnetic saturation occurs at	1.0 T	Preferred distance to saturation
MS coupling coefficient k_{33}	0.6-0.85	Depending on application
MS strain coefficient d_{33}	8-20 nm/A	Depending on magnetic field
MS quality factor Q^H	3.0-20 0	Depending on application

2.2.1 Terfenol-D Production

Terfenol-D is a rare earth alloy, silver in colour, brittle at room temperature and because the raw materials are highly reactive and contain impurities, not easy to produce. At least four different methods have been developed to produce Terfenol-D and are utilized on a near-production basis [1, 17]. The methods are Free Stand Zone Melting (FSZM), Modified Bridgmann (MB), Sintered Powder Compact and Polymer Matrix Composites of Terfenol-D Powder Techniques [17]. The most used methods are the MB and the FSZM. In the FSZM-method, material in the melting zone is held in suspension by surface stress. This method is also called the Directional Solidification Method. In the MB-method, the material is melted completely and crystals are grown starting with a seed crystal [1]. Because side nucleation from the mould walls tends to overwhelm the primary, axial dendrite crystal growth, the minimum Terfenol-D rod diameter is approximately 10 mm. In both processes the material

solidification is specifically controlled by reducing the heat flow in a way which encourages a crystallographically aligned structure. Both methods are used to produce Terfenol-D rods with high magnetostriction and high energy density. The Sintered and Composite processes are used more for the production of Terfenol-D rods for high frequency (higher than 1 kHz) applications where, otherwise eddy currents would cause high losses [49] The methods based on sinter technology are also suitable for more complex geometries.

Solid rods up to 65 mm in diameter and 200 mm in length, laminated rods, rods with holes or odd shapes, rods with square cross sections, plates, discs, sputtering targets and Terfenol-D powder are all available off-the-shelf or can be produced on specific request [14]. New and optimized processing methods, like directional solidification or powder metallurgy methods, are showing a promising way for high volume and cost-effective production [17, 54].

Characterization methods for evaluation of different production samples have been developed and introduced in the reference article [55].

Terfenol-D material is very brittle in tension. Its tensile strength (28 MPa) is very low compared with its compressive strength (up to 880 MPa) The density of the material is higher than the density of normal grades of steel and is about 9250 kg/m³.

2.2.2 Young's Modulus

Some Terfenol-D features are not constant during an operational cycle. One of these features is the Young's modulus, which varies almost linearly with the magnetic field. A sketch of the ΔE -Effect is depicted in Fig. 6.

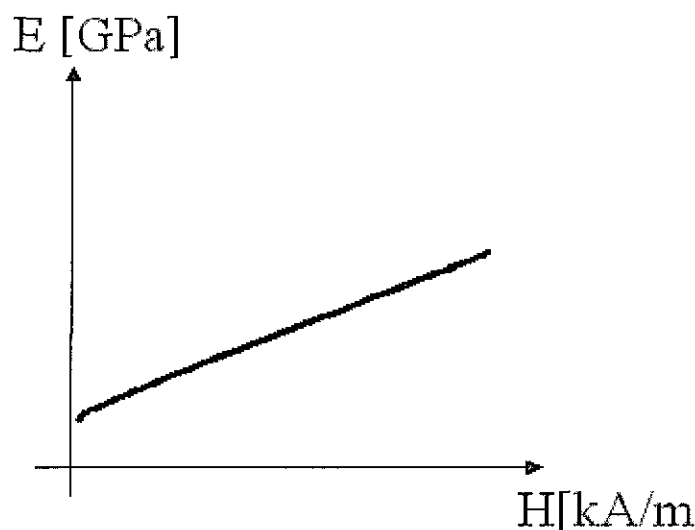


Fig. 6: Young's modulus versus magnetic field

Young's modulus at constant value of magnetic flux density, E^B , can be expressed as follows:

$$E^B = \frac{E^H}{(1 - k_{33})} \quad (6)$$

As equation (6) suggests, theoretically there is a value of flux density at which Young's modulus becomes infinite. When this property occurs in a sample of Terfenol-D, it is said to have reached "a blocked state", and no rotation of magnetic domains is possible and the material is prevented from changing its dimensions in response to stress [18].

2.2.3 The Magnetomechanical Coupling Factor & the Magnetostrictive Coefficient

In the transducer application, magnetic energy is converted into mechanical energy. The efficiency of the energy converting process is governed by the magnetomechanical coupling factor, k_{33} . The value of this factor usually varies between 0.5 and 0.8, indicating that the efficiency varies between 50 and 80% [1, 19, 36 and 46]. In applications where only the longitudinal elongation is of interest (for standard actuator applications) the material properties related to the longitudinal axis are relevant. This mode is called 33-mode and the magnetomechanical coupling factor is called k_{33} . The magnetomechanical coupling factor, k_{33} , is given by equation (7).

$$k_{33}^2 = \frac{d_{33}^2}{\mu_{33}} \cdot E^H \quad (7)$$

In this equation, the magnetostrictive coefficient d_{33} is the slope of the strain λ_{33} versus magnetic field strength H_{33} :

$$d_{33} = \frac{(d \lambda_{33})}{(d H_{33})} \quad (8)$$

In Fig. 7 the magnetostrictive coefficient d_{33} is depicted graphically. There is a region in the graph where the slope is high and the relationship between the strain and the magnetic field is almost linear. This is the optimal working range, and is preferred for converting the magnetic

into mechanical energy because of the minimization of losses and because the relationship is almost linear.

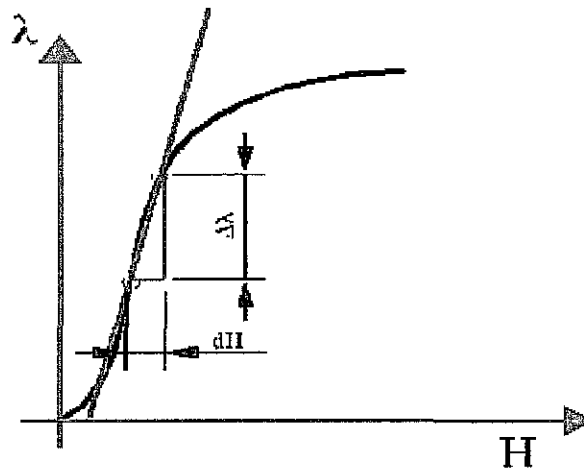


Fig. 7: Strain versus magnetic field

Neither the magnetomechanical coupling factor k_{33} nor the magnetostrictive coefficient d_{33} remain constant throughout the operating conditions in real magnetostrictive applications. Fig. 8 shows the impact of applied pressure on the coefficient d_{33} and on the factor k_{33} for an application where Terfenol-D is used, to illustrate this variability. It is common for both coefficients to show maxima at a given value of pre-stress.

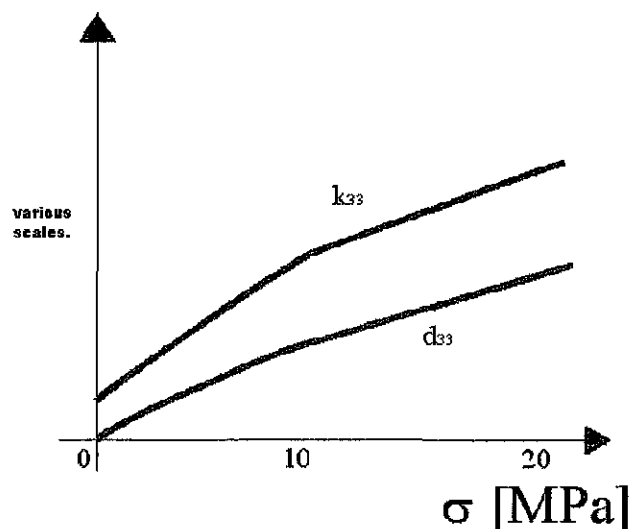


Fig. 8: k_{33} and d_{33} versus applied stress [19]

For effective and efficient operation, both coefficients need to be as high as possible. The magnetostrictive coefficient d_{33} is often called the magnetostrictive strain coefficient. For

Terfenol-D the value of the magnetostrictive coefficient d_{33} is in the range 5-70 nm/A [1, 20]. Both coefficients depend not only on the pre-stress as illustrated above, but also on the applied magnetic field.

2.2.4 Quality Factor

Under quasi-static condition (continuous excitation under a sinusoidal alternating current), assuming zero pre-stress and assuming a linear relationship between the strain and the magnetic field, the strain is given by:

$$\lambda_{33} = d_{33} \cdot H_{33} \quad (9)$$

The coefficient d_{33} is found to be almost constant for most frequencies. However when the frequency approaches a value causing the sample to resonate in its longitudinal direction, the amplitude of the vibration increases abruptly [12]. For this to be observed the sample of Terfenol-D must be free to vibrate, so that if it was in an actuator it would be an unloaded actuator. The strain at resonance is much higher than it is under quasi-static conditions. The strain at the resonance condition is given by:

$$\lambda_{33} = Q_m \cdot d_{33} \cdot H_{33} \quad (10)$$

The amplification factor of the strain at its first resonance over the strain under quasi-static conditions is the quality factor Q_m . In the case where the actuator's vibrating end is totally free, the quality factor Q_m is due to mechanical losses occurring internally in the material [1, 21] and is equal to Q^H . This internal material quality factor Q^H is in the range of 3-20 [1, 21]. On the other hand, when there is a load, when the sample of Terfenol-D encounters a resistance to its free movement because of the surrounding assembly, a damping feature is introduced into the vibration and the quality factor Q^H is reduced to a value Q_m .

2.2.5 Permeability

The constant $\mu_0 = 4\pi \cdot 10^{-7}$ H/m defines the magnetic permeability of free space. The permeabilities of most materials are close to the permeability of the free space. These materials are called paramagnetic or diamagnetic. In the case of ferromagnetic materials the

permeability is very large and it is common to express the permeability in terms of a new property, the relative permeability. This is the number of times the permeability of free space must be multiplied by in order to arrive at a value for the permeability of the material. Since this is a number, values of relative permeability are dimensionless. The relative permeability therefore indicates the amplification of magnetic effects in a magnetic material, which is expressed as the amplitude of the magnetic flux density in a magnetic material in response to a given magnetic field. The relative permeability of Terfenol-D is much smaller than of a magnetic iron. Table 5 presents a range of relative permeabilities including Terfenol-D.

Table 5· Relative permeability [22]

Relative permeability	Value range
Mu-metal	20000
Permalloy	8000
Magnetic iron	200
Nickel	100
Terfenol-D	<10
Aluminum	1

When a ferromagnetic material has been magnetized using a magnetic field and that field is removed, the material will not relax back exactly to zero magnetization when the magnetic field is removed. It must be driven to zero by imposing a magnetic field in the opposite direction. So, the magnetization curve is a loop and this loop is called a hysteresis loop. The lack of retraceability is defined as hysteresis. It requires some energy in order to cause magnetic domains to become oriented in the same direction as a magnetic field [22]. For an actuator or sensor smart material, the aim is to develop materials with the smallest hysteresis. On the other hand, a material to be used for magnetic memory with a high capacity, a large hysteresis is required, which is also the case in most permanent magnet applications Fig. 9 is taken from a website called HyperPhysics. The hysteresis loop is explained using some graphical indications of the magnetic domains.

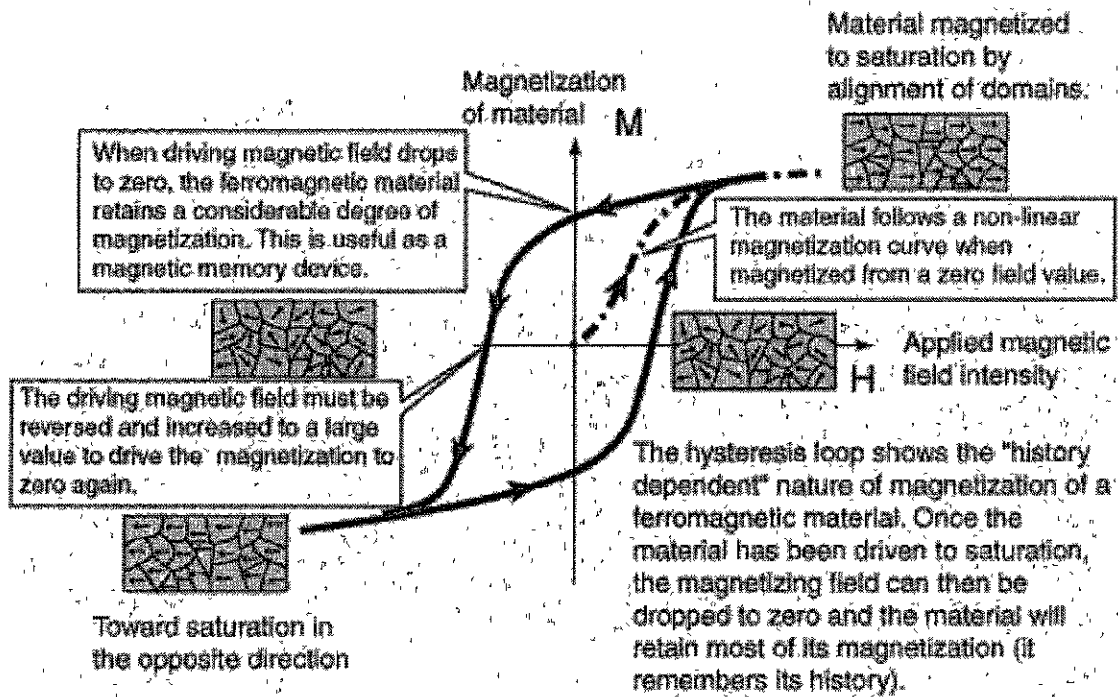


Fig. 9. Magnetization curve [22]

The following figure, Fig. 10 indicates the typical magnetic behavior of iron and compares it with that of aluminum.

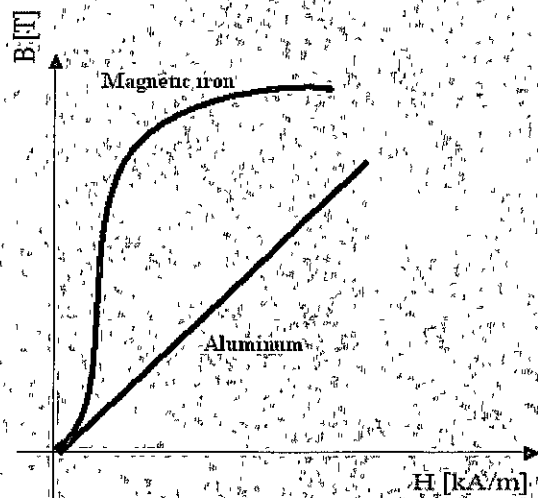


Fig.10: B-H curve for comparison

When the material has a very small response to an applied magnetic field, as in the case of aluminum the behavior is similar to that of free space and the relative permeability is almost equal to one.

Another way to specify the magnetic behavior is to use the term magnetic susceptibility κ_m . The magnetic susceptibility κ_m specifies how much the relative permeability differs from value of one.

$$\kappa_m = \frac{\mu_{33}^T}{\mu_0} - 1 \quad (11)$$

In the case of an active material like Terfenol-D the relative permeability depends on the pre-stress and the frequency used in its operation. Fig. 11 represents the magnetic behavior of Terfenol-D. It shows how the material responds to an applied magnetic field (H) by developing a magnetic flux, with a flux density (B). The permeability is the value of B/H. The diagram shows the hysteresis loops [similar to 57].

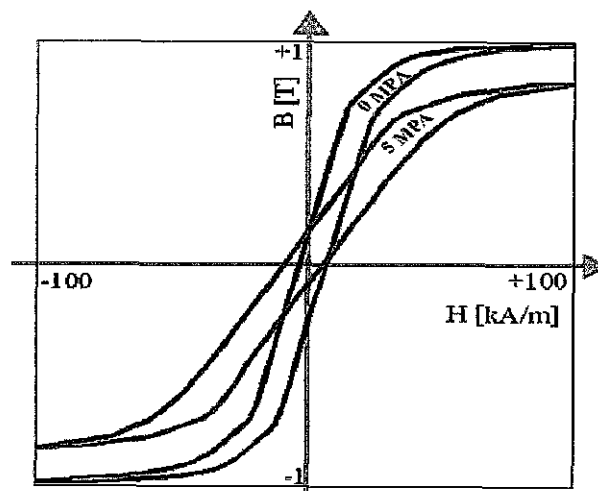


Fig. 11: General B-H curve

It is found that higher amounts of pre-stress reduce the relative permeability. For positive magnetostrictive materials an explanation for this could be that it is because when the pre-stress is high the domain movement requires more mechanical energy, and therefore the material is unable to respond to the magnetic field as well as it can when the pre-stress is lower. For magnetostrictive materials there is another response to the magnetic field in addition to the ferromagnetic effect (amplifying the magnetic flux) and this is the change in strain. The two effects are related, but the relationship between them is complex. For these materials there is also a hysteresis feature associated with the magnetostrictive effects [37]. Some hysteresis models to calculate the hysteresis have been introduced [42, 45]. A typical

hysteresis loop, showing magnetostrictive strain in response to a magnetic field for a sample of Terfenol-D is illustrated in Fig. 12.

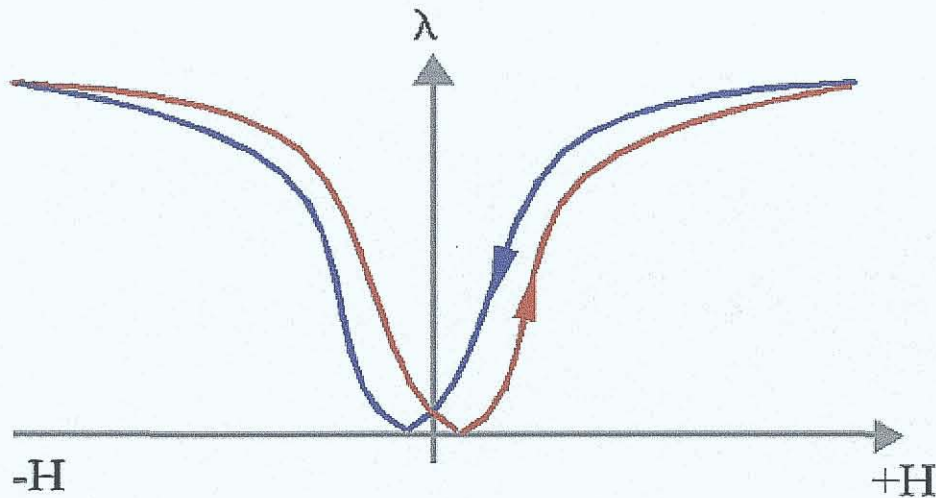


Fig. 12: Full loop of magnetization [23]

Also for these materials another property connected with permeability can be defined. The permeability at constant strain is defined by:

$$\mu_{33}^S = \mu_{33}^T \cdot (1 - k_{33}^2) \quad (12)$$

This property applies to a smart material and is useful when it is in the “blocked” state. In the blocked state the material is prevented from increasing its strain by external forces and so no further rotations of magnetic domains are possible [18].

2.2.6 Blocked Force

The maximal achievable force is called the “blocked force”. A simple force-displacement relationship is valid for elastic behavior:

$$F_T = S_m \cdot \Delta L \quad (13)$$

In this equation S_m is the stiffness of the active element and is defined by the Young's

modulus (at constant magnetic field), the cross sectional area and the length of the Terfenol-D element:

$$S_m = \frac{E^H \cdot A}{L} \quad (14)$$

Combining the last two equations with substitution of the stiffness, and also substituting magnetostrictive strain ($\lambda = \Delta L/L$) leads to equation of definition for a blocked force.

$$F_B^H = A \cdot E^H \cdot \lambda_{max}^H \quad (15)$$

There is an axial force which refers to the maximum amount of magnetostrictive strain that can be applied to a sample of Terfenol-D. This occurs at very high magnetic field strengths (at λ_{max}). According to this relationship the blocked force F_B^H is proportional to the Young's modulus and the maximal strain at an applied magnetic field. Blocked forces of about 12000 N are achievable with a Terfenol-D shaft with a diameter of 20 mm and with a moderate magnetic field [19].

2.2.7 Typical Optimization

All the above described material properties have highly variable characteristics due to the changing conditions during an operational cycle. To achieve the desirable functionality with accuracy, good controllability and high power density, a number of additional arrangements are required to optimize the performance of a Terfenol-D transducer. One of the typical optimizing arrangements is to create a magnetic field with a permanent bias using permanent magnets, in order to operate in a region of the performance curve where the slope is at a maximum value. This condition is shown in Fig.13.

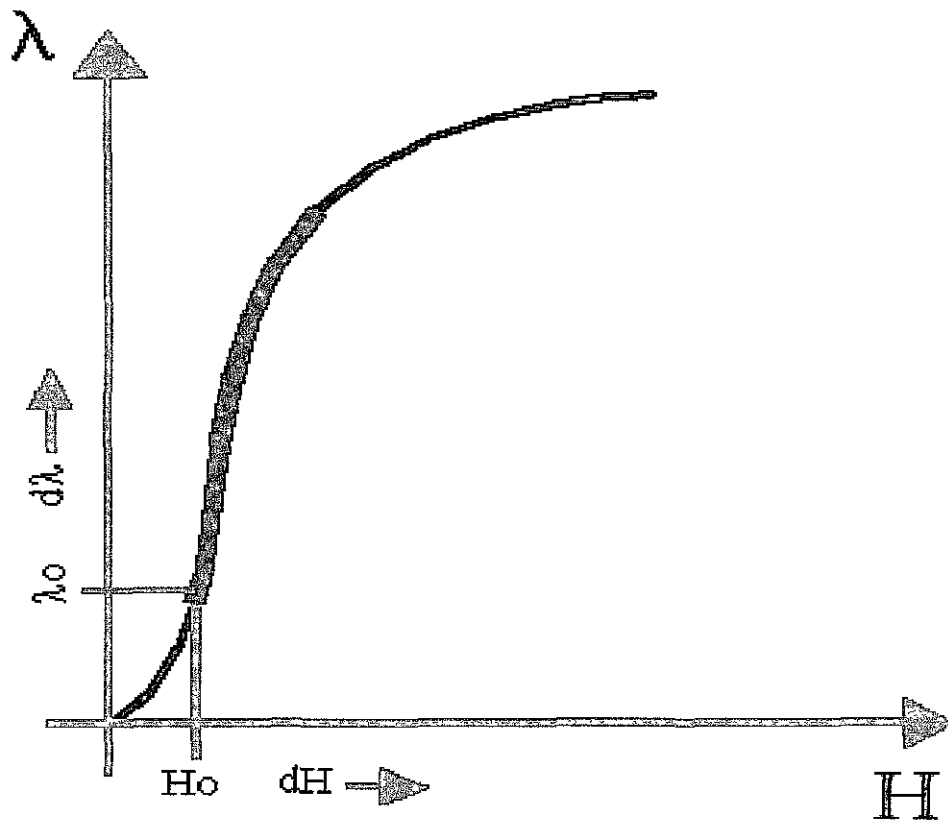


Fig.13: Typical optimization with magnetic bias

The level of pre-magnetization depends on the transducer design and is usually about some 10 kA/m. The other method of optimization is to apply a defined mechanical pre-stress which can cause rotations of magnetic moments in a way that they are aligned perpendicularly to this applied stress. In this condition the smallest increase in the applied magnetic field will produce the greatest magnetostrictive strain. The applied mechanical pre-stress is not very large.

It can be observed that larger magnetostrictive strains can be produced by the same magnetic field strengths when the pre-stress is increased. This is illustrated for Terfenol-D in Fig. 14.

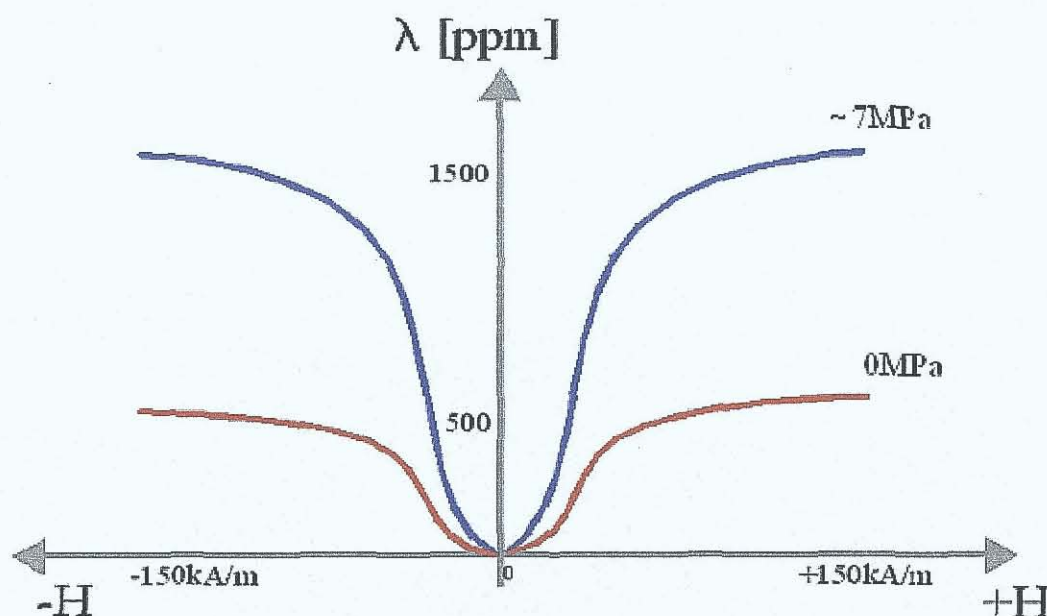


Fig.14: Typical optimization with mechanic bias [similar to 24, 25 and 50]

For larger pre-stress values, another effect is observed. The energy required to overcome the pre-stress when producing a positive magnetostrictive strain becomes the dominant factor, with the result that magnetostrictive strain becomes smaller for very large values of pre-stress. There is therefore a pre-stress value where the magnetostrictive strain reaches a maximum. The optimal pre-stress is the stress which causes the magnetic moments to be aligned predominantly perpendicular to the rod's longitudinal axis without introducing so much load that the work required to overcome it becomes overwhelming [25]. The butterfly curves, showing strain versus applied magnetic field at various pre-stresses, as illustrated above, are typically used to quantify the optimal pre-stress. The strain capability of a Terfenol-D element in a transducer can be increased by factor ~ 3 as a result of the correct pre-stress selection. The pre-stress is applied using a spring. There is interdependence between the choice of magnetic bias and mechanical pre-stress, with one factor having an effect on the other. The choice of magnetic bias and mechanical pre-stress is investigated in several studies. A general overview of this effect is given in reference articles [24, 25, 38, 39 and 40]. Furthermore, the impact of cyclic stress on Terfenol-D on durability has to be taken into account; some information can be viewed in reference article [35].

Further optimization, linked to the same physical background, is possible by choosing the best manufacturing method [17] or annealing process [26] to improve the material texture, which has an effect on the direction of the magnetic moments. Some additional optimizations are feasible in terms of using a specific layout for the magnetostrictive transducer. It depends on

the exact location of the active coil and permanent magnet in the transducer. Typical actuator layouts, with their advantages and disadvantages, are depicted in Table 5 schematically.

Table 6: Typical layouts in comparison [1, 2]

Actuator Layout	TC	TCM	TMC	MTC
Typical actuator features	1	1	1	1
Magnetic bias with	DC coil	Permanent magnets		
Magnetic bias level	Low	Medium	Medium, high	High
Terfenol-D shape	Rod, bar	Rod	Rod	Hollow rod
Structure	Simple	Medium	Medium	Complex
Field inhomogeneity	Low	Low	Medium	High

For a simple, cost-effective actuator with a high energy density the TC & TCM configurations should be given priority. Finally the required functionality, cost level and available packaging can have an influence also on the best actuator configuration.

2.3 Applications of Terfenol-D

Magnetostrictive technology has been successfully employed in low and high volume products. The magnetostrictive effects discussed in the previous sections have been put to use in several applications of Terfenol-D. The two main areas of Terfenol-D applications are actuators and sensors. The following section of this thesis gives an overview of typical GMM applications.

2.3.1 Reaction Mass Actuator

Etrema [27] has designed, built and validated an actuator device, which is capable of generating useful forces although it can operate over a wide bandwidth of frequencies. This particular reaction mass actuator was designed to operate over a bandwidth from 150 to 2000 Hz. It was also able to generate a force of 4000 N or an acceleration of 30 g at the device's resonant frequency of 635 Hz [27]. Generating seismic waves with this actuator and analyzing the reflection provides an indication of underground and hidden structures and

formations. Fig. 15 shows a cross section of a reaction mass actuator.

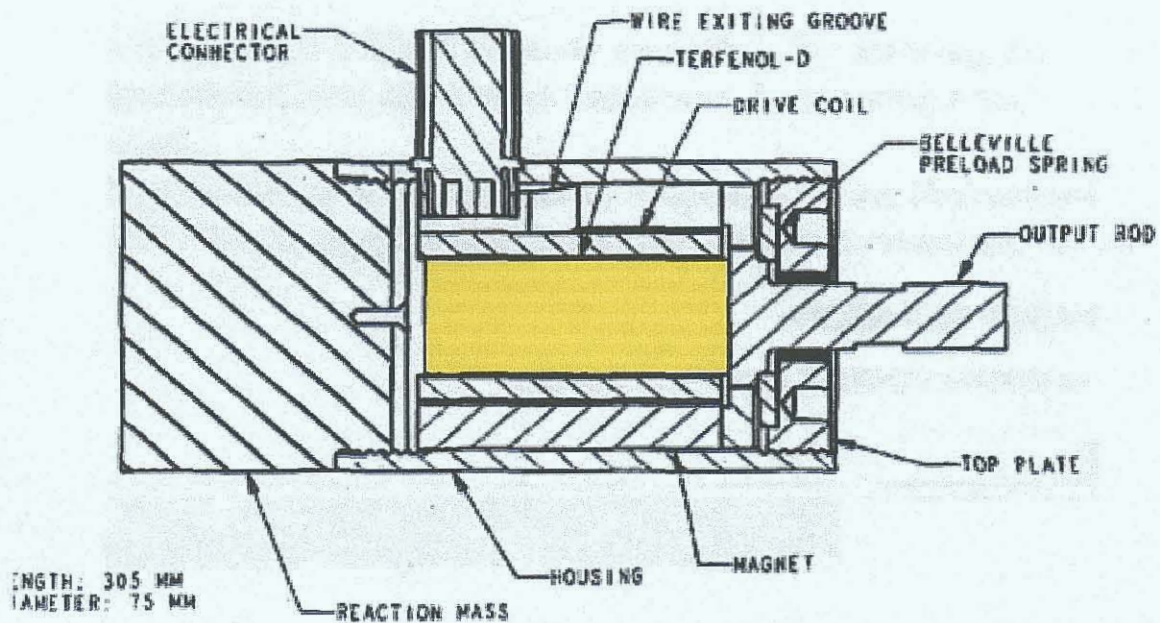


Fig. 15: Reaction mass actuator [27]

One example of a further direct magnetostrictive microactuator has been introduced in the reference article [53]. The goal for this application was a structure in millimeter size with nanometer resolution. Axial force of 25 N and 3 micrometer in displacement at 1.5 A, and resolution of 250 nm per 0.1 A, has been achieved [53].

2.3.2 A standard Terfenol-D Actuator

Etrema also designed, build and validated several other actuators for different purposes. An actuator with its layout depicted in Fig. 16 is available off-the-shelf, giving displacements up to 250 μm and forces up to 2,200 N, and operating at frequencies up to 2500 Hz. The operational temperature of this actuator is typically in the range from $-20\text{ }^{\circ}\text{C}$ up to $+100\text{ }^{\circ}\text{C}$. In addition, ultrasonic actuators for higher frequencies are available. Other types of Terfenol-D actuators have been developed by Cedrat Recherche [14].

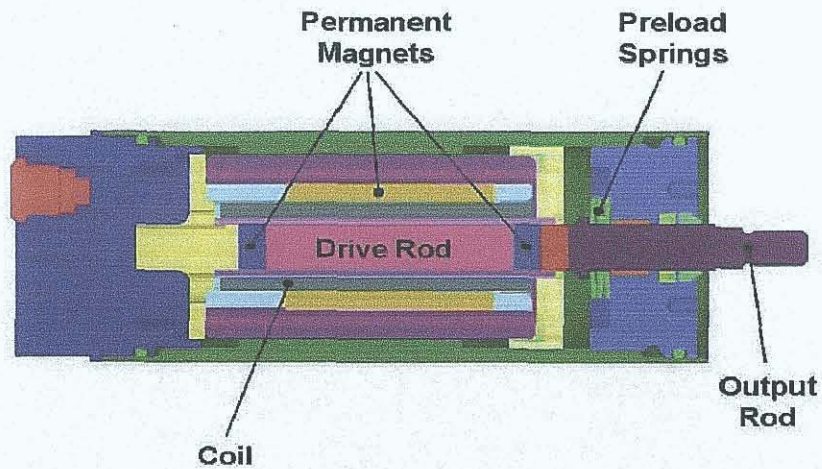


Fig. 16: Standard actuator [14]

2.3.3 Linear Motor Based on Terfenol-D (Worm Motor)

Energen, Inc. [15] has designed and built a compact linear motor based on the smart material Terfenol-D. The central feature of this linear motor is a rod of Terfenol-D surrounded by an electric coil which, when energized, causes the rod to elongate. The actuator is mounted between two clamps. By operating the actuator and the clamps in an appropriate sequence the rod of smart material moves forwards or backwards. Fig. 17 shows the principle by which the functionality is achieved.

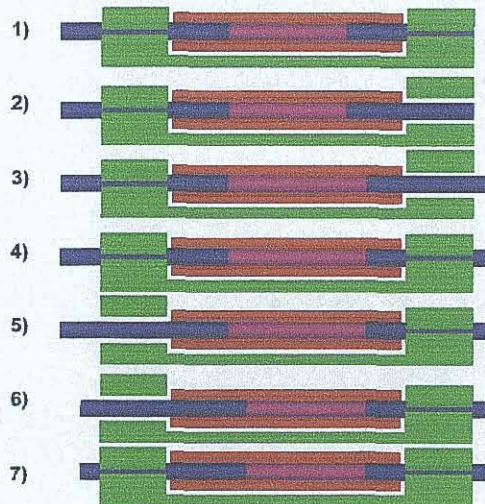


Fig. 17: Worm motor [15]

In the first step the power is off and both ends are clamped. Then one of the clamps is released by energizing (step 2) and after this by energizing the actuator coil (step 3) the front

end of the rod is moved forwards due to the elongation of the Terfenol-D. During this elongated condition the forward clamp is closed to hold the rod (step 4). Then the rear clamp is energized to allow movement (step 5). Next in the sequence the actuator coil is switched off and the rear end of the rod moves forwards (step 6) In the last sequence the rear clamp is closed again to provide the full hold force capability. This arrangement achieved very accurate control of position to within a few microns over a total stroke length of 20 mm. The holding force capability was up to 3000 N [15]. A similar application of the worm motor has been introduced in a micro mobile robot [34].

2.3.4 Terfenol-D in Sonar Transducers

A good sonar transducer should produce high mechanical power at low frequencies. Often an additional trade-off must be achieved between a broad bandwidth of operating frequencies, and a low quality factor Q [6]. The original, widely employed, transducers based on nickel, with a magnetomechanical coupling coefficient of 0.3, have been replaced by newer technology based on the newer magnetostriction materials. In fact Terfenol-D transducers are able to operate with high mechanical power and at low frequencies because their magnetomechanical coupling coefficients can be as high as 0.8 and their quality factor Q is low. Fig. 18 shows various types of transducers. Layout a) depicts the typical Tonpilz sonar transducer which can operate over a bandwidth of 200 Hz at the resonant frequency of 2000 Hz ($Q=10$) and a source level of 200 dB [6]. Layout b) and c) from reference [6] show various designs to convert the linear motion of Terfenol-D into appropriate controllable vibrations. Further details for various applications are given in the references [6 and 9].

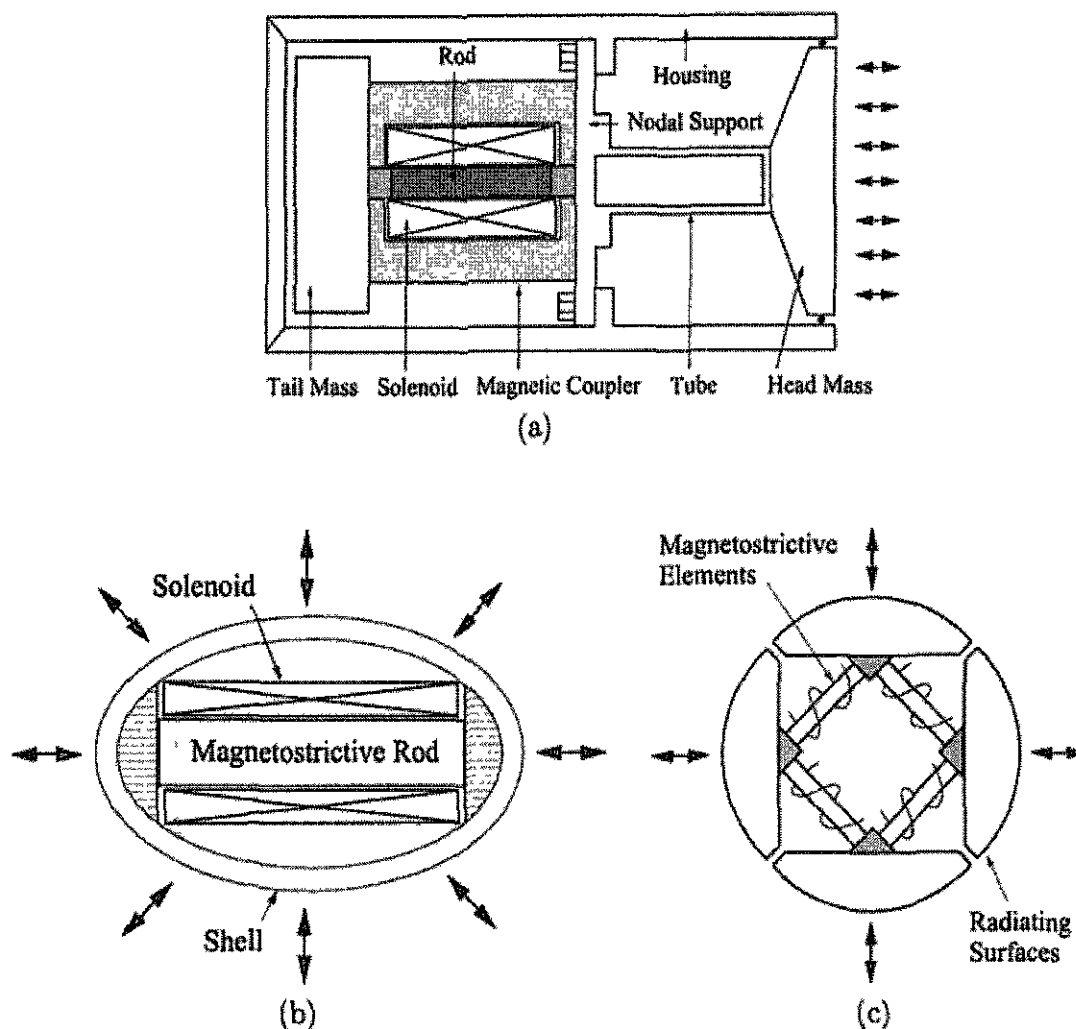


Fig.18: Sonar transducers [6]

2.3.5 Terfenol-D Wireless Rotational Motor

A structure has been developed to convert the elongation movement of a magnetostrictive material into a rotary motion to form a micro-stepping rotary motor [28]. The principle of operation is based on “Inch worm” functionality. A prototype based on this technology provides high torque and precise *positional control in a power-off self-blocking arrangement*. The magnetostrictive micro-stepping motor consists of two sets of pole pairs, and two sets of driving elements, which work in engagement and disengagement sequences to enable the micro-stepping movement. Part of the energy is stored in u-shape springs between the pole pairs. A prototype with dimensions of 260 x 115 x 108 mm was capable of producing 12.2 Nm torque at 0.5 rpm rotational speed using 600 W power. The stepping resolution

achieved was 800- μ rad. More details are depicted, analyzed and discussed with test results in reference [28]. Fig. 19 shows the layout of the micro-stepping rotary motor.

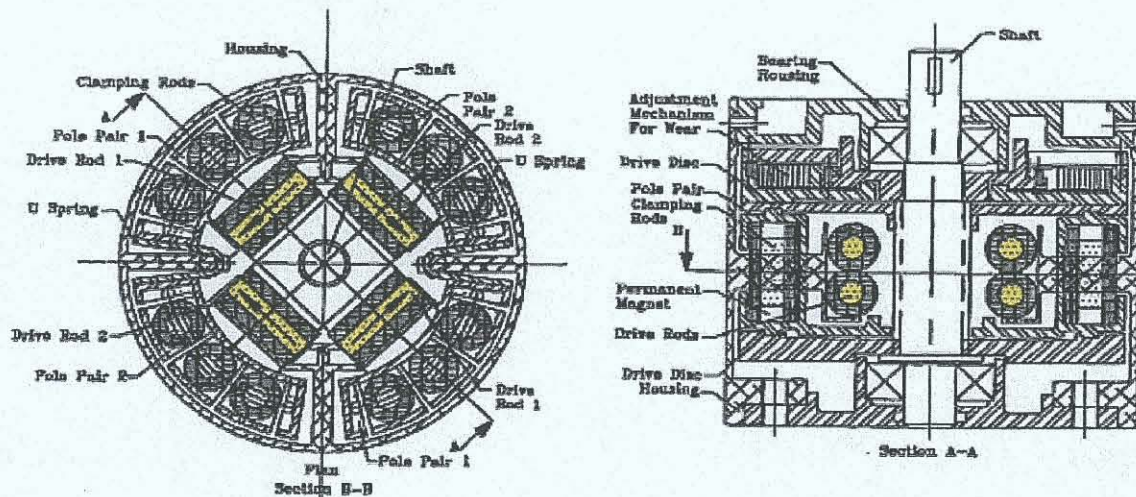


Fig. 19: Rotational stepping motor [28]

2.3.6 Terfenol-D Electro-Hydraulic Actuator

Magnetostriction can be used in linear motion actuators in combination with conventional technologies like hydraulic technology. Small elongations, added step-by-step, can be used as the working principle in a simple pump for high pressure fluid flow. A system combining the magnetostrictive functionality with hydraulic non-return valves has been introduced in reference [29]. The system consists of a magnetostrictive pump, a hydraulic flow distribution sub-system, a sub-system to convert hydraulic energy (pressure [Pa] x fluid flow [m^3/s]) into mechanical energy (force [N] x movement [m]) and control electronics. Fig. 20 depicts the structure of the magnetostrictive pump. A prototype using this structure achieved an operational pressure of 4.2 MPa and a fluid flow rate of more than 3 l/min [29]. The simplicity, high power density and fast response are very promising. More details with a discussion of testing and simulation results are published in reference article [29].

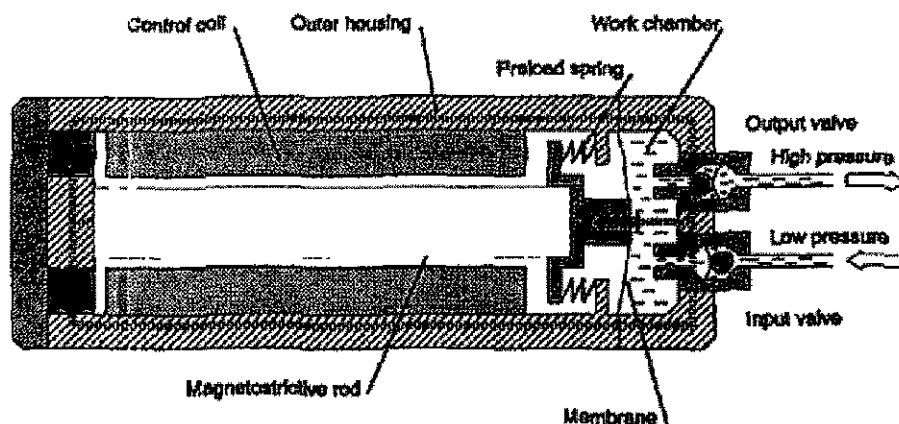


Fig. 20: Electro-hydraulic actuator [29]

2.3.7 Wireless Linear Micro-Motor

Various types of standing-wave ultrasonic motors have been developed at Cedrat Recherche. This is one of the magnetostrictive film applications. The linear micro-motor is achieved as a self moving silicon plate with small magnetostrictive films applied to its surface. The major advantage of using a smart material like Terfenol-D is that actuation can be achieved without contact using a magnetic field produced by an electric coil which could be located some distance from the moving parts. The applied magnetic field produces a resonating flexing shape; this leads to the vibration of the plate and causes a motion of approximately 10-20 mm/s [1, 2 and 12]. A similar principle is used in a rotational motor. At a 20 mT excitation field the typical performance is a rotating speed of 30 rpm with a torque of 1.6 μNm . Fig. 21 shows the functional principle of the thin film actuator based on magnetostrictive materials.

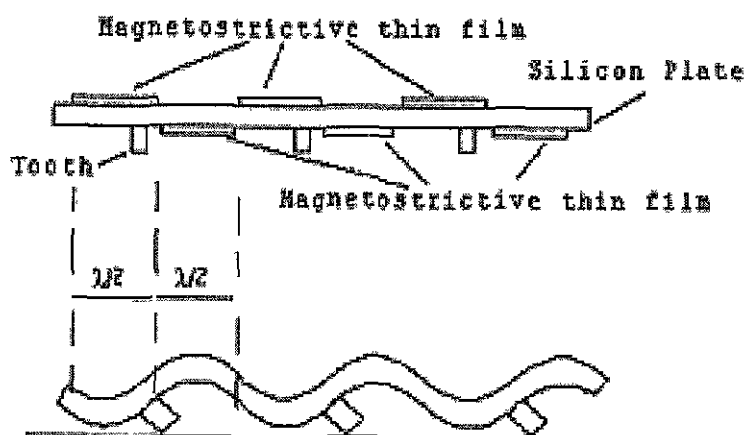


Fig. 21, Magnetostrictive thin film actuator [12]

Further micro-pump mechanism, based on magnetostrictive films, has been introduced in reference article [47].

2.3.8 Other Magnetostrictive Film Applications

Coating methods suitable for Terfenol-D and other magnetostrictive materials have been developed for a number of applications based on using the magnetostrictive properties of the film. Sputter-deposited magnetostrictive films are used in actuators in microstructures to work in simple, cost-effective, contact-less arrangements at high operational frequencies [30]. Depending on the composition and sputtering conditions a strain of up to 700 ppm at 0.5 T for TbDyFe is achievable. Various layouts of cantilever-type and membrane-type microsystems have been published in recent years. Lateral patterning of the magnetostrictive film is essential in order to obtain large and predictable deflections. The deflection of a double-clamped cantilever produces a curvature of the substrate, which can be either convex or concave. If only one side is coated the deflection under the magnetic field is predictable and can be controlled for different purposes. A possible structure for a control valve is shown in the following figure, Fig. 22. The coated area of the bilaterally fixed transverse substrate is shown in colour. The arrangement has the advantage that the fluid flow could be controlled contact-less to moving parts by a magnetic field, and a promising functionality can be obtained using this micro-valve structure [1, 2 and 30].

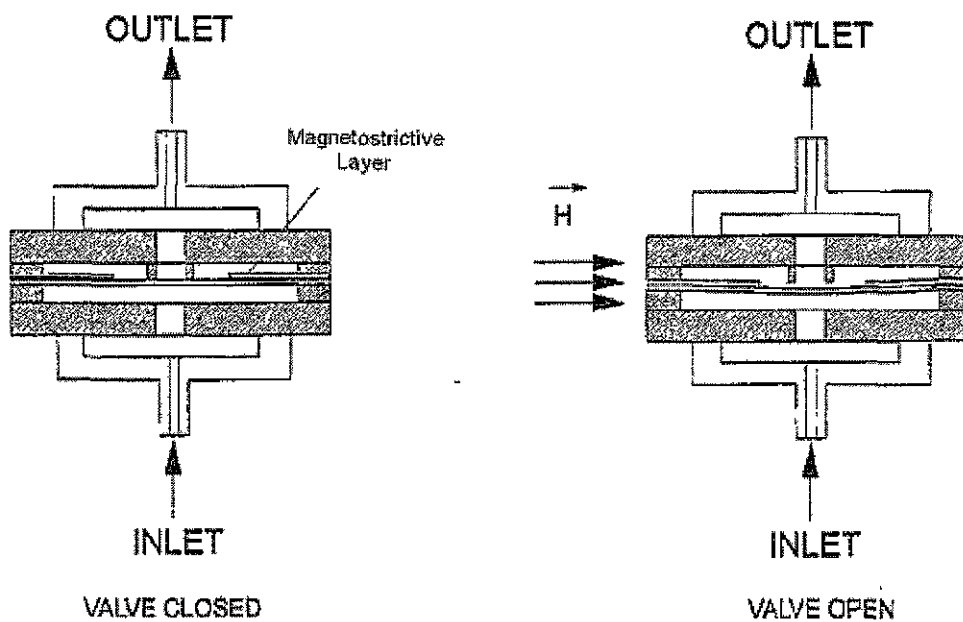


Fig. 22. Thin film application in valves [30]

2.3.9 Magnetostrictive Contactless Torque Sensors

The high efficiency in converting magnetic energy into mechanical energy, and vice versa, enables magnetostrictive technology to be used in contact-less sensor applications. In these applications the Wiedemann, the Villari, the ΔE and the Matteucci effects are used to detect the measurable magnetostrictive changes and so to provide quantifiable data on stresses, forces or torques. Changes in mechanical properties like stresses and strains produce predictable changes in magnetic properties in magnetostrictive material. In the sensor applications mechanical energy changes generate magnetic energy changes. Often pick-up coils surrounding the magnetostrictive material are used to detect changes in permeability properties and electronics are used to convert, filter and amplify the basic data to produce data on strains and stresses, which in turn give estimates for loads (pressure, force, torque) In the following Fig. 23 a) [12] a sensor based on magnetostrictive technology has been sketched. In this application torque was applied to the shaft, and shear stress is generated along the length of the shaft. This also produces tensile and compressive stresses in the directions of $\pm 45^\circ$ to the longitudinal shaft axis. The two stress vectors are oriented 90° to each other and have opposite signs (to indicate tensile and compressive stresses). When the shaft contains a magnetostrictive material, or has a collar containing a magnetostrictive material attached to it, the magnetic permeability measured along these directions will change. Changes in magnetic flux can be measured without any physical contact being necessary using the Hall Effect or with perpendicular coils. Applications like this have been developed and are close to a possible high volume application in the automotive area. Another type of contact-less sensor application is shown in Fig. 23 b) [12]. The principle is based on the change of permeability due to shear stress. For less sensitive measurements, i.e. for restricting the torque, less expensive magnetic steels or alloys can be used. In the diagram the torque in the drill shaft is measured by two pick-up coils connected in series. One coil is located over the flutes and the other over the shank. The permeability change of the shank is less sensitive to the torque change than the permeability change of the flutes. An additional excitation coil provides a magnetic field, while the sensor output is the difference in voltage from the two pick-up coils due to the different permeability sensitivity of the shank and flutes. More details and linked references are given in reference article [12]

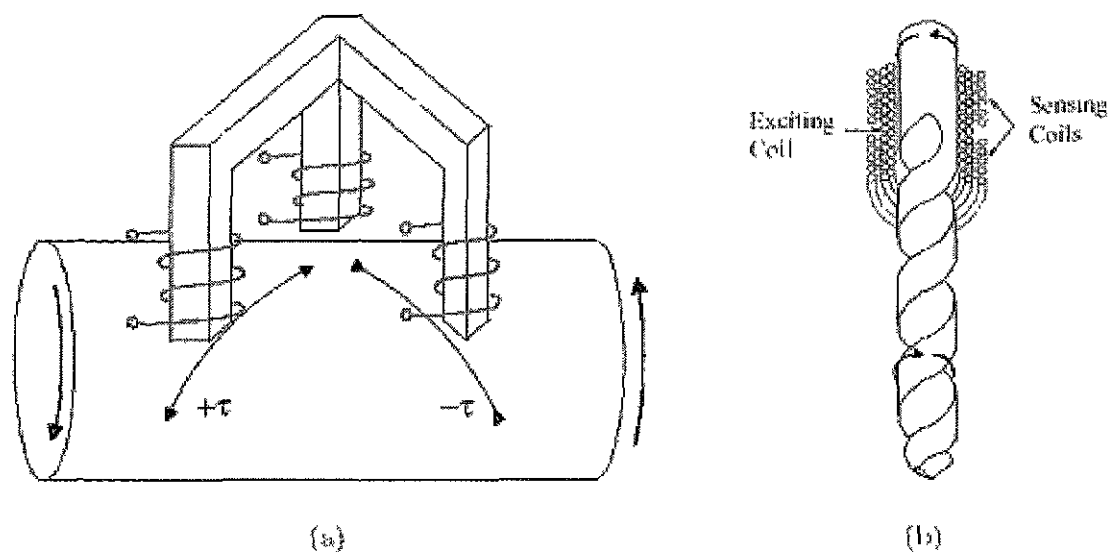


Fig 23: Contactless sensor application based on magnetostrictive materials [12]

Another example where the inverse magnetostrictive or magnetoimpedance effect is used in sensor applications is the remote-interrogation strain gauge [31]. When using the inverse magnetostriction effect, it is common to use films of magnetostrictive materials or amorphous multilayer of these materials. The instruments operate at frequencies in the range from 10 MHz to 8 GHz [31]. The remote-interrogation principle is shown in following graph. The high frequency allows the sensor antenna to be small in size and a broad bandwidth of frequencies can be used to produce valid measurements. Basically the change in mechanical stress (or strain) produces a corresponding change in the AC-permeability of the strained / stressed material. The use of a magnetostrictive material with a high efficiency in converting mechanical energy into magnetic energy increases considerably the sensitivity at high stress when compared with more conventional strain gauges sensors. Fig. 24 shows the remote-interrogation functionality principle [31] for sensor applications in two configurations. In configuration a) the sensing element is wrapped around a core containing the magnetostrictive material and in configuration b) the sensing element is coated with a film of a magnetostrictive material.

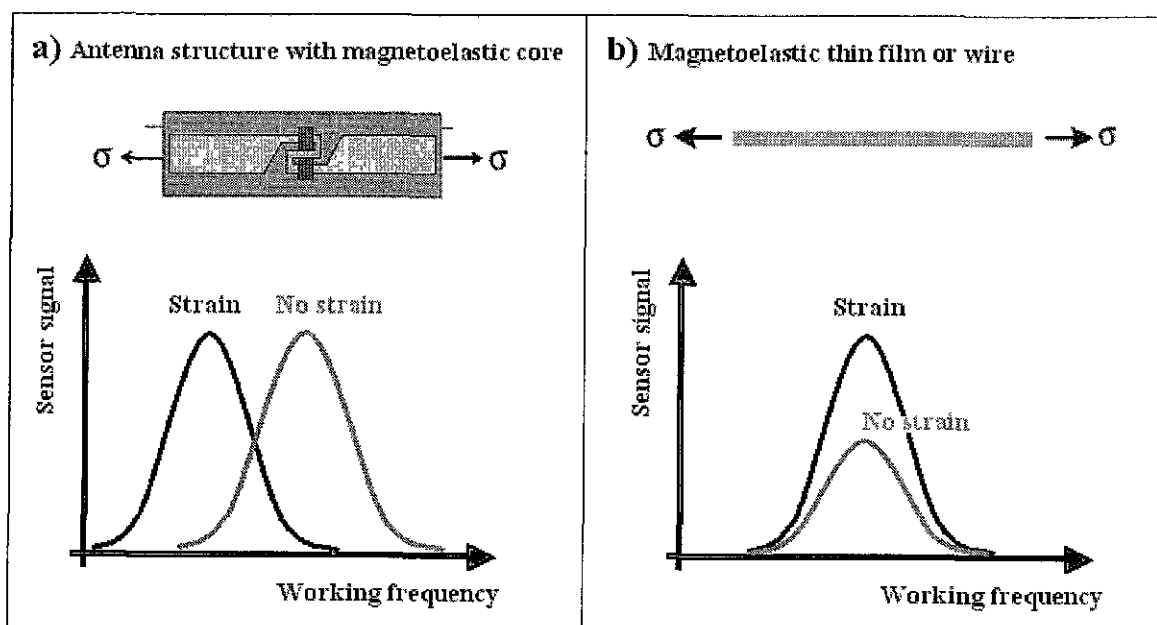


Fig. 24: Sensor applications, similar to [31]

This list of applications is not comprehensive but gives an overview of applications based on magnetostrictive materials, mainly on Terfenol-D, with a potential for high volume production. It illustrates the area of the greatest interest for many research projects. Several companies and universities are involved in research areas closely related to magnetostriction, especially related to materials like Terfenol-D. Applications such as micro-positioners, fluid injectors, active damping systems, helicopter blade control systems, as well as some hybrid-applications using a combination with piezoelectric effects have been introduced into the public domain.

2.4 Remarks on MS Technology

The Magnetostrictive (MS) technology is one of the older “newcomers” coming to the market at high speed. Magnetostrictive technology has been successfully employed in several automotive and non-automotive applications. The market readiness is growing for magnetostrictive applications with more intelligence in the functionality keeping with, or even improving on, the simplicity of the operating system. Features of magnetostrictive applications like power density, accuracy and dynamic performance are excellent catalysts for the implementation of the technology in high volume applications. Since some active materials like Terfenol-D have been developed with stable characteristics over a wide range of temperatures and have a high magnetoelastic coefficient, interests in the technology is

growing quickly. The appropriate manufacturing technologies for high volume applications have also been developed. Further work in devising new structures and various combinations of different technologies still needs to be carried out to illustrate the capabilities of "MS" technology regarding superiority in functionality.

Chapter Three

Literature survey of magneto-rheological (MR) technology

3.1 Rheological Background of the MRF Technology

Rheology is the study of flow and deformation. Flow capability and deformation, which is either elastic or plastic, have common features and the study of both subjects must overlap. In a conventional application with conventional liquids i.e. a hydraulic pump or damper the characteristic depends on viscosity and the viscosity change of viscosity with temperature. Because of this, temperature would normally be considered as an uncontrollable feature. There are two ways of expressing the viscosity – dynamic and kinematic viscosity. Dynamic viscosity η is defined by:

$$\eta = \frac{\tau}{\dot{\gamma}} \quad (16)$$

In this equation η is in [Pa·s], the τ [Pa] is the shear stress and the $\dot{\gamma}$ [1/s] is the shear rate.

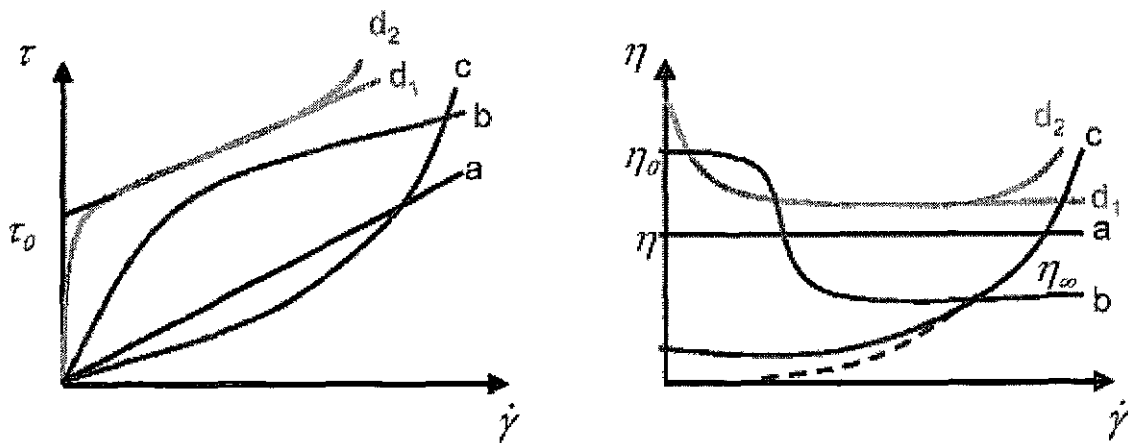
Kinematic viscosity ν [m²/s] is defined by following equation:

$$\nu = \frac{\eta}{\rho} \quad (17)$$

In this equation ρ is the density in [kg/m³] and η is the dynamic viscosity. The temperature dependency of the conventional fluid i.e. silicon oil or mineral oil is defined by approximation:

$$\eta(\theta) = A \cdot e^{\left(\frac{b}{(\theta + 273)}\right)} \quad (18)$$

The factors A and b are experimentally defined for specific liquids, θ is temperature in °C. Newton evaluated the relationship between shear stress and shear rate for various materials. In the case of water this relationship is linear. The common name for such a fluid is a Newtonian fluid. For a Newtonian fluid the dynamic viscosity has a constant value. Typical relationships between shear rate and shear stress, and the corresponding relationships between dynamic viscosity and shear stress for various fluids are shown in Figure 25. In addition to the graphical representation, equations have been developed to quantify the relationships between these rheological parameters. In these equations, k and n are characteristic parameters describing the rheological behaviour of the particular fluid.



$$(a) \quad \tau = \eta \dot{\gamma} \quad \text{Newton}$$

$$\eta = \text{const.}$$

$$(b) \quad \frac{\eta - \eta_{\infty}}{\eta_0 - \eta_{\infty}} = \left[1 + \lambda^a \dot{\gamma}^2 \right]^{\frac{n-1}{a}} \quad \text{Yasuda}$$

$$\frac{\eta - \eta_{\infty}}{\eta_0 - \eta_{\infty}} = \frac{1}{1 + k \dot{\gamma}^{1-n}} \quad \text{Cross}$$

$$(c) \quad \tau = k \dot{\gamma}^n \quad \text{Ostwald}$$

$$(d) \quad \tau = \tau_0 + k \dot{\gamma}^n \quad \text{Herschel -}$$

$$\eta = \frac{\tau_0}{\dot{\gamma}} + k \dot{\gamma}^{1-n} \quad \text{Bulkley}$$

Fig. 25: Different types of fluids models [74]

The relationship between the shear stress, viscosity and shear rate depends on the fluid type. In the case of the black curve marked with the small letter (a), the fluid can be recognised as a Newtonian fluid. The viscosity does not change despite different shear rate values, and the shear stress has a linear relationship with the shear rate. The representative fluid with this behaviour is water. In the cases of curves (b) and (c), the shear stress has a reducing (b) or increasing (c) dependency with shear rate. There is an analogous relationship between viscosity and shear rate, which corresponds to each of these fluid behaviours. The representative fluids with these behaviours are ketchup tooth pastes, etc. The curve (d) describes behaviour, which is close to the behaviour of MRF. The rheological behaviour of MR fluids, where no magnetic field is present, is very similar to the pattern of the carrier fluids, except that the metal powder content of the MR fluid makes the liquid slightly “thicker” [65,66 and 68].

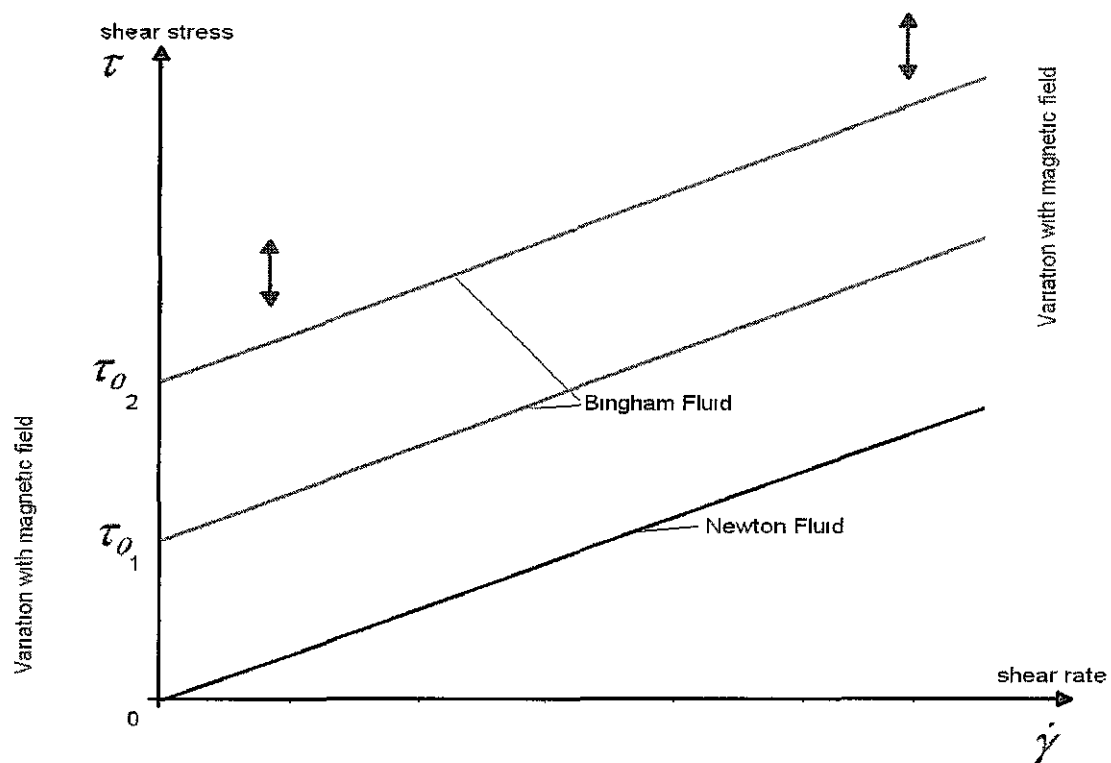


Fig. 26: Shear stress against shear rate for various fluids

Fig. 26 shows the typical relationship between shear stress and shear rate for a Bingham fluid and compares this with a Newtonian fluid. It is recognised that the Bingham model is valid for use in describing the rheological features of an MR fluid [65, 66 and 68]. When a magnetic field is not present an MR fluid behaves like a Newtonian fluid. When a magnetic field is present, the MR fluid shows a characteristic of Bingham fluids. At zero shear rate there is some resistance to flow. The force causes a plastic deformation, but there is no continuous movement. In this condition, the maximum stress, which can be applied without causing continuous movement, is the yield stress and this is a function of the magnetic field strength. For an MR fluid, the yield stress can be controlled, increasing or decreasing with the strength of the magnetic field.

$$\tau = \tau_0(H) + \eta \dot{\gamma} \quad (19)$$

In the magnetic field each metal particle becomes a dipole (North / South) and there is a tendency for a chain to be created with neighbouring particles. The chains have a mechanical

resistance to the fluid flow, and because of this the viscosity of the fluid increases. In the magnetic field, the particle chains are structured according to the pattern of magnetic flux paths. The mechanical resistance to flow of this chain structure can be controlled by the magnetic field strength and results in viscosity changes from free flowing liquid to a semi-solid condition. The MR effect is reversible. When the magnetic field is removed, the original condition of the liquid is re-established. The magnetic field controls the level of the MR effect. The magnetic field required to impose this control depends on the fluid formulation, especially on the quality and quantity of the metal powder. To increase the yield stress capability it is necessary to have a higher percentage of metal powder and larger particles to support the chain structure. The yield stress capability also depends on the magnetization characteristics of the fluid. This magnetization is expressed as the Flux density, B (Tesla) as it varies with the magnetic field strength, H (A/m). It depends on the concentration of metal powder in the liquid and on the actual nature of the material in the particles. MR fluids based on carbonyl iron are capable of operating with yield stresses of 100 kPa. In order to have a predictable behaviour it is recommended the equipment should be operated in the linear section of the $B = f(H)$ curve, and it is better if the hysteresis effect is very small. Detailed design must manage a trade-off between mechanical, magnetic and rheological factors. Depending on the fluid flow and on the rheological stress, there are three different modes of MRF operation: the Direct Shear Mode, the Valve Mode and the Squeeze Mode. The basic working principles of each of these are shown in Table 7.

Table 7: MRF operational modes

Operational mode	Valve mode	Shear mode	Squeeze mode
Functional principle			

3.2 MRF Components

A Magneto-Rheological-Fluid is a fluid with rheological behavior which depends on the strength of a magnetic field. The rheological status changes reversibly from liquid to the solid. The Greek word “rheos” means flowing and rheology is the science of deformation behavior of materials which are able to flow. Normally the rheological property of viscosity changes with other physical properties, such as chemical composition, shear stress and temperature. These features are not easily controlled in most applications because they are fixed by the environment in a particular situation. In the case of all fluids the variation of viscosity with temperature is reversible but this does not allow the viscosity to be controlled easily. In the case of MR the fluid viscosity becomes intelligently controllable using the magnetic field. This change of viscosity up to the solid condition is reversible and is the basic feature of MRF technology. The MRF effect is the difference in rheological properties with and without a magnetic field.

There are basically three components in an MR fluid: basic fluid, metal particles and stabilizing additives [1, 2, 65-79, 56].

The *Base fluid* has the function of the carrier and naturally combines lubrication (in combination with additives) and damping features. For the highest MRF effect the viscosity of the fluid should be small and almost independent of temperature. In this way the MRF effect will be the dominant effect when it is compared with the natural physical viscosity varying with temperature and shear stress. Basically in the off-state (without any magnetic effects) MR fluids behave like the base fluid in accordance with their chemical compositions. There are different types of liquid which can be used as the carrier fluid i.e. hydrocarbon oils, mineral oils or silicon oils. As with any type of particle suspended in a fluid, the base fluid will have a higher viscosity when the concentration of metal particles is very high. The fluid will appear to be “thicker” [69]. So even in the off-state, the fluid with the powder will have an increased viscosity. Usually the dynamic viscosity η_d at ambient temperature is around 100 mPa [68, 71].

In the on-state (with a magnetic field in place) the *Metal particles* are guided by the magnetic field to form a chain-like structure. This chain-like structure restricts the motion of the fluid [68] and therefore changes the rheological behavior of the fluid. The MR-effect is produced because of this resistance to flow caused by the chain-like structure. The metal particles are usually made of carbonyl iron, or powder iron, or iron/ cobalt alloys to achieve a high

magnetic saturation. The amount of metal powder in MRF can be up to 50% by volume [1, 2, 65-80]. The particle size is in the μ -meter range and varies depending on the manufacturing processes. The particle size can be chosen to achieve various purposes. In the case of carbonyl iron the particle size ranges between 1-10 μ -meter. Larger particles and higher fractions of powder in the MR fluid will provide higher torque in the on-state, but at the same time the viscosity of the MR fluid in the off-state will also be higher under these conditions. The material specification, especially the permeability is also a very important factor for controlling the MR-effect.

The additives include stabilizers and surfactants [70]. Additives are suspending agents, thixotropes, friction modifiers and anti-corrosion/wear components. Highly viscous materials such as grease or other thixotropic additives are used to improve settling stability [76]. Ferrous naphthanate or ferrous oleate can be used as dispersants and metal soaps such as lithium stearate or sodium stearate as thixotropic additives [77]. Additives are required to control the viscosity of the liquid and the settling rate of the particles, the friction between the particles and to avoid the in-use thickening for a defined number of off-duty cycles. All three components define the magneto-rheological behavior of the MR fluid. The total density depends on the formulation and is approximately by 3-4 g/cc. The change of one of the MRF components will lead to rheological changes (in the off-state) and to magneto-rheological changes in behavior (in the on-state) . Finally a trade-off between the achievable performances of all three components in combination is required in order to optimize a formulation.

There are some similarities between **MR fluids and Ferrofluids**. The magneto-rheological behaviors of the two types of fluid are different because there is a difference in both the quality and the quantity of the metal powders. Common to both is that they contain iron particles, a basic fluid and additives. The main difference is the size, the quantity and the quality of the iron particles. In the case of MR fluids the iron particles are large, larger than 1 μ m. In the case of Ferrofluids the iron oxide particles are much smaller, about 30 nm [69, 79]. With MRF there is a change of state from liquid to solid when a magnetic field is switched on, whereas a Ferrofluid remains liquid even in a high magnetic field [69, 72]. In the Ferrofluid effect the strong yield stress behavior is almost nonexistent, whereas it is the ability to create the chain structure in MR fluids with mechanical resistance to flow which is of paramount importance in the MRF effect. Carbonyl iron based MR fluids are able to develop yield stresses of 100 kPa, but a typical yield stress for a Ferrofluid is 10 kPa. The viscosity

dependency due to a magnetic field in a Ferrofluid is a secondary effect. The main Ferrofluid effect is to guide and attract the fluid according to the magnetic field intensity. Ferrofluids are very stable due to the particle sizes. The particles are also less abrasive than in the case for MR fluids.

The above description indicates the differences between the two types of fluid in terms of functionality. It is also possible to differentiate between MRF and ERF using the proportion between the Brownian thermal and the magnetic energies for individual particles. The thermal energy can be expressed as follows:

$$Energy_{thermal} \sim k T \quad (20)$$

In this term k is the Boltzmann's constant $1.38 \cdot 10^{-23}$ J/K and T is temperature in K. The main desirable feature in MRF is to control the shear stress. In the case when the magnetic energy is bigger than the thermal energy, the shear stress can be controlled. Otherwise the thermal energy is bigger and the magnetic energy would just guide the particles according to the flux density. An overview of representative features is shown in Table 8.

Table 8: MRF versus Ferrofluid [1, 2, 65-79, 56]

<i>Representative Feature</i>	<i>MRF</i>	<i>Ferrofluid</i>
Relation between magnetic and thermal energy	Magnetic energy is higher than the thermal energy	Thermal energy is higher than the magnetic energy
Max. Yield Stress	100 kPa	10 kPa
Particle size	some μm	some nm
Particle material	carbonyl iron	iron oxide
Fraction by volume	up to 50%	up to 10%
Stability	medium	good
Functionality	controllable shear stress	controllable liquid flow

3.3 MRF Operational Modes and Applications

Depending on the fluid flow and the rheological stress there are three different modes of MRF operation: Direct Shear Mode, Valve Mode and Squeeze Mode.

3.3.1 Valve Mode

The valve mode as an operational mode is used in dampers, shock absorbers and is shown schematically in Fig. 27.

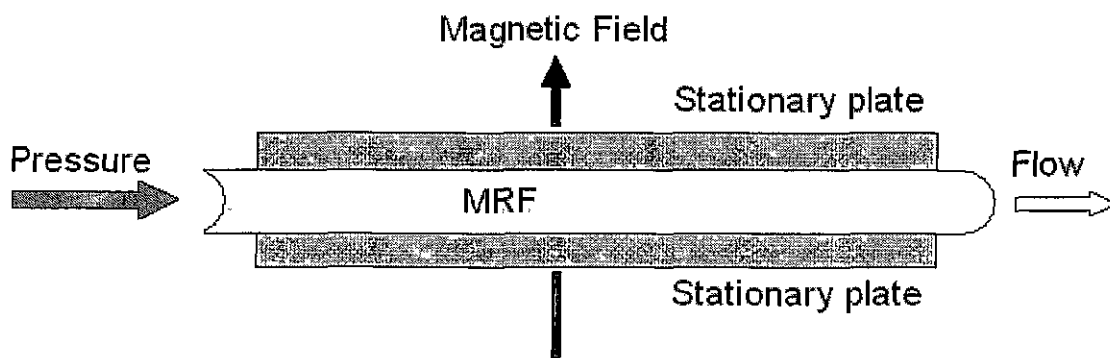


Fig. 27. Valve Mode

The pressure drop created in this mode e.g. in a damper, is the sum of the viscous (pure rheological) component ΔP_r and the magnetic field dependent (magneto-rheological) component ΔP_{mr} . The level of this pressure drop is defined using the following approximation:

$$\Delta P = \Delta P_r + \Delta P_{mr} = \frac{[12 \cdot \eta \cdot Q \cdot L]}{[g^3 \cdot w]} + \frac{[f \cdot \tau_{mr} \cdot L]}{g} \quad (21)$$

In the viscous component in this equation $\eta [Pa \cdot s]$ is the dynamic viscosity, $Q [m^3/s]$ is the flow rate and $L, w, g [m]$ are the geometric length, width, gap size of the flow channel respectively. In the magnetic field dependent component $\tau_{mr} [N/mm^2]$ is the yield stress developed in response to the applied magnetic field, $L, w, g [m]$ are the same geometry data as in the rheological pressure drop part.

The other factor $f [-]$ (no units) is an empirical factor and is determined experimentally. It is

necessary to explain the difference between the observed pressure drop ΔP and the pressure drop calculated from rheological principles alone ΔP_r . The ΔP_r term of Eq. 21 is valid for rectangular ducts. In case of circular ducts with radius r , ΔP_r is described with the following equation:

$$\Delta P_r = \frac{8 \cdot \eta \cdot L \cdot Q}{\pi \cdot r^4} \quad (22)$$

The pressure drop due to magneto-rheological principles ΔP_{mr} is clearly dependent on the yield stress developed in response to the applied magnetic field and to the above geometrical data, but there are also other factors which have an effect on this pressure drop, and the influence of these other factors is represented by the empirical factor f [-]. The factor is found experimentally to be dependent on the proportion of the purely rheological pressure drop to the total observed pressure drop. To differentiate the two extreme regimes of operation there is Eq. (23) defined:

$$\frac{[\Delta P_{mr}]}{[\Delta P_r]} = \text{Proportional factor} \quad (23)$$

In the case that the proportion factor from Eq. (23) is below 1, the factor f [-] is equal to 2. In the case that the proportion factor from Eq. (23) is below 100, the factor f [-] is equal to 3 [67]. Equation (21) could be used for the design of MRF applications in valve mode. Using this equation the minimum active fluid could be established as:

$$V = L \cdot w \cdot g = \left[\frac{12}{f^2} \right] \cdot \left[\frac{\eta}{\tau^2} \right] \cdot \left[\frac{[\Delta P_r]}{[\Delta P_{mr}]} \right] \cdot Q \cdot \Delta P_{mr} \quad (24)$$

This minimum of fluid is required to achieve a desired MRF effect at given flow rate Q with the specified pressure drop.

The Rheonetic linear damper shown below is designed for use as secondary suspension element in on- and off-highway vehicles [67]. This application is a damping control unit and is one of the first applications of MRF in automotive industry. A magnetic coil integrated into the piston of the damper generates a magnetic field and this magnetic field regulates the MRF flow resistance within the damper. Fig. 28 and Table 9 show the application features for

this mode related with damper applications. Some values have been approximated.

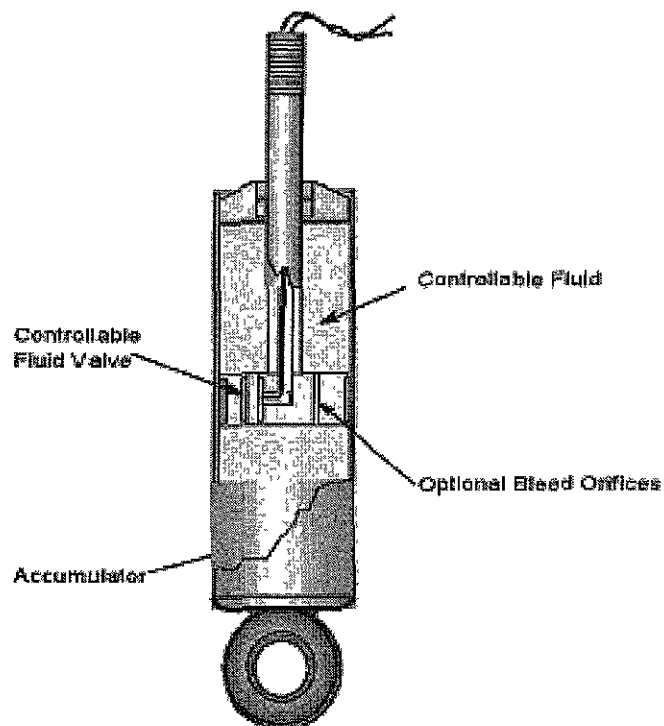


Fig. 28: Functional principle of MRF damper [65-69]

Table 9: Valve mode features [65-69]

<i>Application features</i>	Rheonetic™ (seat suspension damper)
Operational mode	Valve mode
Shear stress level	100 kPa
Shear rate level	50.000 1/sec
Packaging	Diameter 35, length 100 mm
Operational input energy	4 Watts (1 A, 4 V)
Power level in the application	600 W
Active fluid volume	0.3 ml
Total fluid volume	50 ml
MRF Ratio (Fon / Foff) approx.	2200 N / 400 N = 5.5

Using this simple mechanical principle the damping arrangement becomes controllable and the vibration transmission and excitation frequency for a suspended seat could be adjusted

accordingly. Proper choice of MRF parameters extended to seat suspension could eliminate any resonance problems and allow the system to be isolated from high frequencies [67]. Since 2002 the valve mode is used in the damper from automotive vehicle suspensions by GM / Delphi. Further application of the valve mode, has been presented in the reference article [64] and article [75]. These MRF applications bring additional functionality whilst keeping the simplicity. Other possible MRF applications using this mode are dampers for knee prosthesis, vibration dampers, seismic dampers for civil industry, active engine mounts and propshaft mounts.

3.3.2 Direct Shear Mode

The second operational mode is the direct shear mode. The direct shear mode is used in brakes, clutches and is shown schematically in Fig. 29.

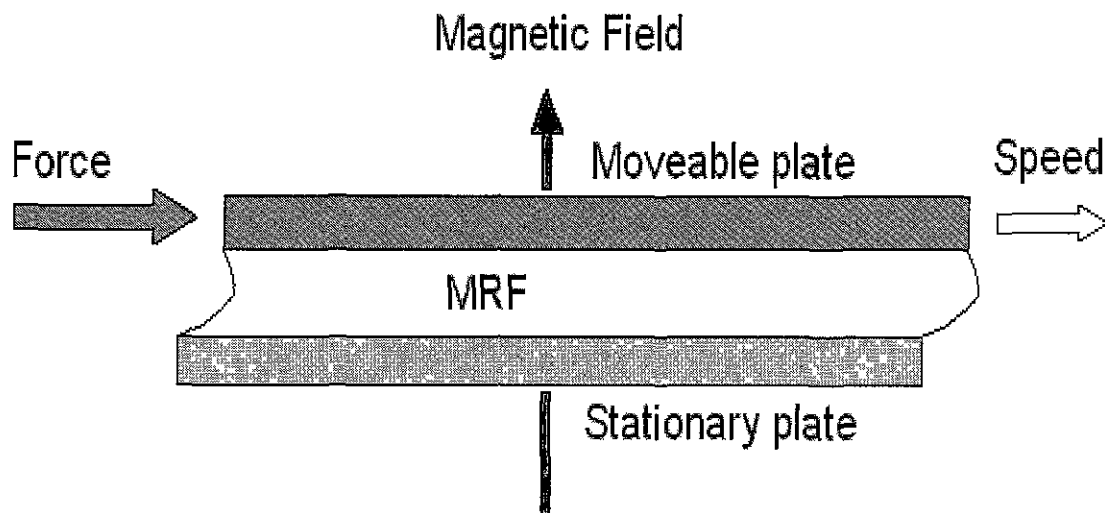


Fig. 29: Direct Shear Mode

The total force in the shear mode could be split into viscous (pure rheological) component F_v and the magnetic field dependent (magneto-rheological) component F_{mr} . The total shear force is defined through the following approximation:

$$F = F_v + F_{mr} = \frac{[\eta \cdot S \cdot A]}{g} + \tau \cdot A \quad (25)$$

In this equation η [Pas] is the dynamic viscosity, S [m/s] is the relative speed, $A=L \cdot w$ is the

working interface area and L , w , g [m] are the length, width, gap size of the flow channel respectively. In the magnetic field dependent component τ_{mr} [N/mm²] is the yield stress developed in response to the applied magnetic field and $A=L w$ is again the working interface area.

Equation (25) could be used for design of MRF applications in direct shear mode. Using this equation the minimum active fluid can be established:

$$V = L \cdot w \cdot g = \left[\frac{\eta}{\tau^2} \right] \cdot \left[\frac{[F_y]}{[F_{mr}]} \right] \cdot F_{mr} \cdot S \quad (26)$$

This minimum volume of fluid is required to achieve a desired MRF effect $\frac{[F_y]}{[F_{mr}]}$ at given speed S with the specified drag torque.

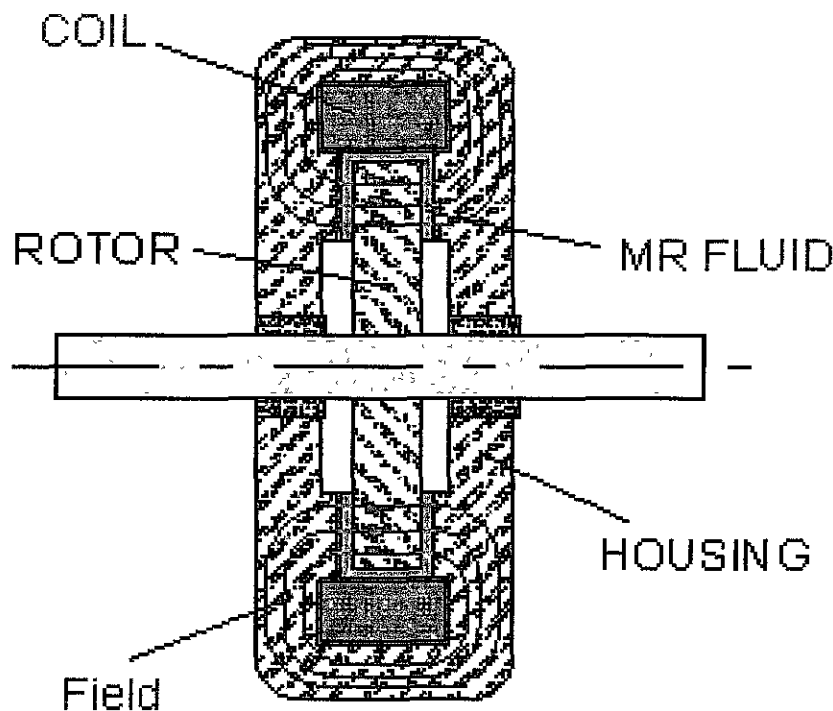


Fig. 30: Functional principle of MRF brake [65-69, 79]

The brake, shown in Fig. 30, contains just a few parts: shaft, bearings, sealing devices, housing with coil, interface disc and MRF. The simplicity and ease of control makes them a cost effective choice for a controllable exercise equipment [67]. A MR fluid brake is currently

being manufactured and sold a controllable resistance element for programmable aerobic exercise equipment [67]. The Table 10 shows some MRF features related to the brake or clutch applications. Some values have been approximated.

Table 10: Shear mode features [65-69, 79]

Application features	Rheonetic™ (exercise brake)
Operational mode	Shear mode or called direct-shear mode
Shear stress level	100 kPa
Shear rate level	10.000 1/sec
Packaging	Diameter 92, length ~35 mm
Operational input energy	~10 Watts (0.8 A, 12 V)
Power level in the application	700 Watts
Active fluid volume	~5 ml
Total fluid volume	5 ml
MRF Ratio (Ton / Toff) approx.	7 Nm / 0.25 Nm = 28

A further application using the shear mode has been presented in the reference paper [83]. Torque level of approximately 8 Nm at 4 Amps without a significant speed dependency has been achieved. Another coupling with optimized magnetic properties has been discussed reference paper [73]. Torque level of approximately 12 Nm at 8 A has been achieved [73]. The direct-shear mode and the valve mode have been studied in detail. Applications using these modes are today already present in many automotive products. The initial unrecognized issue of in-use-thickening has been solved. Good MR fluids show no measurable thickening in-use after more than 10 million cycles in the MotionMaster™ RD-10005 damper [66]. The degree of deterioration of the MR fluid depends on the application parameters like shear rate, temperature and duration of operation. The total amount of MRF dissipated energy, which can be controlled by the MRF unit, is defined by the following equation [66]:

$$\text{Lifetime dissipated energy (LDE)} = \frac{1}{V} \cdot \int_0^{\text{Lifetime}} P \cdot dt \quad (27)$$

where $V[\text{m}^3]$ is the total MRF volume in the application and $P[\text{W}]$ is the mechanical power converted to heat in the MRF unit. The Lifetime Dissipated Energy "LDE" is the total mechanical energy dissipated per unit volume of MRF over the lifetime of the device [66]. Today's MRF applications are operating within the LDE range of approximately $3 \text{ MJ}/\text{cm}^3$. If the LDE limit is exceeded, the MR fluid becomes thickened to a level where the MR effect is no longer significant enough to be considered as a controllable feature. The next steps in MRF development will be the conversions of various other conventional applications into devices using MR principles. There is also a need to develop fluids for the high shear regime from 10^4 1/s to 10^6 1/s , with acceptable values of the LDE being higher than $10^7 \text{ J}/\text{cm}^3$.

Observing patent databases and other information in the public domain it is clear that many feasibility studies are on-going where MR technology is being considered as a competitive technology for the future. Excellent features like simplicity, fast response, simple interface between electrical power input and mechanical power output using a magnetic field, and the controllability make the MRF technology the future technology for many applications. However some application requirements are challenging the capabilities of the direct-shear mode and the valve mode, especially regarding the MRF-ratio. In some applications a higher ratio of the MRF effect is required to meet the specifications.

3.3.3 Squeeze Mode

Some publications report that there is an additional operational mode feasible with a higher MRF effect than can be achieved with either the shear or the valve mode [1, 78 and 82]. This third mode, called squeeze mode, is less well studied than direct-shear mode and valve mode. This mode of operation is shown schematically in Fig. 31.

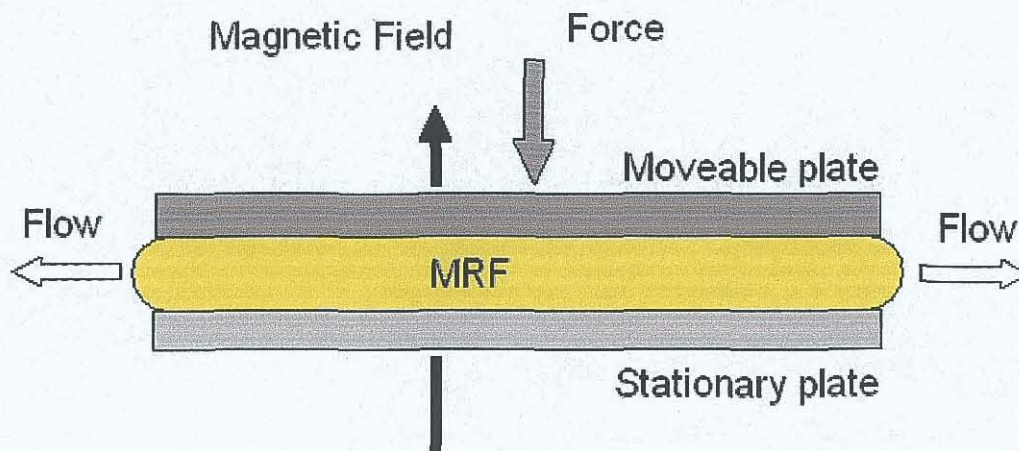


Fig. 31: MRF in squeeze mode

Some small-amplitude vibration dampers use this mode. For small motions, this mode seems to offer the possibility of very large forces which can be controlled by the MRF effect [1, 78 and 80]. In one of the most recent theoretical evaluations of the squeeze-strengthen effect in magneto-rheological fluids [78] the operation of this mode is described. It is suggested that a yield stress could be achieved which would be ten times as large as that which is possible with either the direct-shear or the valve mode. Zhang et al. [78] evaluated theoretically and confirmed with some experiments the higher capability of this specific operational mode. The higher yield stress under magnetic field means a higher ratio between on- and off- states. A stronger MRF effect in combination with advantages already described above would make MRF technology even more attractive and the technology of choice for the next generation of some automotive and industrial applications.

3.4 Remarks on MRF Technology

The Magneto-Rheological-Fluid (MRF) technology is one of the old “newcomers” coming to the market at high speed. Various industries are full of potential MRF applications. For every system where it is desirable to control motion using a fluid with changing viscosity, a solution based on MRF technology may be an improvement in functionality and costs. Simplicity and more intelligence in the functionality are key features of the MRF technology. Excellent features like fast response, simple interface between electrical power input and the mechanical power output make MRF the next technology of choice for many applications. Direct shear mode (used in brakes and clutches) and valve mode (used in dampers) have been studied thoroughly and several products are already present in the market. Future developments include an increase in the acceptable lifespan of MRF devices, in terms of the total energy dissipated from the device throughout its working lifetime, and fluids with higher shear regimes.

Chapter Four

Actuator layout analytical calculations

4.1 Actuator Introduction

This study is about the design, calculation, simulation and experimental evaluation of “MS”-based actuator and a possible “MR”-based control arrangement. The combination of “MS” and “MR” technologies is used in two different actuator layouts. The first actuator layout is using two conventional check valves and the “MR”-based release valve for pressure control. Fig. 32 shows the arrangement based on magnetostrictive actuation and simple magnetorheological control as release valve.

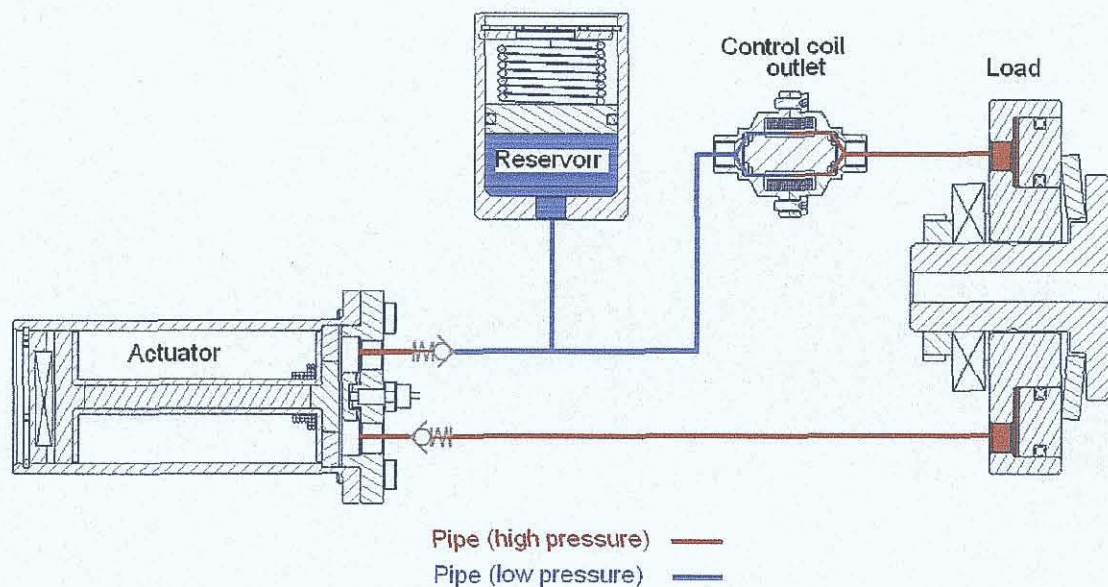


Fig. 32: Arrangement for the study

The assembly for this study includes three main sub-assemblies. The first sub-assembly is the magnetostrictive actuator. The Terfenol-D shaft is surrounded by the main coil. An actuator piston is moved by Terfenol-D shaft elongation. A spring is used to pre-stress the shaft for improvements in the output strain capability. A one-way-valve arrangement enables the fluid motion from the reservoir to the main piston. The second sub-assembly is the load side, which uses a spring to represent the typical elasticity of a wet clutch. As the result of the actuation, an axial force and movement of the main piston against the elasticity of the spring will be

observed. The “MS”-based actuator with check-valves combines the functionality of an electric motor and a hydraulic pump. The third sub-assembly is the “MR”-based release valve. The MRF technology offers the controllable liquid valve with a simple interface between electric and hydraulic power. In this layout the micro pumping mechanism, caused by actuator piston movement and the one-way-valve arrangement, is used to increase pressure. The pumping action is achieved by micro-stepping operations of the “MS”- actuator. During the micro-stepping operations, the MRF control coil is energized with DC current in order to hold the pressure. To decrease the pressure the MRF control coil has to be de-activated by switching off the power. The extended version of the fully “MR” controlled actuator is shown in Fig. 33.

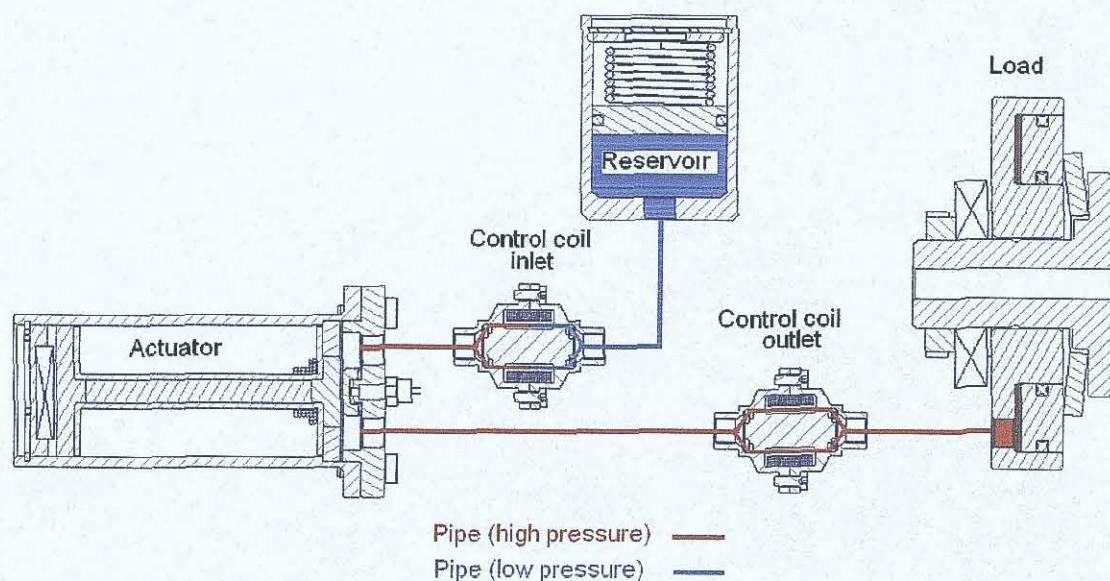


Fig. 33: Alternative arrangement for the study

This alternative layout does not contain check valves. The pressure build up is fully controlled by the “MR”-based inlet and outlet valves. The operation of the valves in appropriate sequence to the “MS”-actuator would enable the fully active increasing of pressure. At the starting point of the operation, no system is energized. Firstly, the inlet valve coil is energized. The outlet valve coil is not energized and the “MR”-fluid can pass through to the main piston. Then the actuator coil is energized and the “MS”-shaft elongates and introduces the first step of micro pumping. At the point where the elongation is at maximum the outlet valve coil is energized and the inlet valve coil becomes no longer energized to enable the sucking of the fluid from the reservoir for the next pump sequence. This leads to the flow of “MR”-fluid into the working chamber area. As the result of the actuation, an axial force and

movement of the main piston against the elasticity of the spring will be observed. A general power flow chart from signal to power is sketched in Fig. 34.

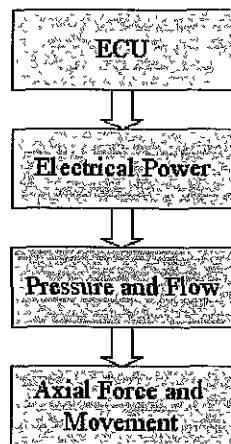


Fig. 34: Actuation flow chart

Fig. 35 depicts the experimental actuator assembly based on magnetostrictive technology. All relevant experimental rig drawings are summarized in the appendix A1.

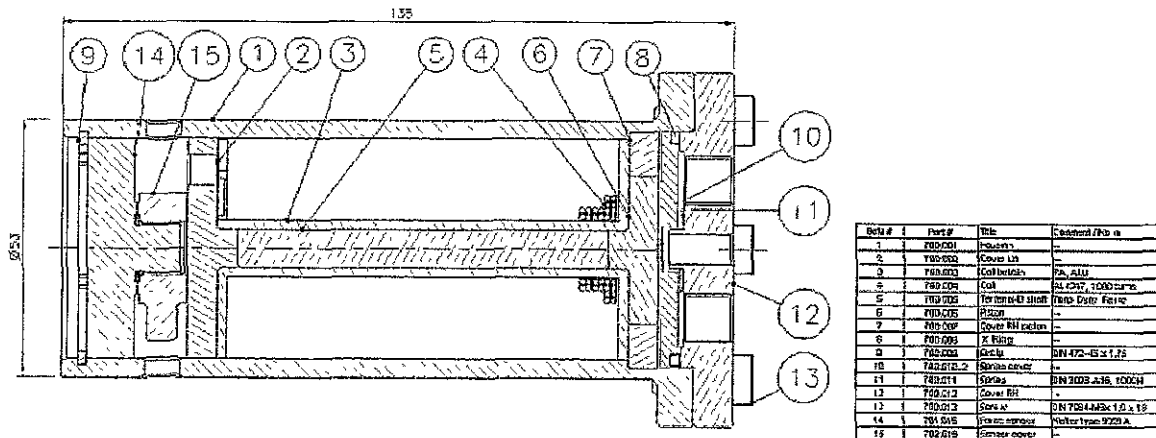
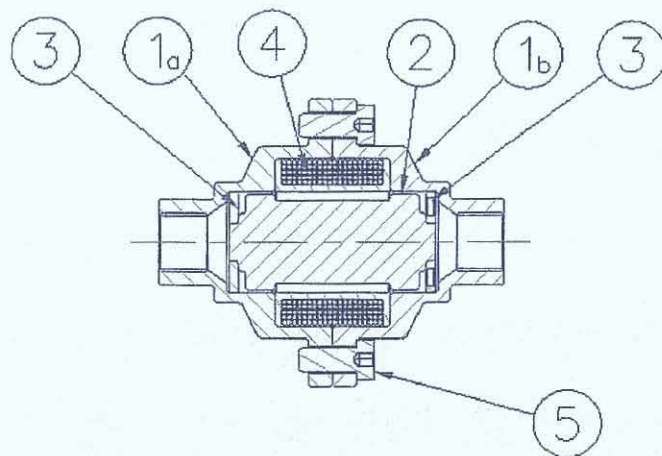


Fig. 35: Cross-section of the actuator used in the study

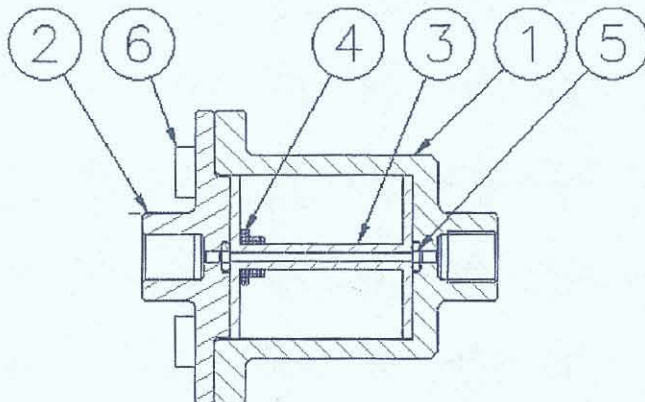
Fig. 36 depicts the main content of the valve control hardware 802.000 based on magneto-rheological technology. In this arrangement, called valve mode, the magnetic field is perpendicular to the direction of fluid flow. All experimental rig drawings form the valve assembly are summarized in the appendix B.



BoM#	Part #	Title
1a	802.001	Housing
1b	802.001	Housing
2	802.002	Shaft
3	802.003	Washer
4	802.005	Coil with bobbin
5	802.006	Screw

Fig. 36: Cross-section of the “MR” control valve

More details about the design and instrumentation for the experimental rig are discussed in chapter 6. An alternative design of a “MR”-based orifice is shown in Fig. 37. In this arrangement, called orifice mode, the magnetic field is parallel to the direction of fluid flow.



BoM #	Part #	Title
1	800.001	Housing
2	800.002	Cover LH
3	800.003	Coil bobbin
4	800.004	Coil
5	800.005	O-Ring
6	800.006	Screw

Fig. 37: Cross-section of the “MR” control orifice

All shown assemblies of actuator and control devices have been calculated, simulated and designed for experimental rig evaluation. The experimental rig drawings form the “MR”-orifice components are summarized in the appendix C.

4.2 Basic Performance Calculations

The pump functionality is achieved by a sequence of micro-stepping operations. Fig. 38 depicts the actuation sequence to increase to the maximum pressure in the micro steps.

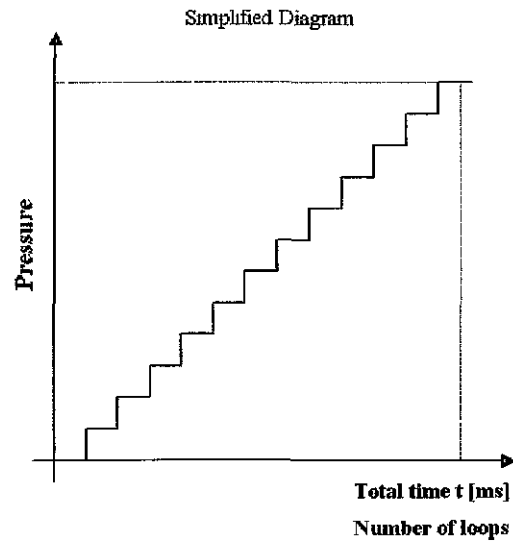


Fig. 38: Micro stepping hydraulic actuator

4.2.1 The choice of mechanical load as reference for the study

To test the functionality and performance of the proposed actuator layout, a specific mechanical load should be selected in order to provide a realistic reference. Various types of actuation, mechanical and hydraulic, are used today in the automotive area in wet clutch mechanisms. Fig. 39 presents a diagram showing the variation of force with axial displacement in a typical wet clutch assembly.

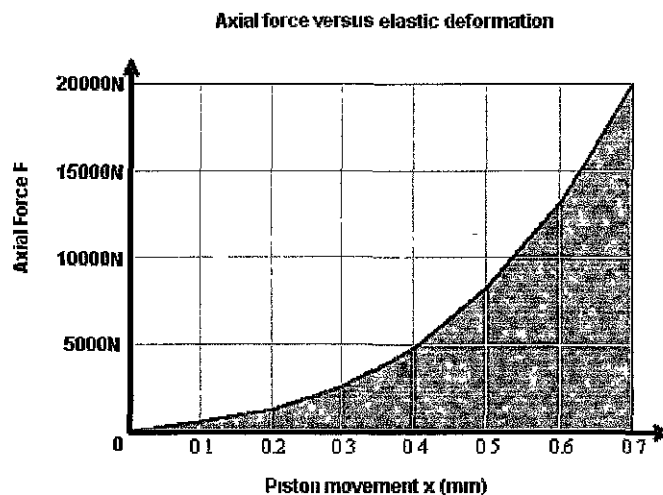


Fig. 39: Axial force versus elastic deformation

The work done during actuation can be calculated using the following equation:

$$W = \int_{x_{max}}^{x_0} F(x) dx \quad (28)$$

This movement is usually achieved in several actuation loops using conventional components like electric motor with pump & piston or electric motor with reduction gear & ball ramp. The power required to energize the system depends on the time taken:

$$P = \frac{\int_{x_{max}}^{x_0} F(x) dx}{t_r} \quad (29)$$

Typical response time of the actuation system is a few hundred milli seconds. Fig. 40 depicts the main content of the reference load assembly.

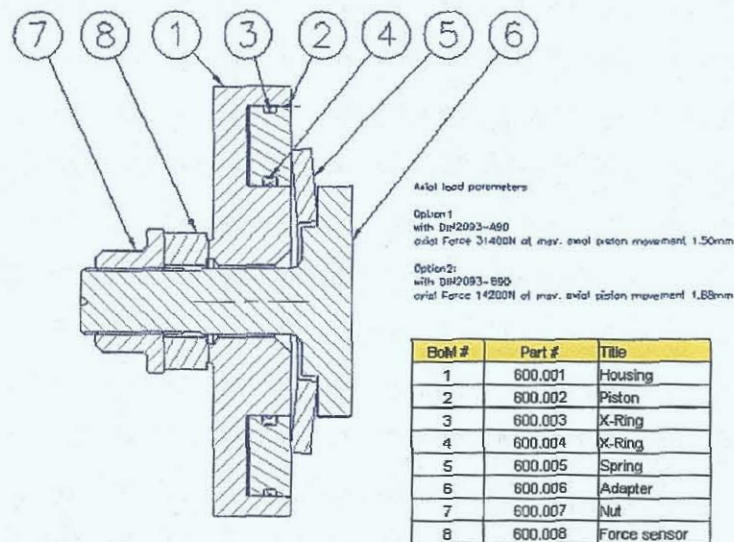


Fig. 40: Cross-section of the load assembly

The common way to represent the realistic clutch elasticity is to use a belleville spring with similar elasticity to a clutch pack. The hydraulic piston used in the assembly has the outer diameter of 115 mm and inner diameter of 68 mm. Specific sealing devices (called “quad-ring” or “x-ring”) have been used to seal the piston against the housing. The typical range of

the axial force is between 5 kN up to 30 kN. To achieve this axial force a fluid pressure of about 0.75 MPa up to 4.5 MPa will be required. The piston movement caused by elasticity of the clutch pack leads to the required volume of liquid which must be pumped into the piston housing. Typical piston movement caused by elasticity lies between 0.5 mm up to 1 mm. This elasticity will lead to 3378 mm³ up to 6755 mm³ of the required fluid. More details depend on specific design and further application details. Above calculated load data will be used as the realistic reference of the experimental evaluation for the proposed system. Based on chosen packaging for the actuator, lower pressure range will be the reference for the experimental evaluation. The experimental rig drawings form the load assembly are summarized in the appendix E

4.2.2 Terfenol-D Shaft and MRF Capability Parameter Calculations

Based on known actuation performance and packaging, a solid Terfenol-D shaft with diameter of 8mm has been chosen. A set of parametric calculations has been prepared in order to create a basis for the component design. MathcadProfessional-Software has been used for the following calculations. This calculation has been created considering the received specification from the manufacturer of the Terfenol-D shaft (Etrema Inc.). The Terfenol-D shaft length has been chosen as constant 67.5 mm and the magnetostrictive strain for the available experimental part has been specified to 800 ppm up to 1200 ppm. Fig. 41 shows the length change of the magnetostrictive shaft versus magnetostrictive strain.

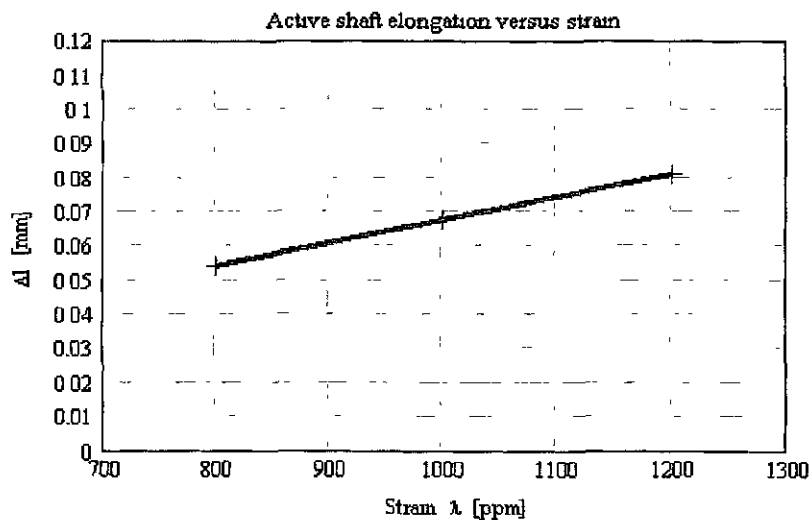


Fig. 41: Length change versus strain

The output strain from the experimental shaft for the magnetostrictive actuator depicted in Fig. 35 including the dependency on frequency and pre-stress will be evaluated experimentally. Fig. 42 shows the characteristic and specification of the delivered Terfenol-D shaft. The shown data have been used as reference for the parameter calculation.

TERFENOL-D PHYSICAL PROPERTIES	
Nominal Composition	Tb _{0.3} Dy _{0.7} Fe _{1.92}
Mechanical Properties	
Young's Modulus	25-35 GPa
Sound Speed	1640-1940 m/s
Tensile Strength	28 Mpa
Compressive Strength	700 Mpa
Thermal Properties	
Coefficient of Thermal Expansion	12ppm/°C
Specific Heat	0.35kJ/kg-K
Thermal Conductivity	13.5 W/m-k
Electrical Properties	
Resistivity	58 x 10 ⁻⁸ Ω-m
Curie Temperature	380 °C
Magnetostrictive Properties	
Strain (estimated linear)	800-1200ppm
Energy Density	14-25 kJ/ m ³
Magnetomechanical Properties	
Relative Permeability	3-10
Coupling Factor	0.75

Fig. 42: Supplier characteristic and specification for Terfenol-D shaft [14]

Based on the information provided by the Terfenol-D shaft manufacturer the Young's modulus varies between 25 GPa and 35 GPa. Fig. 43 shows the relationship between achievable operational force and both performance parameters, the upper limit of the magnetostrictive strain that can be realized and the Young's modulus of the material under these conditions. Equation (15) describes these tendencies mathematically.

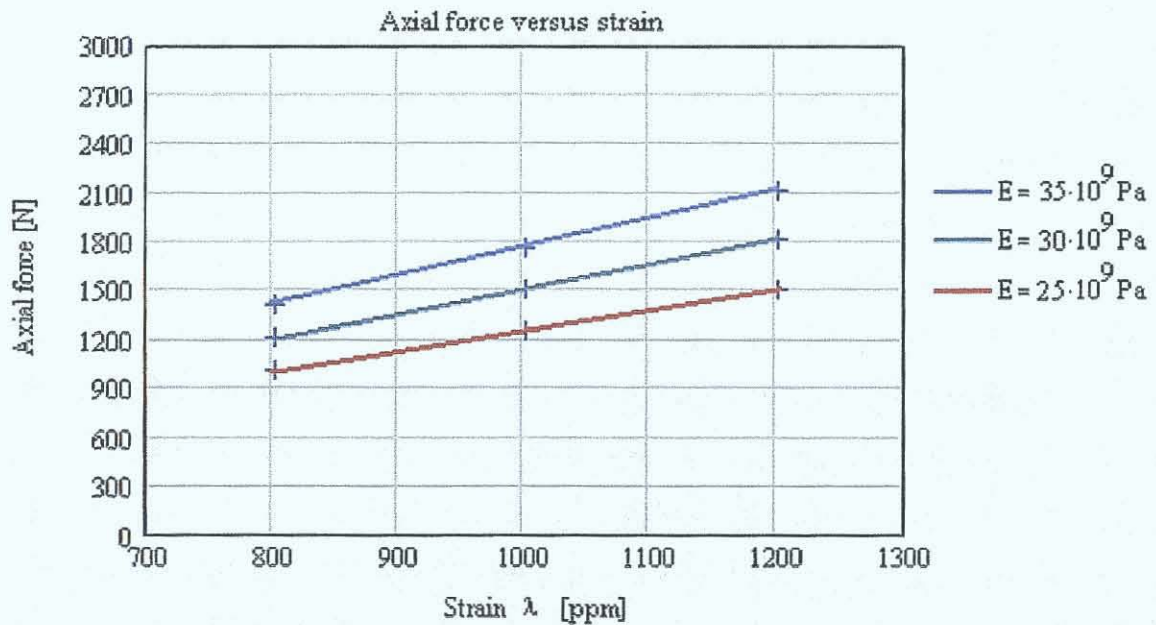


Fig. 43: Axial force versus strain and Young's modulus E as parameter

The Terfenol-D shaft has a diameter of 8 mm, but when it expands it pushes against a pilot piston, which is in contact with the fluid via the elastic membrane. Details of the mechanical arrangements are depicted in Fig. 35 and in appendix A. Using the range of achievable axial force (15), where acceptable strain could be produced, the achievable pressure level can now be calculated. The achievable pressure range is presented in Fig. 44 with the specified Young's modulus.

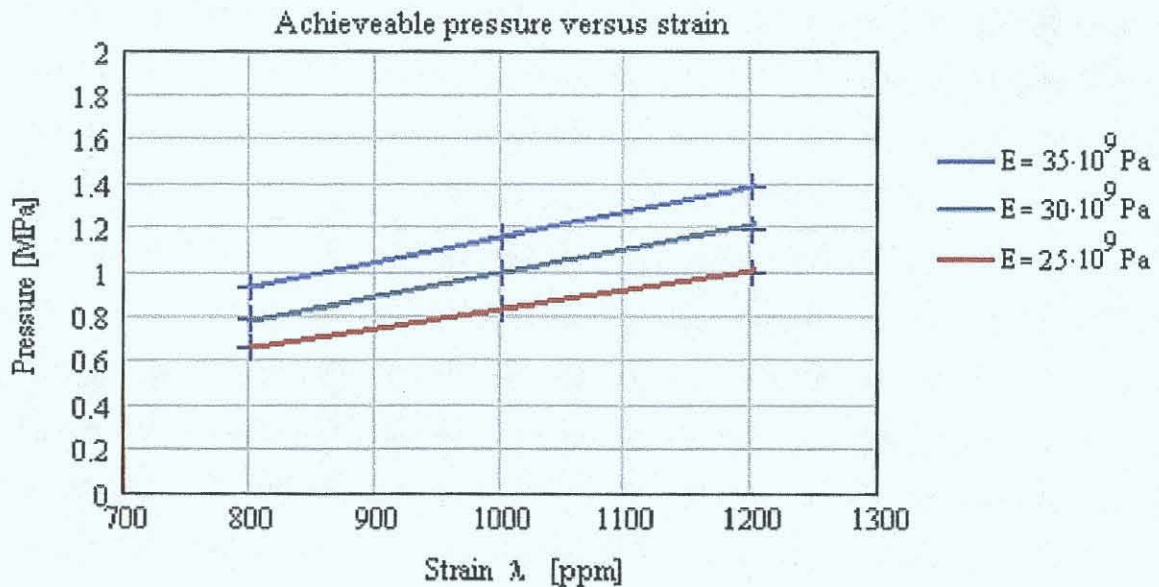


Fig. 44: Achievable pressure versus strain

The variation of the piston diameter can be used to adjust the pump displacement and the desirable pressure level. It is therefore concluded that this Terfenol-D actuator is capable of providing pressures in an acceptable range of those required in some applications from the automotive industry. When the blocked force has been achieved, no significant strain could be produced. Therefore, the operational axial force should be lower than the blocked force. The blocked force will be evaluated experimentally. However, the final performance of the actuator system depends very much on strain capability and Young's modulus of the particular sample of delivered Terfenol-D shaft. Assuming the strain in the Terfenol-D rod when activated changes from zero to some value between 800 ppm and 1200 ppm, the volume delivered by the stroke of the pump is defined as product of rod elongation and cross-sectional area of the actuator piston. The actuator piston is the part which moves with the end of the Terfenol-D rod. Fig. 45 depicts the pump volume per loop when the piston will be moved by the end of the Terfenol-D shaft.

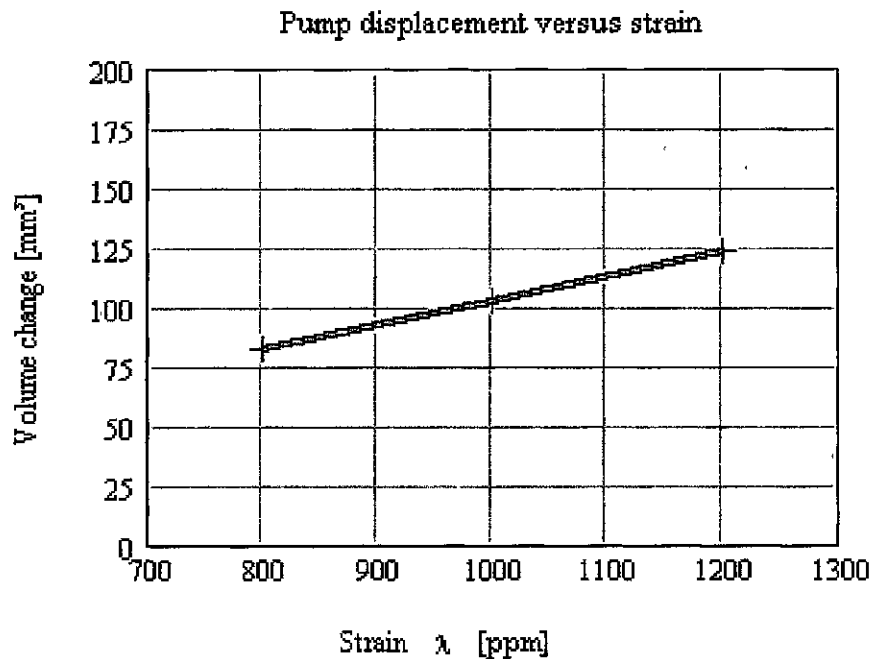


Fig. 45: Pump volume per loop versus strain

The final setup of parameters is a trade of achievable pressure and pump displacement. Packaging restrictions, limitation of electric current in the application and further parameters like operational frequency have to be taken into the account to freeze the particular design proposal. Fig. 46 shows the achievable flow rates at various frequencies of micro-step pumping.

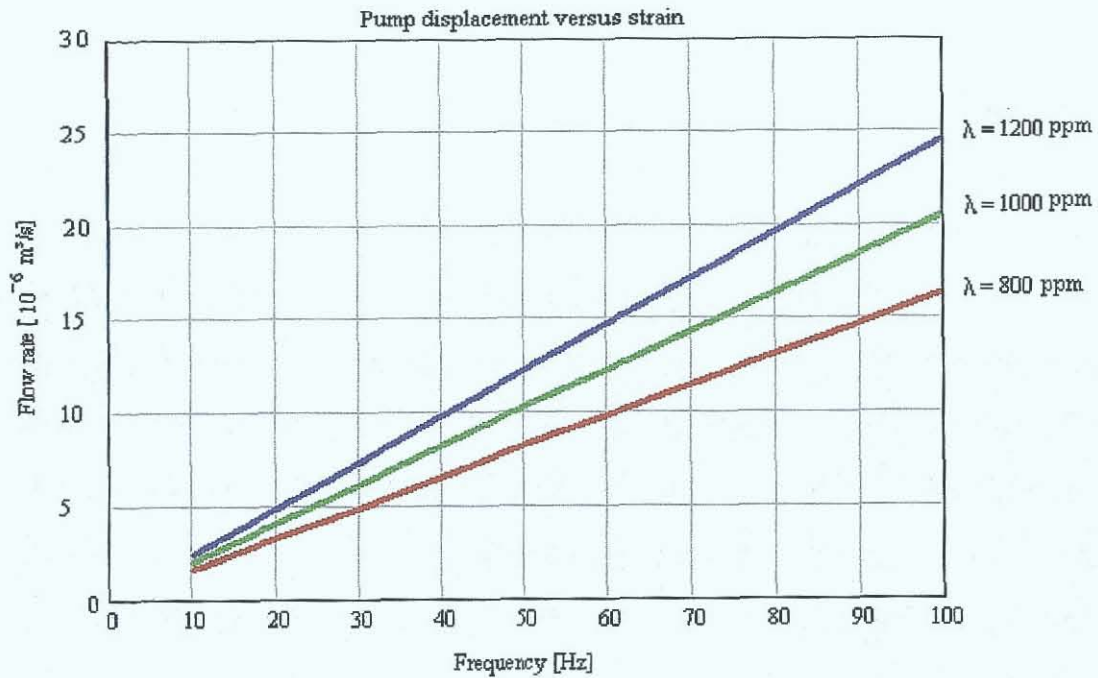


Fig. 46: Flow rate versus frequency with strain as parameter

This graph has been plotted assuming the sinusoidal AC input power to the main actuator coil. The efficiency of the valve layout has been set up to 100%. It should be mentioned that the electric frequency of operating electric power is the half of the mechanical pumping frequency. The doubling of the frequency is based on the fact that the strain peak appears twice within one electric power frequency loop. Finally, a trade off between achievable strain versus frequency performance and pressure level has to be taken into account. When describing the wet clutch system, it was calculated that the piston movement, called axial displacement, is in the range of 0.5 mm to 1 mm. In order to be able to achieve this delivery, the Terfenol-D pump must be activated and de-activated a defined number of times and complete a certain number of loops. The number of required loops during the micro step pumping for the maximal engagement is shown in Fig. 47.

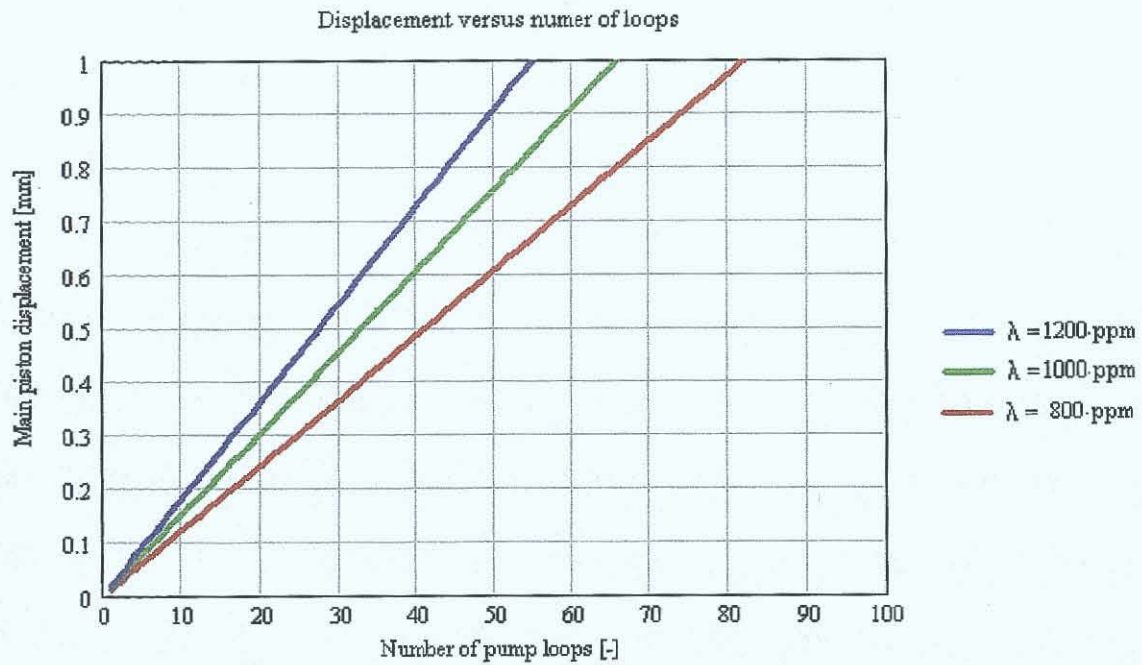


Fig. 47: Main piston displacement versus number of pump loops

The complete number of loops must be carried out in the time required to activate the clutch mechanism. This time is about few hundred milli-seconds. Therefore the Terfenol-D pump must be operated by an electrical current with a defined frequency to achieve the specified performance.

4.2.3 MRF Capability Parameter Calculations

By using Eq. (21) from chapter three of this thesis the pressure capability of the valve mode could be analyzed. The cross-section on Fig. 36 depicts the content of the control arrangement. Fig. 48 shows the control arrangement with red marked gap area where MRF is working as a controlled valve.

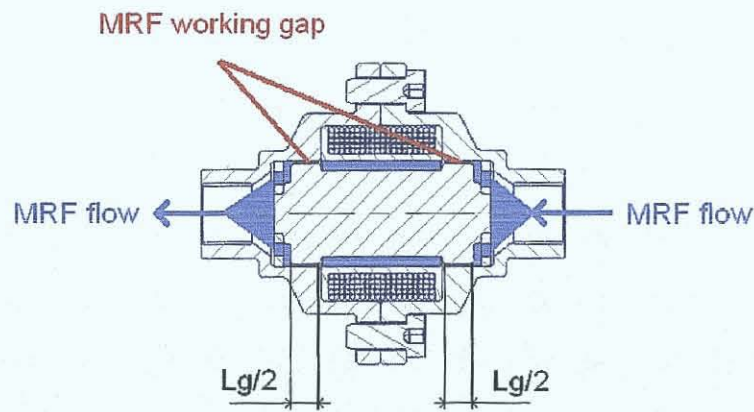


Fig. 48: Cross section of the control valve

The detailed design of this control arrangement is summarized in the appendix B of this thesis. For the final design of this proposal, a number of iterative parameter calculations has been done in order to evaluate the achievable performance. In the arrangement shown in Fig. 48 the magnetic field is perpendicular to the direction of fluid flow. An alternative for the control arrangement has been proposed and evaluated. In the alternative arrangement, called orifice mode, the direction of the fluid flow is parallel to the direction of the magnetic field. Fig. 49 depicts the alternative design of the control arrangement as a controllable orifice.

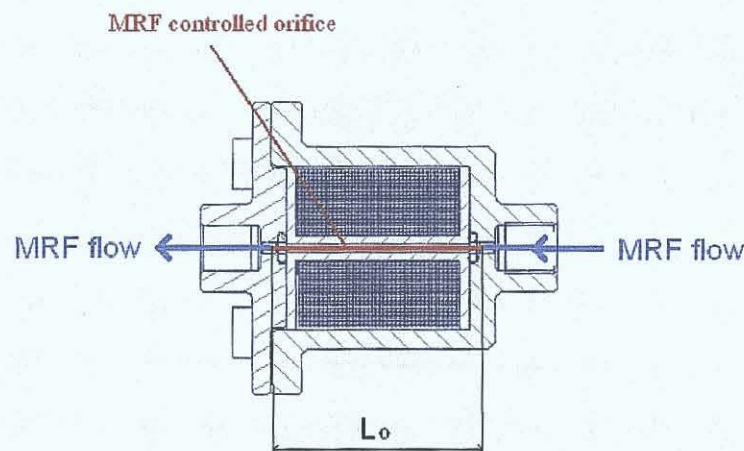


Fig. 49: Cross section of the control orifice

The coil bobbin inner diameter was designed to be equal to the orifice diameter. In this study, the MRF-132-AD and MRF-336-AG have been used. Fig. 50 depicts specification including achievable yield stress versus field intensity from hydrocarbon based MRF-132-AD. Fig. 51 depicts specification including achievable yield stress versus field intensity from the silicon based fluid MRF-336-AG.

Yield Stress Versus Magnetic Field Intensity
of Lord Corporation's Hydrocarbon-Based MR Fluid (MRF-132AD)

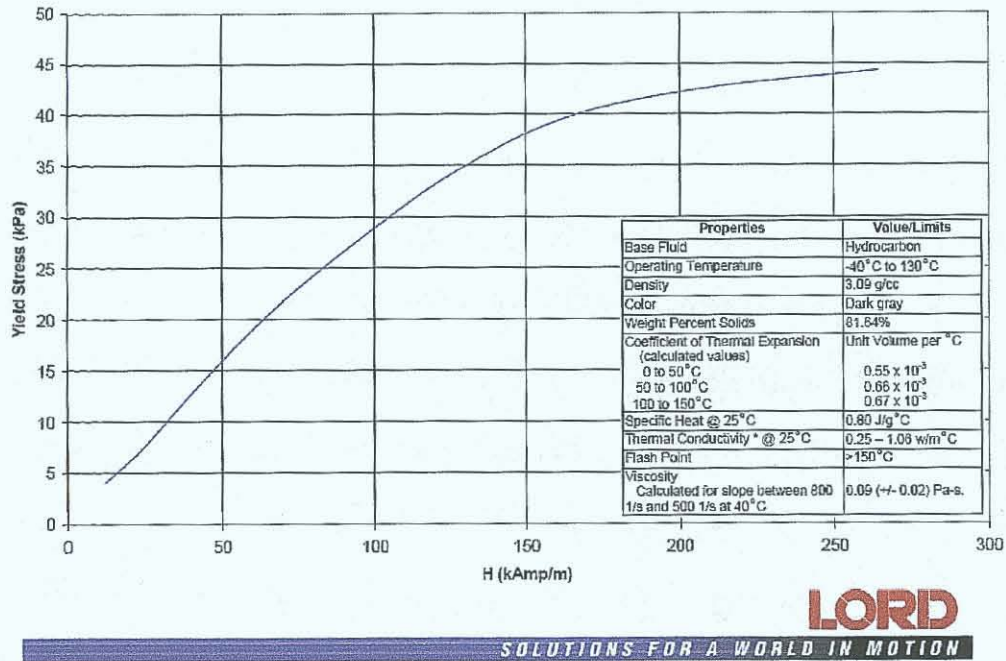


Fig. 50: Supplier specification of reference MRF-132-AD [68, 69 and 79]

Yield Stress Versus Magnetic Field Intensity
of Lord Corporation's Silicone-Based MR Fluid (MRF-336AG)

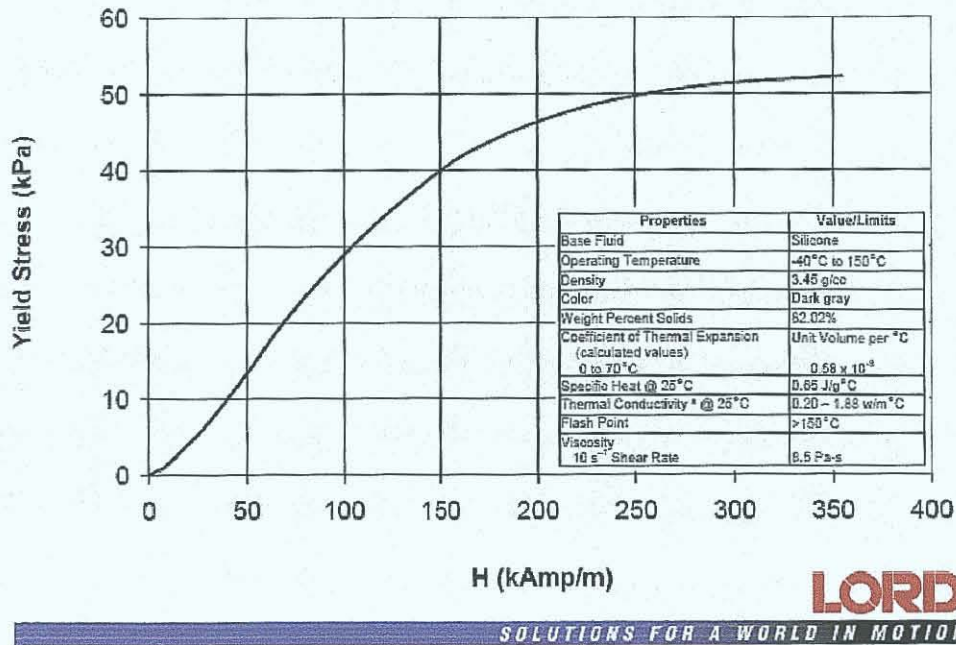


Fig. 51: Supplier specification of reference MRF-336-AG [68, 69 and 79]

Fig. 52 shows the relationship for achievable pressure in the MRF valve, shown in Fig. 36, versus the gap size using the yield stress range up to 45 kPa. The required magnetic field intensity to achieve the highest yield stress is about 200 kA/m. To calculate the pressure capabilities of this arrangement Eq. (21) has been used. The geometrical data from the control valve used for this parameter calculation could be viewed from the detailed drawing in the appendix B from this thesis.

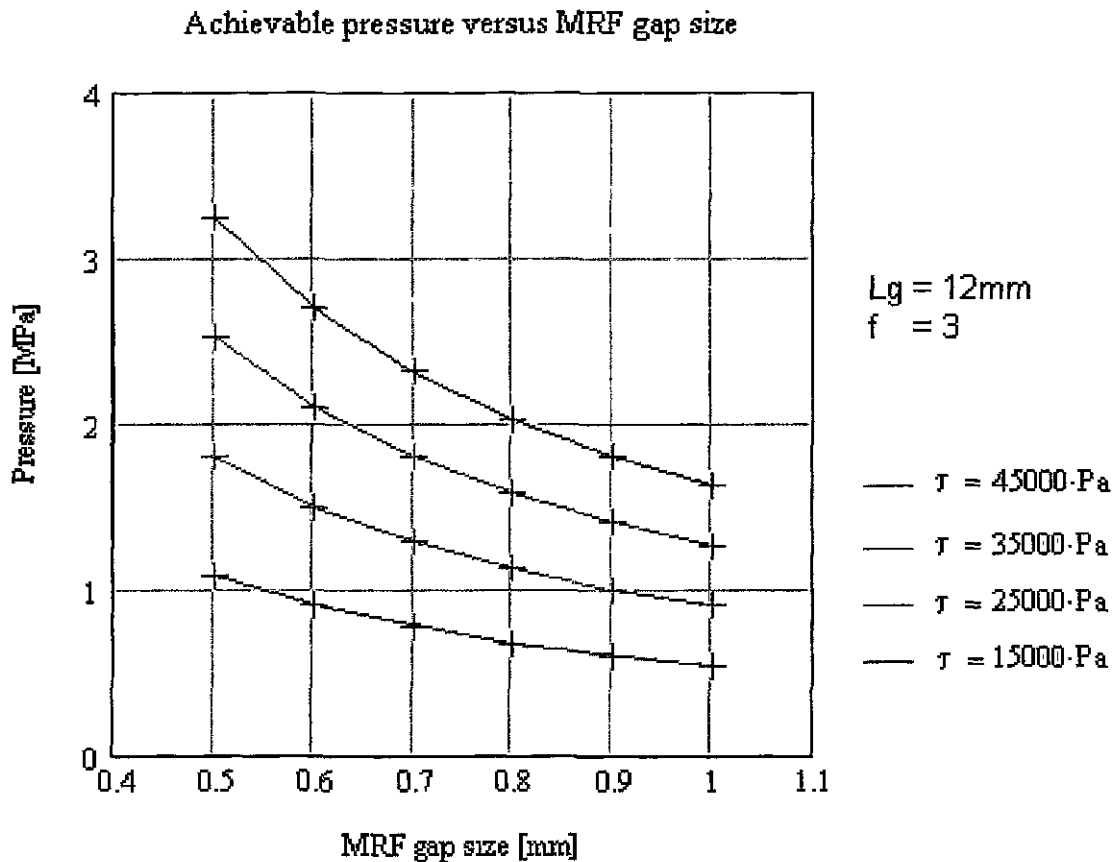


Fig. 52: Pressure versus gap size with yield stress as parameter

The pressure drop in the rectangular channel caused by fluid flow Q [m^3/s] through the gap g [mm] with particular dynamic viscosity η [Pa s] is defined with the following equation:

$$\Delta p = \frac{12 \cdot \eta \cdot L \cdot Q}{w \cdot g^3} \quad (30)$$

Fig. 53 depicts the pressure drop through the valve considering the achievable flow rate has

been shown in Fig. 46. Eq. (30) for the viscous component and the MRF 132-AD specification has been used.

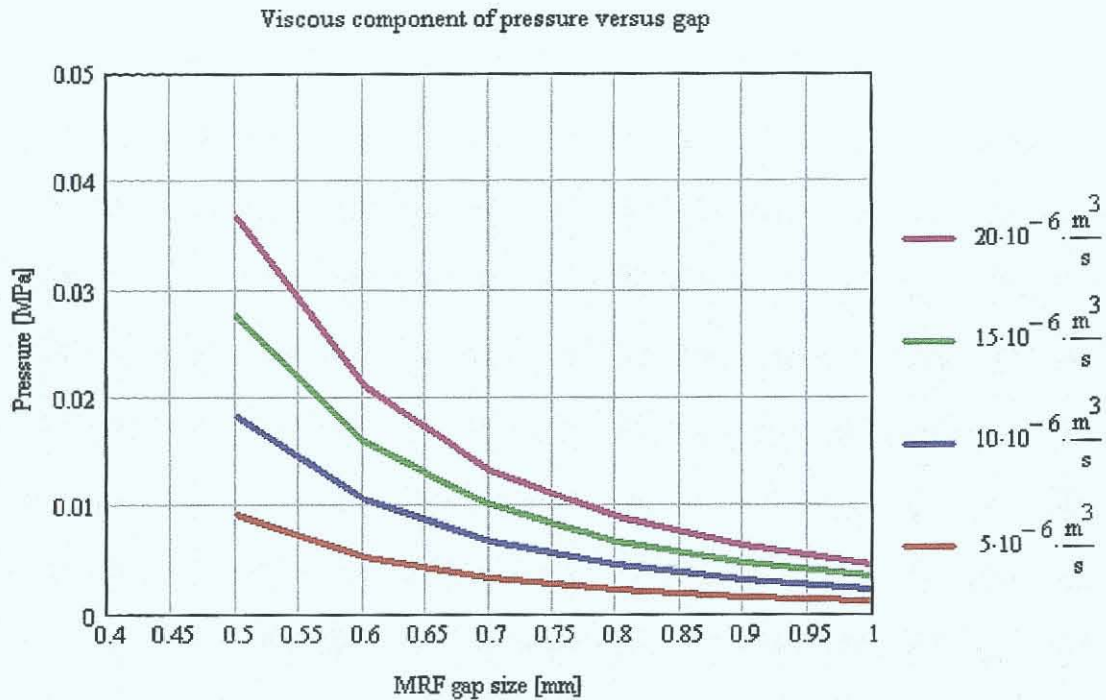


Fig. 53: Pressure versus gap size at various flow rates

The wall shear rate ψ [s^{-1}] in the rectangular channel can be calculated with following equation:

$$\psi = \frac{6 \cdot Q}{w \cdot g^2} \quad (31)$$

Fig. 54 shows the results of calculations for the wall shear rate ψ [s^{-1}] in the rectangular channel in the MRF valve. The maximal speed, at the maximal flow rate of $20 \cdot 10^{-6} \text{ m}^3/\text{s}$ through the gap of 0.5 mm, leads to fluid speed below 1 m/s and to the Reynolds Number of approximately 50. Reynolds Number below 2000 (= velocity x density x length / viscosity), it represents laminar flow [79]. For higher Reynold's Numbers, over 2000, the fluid flow becomes turbulent and could not be predicted with the presented equations.

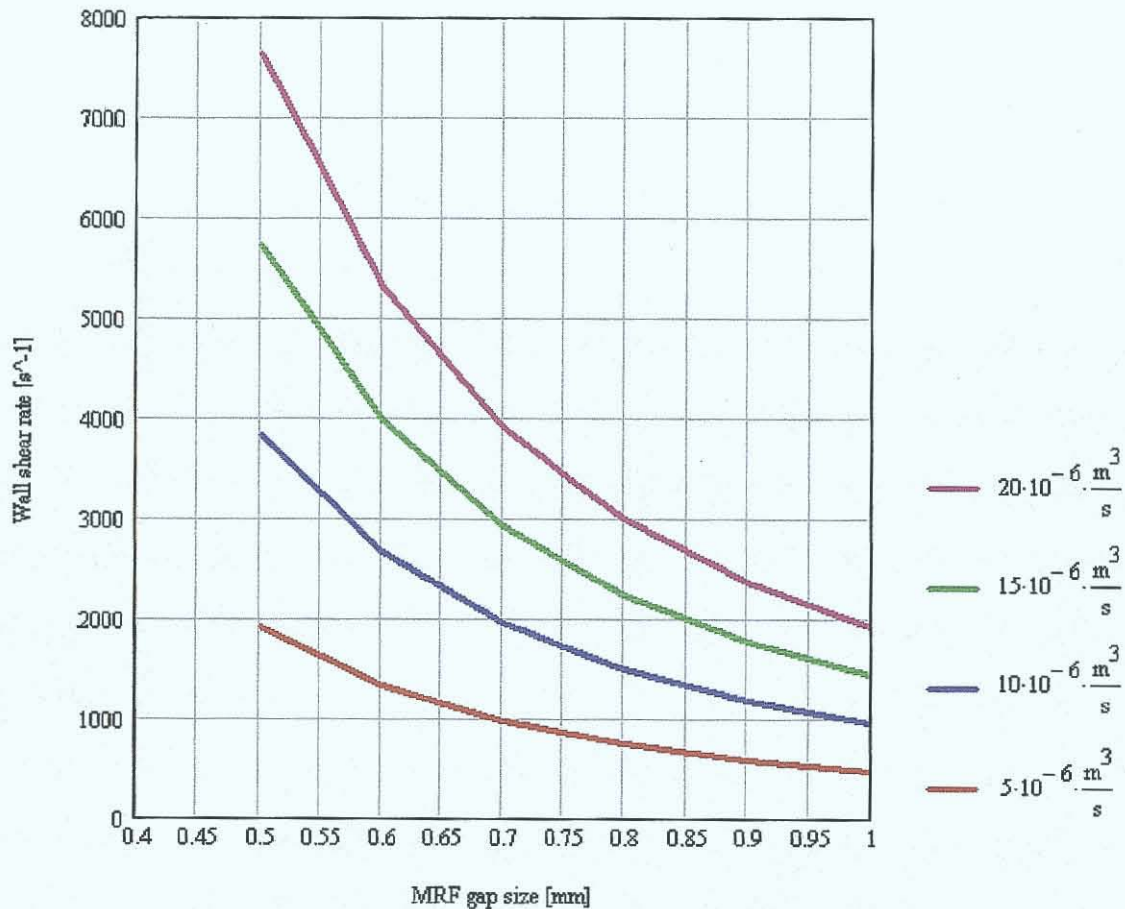


Fig. 54: Wall shear rate ψ [s^{-1}] in the rectangular channel

In the arrangement shown in Fig. 37, the magnetic field is parallel to the direction of fluid flow. To calculate the pressure capabilities of this arrangement Eq. (21) has to be adjusted for cylindrical shape of the channel.

$$\Delta P = \Delta P_r + \Delta P_{mv} = \frac{8 \cdot \eta \cdot Q \cdot L_o}{\pi \cdot \left(\frac{d_o}{2}\right)^4} + \frac{[f \cdot \tau_{mv} \cdot L_o]}{d_o} \quad (32)$$

In the viscous component in this equation η [$Pa \cdot s$] is the dynamic viscosity, Q [m^3/s] is the flow rate and L_o and d_o [m] is the geometric length and the diameter of the flow channel. The factor f [-] (no units) is an empirical factor. The performance of this arrangement will be evaluated experimentally. Fig. 55 shows the relationship for achievable pressure in the MRF orifice, shown in Fig. 37, versus the orifice diameter using the yield stress range up to 45 kPa. The required magnetic field intensity to achieve the highest yield stress is about 200 kA/m. Since this operational mode, orifice mode, has not been studied yet, the factor f [-] in Eq. (32)

has been set to value of 1. The geometrical data from the assembly used for this parameter calculation could be viewed from the detailed drawing in the appendix C from this thesis.

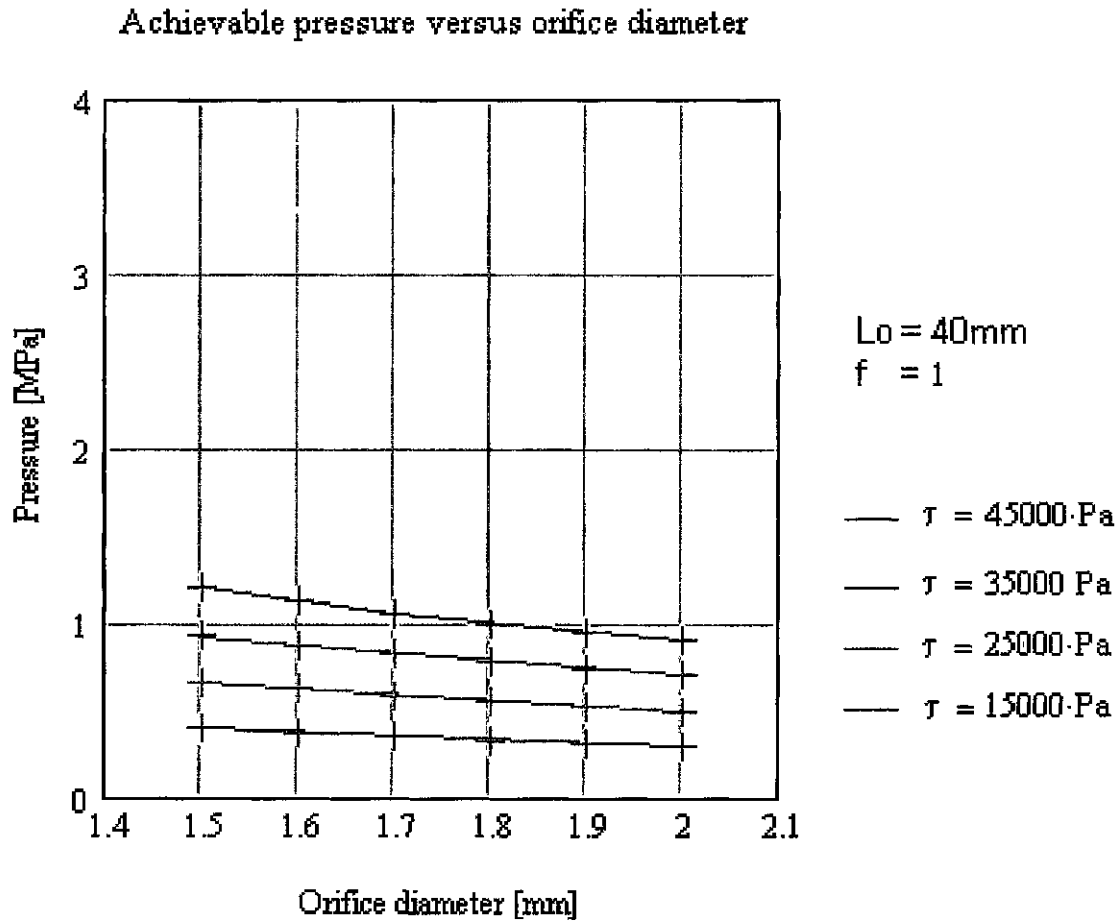


Fig. 55: Pressure versus orifice diameter with yield stress as parameter

The pressure drop in the cylindrical channel caused by fluid flow Q [m^3/s] with particular dynamic viscosity η [Pa s] is defined with the following equation:

$$\Delta p = \frac{8 \cdot \eta \cdot L \cdot Q}{\pi \cdot r^4} \quad (33)$$

Fig. 56 depicts the pressure drop through the orifice considering the achievable flow rate has been showed in Fig. 46. Eq. (33) for viscous component and the MRF 132-AD specification have been used for calculation.

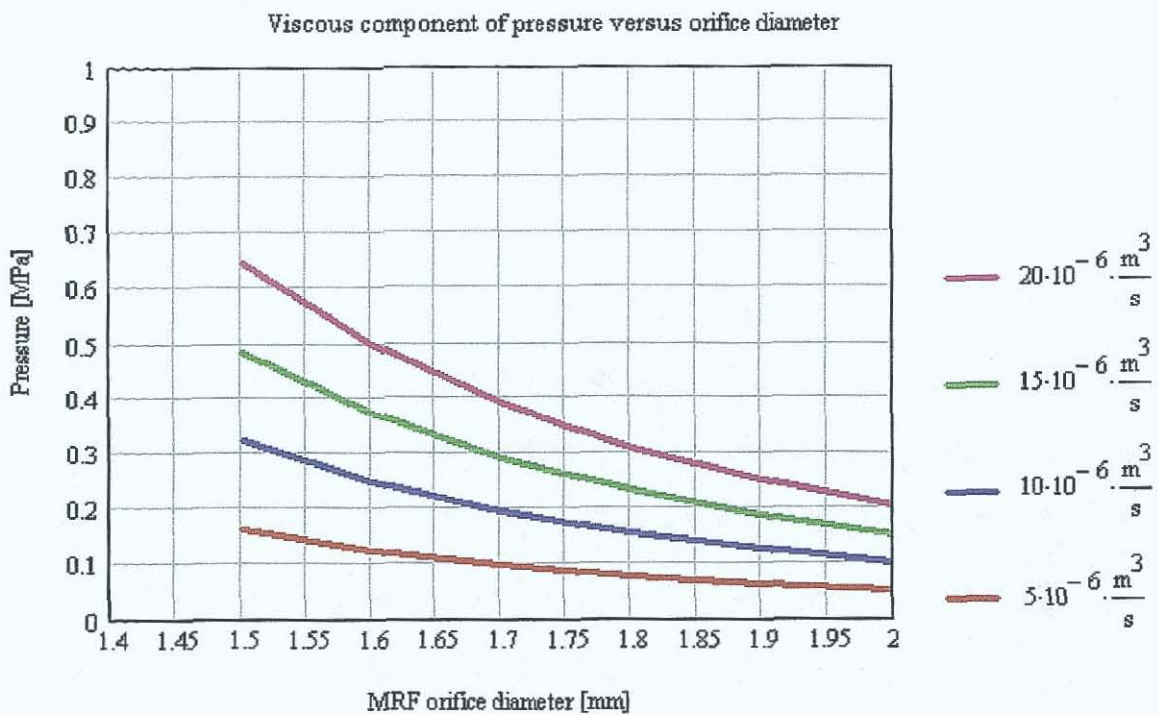


Fig. 56: Pressure versus orifice diameter at various flow rates

The wall shear rate ψ [s^{-1}] in the cylindrical channel could be calculated with the following equation:

$$\psi = \frac{4 \cdot Q}{\pi \cdot r^3} \quad (34)$$

Fig. 57 shows the results of calculations for the wall shear rate ψ [s^{-1}] in the cylindrical channel in the orifice. The maximal speed, at the maximal flow rate of $20 \cdot 10^{-6} \text{ m}^3/\text{s}$ through the orifice of 1.5 mm diameter, leads to fluid speed of 11 m/s and to the Reynolds Number of approximately 1400. Reynolds Number below 2000 (= velocity x density x length / viscosity), it represents laminar flow [79]. For higher Reynolds Numbers, over 2000, the fluid flow becomes turbulent and could not be predicted with the presented equations.

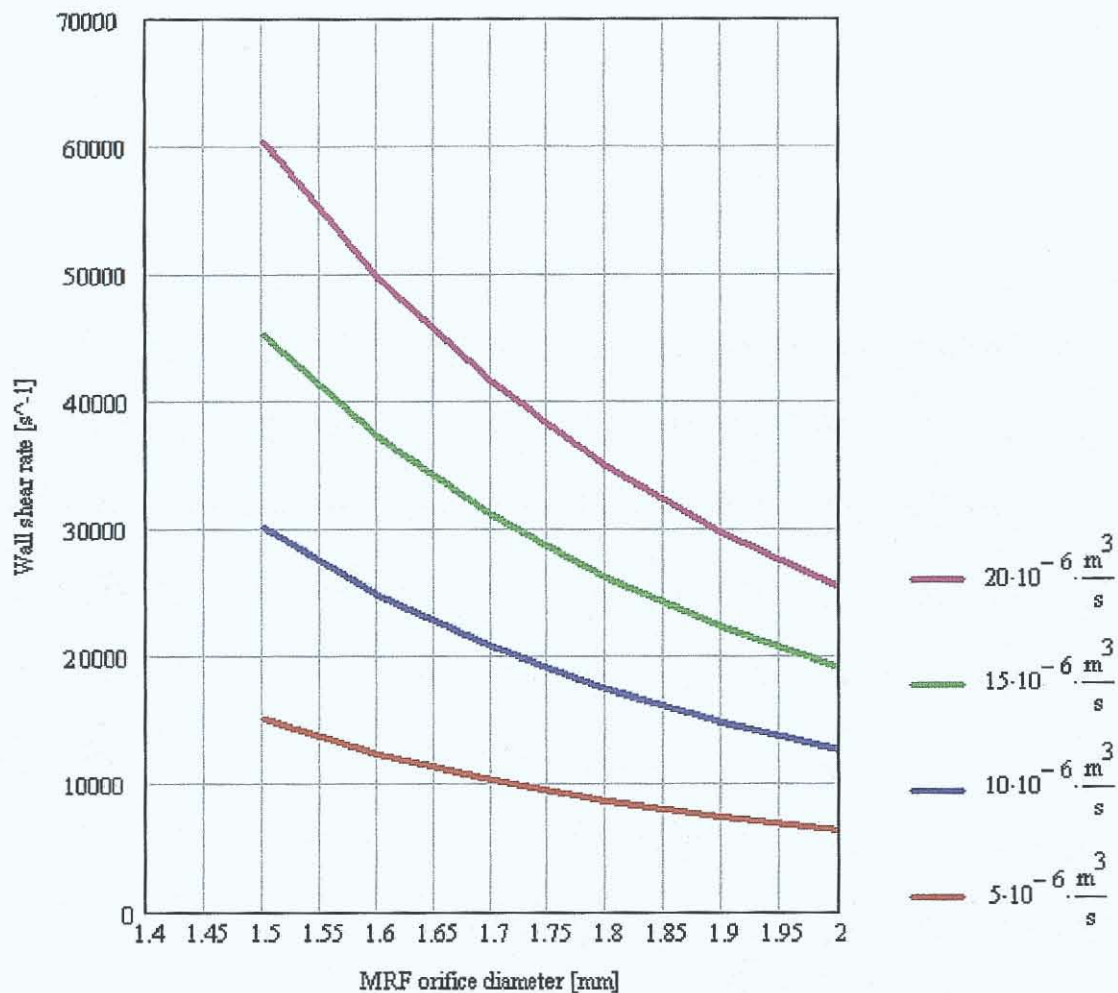


Fig. 57: Wall shear rate ψ [s^{-1}] in the cylindrical channel

From above shown parametrical calculations, it can be concluded that the MR control valve, shown in Fig. 36, is the favorite for this study. This conclusion is based on the fact that the valve layout shows higher achievable pressure than the orifice layout. Furthermore, the parasitic pressure caused through fluid flow and the wall shear rate in the proposed valve is lower than in the orifice, shown in Fig. 37.

The fluid flow rates through the pipes, MRF control valve and check valves have to be taken into account. High liquid flow through narrow areas leads to additional parasitic losses in the system. This difficulty can be easily overcome using lower flow rates and therefore larger pipe diameter and gaps. On the other side, using larger gaps in the MRF control arrangement leads to a limitation of achievable pressure. In the arrangement, shown in Fig. 32, an miniaturized one-way valves from Lee Incorporation will be used. A cross section with basic performance data is shown in Fig. 58.

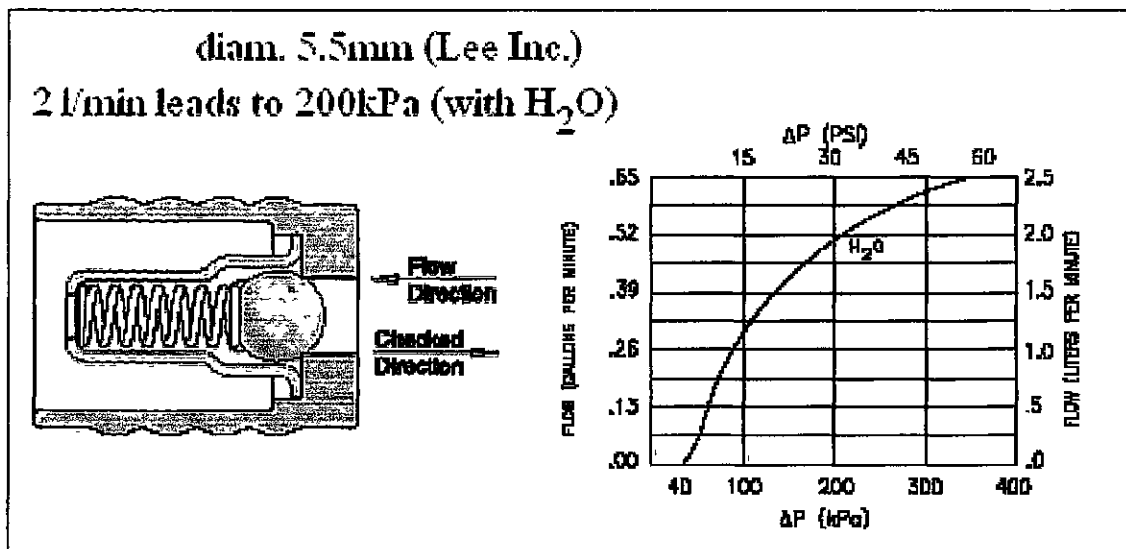


Fig. 58: Check valve from Lee Incorporation [93]

Common failsafe definition is that the system is pressure-less without power. The specification of the dis-engagement time, a few hundred milli-seconds, is essential for compatibility of the actuator system in the automotive environment (ABS/TC/ESP). Based on above determined parameter calculation, achievable pressure and parasitic pressure drop, the control valve shows significantly better performance in comparison with the orifice. Further capabilities related to magnetic field of both assemblies will be evaluated in chapter 5. The performance of both control assemblies with two different fluids, MRF-132-AD MRF-336-AG, will be evaluated experimentally. Both arrangements, shown in Fig.32 and 33, will be prepared for testing on the rig to confirm the basic functionality and the analytical calculations with experimental results.

Chapter Five

Magnetic field calculation and simulation

This chapter of the thesis is covering the magnetic field calculation and simulation for "MS" and "MRF" device. Various tools have been used to complete this approach.

5.1 Electric circuit of the actuator system

Due to control of applied current and voltage to the coil arrangement the magnetic field become controllable. The common way to actuate the magnetostrictive mechanism is AC. For the control of the MRF coil a DC control is proposed. The general form of voltage versus time is depicted in Fig. 59.

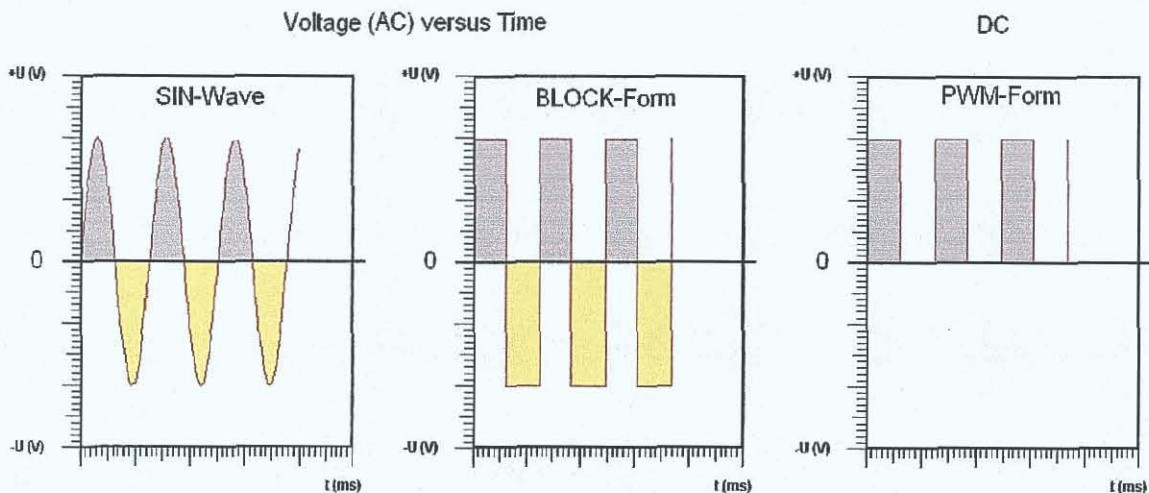


Fig. 59: Alternative voltage versus time relationships

The magnetic field variation versus time for micro-pumping leads to the required variation of the electric power in the actuator and control coil. The most appropriate arrangement for the micro-pump functionality will be the SIN-form. The arrangement with just PWM leads to additional simplicity of the architecture of the electronic components.

Fig. 60 shows the behavior of an inductance in an AC power circle. An idealized inductor, pure inductance without any resistance, leads to a phase shift between the current and the voltage.

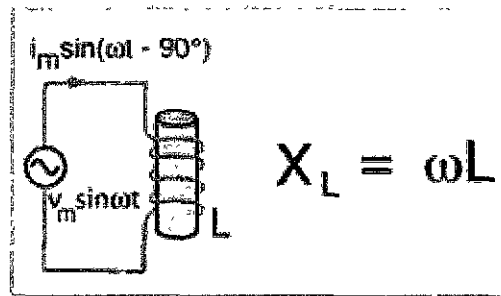


Fig. 60: Inductor response in AC [22]

Current lags voltage, and the 90° shift is a result of the idealized inductance with no resistance. Consequently the simple Ohm's law which applies only to a direct current, where current I is defined by:

$$I_{DC} = \frac{U}{R} \quad (35)$$

It has to be extended and a new term, the impedance is introduced instead of the resistance:

$$I_{AC} = \frac{U}{Z} \quad (36)$$

The value Z is called impedance and differs for a solenoid coil in an AC circuit from the DC circuit. For the pure resistor the impedance Z is equal to R , but because of the contribution of an inductor to the phase shift of 90° a vector relationship has to be considered. Fig. 61 shows this relationship graphically.

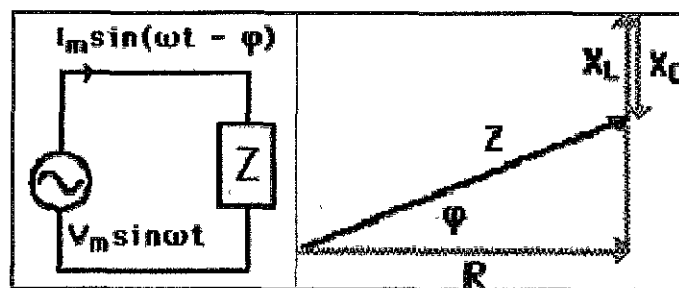


Fig. 61: Impedance [22]

In the Fig. 61, φ is the indication of phase shift between the voltage and the current, R is the resistance and X_L is the inductance. The voltage is defined by:

$$U = U_m \cdot \sin(\omega \cdot t) \quad (37)$$

and the current is.

$$I = I_m \cdot \sin(\omega \cdot t - \varphi) \quad (38)$$

In this new example the circuit has both resistance and inductance, X_L . The impedance is calculated as follows:

$$Z = \frac{U_{\text{eff}}}{I_{\text{eff}}} = \sqrt{R^2 + \omega^2 \cdot L^2} \quad (39)$$

where:

$$X_L = L \cdot \omega \quad (40)$$

and:

$$\omega = 2 \cdot \pi \cdot f \quad (41)$$

where f is the frequency of the alternating current in Hz, and the inductance L of a coil can be calculated from the design of the coil and the properties of the materials:

$$L_{\text{coil}} = \frac{\mu_0 \cdot \mu \cdot A_c \cdot N^2}{w} \quad (42)$$

where μ_0 , the permeability of free space, and μ is the permeability of the material, A_c is the cross section of the inductor and N is the number of windings of the coil around the inductor and w is the length of the inductor.

5.2 The Magnetic circuitry for the magnetostrictive actuator

A coil in an appropriate ferromagnetic housing is defined as the source of the magnetic field. The layout of the magnetostrictive actuator was discussed previously and was depicted in Fig. 35. The chosen diameter of the Terfenol-D shaft is 8 mm and the length is 67.5 mm. This selection has been based on the results of the parametric calculations presented in chapter 4. The magnetic field is the result of electric power flow, current I [A] and voltage U [V], through the actuator coil. The coil is wound around the Terfenol-D shaft and the magnetic field is therefore parallel to the axis of the rod. Fig. 62 depicts the generally the coil layout.

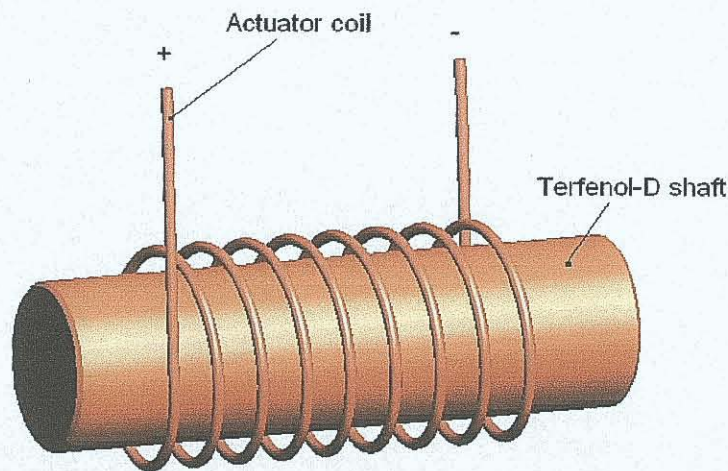


Fig. 62: Layout of the actuator coil

Since not only the coil is involved in the magnetic circuit other ferromagnetic components like housing, Terfenol-D shaft and inserts have to be considered. Fig. 63 presents the main magnetic path through the magnetostrictive actuator.

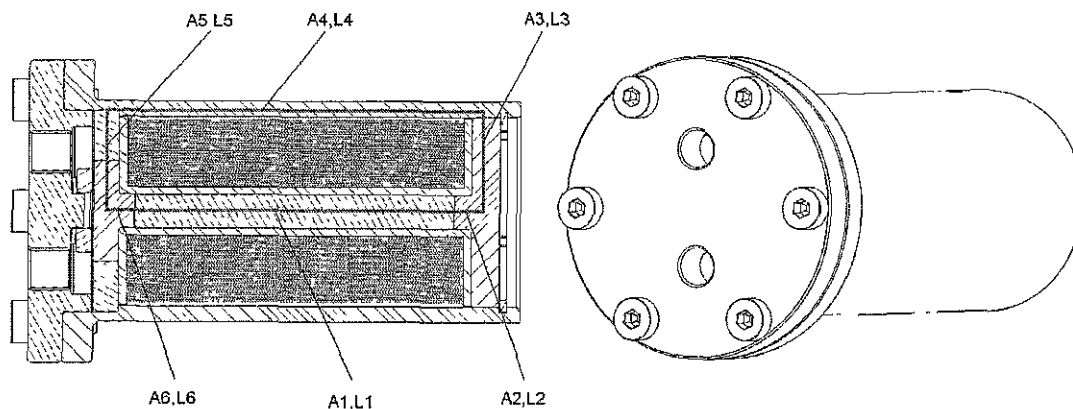


Fig. 63: Magnetic path through the actuator

For Terfenol-D the magnetic field strength, H (A/m), which is required to achieve the expected performance, is considered as moderate. Fig. 64 shows the strain capability of applied magnetic field intensity (A/m) from Terfenol-D material.

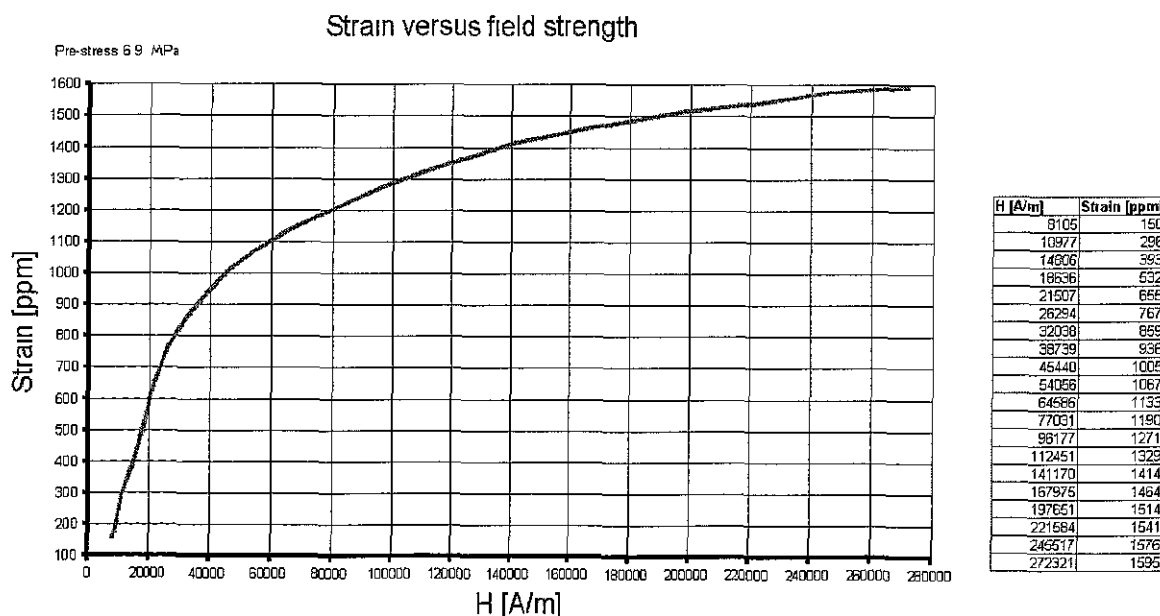


Fig. 64: Strain versus applied magnetic field intensity (A/m)[14]

Above depicted data were taken from the supplier specification for the Terfenol-D shaft at pre-stress about 6.9 MPa. The estimated linear range is up to 900 ppm. The maximal targeting strain range, due to near linear relationship to the applied field, is up to the level of 1200 ppm.

It is common for layouts, involving Terfenol-D actuators where the magnetic flux should be guided and focused in the region of the active material. This is required to maximize the magnetic field energy and minimize the energy losses in the region where the magnetic field is not needed. The frequency range has also to be considered in order to enable the functionality of the actuation system. A nonlinear time harmonic simulation method will be used to determine and optimize the actuator performance. The parameter calculations from this study related to the operational frequency would be used to set up the first set of parameters for the simulation.

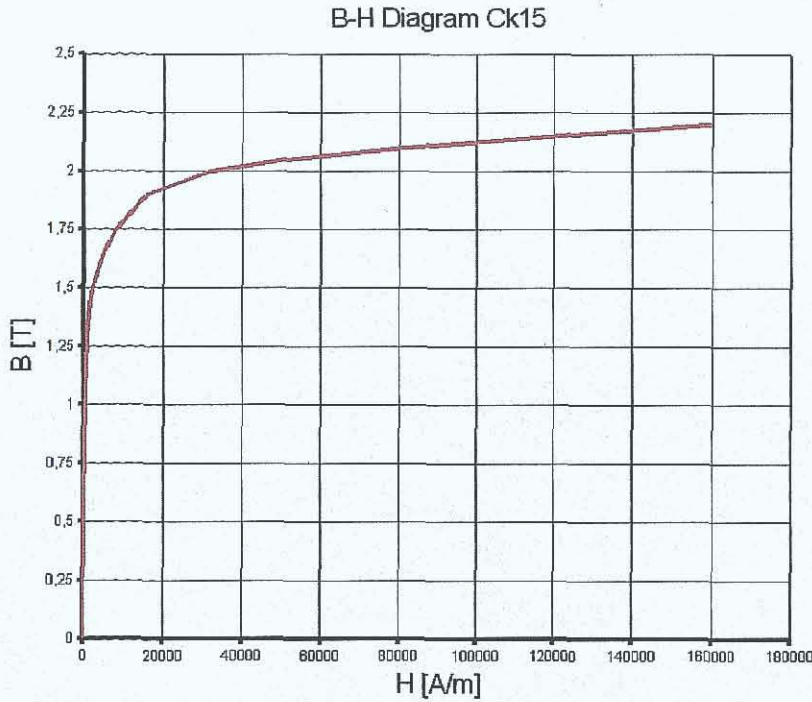
According to the Ampere's Law the relationship between the current (A) and the magnetic field strength (A/m) could be formulated as.

$$\oint H \, dl = N \cdot I \quad (43)$$

In Fig. 63 there are six designated sections of component through which the magnetic flux passes. Therefore:

$$\oint H \, dl_{GMM} = N_{GMM} \cdot I_{GMM} = H_1 \cdot l_1 + H_2 \cdot l_2 + \dots + H_6 \cdot l_6 \quad (44)$$

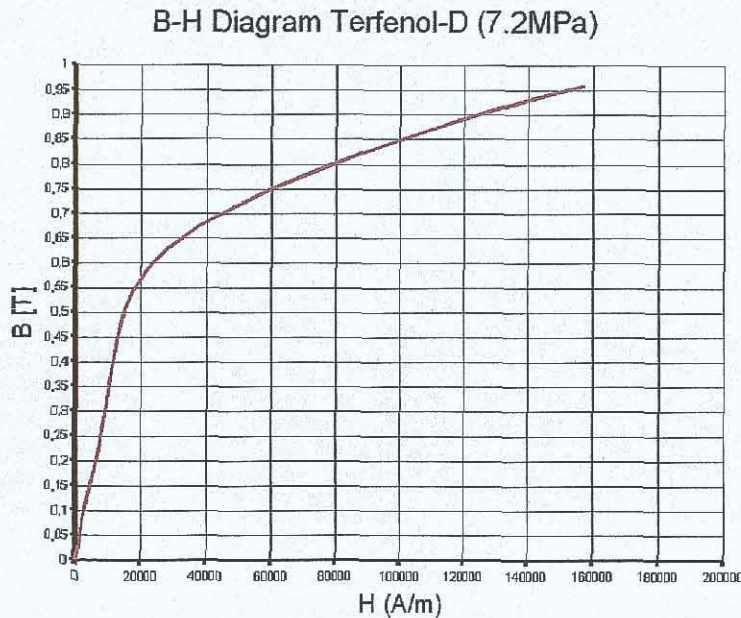
It is important to include all six terms in order to estimate the required total magnetomotive force, and so the return path of the magnetic flux through steel components must also be considered. For each section there is a length of the magnetic path, l , and a value for the magnetic field strength, H . The length is fixed by the geometry of the system, but the value of H must be determined by making use of the magnetic properties of the material. For the housing of the actuator the low carbon steel, Ck15, has been used. The magnetic properties of Ck15 are shown in Fig. 65.



H	B	μ	μ_r
0	0	-	-
100	0,26	2,62E-003	2087
200	0,5	2,48E-003	1976
300	0,7	2,36E-003	1866
400	0,89	2,21E-003	1763
500	1,02	2,04E-003	1624
600	1,11	1,86E-003	1476
700	1,17	1,68E-003	1336
800	1,22	1,53E-003	1215
900	1,26	1,40E-003	1112
1000	1,29	1,29E-003	1026
1100	1,32	1,20E-003	952
1200	1,34	1,12E-003	889
1300	1,36	1,05E-003	834
1400	1,38	9,86E-004	786
1500	1,4	9,32E-004	742
1600	1,41	8,84E-004	703
1700	1,43	8,40E-004	669
1800	1,44	8,01E-004	637
1900	1,45	7,66E-004	609
2000	1,47	7,33E-004	583
2400	1,5	6,27E-004	499
2800	1,54	5,49E-004	436
3200	1,56	4,89E-004	386
3600	1,58	4,40E-004	350
4000	1,61	4,01E-004	319
4400	1,62	3,69E-004	294
4800	1,64	3,42E-004	272
5200	1,65	3,18E-004	253
5600	1,67	2,98E-004	237
6000	1,68	2,80E-004	223
6400	1,7	2,65E-004	211
6800	1,71	2,51E-004	200
7200	1,72	2,39E-004	190
7600	1,73	2,28E-004	181
8000	1,74	2,17E-004	173
8400	1,75	2,08E-004	166
8800	1,76	2,00E-004	159
9200	1,77	1,92E-004	153
9600	1,78	1,85E-004	147
16000	1,9	1,19E-004	96
32000	2	6,25E-005	50
50000	2,05	4,10E-005	33
80000	2,1	2,63E-005	21
160000	2,2	1,38E-005	11

Fig. 65: B-H diagram of Ck15 with measurement data

The magnetic properties of Terfenol-D at various pre-stress levels have been provided by the Terfenol-D supplier. Fig. 66 depicts the B-H characteristic of the preferred pre-stress about 7.2MPa.



H (A/m)	B (Tesla)	μ	μ_r
0	0	-	-
418	0,01	3,39E-005	26,94
1115	0,05	4,24E-005	33,72
1811	0,08	4,27E-005	33,95
2747	0,11	3,84E-005	30,55
3653	0,13	3,57E-005	28,43
4538	0,16	3,41E-005	27,16
5759	0,18	3,17E-005	25,25
6667	0,21	3,15E-005	25,05
7618	0,24	3,15E-005	25,03
8313	0,27	3,24E-005	25,61
9242	0,3	3,24E-005	25,78
9706	0,33	3,41E-005	27,11
10403	0,36	3,45E-005	27,52
11099	0,39	3,49E-005	27,8
11756	0,41	3,51E-005	27,91
12453	0,44	3,57E-005	27,86
13169	0,45	3,45E-005	27,67
13866	0,48	3,44E-005	27,37
14582	0,48	3,39E-005	26,98
15279	0,51	3,39E-005	26,62
17601	0,54	3,08E-005	24,62
22942	0,6	2,61E-005	20,73
28203	0,63	2,23E-005	17,74
37571	0,67	1,80E-005	14,29
47788	0,71	1,49E-005	11,83
58115	0,75	1,29E-005	10,24
67757	0,77	1,14E-005	9,07
77742	0,81	1,03E-005	8,18
87495	0,82	9,38E-006	7,45
97944	0,84	8,62E-006	6,86
107699	0,87	8,04E-006	6,39
117913	0,89	7,59E-006	5,99
127668	0,91	7,10E-006	5,65
137651	0,93	6,73E-006	5,35
147636	0,94	6,40E-006	5,09
157155	0,95	6,11E-006	4,86

Fig. 66: B-H diagram of Terfenol-D with measurement data [14]

In order to enable the actuation mechanism to work at high dynamic level, the amount of the ferromagnetic steel has to be minimize. For a magnetic circuit the total flux, Φ , remains constant. The flux is related to the flux density, B , and is equal to the flux density multiplied by the integral of cross-sectional area [33].

$$\phi = \int B dA \quad (45)$$

Where this area is constant throughout the magnetic pathway, the integral of cross-sectional area is equal to the area. Since the flux is constant, the product of flux density and cross-sectional area must be constant for each material:

$$\phi_{Terfenol} = \phi_{steel} \quad (46)$$

$$B_{Terfenol} \cdot A_{Terfenol} = B_{steel} \cdot A_{steel} \quad (47)$$

The flux density B (T) depends on the properties of the medium and specially the relative μ_r (-) and absolute permeability μ . They are sometimes written in the form:

$$B_{steel} = \mu_0 \cdot \mu_{steel} \cdot H_{steel} \quad (48)$$

$$B_{Terfenol} = \mu_0 \cdot \mu_{Terfenol} \cdot H_{Terfenol} \quad (49)$$

where μ_0 , the permeability of free space is constant, and μ_r , the relative permeability is another variable with different values for each value of magnetic field strength and for each material. The reluctance, \mathfrak{R} , is an analog to the resistance in the electric circuit. For the calculation of the reluctance the following equation could be stated:

$$\mathfrak{R} = \frac{MMF}{\phi} = \frac{N \cdot I}{\phi} \quad (50)$$

The reluctance is sometimes written in the form:

$$\mathfrak{R} = \frac{l}{\mu_0 \cdot \mu_R \cdot A} \quad (51)$$

The total system reluctance can be calculated as follows:

$$\mathfrak{R}_{total} = \mathfrak{R}_1 + \mathfrak{R}_2 + \mathfrak{R}_3 + \dots + \mathfrak{R}_n \quad (52)$$

Ohm's law for magnetic circuit could be formed as:

$$MMF = \phi \cdot \mathfrak{R} \quad (53)$$

In the magnetic path through an assembly, components specific reluctance has to be considered separately:

$$MMF = \phi \cdot (\mathfrak{R}_1 + \mathfrak{R}_2 + \mathfrak{R}_3 + \dots + \mathfrak{R}_n) \quad (54)$$

The inductance (weber-turns per ampere) of the magnetic circuit is defined as:

$$L = \frac{N^2}{\mathfrak{R}_{total}} \quad (55)$$

For the proposed type of actuation system the maximal current is limited in automotive area. Conventional actuation systems are working with high current, up to 50 A, which is always a critical feature for some automotive applications. Current demand in the range of 10 A would be a good trade off between low current and good performance requirements. Due to combination of equations (50) with (51), considering equations (47) to (49), following equation could be introduced:

$$N = \frac{\mathfrak{R}_{total} \mu_0 \cdot \mu_{Terfenol} \cdot H_{Terfenol} \cdot A_{Terfenol}}{I} \quad (56)$$

It is now possible to follow the procedure to calculate the required number of turns to achieve the required magnetic field strength. For the parametric calculation, to determine the number turns, the relative permeability of Ck15 and Terfenol-D has been set constant. These constants, μ_{Ck15} and $\mu_{\text{Terfenol-D}}$, have been set to average value for specific material based on measurements. Fig. 67 depicts the results from the parametric calculation for the required number of turns. The geometries have been taken from drawings in the appendix A of this thesis.

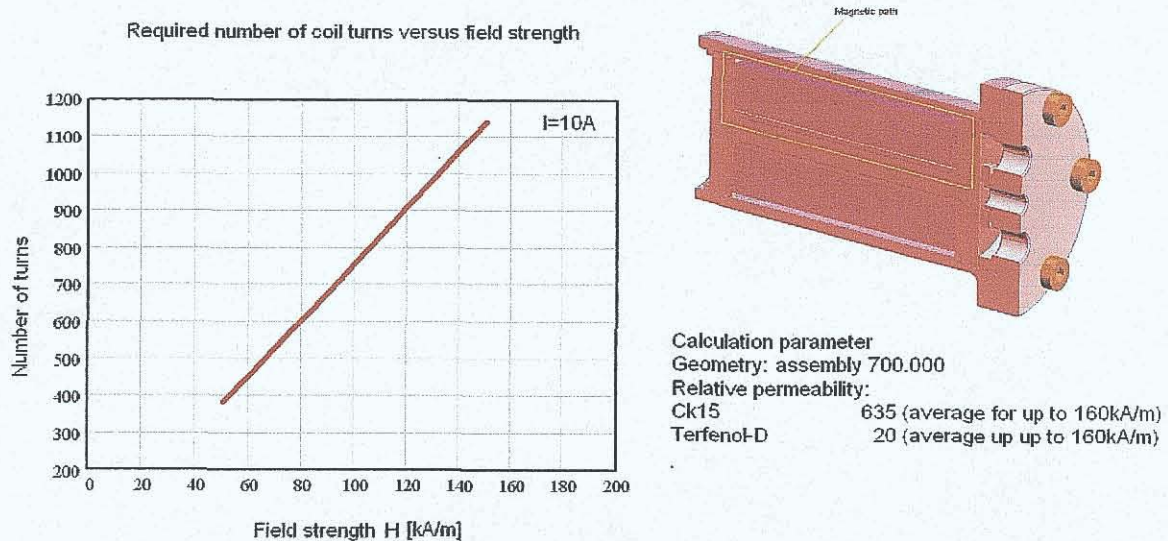


Fig. 67: Number of turns versus achievable magnetic field strength

These calculations are prepared as the first input for simulation of the magnetic circuit. The nonlinear B-H characteristic and the real, not constant permeability of each material will be used in the magnetic field simulation. The proposed approach, outlined above, was also used to calculate the reluctance of the circuit; it is $60 \times 10^6 \text{ H}^{-1}$. For above parametrical calculation it was necessary to perform a trial and error series of operations to find out how many turns the coil needs to have in order to provide the required field strength and how much space this coil will need. To perform these calculations, layout geometries had to be assumed initially, i.e. the outer diameter of the housing, and then tuned to the optimum. Finally, magnetic field simulation has been used to confirm the magnetic field calculations. Presented calculation results have been used as the initial input for the magnetic simulation software for further optimization.

5.3 The Magnetic circuitry for the magnetorheological arrangement

Two different layouts, valve and orifice, have been introduced with parametrical calculations in chapter 4. The favorite has been identified due to better performance regarding drag pressure drop and achievable pressure. The orifice is simpler and less expensive than valve. Therefore both layouts will be used for the magnetic calculations and for experimental evaluation. With this approach an alternative control arrangement can be verified theoretically and experimentally.

The favorite arrangement has been introduced in Fig. 36. A coil in an appropriate ferromagnetic housing was defined as the source of the magnetic field. The chosen diameter of the internal shaft is 10 mm and the MRF gap is 0.5 mm. This selection has been based on the results of the parametric calculations. The magnetic field is the result of electric power flow, current I [A] and voltage U [V], through the coil. The coil is wound around the bobbin and the magnetic field is guided through the MRF gap perpendicularly to the fluid flow. Fig. 68 depicts the coil layout with fluid motion and magnetic field direction.

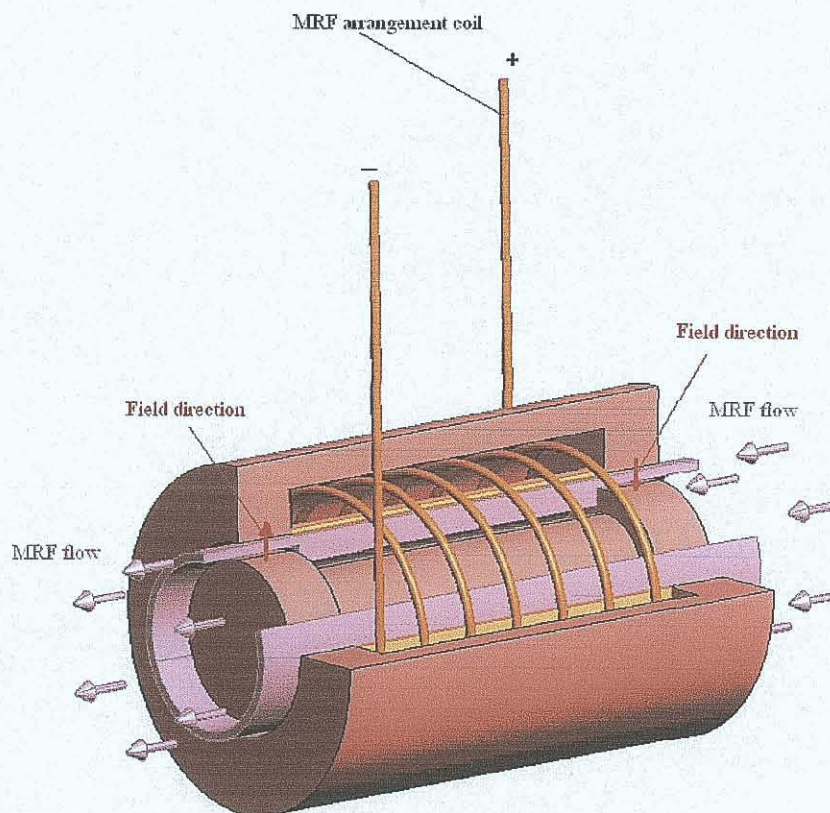


Fig.68: Layout of the valve control arrangement

Fig. 69 depicts the same arrangement as shown above but with the experimental assembly.

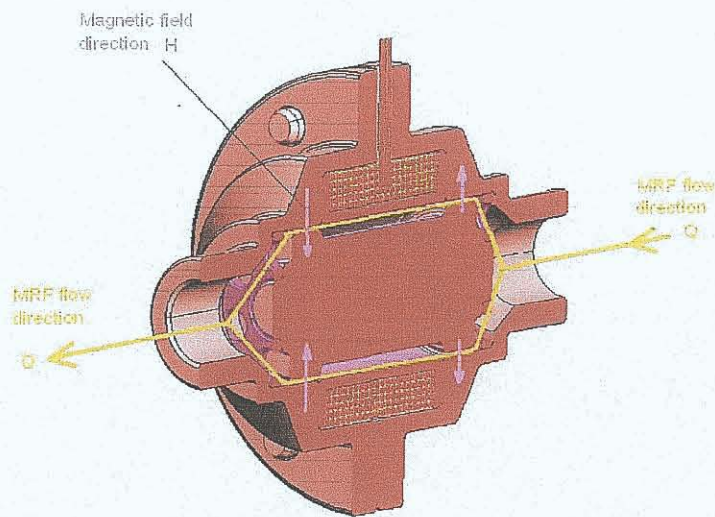


Fig.69: Layout of the control valve

All ferromagnetic components, housing with internal shaft and MRF, have to be considered for the evaluation of the magnetic circuitry. Fig. 70 shows the main magnetic path through the favorite MRF valve arrangement.

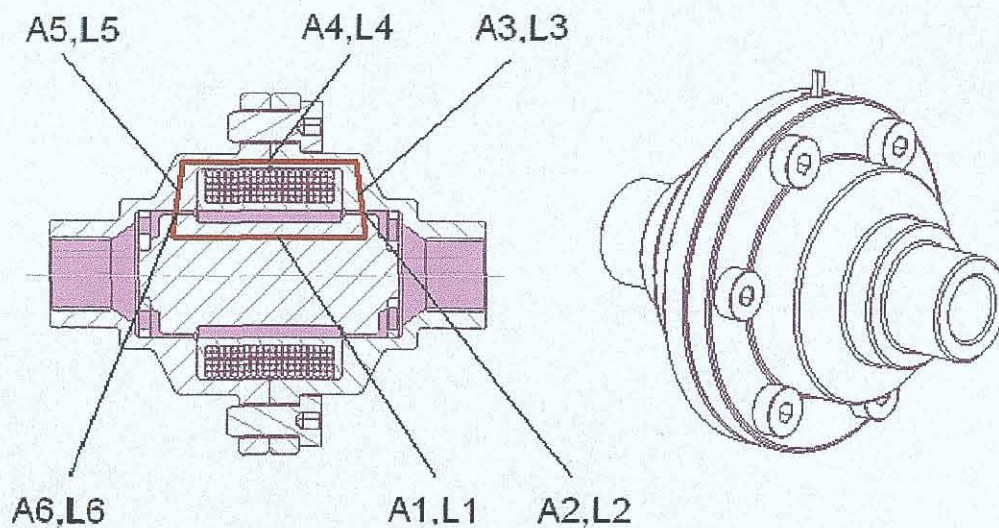


Fig. 70: Magnetic path through the valve

The requirement of the magnetic field strength for the MRF is in the range up to 200 kA/m. The alternative arrangement has been introduced in Fig. 37. A coil in an appropriate

ferromagnetic housing was defined as the source of the magnetic field. The chosen diameter of the orifice is 1.5 mm. This selection has been based on the results of the parametric calculations. The magnetic field is the result of electric power flow, current I [A] and voltage U [V], through the coil. The coil is wound around the bobbin and the magnetic field is guided directly into the MRF, which is in the orifice. The bobbin inner diameter is the orifice diameter. The magnetic field direction is inline with the fluid flow direction. Fig. 71 depicts the coil layout with fluid motion and magnetic field direction.

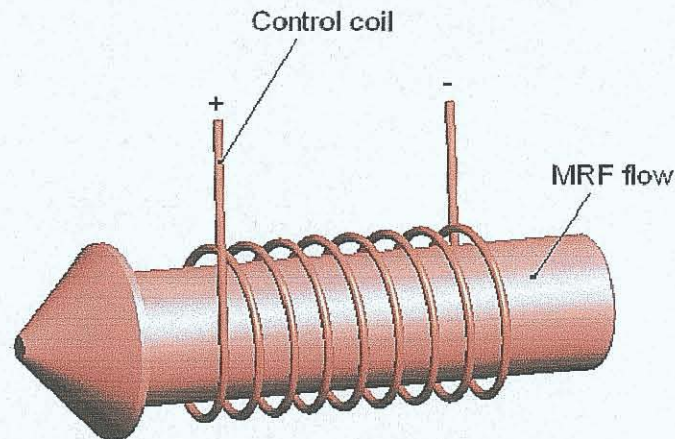


Fig.71: Layout of the orifice control arrangement

Fig. 72 depicts the same arrangement as shown above but with the experimental assembly.

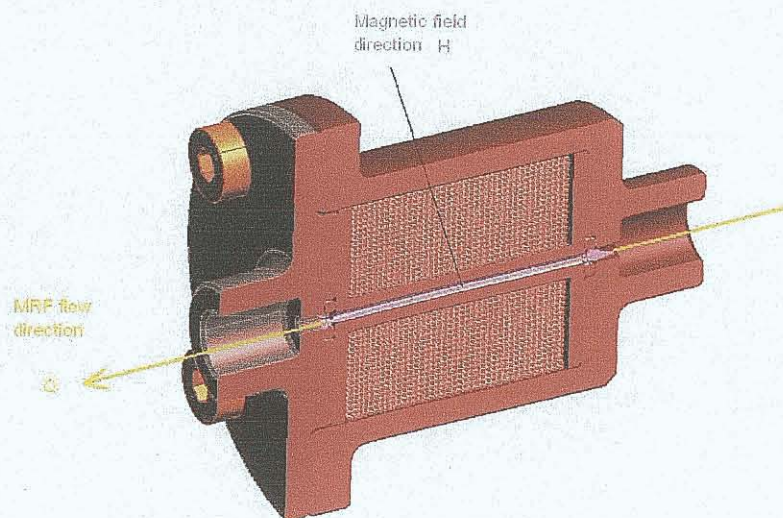


Fig.72: Layout of the control orifice

The ferromagnetic components, housing and MRF, have to be considered for the evaluation of the magnetic circuitry. Fig. 73 shows the main magnetic path through the alternative MRF orifice arrangement.

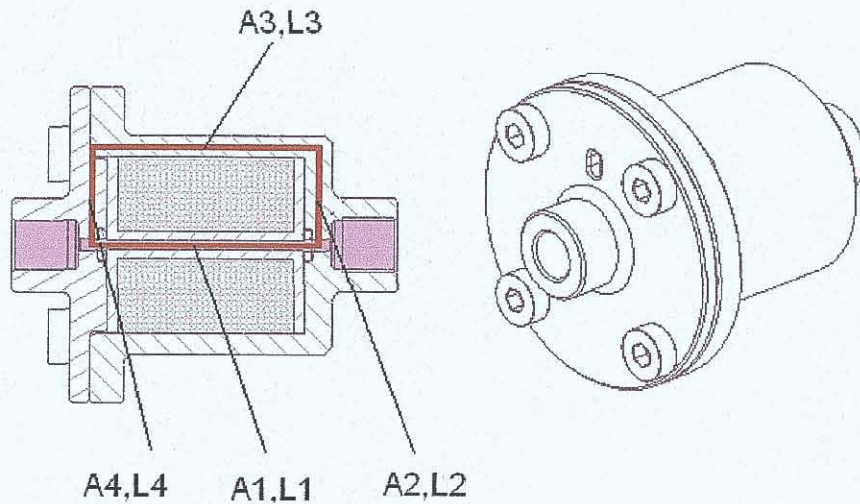


Fig. 73: Magnetic path through the control orifice

Also here, the target range of the magnetic field is up to 200 kA/m. For the housing in the valve assembly (favorite) and the orifice (alternative) the low carbon steel, Ck15, has been used. The magnetic property of Ck15 has been shown in Fig. 65. Fig. 74 depicts the magnetic properties of the favorite MRF132 taken from the MRF supplier [69 and 79].

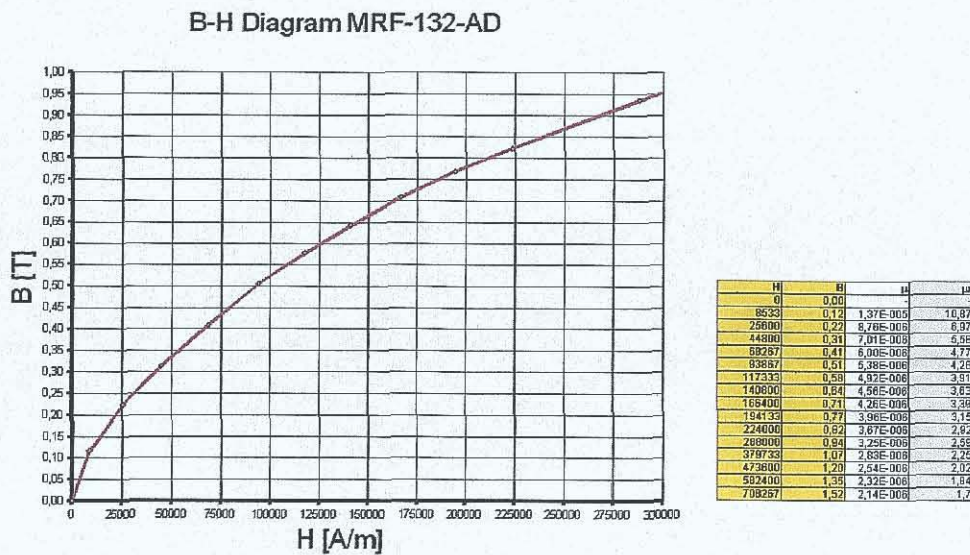


Fig. 74: B-H diagram of MRF132-AD [69 and 79]

Fig. 75 depicts the magnetic properties of alternative MRF336 taken from the MRF supplier [69 and 79].

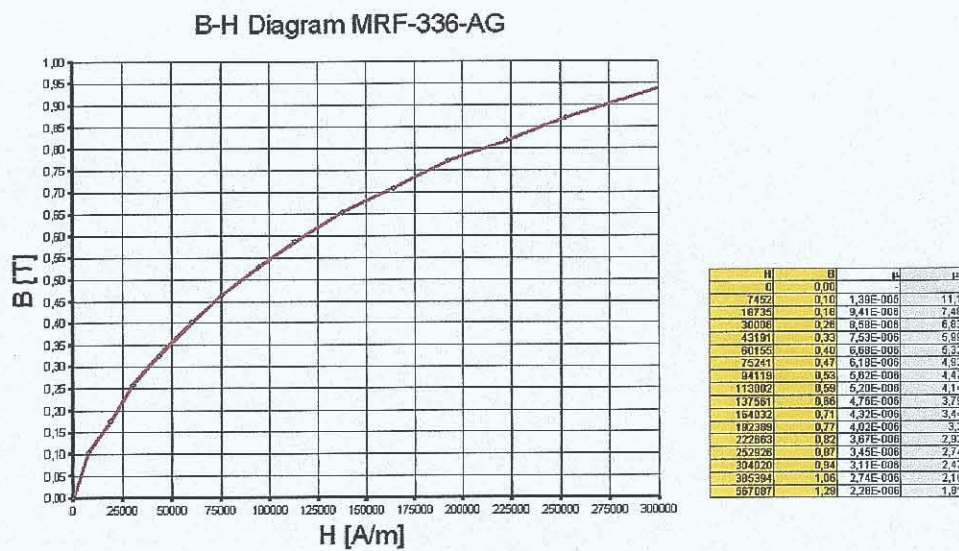


Fig. 75: B-H diagram of MRF 336-AG [69 and 79]

In order to achieve fast response it is obtained to minimize the amount of the ferromagnetic steel in the magnetic circuit. The approach of magnetic field calculation, which has been implemented using equations (45) to (55), would be used as well to define desired coils for the valve and the orifice.

In Fig. 70 there are six designated sections of component through which the magnetic flux passes. Therefore, in analog to Eq. (43):

$$\oint H dl_{MRF} = N_{MRF} \cdot I_{MRF} = H_1 \cdot l_1 + H_2 \cdot l_2 + \dots + H_6 \cdot l_6 \quad (57)$$

And for the alternative design according Fig. 73:

$$\oint H dl_{MRF} = N_{MRF} \cdot I_{MRF} = H_1 \cdot l_1 + H_2 \cdot l_2 + \dots + H_4 \cdot l_4 \quad (58)$$

Since the flux is constant, the product of flux density and cross-sectional area must be constant for each material:

$$\Phi_{MRF} = \Phi_{steel} \quad (59)$$

$$B_{MRF} \cdot A_{MRF} = B_{steel} \cdot A_{steel} \quad (60)$$

The flux density B (T) depends on the properties of the medium and specially the relative μ_r (-) and absolute permeability μ . They are sometimes written in the form:

$$B_{MRF} = \mu_0 \cdot \mu_{MRF} \cdot H_{MRF} \quad (61)$$

where μ_0 , the permeability of free space is constant, and μ_r , the relative permeability is another variable with different values for each value of magnetic field strength and for each material.

For the MRF control arrangement the maximal current was set to be up to 6A. Due to combination of equations (50) with (51), considering equations (57) to (61), following equation could be introduced:

$$N = \frac{\mathcal{R}_{total} \mu_0 \cdot \mu_{MRF} \cdot H_{MRF} \cdot A_{MRF}}{I} \quad (62)$$

It is now possible to follow the procedure to calculate the required number of turns to achieve the required magnetic field strength. For the parametric calculation, to determine the number turns, the relative permeability of Ck15 and MRF-132-AD have been set as constant. These constants, μ_{Ck15} and $\mu_{MRF-132-AD}$, have been set to average value for specific material based B-H diagram. Fig. 76 depicts the results from the calculation for the required number of turns for the favorite design.

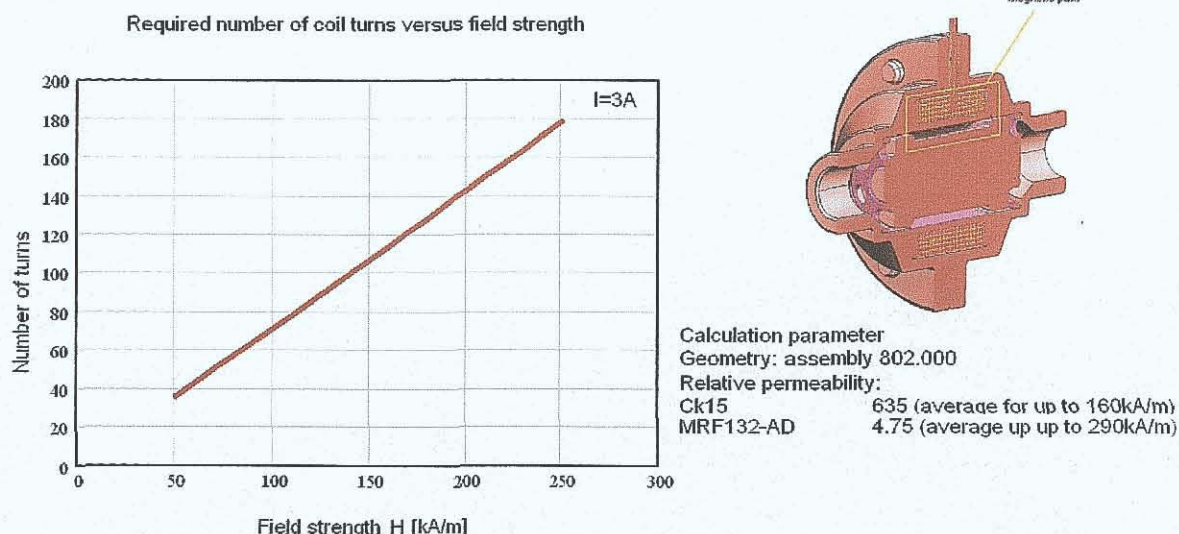


Fig. 76: Number of turns versus achievable magnetic field strength for the valve

Fig. 77 depicts the results from the calculation for the required number of turns for the alternative orifice design.

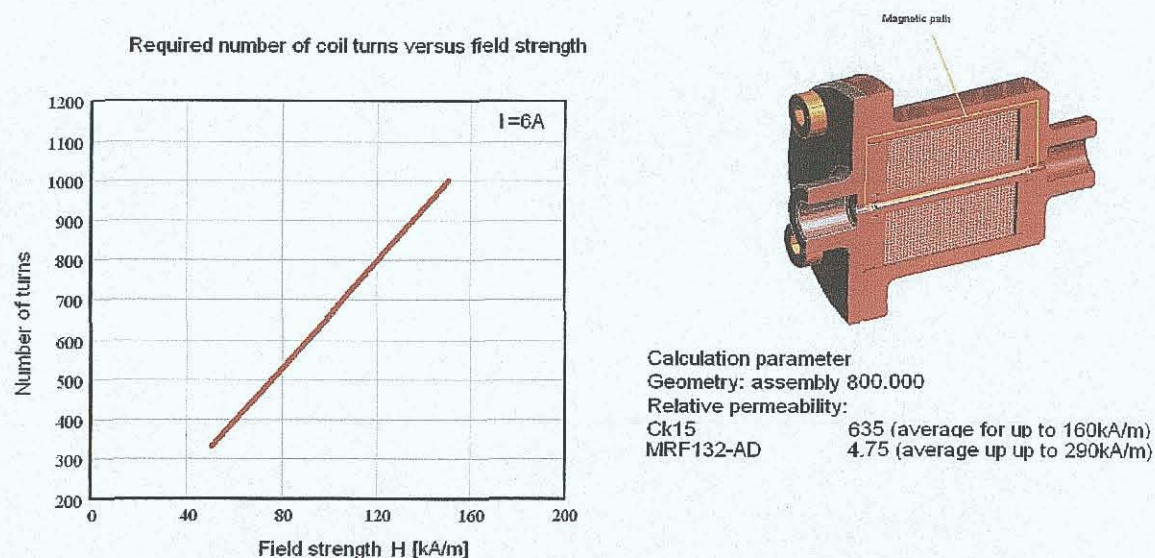


Fig. 77: Number of turns versus achievable magnetic field strength for the orifice

It is again obvious for both, magnetic and geometric dimensions, that the valve layout should be preferred. All geometries have been taken from drawings the in the appendices B and C. These calculations are prepared as the first input for simulation of the magnetic circuit. The nonlinear B-H characteristic and the real, not constant permeability of each material will be

used in the magnetic field simulation. Further details regarding the coil and wire geometry will be discussed in section 5.4. The proposed approach, outlined above, was also used to calculate the reluctance of the circuit; it is in the favorite arrangement $0.9 \times 10^6 \text{ H}^{-1}$. For the above parametrical calculation it was necessary to perform a trial and error series of operations to find out how many turns the coil needs to have in order to provide the required field strength and how much space this coil will need. To perform these calculations, layout geometries had to be assumed initially, i.e. the outer diameter of the housing, and then tuned to the optimum. Finally, magnetic field simulation has been used to confirm the magnetic field calculations. The above shown calculation results have been used as the initial input for the magnetic simulation software for further optimization.

5.4 Electric coil for actuator and magnetorheological arrangement

In the following calculation it was necessary to perform a trial and error series of operations to find out how many turns the coil needs in order to provide the required field strength and how much space this coil will need. The proposed approach with the calculation of the reluctance enables to indicate the dynamic capability of the proposed arrangement. Fig. 78 shows the cross section of an air coil. The bobbin of the coil is made of aluminum and does not affect the magnetic field.

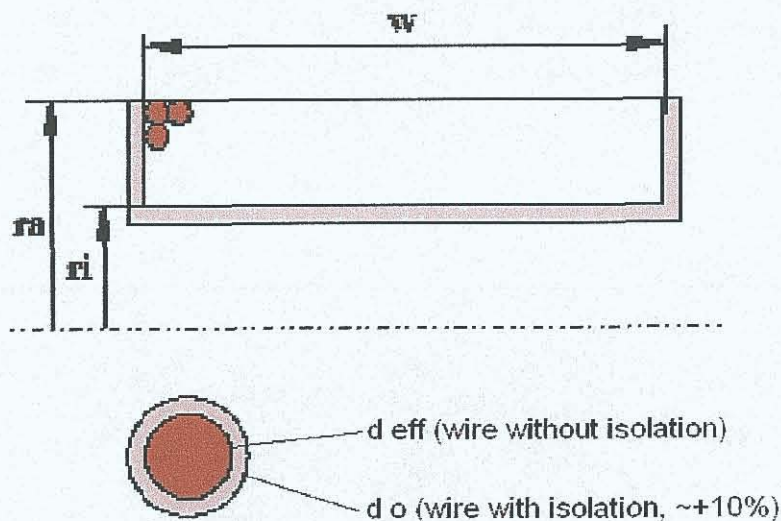


Fig. 78: Air coil geometry

Each strand of the copper wire is coated with an insulating layer to avoid electrical short circuits. The insulated wire is about 10% larger than the un-insulated wire. The overall

resistance of the copper wire in the coil can be calculated if the geometry, length and cross-sectional area, are known and the resistivity of copper is known.

$$R_{dc} = \frac{\delta \cdot l_{wire}}{A_{wire}} \quad (63)$$

The resistivity of copper, δ with units, is defined by:

$$\delta_c = 0.01786 \cdot \frac{\Omega \cdot mm^2}{m} \quad (64)$$

There is also a variation of the resistivity of copper with temperature, and this also must be taken into consideration. Over the temperature range of interest:

$$R_{\theta} = R_{20} \cdot (1 + \alpha_{20} \cdot (\theta - 20^{\circ}C)) \quad (65)$$

where θ is the temperature in degrees centigrade and the temperature constant, α at 20°C with units 1/°C, is defined by:

$$\alpha_{20} = 0.0039 \frac{1}{^{\circ}C} \quad (66)$$

Fig. 79 shows the result of the parametric calculation of current density versus wire diameter. The specified current range 1-10 A has been used. Typical current density in automotive applications is lower than 7 A/mm². The current density limitation, given by wire supplier, is up to 10 A/mm². Generally, the limitation is given by thermal conditions and the isolation layer specification.

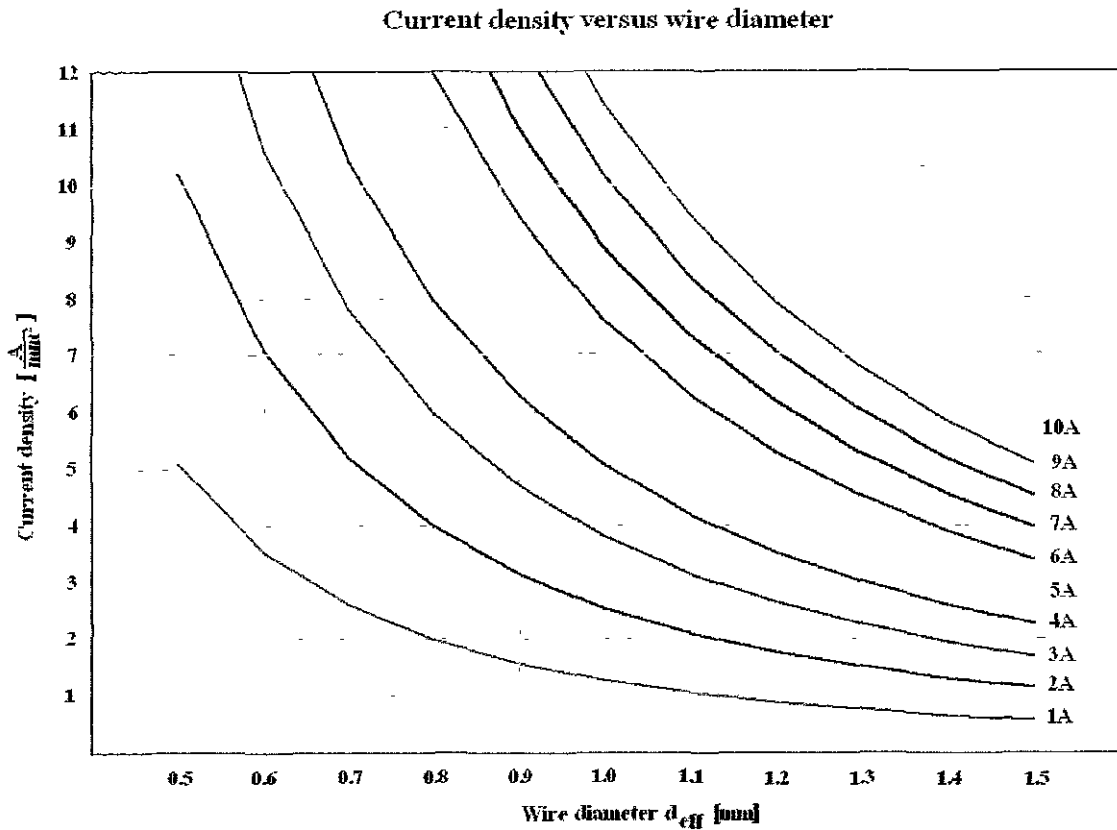
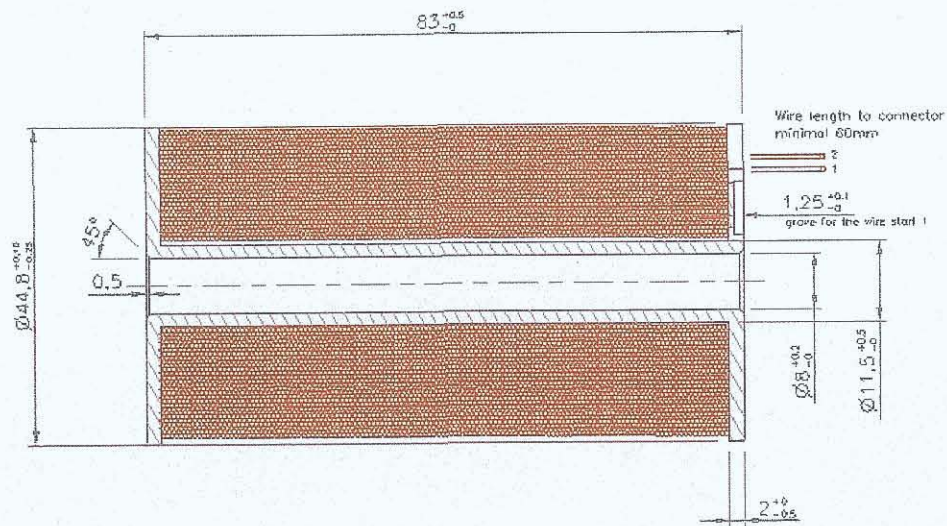


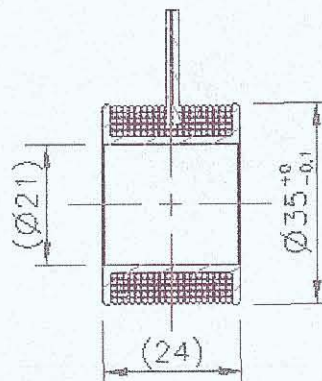
Fig. 79: Current density versus wire diameter with current as parameter

It is now necessary to perform a trial and error series of operations to find out how many turns the coil needs to have in order to overcome the reluctance. Another way to calculate is the definition of required magnetomotive force. The result of both ways of calculation leads to the same coil specification. The parametrical calculation results, used to specify the prototype coil, have been proven by non-linear magnetic field simulation. Based on above discussed analytical calculations and the results from the magnetic field simulations, prototype specification for coils has been proposed. Fig. 80 depicts geometry and reference coil specification of magnetostrictive actuator. Fig. 81 depicts geometry and coil specification of the favorite MRF control valve.



Actuator coil for rig tests
 Temperature range: -20°C up to $+120^{\circ}\text{C}$
 Supplied voltage: $12\text{V} \pm 3\text{V}$,
 Frequency: 0Hz at DC and 1000Hz at AC
 Resistance at R_t : >1.52 Ohm at DC
 Inductance: 23mH
 Nominal current: <9.8 A
 Number of turns: >1000
 Wire material: Copper
 Wire bare diameter: 1.15mm (AWG17)

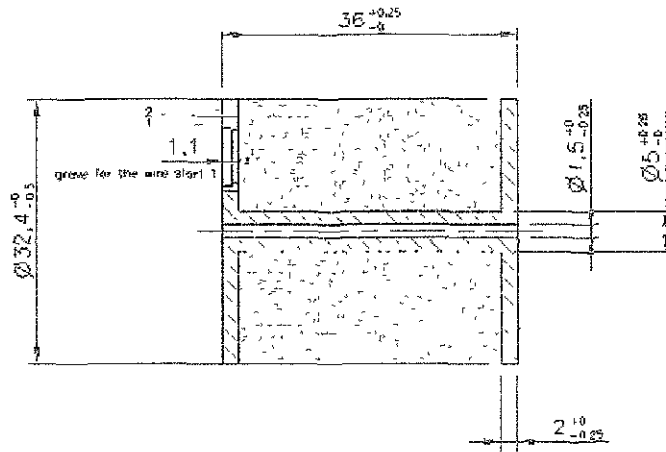
Fig. 80: Geometry and coil specification of the magnetostrictive actuator



Control coil for rig tests
 Temperature range: -20°C up to $+120^{\circ}\text{C}$
 Supplied voltage: $2\text{V} \pm 0.5\text{V}$,
 Frequency: 0Hz at DC and 1000Hz at AC
 Resistance at R_t : >0.33 Ohm at DC
 Inductance: 1mH
 Nominal current: <6.2 A
 Number of turns: >120
 Wire material: Copper
 Wire bare diameter: 0.9mm

Fig. 81: Geometry and coil specification of the control valve

Based of calculations, magnetic field simulations and the desired simplicity of the assembly, the coil for the orifice control has been proposed. Fig. 83 shows geometry and coil specification of the control orifice.



Control coil for rig tests
 Temperature range -20 C up to $+120\text{ C}$
 Supplied voltage $5\text{V} \pm 1.5\text{V}$
 Frequency 0Hz at DC and 1000Hz at AC
 Resistance at Rt: $>0.81\text{ Ohm}$ at DC
 Inductance 8mH
 Nominal current: $<6.2\text{ A}$
 Number of turns >510
 Wire material: Copper
 Wire bare diameter: 0.92mm (AWG19)

Fig. 82: Geometry and coil specification of the control orifice

5.5 Magnetic Field Simulation

In order to optimize the design of the actuator, a simulation of magnetic field, including the real magnetic properties of used material, is required. The nonlinear simulation method was used to determine and optimize the actuator and control performance. Due to nonlinear $B-H$ function the system has to be solved by an iterative way [87]. The “MS”-actuator, “MR”-valve and “MR-orifice have been simulated regarding magnetic field. Finite element modelling methods of the magneto-mechanical phenomena have been proposed in several publications in [20] and [86] to [92]. Terfenol-D is a smart material in that the magnetic properties are coupled with mechanical state and vice versa. For an accurate simulation a nonlinear method with coupling between magnetic and mechanic properties are recommended.

One method involves a simultaneous solving process using the magnetostrictive characteristics of Terfenol-D rods: $\sigma(S, H)$ and $H(B, \sigma)$ [86]. Another method uses the direct dependency of the strain λ [ppm] versus field intensity H [A/m]. Special software packaging for smart materials and structures i.e. Atila FEM software is available for this purpose. Atila-Software has been developed by ISEN, France and distributed by Cedrat in Europe & Magsoft in USA. For the proposed actuator structure with stepwise accumulation of the smart material motion the knowledge of the pre-stress and pre-magnetization has to be considered to obtain the required functionality. For the optimization of the proposed structure the software packages Opera from Vector Fields and free available FEMM have been used. Some simulations have been done with both software modules for comparison reasons. The simple user interface and efficiency has been found in using the free available FEMM software packaging developed by David Meeker, Senior Engineer at Forster-Miller Inc. Results from the magnetic field simulation from FEMM and Opera have been evaluated and positively verified with measurements on the rig for several coil layouts. For low-frequency evaluations only a part of the complete Maxwell's equations is considered. Displacement currents are typically relevant only at radio frequencies [84]. For magnetic field simulation, the operational frequency for the actuator and control device has been investigated up to 1000 Hz. For simulation of the actuator and the control device at that low-frequency the problems of displacement currents can be neglected.

In the Finite Element method the partial differential and integral equations describe the variation of the magnetic field either directly as field variable i.e. flux density B , but more often using a potential function that is related to the field by gradient ∇ or by curl ($\nabla \times$) operation [85]. In the magneto-static case fields are constant over the time and the current density J is defined by equation:

$$J = \nabla \times H \quad (67)$$

Flux density B has zero divergence and is expressed by:

$$\nabla \cdot B = 0 \quad (68)$$

For a non-linear material the permeability is expressed with:

$$\mu = \frac{B}{H(B)} \quad (69)$$

The software modules are finding a magnetic field that satisfies equations (67) and (68) by iteration using the magnetic potential vector A . The magnetic flux density is expressed with

the vector A and is defined as:

$$B = \nabla \times A \quad (70)$$

Equation (67) for the static magnetic field using a magnetic vector potential could be rewritten as:

$$J = \nabla \times \left(\frac{1}{\mu(B)} \cdot \nabla \times A \right) \quad (71)$$

In 3D problems, feasible with FEM Opera from Vector Fields, this magnetic vector potential A becomes a three component vector. For simulation of the proposed actuator and control device a 2D and axisymmetric model has been applied. In this case the first two of the three components are zero and just the “out of the page” vector component has to be considered. In case that material behaves linear in the magnetic field, a simplification of the previous equation could be established:

$$B = \mu \cdot H \quad (72)$$

Further, for the linear isotropic material the following is valid:

$$\nabla \cdot A = 0 \quad (73)$$

Following, equation (71) with the linear isotropic material and 2D an axisymmetric problem could be rewritten as:

$$J = -\frac{1}{\mu} \cdot \nabla^2 \cdot A \quad (74)$$

In the case that the magnetic field is not constant over the simulation period time, further Maxwell's equations have to be applied. The current density J , the electric field intensity E and conductivity σ are linked by:

$$J = \sigma \cdot E \quad (75)$$

The induced electric field could be expressed with:

$$\nabla \times E = -\frac{dB}{dt} \quad (76)$$

Due to substitution of the magnetic vector potential A from B into equation for induced electric field as presented in Eq. 77:

$$\nabla \times E = -\nabla \times \dot{A} \quad (77)$$

The integration and simplification to a 2-D problem lead to

$$E = -\dot{A} - \nabla \cdot V \quad (78)$$

By substitution of E into Eq. (75), the relationship for current density could be rewritten to:

$$J = -\sigma \dot{A} - \sigma \cdot \nabla \cdot V \quad (79)$$

With further substitution of equation for the current density the partial differential equation can be presented as follows:

$$\nabla \times \left(\frac{1}{\mu(B)} \cdot \nabla \times A \right) = -\sigma \dot{A} + J_{src} - \sigma \cdot \nabla \cdot V \quad (80)$$

In equation (80) \hat{J}_{src} stands for the applied currents sources and the term $\nabla \cdot V$ is the additional voltage gradient over a conducting body [84]. FEMM considers equation (80) for evaluations of the magnetic field oscillating at one constant frequency. With additional transformation shown in equation (81), where a is the complex number:

$$A = Re[a(\cos \omega t + j \sin \omega t)] = Re[ae^{j\omega t}] \quad (81)$$

and substitution into equation (80) with dividing out of the complex exponential term equation (81) could be presented in following form:

$$\nabla \times \left(\frac{1}{\mu(B)} \cdot \nabla \times a \right) = -j\omega\sigma a + \tilde{J}_{src} - \sigma \cdot \nabla \cdot V \quad (82)$$

FEMM software uses equation (82), with as the phasor transform of applied current sources, for harmonic magnetic problems. FEMM software package enables the evaluation with a complex and frequency-dependent permeability in time harmonic problems. This feature could be used to model thin laminations and model of hysteresis effects.

To enable a particular magnetic simulation, a boundary condition has to be defined. The FEMM package offers three different types of boundary conditions: Dirichlet, Neumann and Robin. In the Dirichlet-condition the value of A is explicitly defined at the boundary, i.e. $A=0$. This condition will guarantee that the flux is not passing the boundary. In the Neumann-condition the normal derivative of A is specified. This condition forces the flux to leave the boundary at exactly 90° , i.e. like into the very highly permeable metal. And finally, the Robin-condition is a mix between Dirichlet and Neumann. Under this condition the value of A and its normal derivative at the boundary are specified [84]. For the evaluation of the proposed actuator, as well the control device, an axisymmetric problem is established and following $A=0$ on the line $r=0$.

All above discussed equations have to be satisfied by iteration and approximation. Even for evaluation of simple structures the final element analysis is very useful. The basic idea of the final element analysis is to split the structure in a large number of small sub-structures, each of them of simple standardized geometry (i.e. triangle). In this way the small but difficult to solve problem becomes to a large but simple to solve problem [84]. In particular, due to triangulation the differential equations become to x linear equation with x variable, what a computer can solve in a view seconds. Specially, FEMM uses triangular elements only. The approximation of a sufficient number of solutions for simple triangular regions leads to an accurate result for the magnetic vector potential A . The following section of this chapter contains results of the magnetic field simulation with the software packaging FEMM, some key simulation results have been calculated with the professional magnetic field simulation software tool Opera from Vector Field. Both software packages have been very useful and powerful tools for optimization of the actuator and control device geometry.

The first simulation loop has been created using the magnetic field simulation software FEMM, Version 4.0.1. Figure 83 shows the FEMM software window with user interface.

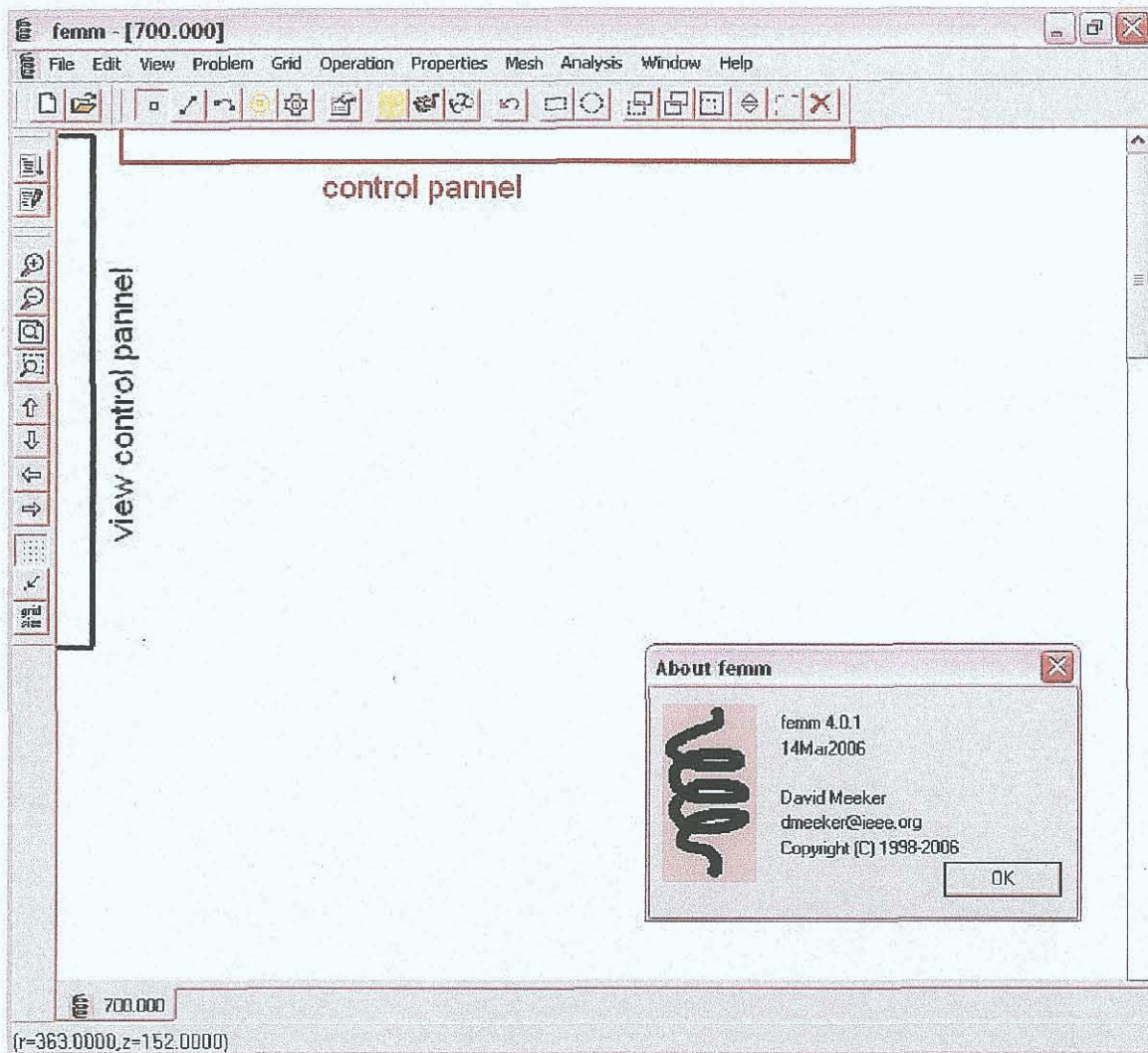


Fig. 83: FEMM software window with user interface [84]

For geometry input the CAD export / import tools has been used. The 3D design and 2D detailed drawings for prototyping as well the DXF-import files for the simulation tools have been prepared with CAD parametrical tool Pro-Desktop. More details can be obtained from the appendices A to D. The measured B-H characteristics, shown in previous section, have been used in the simulation of magnetic circuit.

5.5.1 Magnetic field simulation results from "MS"-actuator

Fig. 84 shows the meshed structure of the magnetostrictive actuator. The simulated model has been set up to an "axisymmetric problem", and the "asymptotic boundary conditions" have been applied. The results of the parametric calculation for the electric circuit have been used to set up the simulated model of the actuator assembly. The measured B-H characteristic for each material has been used as input for the magnetic field simulation software.

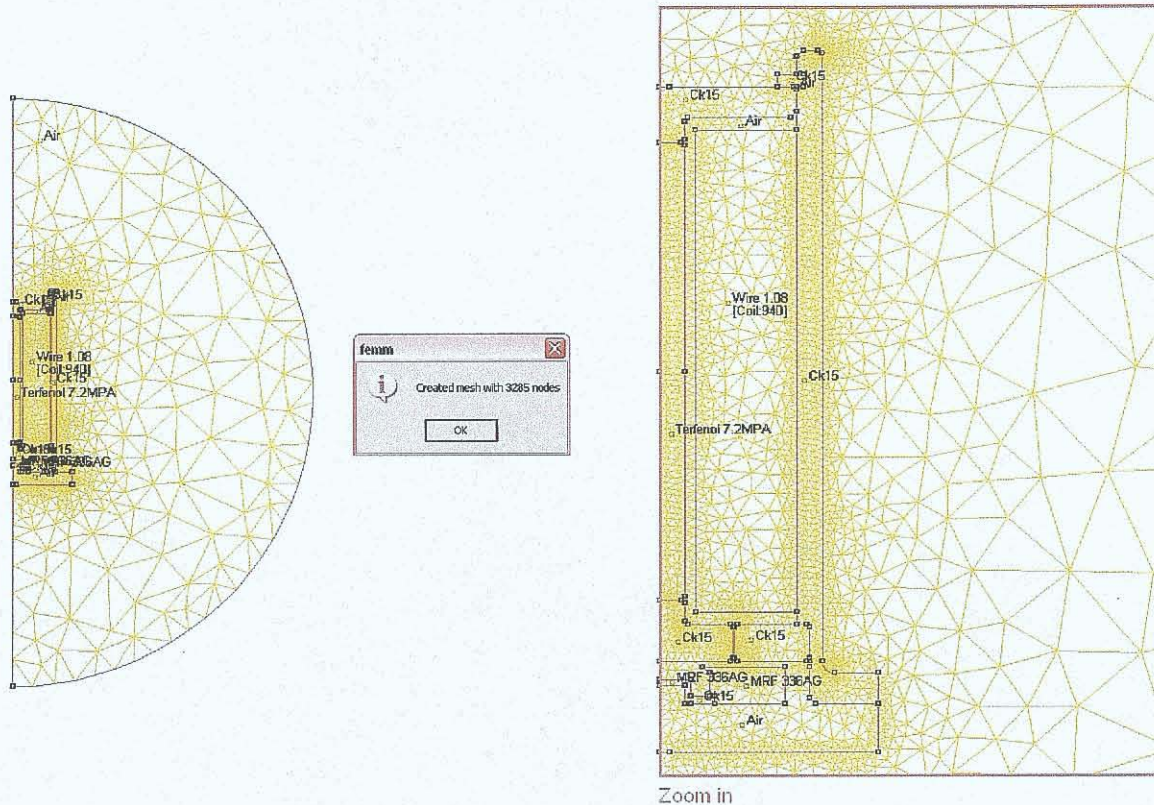
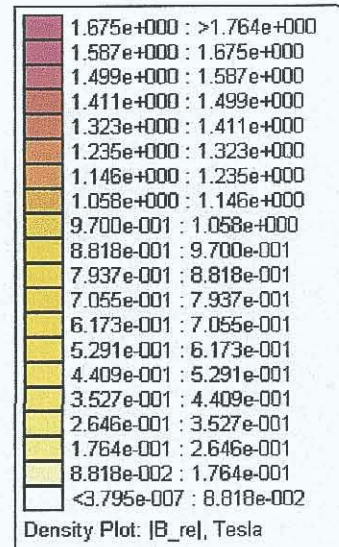
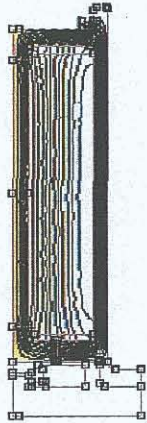


Fig. 84: Meshed actuator with FEMM

Fig. 85 shows the density plot for the real part of B (T) related to the center line of the Terfenol-D shaft. The results shown in Fig. 85 has been obtained using FEMM software package, version 4.

Center line



Title: 700.000
 Length Units: Millimeters
 Axisymmetric Solution
 Frequency: 500 Hz

3285 Nodes
 6389 Elements

Fig. 85: FEMM Flux density B (T) in the actuator

Based on the parametric calculations the nominal current for the actuator coil has been set up to 9 A. Various types of output information could be used to evaluate the magnetic field. For the evaluation of the magnetic circuit voltage drop, flux linkage, inductance, resistance and electrical power have been calculated. All calculations has been obtained with frequencies 0 Hz, 10 Hz, 50 Hz, 250 Hz, 500 Hz and 1000 Hz. Fig. 86 shows various types of additional result information from FEMM.

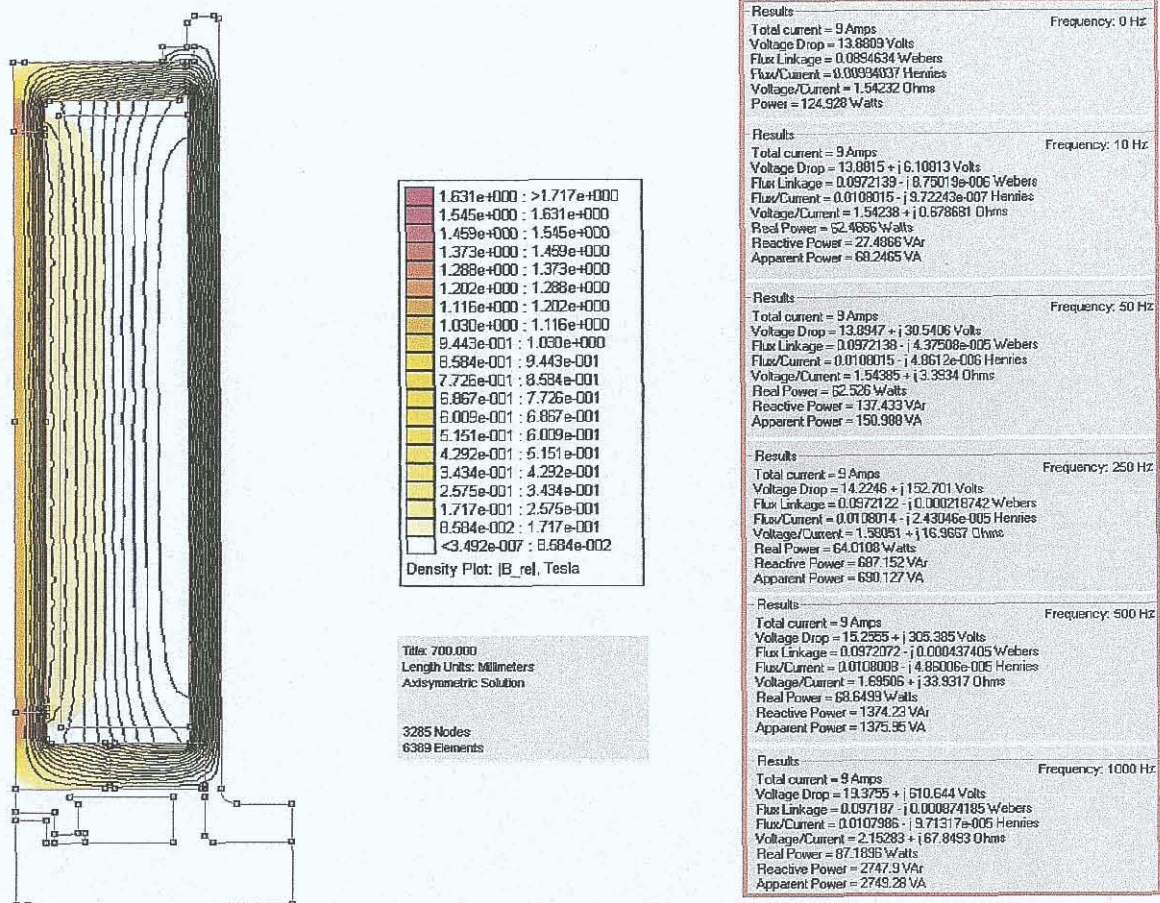


Fig. 86: FEMM Magnetic Circuit Results for the actuator

The frequency impact on resistance and inductance could be obtained in the simulation results. It should be mentioned that the electric frequency of operating electric power is the half of the mechanical pumping frequency. The frequency interference, doubling of the frequency, is based on the fact that the strain peak appears twice within one frequency loop from the electric power working with sine waves.

Fig. 87 presents the assembly reference picture for 2D-plots for magnitude of field density B (T) and magnitude of field intensity H (A/m) of the Terfenol-D shaft along the defined path line marked as length.

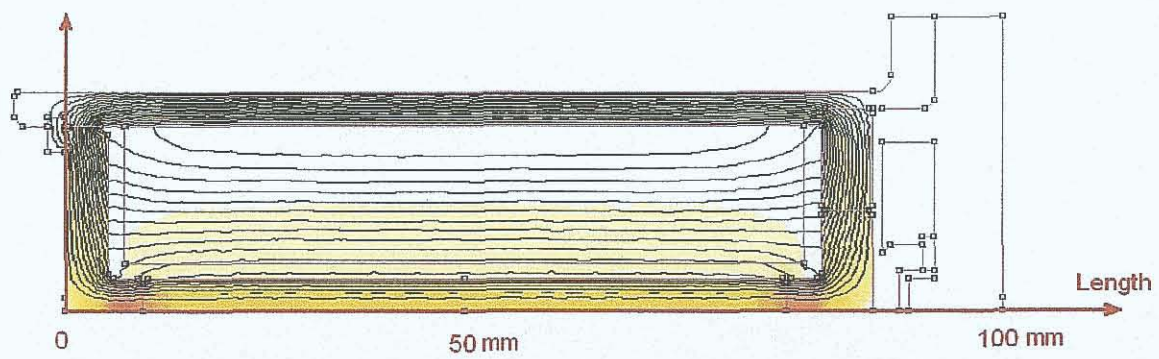


Fig. 87: Reference figure of the actuator plots of B (T) and H (A/m)

Fig. 88 shows the density plot of real part of B (T) related to the center line of the Terfenol-D shaft in the “MS”-actuator assembly.

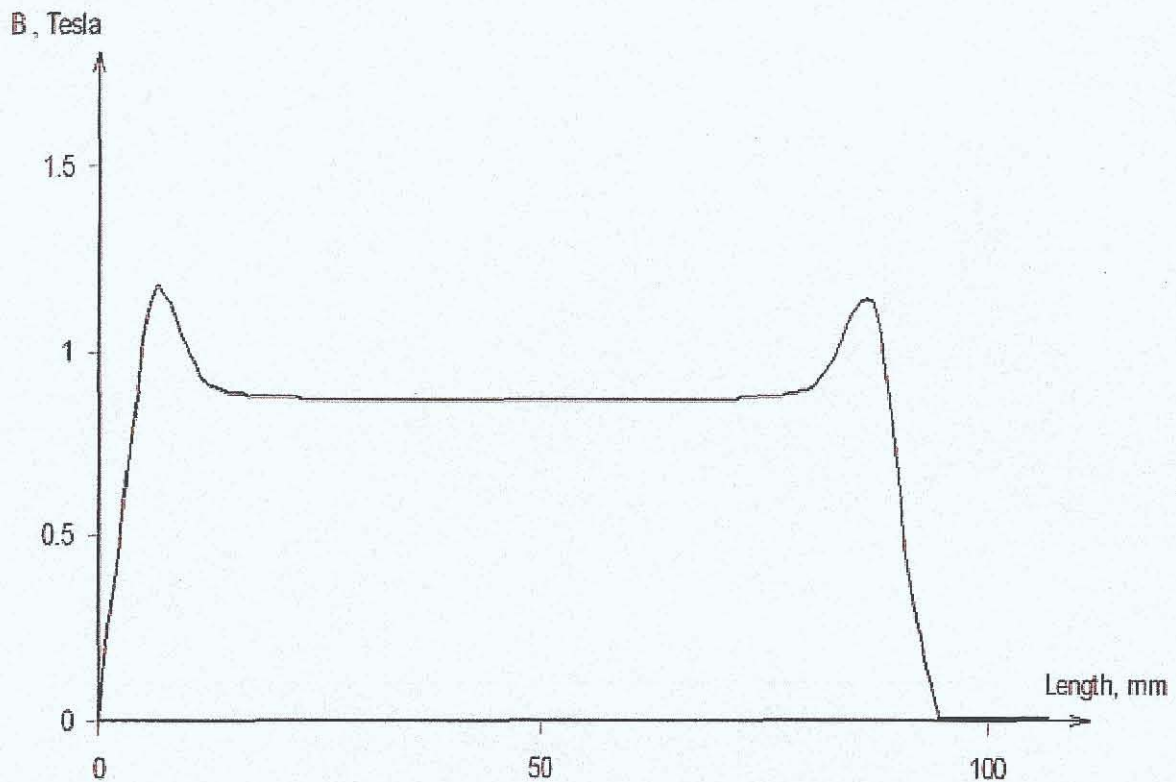


Fig. 88: FEMM Flux density B (T) the actuator

The geometry of the assembly has been verified up to the homogeneous density of the magnetic field along and across the Terfenol-D shaft has been achieved and the flux density level was acceptable. The initial proposed geometry, based on analytical calculation, has been optimized with the simulation tool. Several loops of simulations have been obtained before reaching the prototype stage. At the prestress of 6.9 MPa and the field intensity about

100 kA/m the expected strain of the Terfenol-D shaft should be higher than 1200 ppm. This result will be within the specified range and was rated as acceptable.

Fig. 89 shows the magnitude of field intensity H (A/m) related to the center line of the Terfenol-D shaft.

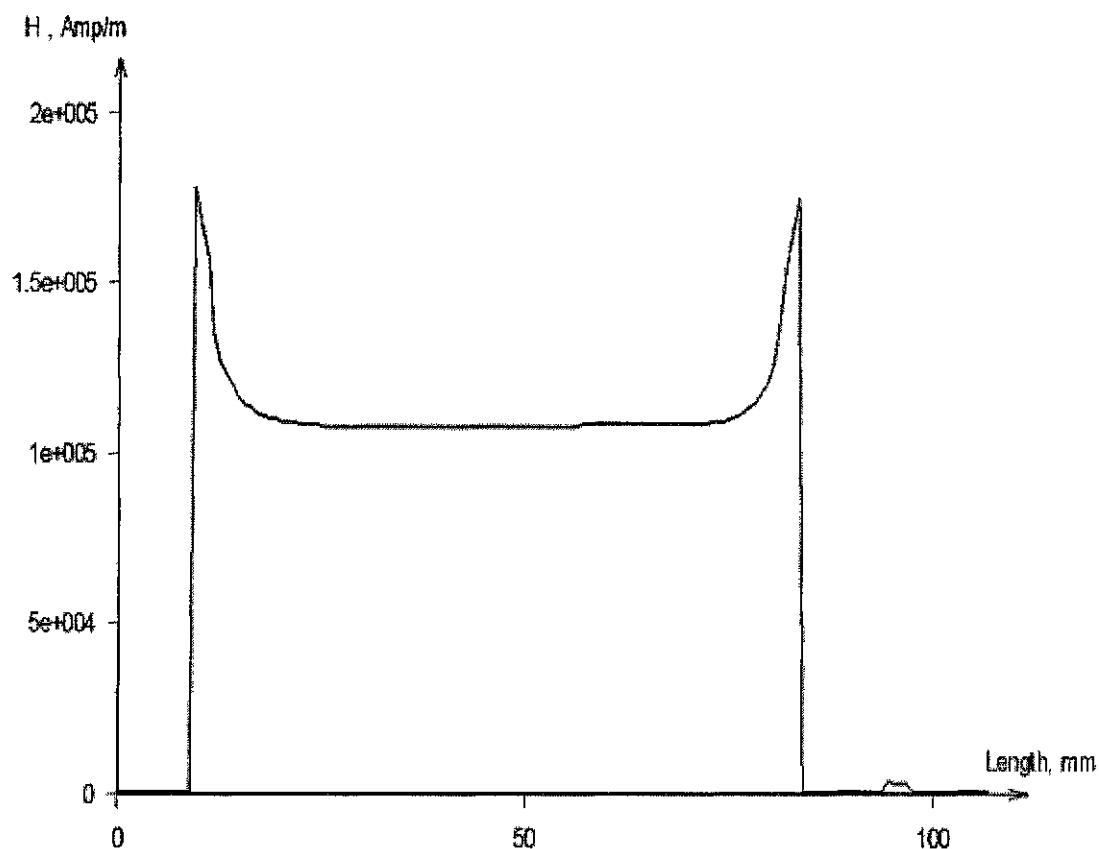


Fig. 89: FEMM Field intensity H (A/m) in the actuator

A homogeneous distribution of the magnetic field intensity (H) along and across the Terfenol-D shaft has been achieved and the intensity level has been rated as acceptable. The results of the magnetic field simulation have been used to set up the final design freeze for experimental rig. For comparison and verification reasons the “MS”-actuator assembly has been evaluated using the Vector Fields Software for magnetic design (Opera). All the geometries and material data as well the boundary conditions have been kept equivalent to the FEMM model. Figure 90 presents the Opera software window with user interface.

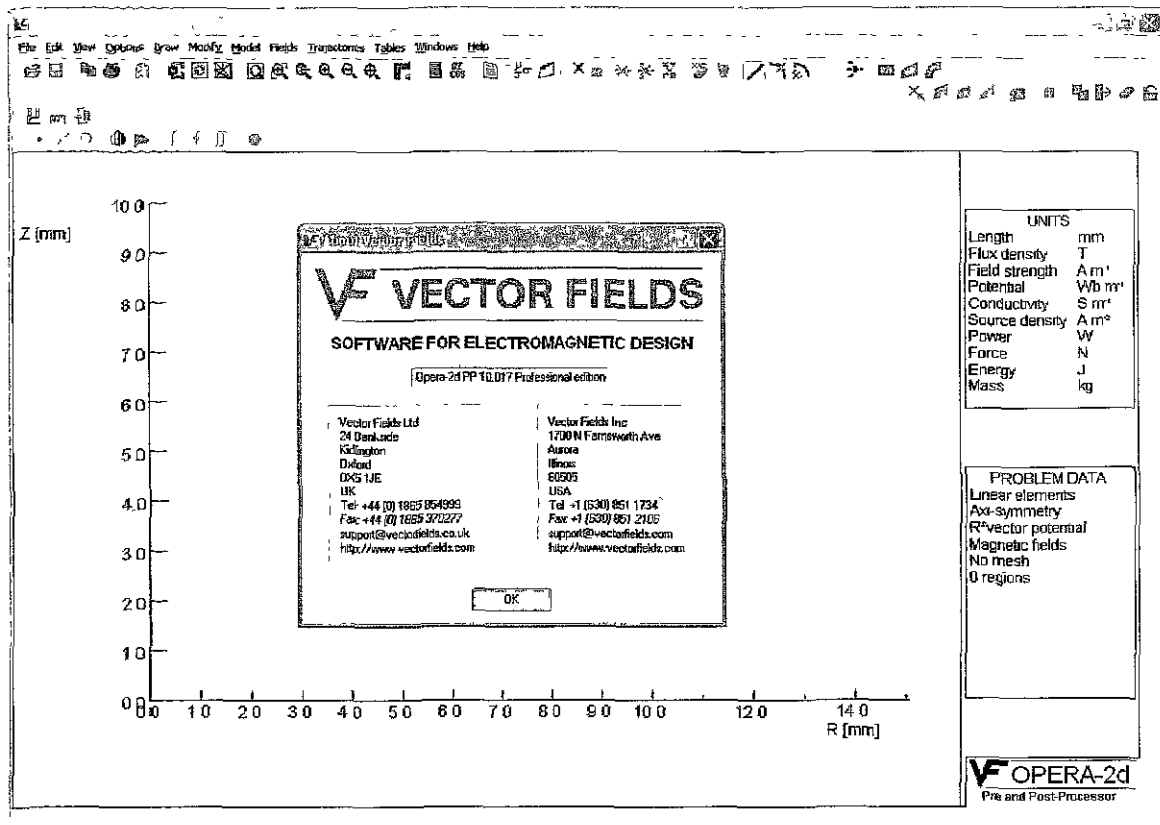


Fig. 90: Opera software window with user interface [85]

For geometry input the CAD export / import tools has been used. Fig. 91 shows the meshed structure of the magnetostrictive actuator using Opera software. The simulated model has been set up to an "axisymmetric problem". The modified vector potential solution, "modified $r \times A$ ", has been selected to improve accuracy near the symmetry axis [85]. The results of the parametric calculation for the electric circuit have been used to set up the complete model of the "MS"-actuator assembly. The measured B-H characteristic for each material has been used as input for the magnetic field simulation software.

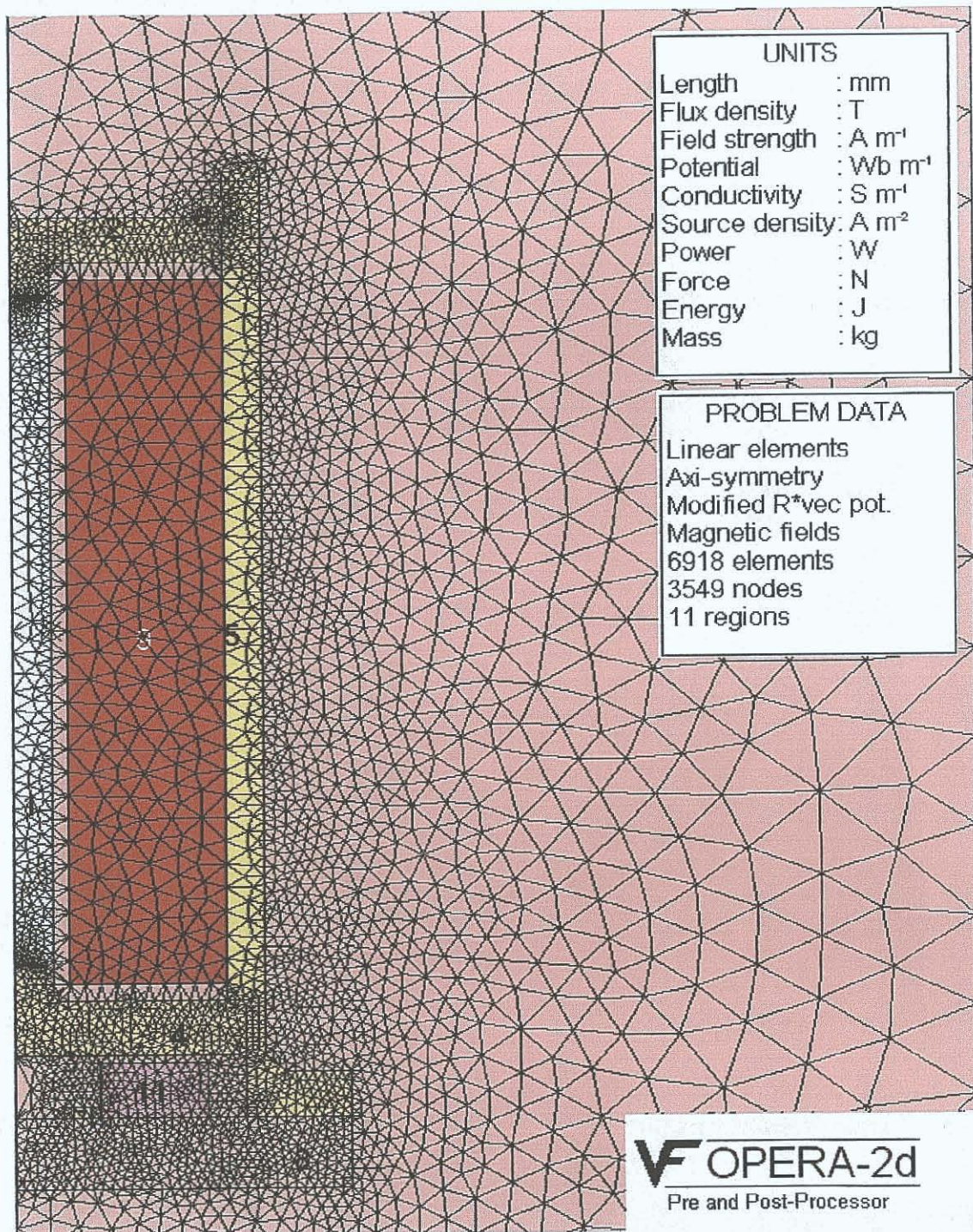


Fig. 91: Meshed actuator with Opera

Fig. 92 shows the potential lines and density plot for the real part of B (T) related to the centre line of the Terfenol-D shaft.

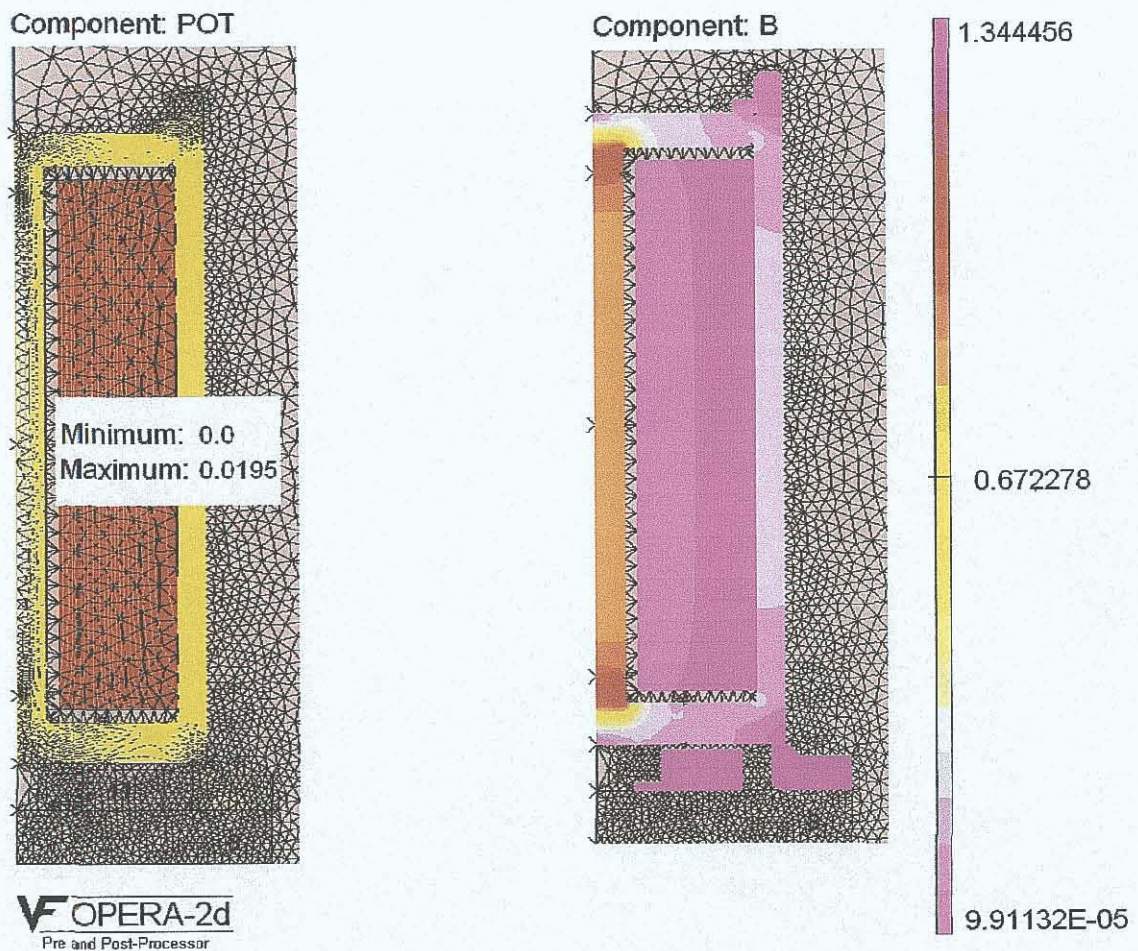


Fig. 92: Opera Potential lines and flux density B (T) in the actuator

Fig. 93 shows the density plot of B (T) related to the centre line of the Terfenol-D shaft (see Fig. 87). The results shown in Fig. 93 have been obtained using Opera software version 10.017 and results using FEMM software version 4.0.1.

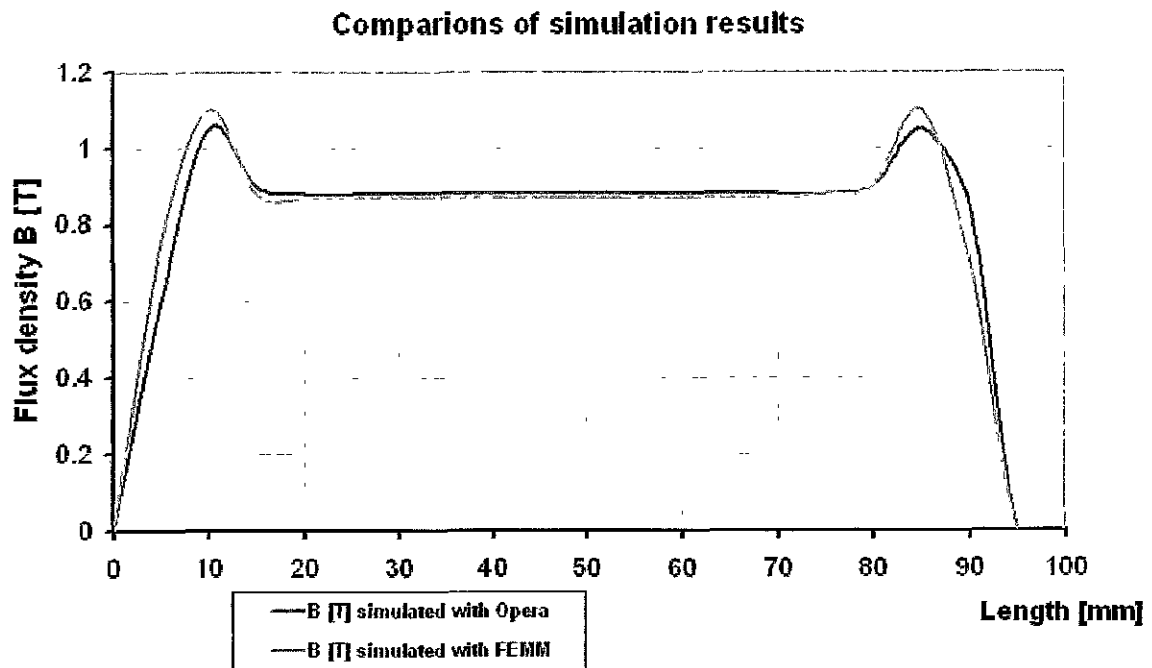


Fig. 93: Comparison of simulation results regarding flux density B (T)

Fig. 94 shows the magnitude of field intensity H (A/m) related to the centre line of the Terfenol-D shaft. Fig. 94 shows results which have been obtained with two different simulation systems, Opera and FEMM.

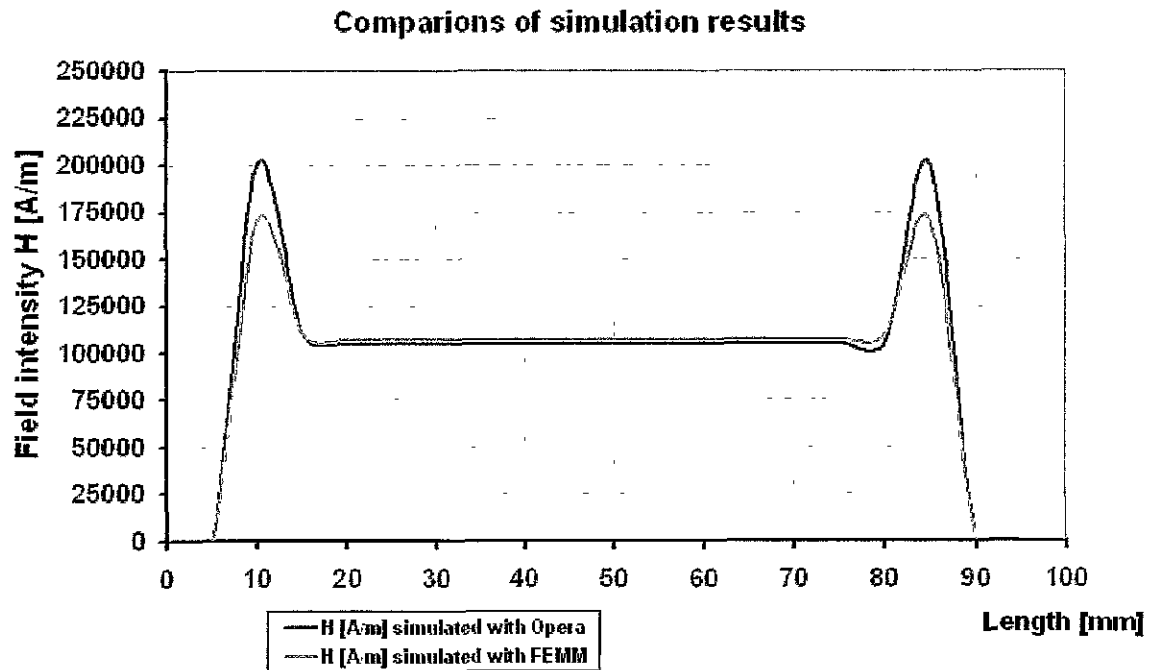


Fig. 94: Comparison of simulation results regarding field intensity H (A/m)

Comparing the simulation results, obtained by FEMM and Opera, it is obvious that both results are in perfect coincidence. It can be noted that the free available software package FEMM offers a very simple user interface. The professional software packaging from Vector Fields is wider purpose software for electromagnetic design. Various types of solutions for the proposed actuation system are available: static analysis module, steady-state module and the transient analysis module.

5.5.2 Magnetic field simulation results from "MR"-valve

Fig. 95 shows the meshed structure of the preferred magnetorheological valve assembly. The simulated model has been set up to an "axisymmetric problem", and the "asymptotic boundary conditions" have been applied. The results of the parametric calculation for the electric circuit have been used to set up the simulated model of the control valve assembly. The measured B-H characteristic for each material has been used as input for the magnetic field simulation software.

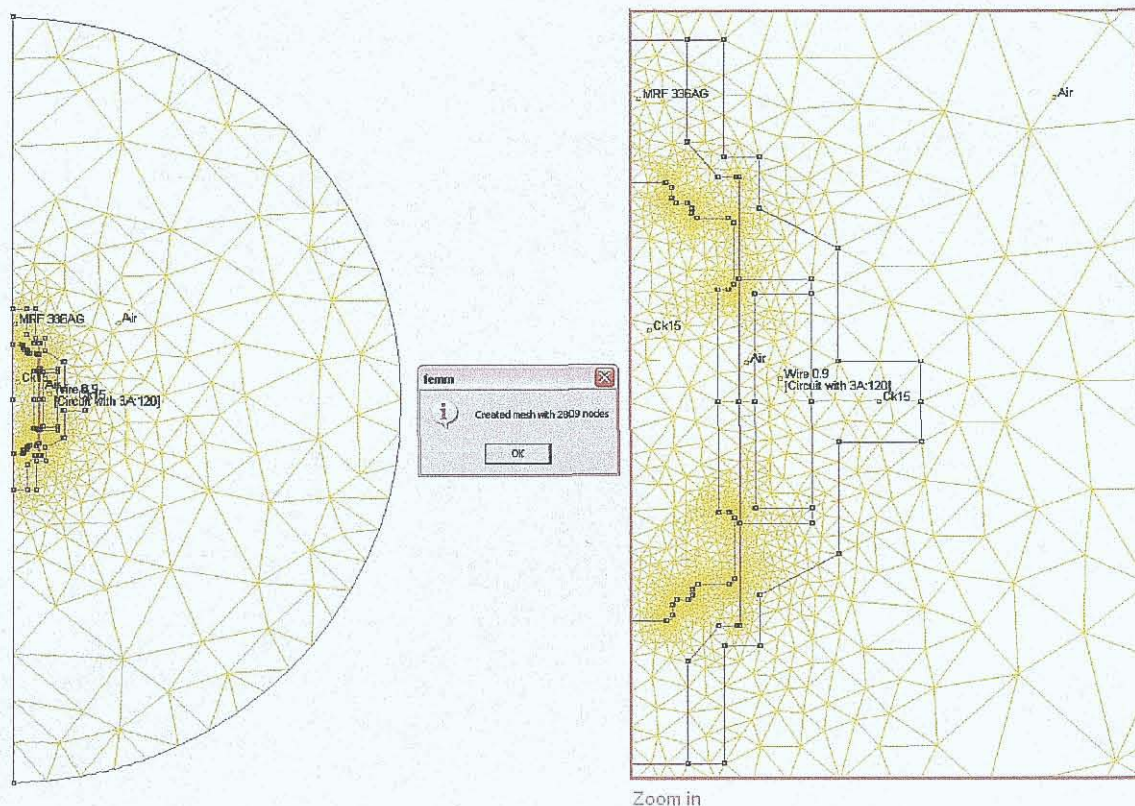


Fig. 95: Meshed control valve with FEMM

Fig. 96 presents the density plot for the real part of B (T) related to the center line of the MRF valve assembly, which has been obtained using FEMM software version 4.

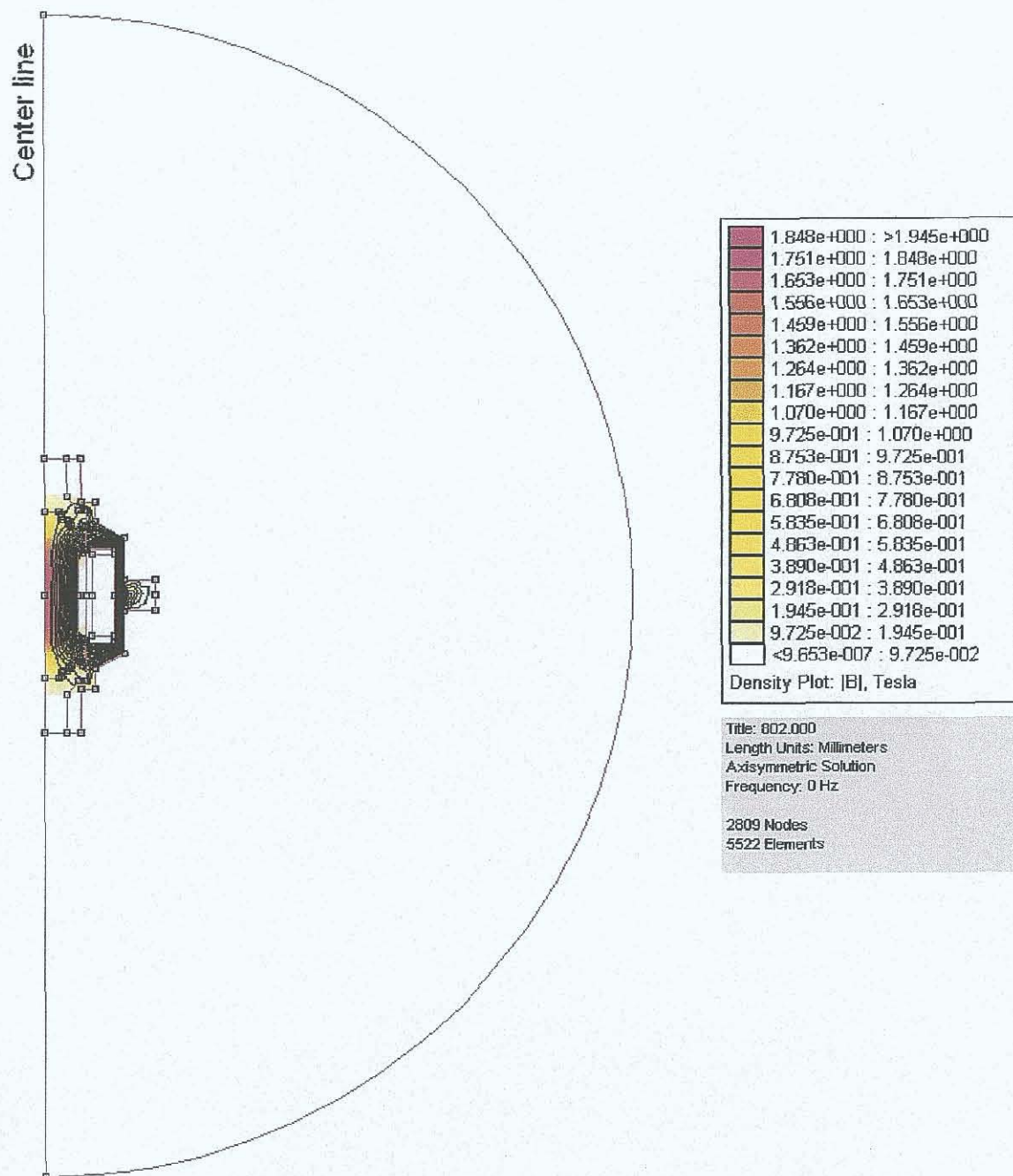


Fig. 96: FEMM Flux density B (T) in the valve

Based on parametric calculations the nominal current for the control coil has been set up to 3 Amperes. Various types of output information could be used to evaluate the magnetic field. For the evaluation purpose of the magnetic circuit voltage drop, flux linkage, inductance, resistance and electrical power have been calculated. All calculations have been obtained with frequencies 0 Hz, 10 Hz, 50 Hz, 250 Hz, 500 Hz and 1000 Hz. Fig. 97 shows various types of additional result information from FEMM.

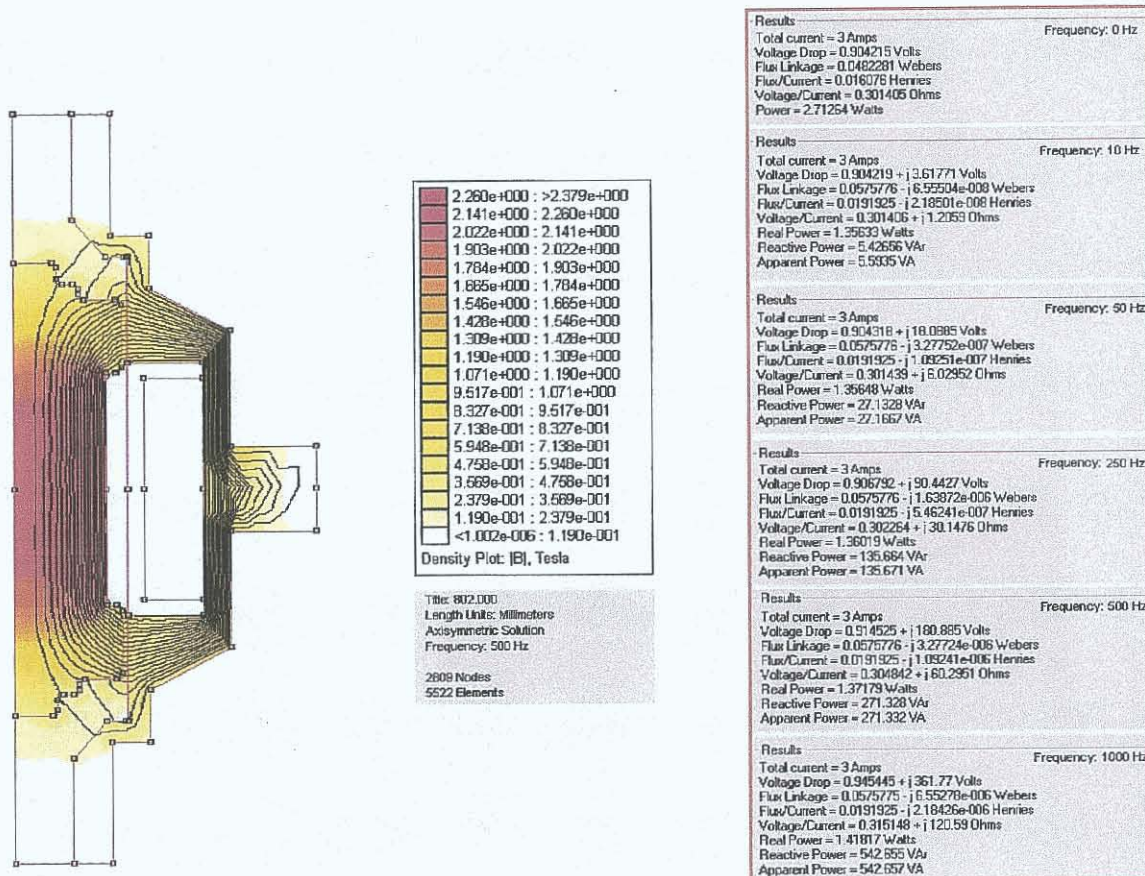


Fig. 97: FEMM Magnetic Circuit Results for valve

The preferred frequency range for the electric circuit using a sine wave should be synchronized with the operating frequency of the actuation. Further details regarding the operational frequencies have been evaluated parametrically in chapter 4.

Fig. 98 shows the assembly reference picture for 2D-plots for magnitude of field density B (T) and magnitude of field intensity H (A/m) of the mid of MRF gap along defined path line marked as length.

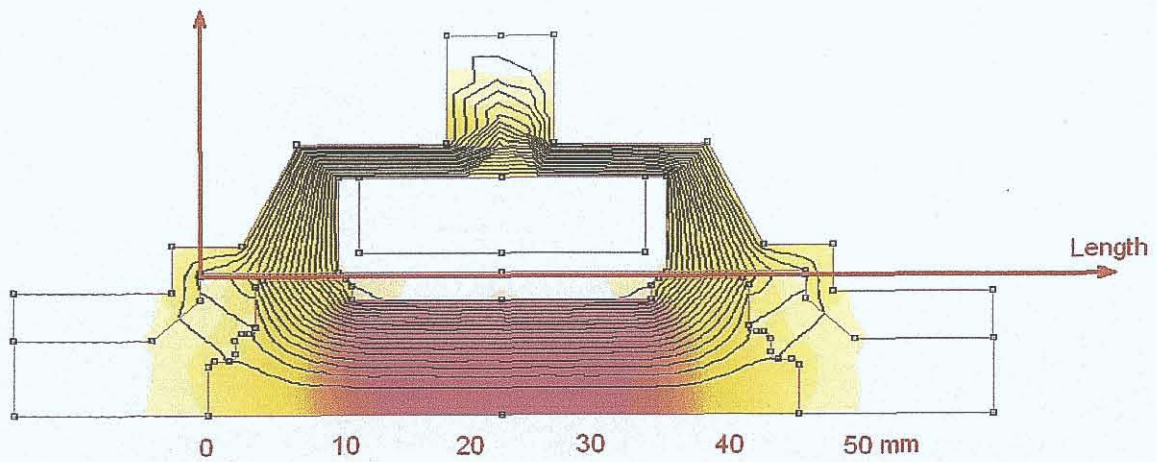


Fig. 98: Reference figure of the valve assembly for plots of B (T) and H (A/m)

Fig. 99 shows the density plot of B (T) at nominal current in the mid of MRF gap in the valve assembly.

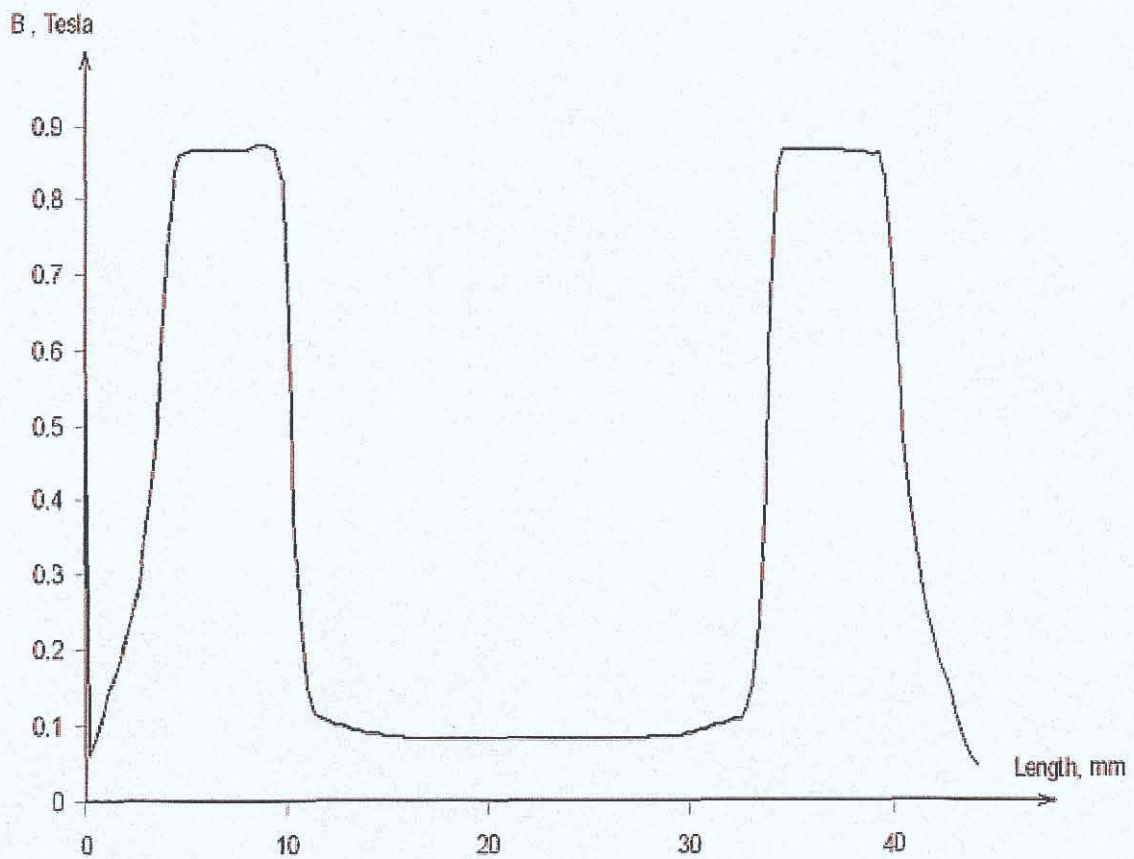


Fig. 99: FEMM Flux density B (T) in the valve

The geometry of the assembly has been verified up to the homogeneous density of the magnetic field along and across the MRF gap. The results show that the density level was acceptable. The initial proposed geometry, based on analytical calculation, has been optimized with the simulation tool. Several loops of simulations have been obtained before reaching the final design. At the magnetic field intensity of about 200 kA/m the expected yield stress of MRF 132-AD should be higher than 42 kPa. It can be noted that the result were in the specified range and was rated as acceptable. Fig. 100 shows the magnitude of field intensity H (A/m) related to the mid of the MRF gap.

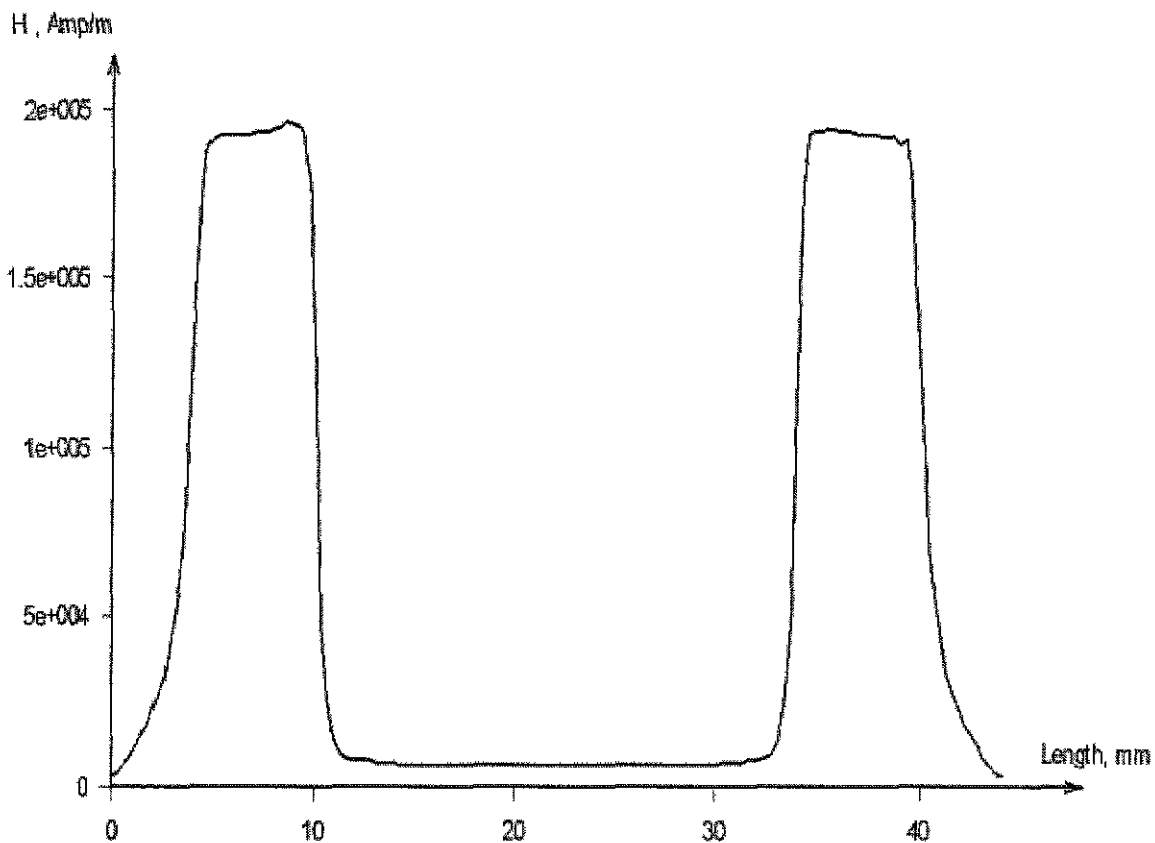


Fig. 100: FEMM Field intensity H (A/m) in the valve, mid of MRF gap

A homogeneous distribution of the magnetic field intensity along and across the MRF gap has been achieved and the intensity level has been rated as acceptable. The results of the magnetic field simulation have been used to present the final design for experimental evaluation on the rig.

5.5.3 Magnetic field simulation results from "MR"-orifice

Fig. 101 depicts the meshed structure of the alternative magnetorheological orifice assembly. The simulated model has been set up to an "axisymmetric problem", and the "asymptotic boundary conditions" have been applied. The results of the parametric calculation for the electric circuit have been used to set up the simulated model of the control orifice. The measured B-H characteristic for each material has been used as input for the magnetic field simulation software.

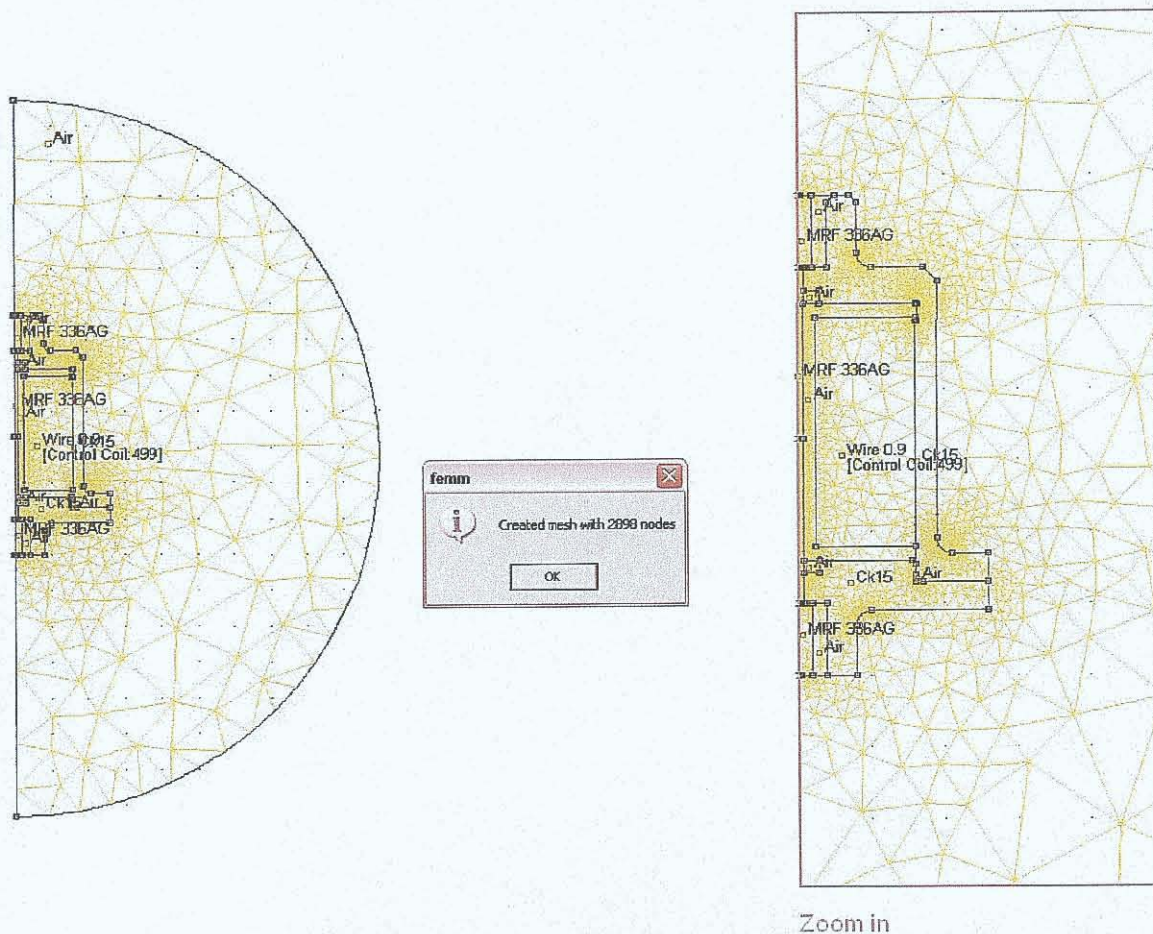
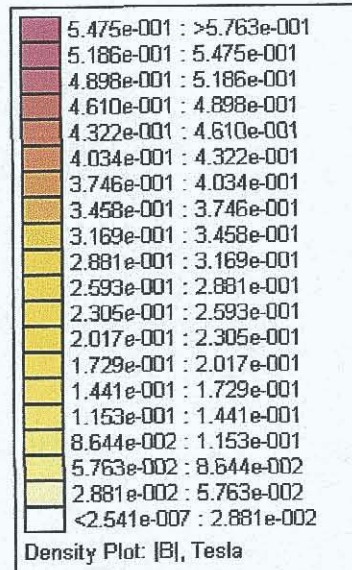
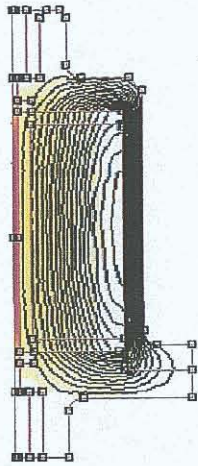


Fig. 101: Meshed control orifice with FEMM

Fig. 102 shows the density plot for the real part of B (T) related to the center line of the MRF orifice assembly. The results shown in Fig. 102 has been obtained using FEMM software package, version 4.

Center line

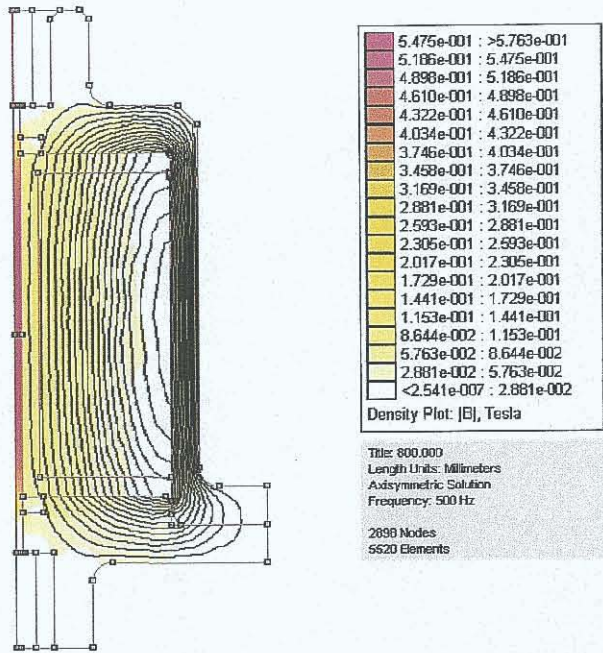


Title: 800.000
 Length Units: Millimeters
 Axisymmetric Solution
 Frequency: 500 Hz

2898 Nodes
 5520 Elements

Fig. 102: FEMM Flux density B (T) in the orifice

Based on parametric calculations the nominal current for the control coil from the orifice has been set up to 6 Amperes. Various types of output information could be used to evaluate the magnetic field. For the evaluation purpose of the magnetic circuit voltage drop, flux linkage, inductance, resistance and electrical power have been calculated. All calculations have been obtained with frequencies 0 Hz, 10 Hz, 50 Hz, 250 Hz, 500 Hz and 1000 Hz. Fig. 103 shows various types of additional result information from FEMM.



Results Total current = 6 Amps Voltage Drop = 5.04681 Volts Flux Linkage = 0.0101156 Webers Flux/Current = 0.00168594 Henries Voltage/Current = 0.841135 Ohms Power = 30.2609 Watts	Frequency: 0 Hz
Results Total current = 6 Amps Voltage Drop = 5.04689 + j0.638892 Volts Flux Linkage = 0.0101683 - j1.18723e-006 Webers Flux/Current = 0.00169471 - j1.97892e-007 Henries Voltage/Current = 0.841148 + j0.106482 Ohms Real Power = 15.1407 Watts Reactive Power = 1.91868 VAR Apparent Power = 15.2515 VA	Frequency: 10 Hz
Results Total current = 6 Amps Voltage Drop = 5.04868 + j3.19446 Volts Flux Linkage = 0.0101683 - j5.93546e-006 Webers Flux/Current = 0.00169471 - j9.89409e-007 Henries Voltage/Current = 0.841446 + j0.63241 Ohms Real Power = 15.145 Watts Reactive Power = 9.98337 VAR Apparent Power = 17.9233 VA	Frequency: 50 Hz
Results Total current = 6 Amps Voltage Drop = 5.09345 + j15.9721 Volts Flux Linkage = 0.0101681 - j2.96816e-005 Webers Flux/Current = 0.00169468 - j4.94639e-006 Henries Voltage/Current = 0.848909 + j2.66201 Ohms Real Power = 15.2804 Watts Reactive Power = 47.9162 VAR Apparent Power = 50.2357 VA	Frequency: 250 Hz
Results Total current = 6 Amps Voltage Drop = 5.23337 + j31.9428 Volts Flux Linkage = 0.0101677 - j5.93588e-005 Webers Flux/Current = 0.00169462 - j9.89314e-006 Henries Voltage/Current = 0.872228 + j5.3238 Ohms Real Power = 15.7001 Watts Reactive Power = 95.8263 VAR Apparent Power = 97.1059 VA	Frequency: 500 Hz
Results Total current = 6 Amps Voltage Drop = 5.79281 + j63.8746 Volts Flux Linkage = 0.0101666 - j0.000118663 Webers Flux/Current = 0.00169433 - j1.97905e-005 Henries Voltage/Current = 0.965469 + j10.6458 Ohms Real Power = 17.3784 Watts Reactive Power = 151.624 VAR Apparent Power = 152.41 VA	Frequency: 1000 Hz

Fig. 103: FEMM Magnetic Circuit Results for orifice

Fig. 104 presents the assembly reference picture for 2D-plots for magnitude of field density B (T) and magnitude of field intensity H (A/m) of the mid of MRF orifice along defined path line marked as length.

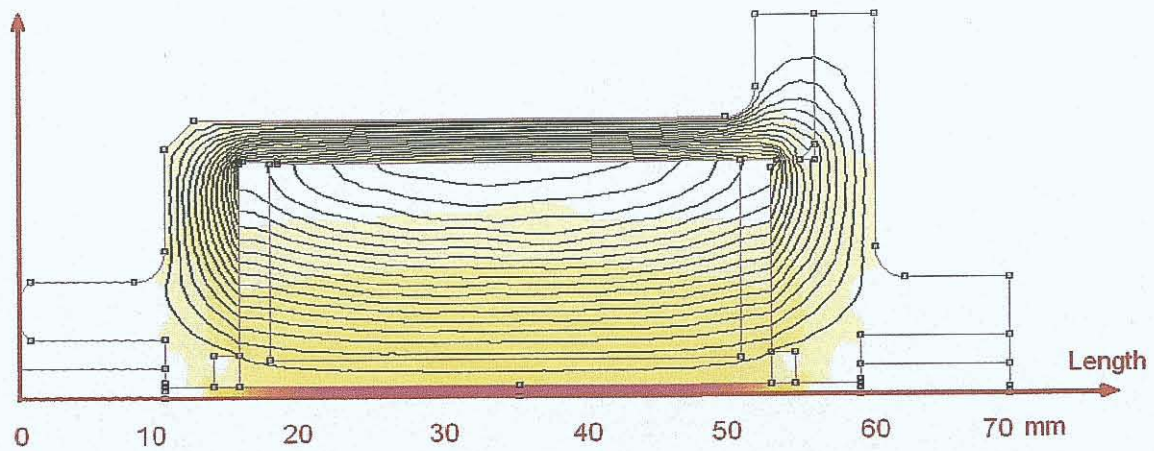


Fig. 104: Reference figure of the orifice for plots of B (T) and H (A/m)

Fig. 105 depicts the density plot of B (T) at nominal current in the mid of MRF orifice.

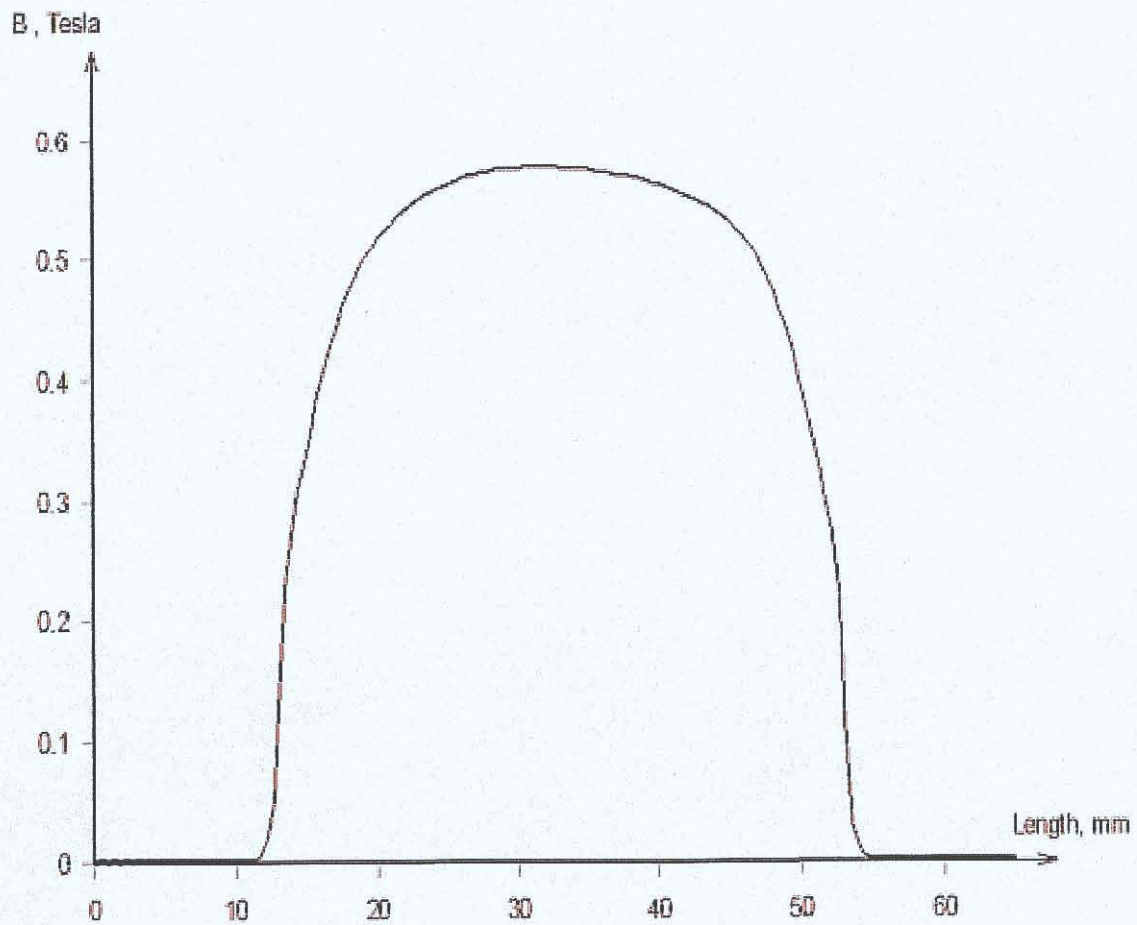


Fig. 105: FEMM Flux density B (T) in the orifice

The geometry of the assembly has been verified up to the acceptable density of the magnetic field along and across the MRF orifice. It is obvious that, the density level was within the expectation. The initial proposed geometry, based on analytical calculation, has been optimized with the simulation tool. Several loops of simulations have been obtained before the design freeze for experimental evaluation on the rig. At the magnetic field intensity about 95 kA/m the expected yield stress of MRF 132-AD should be about 27 kPa. Fig. 106 shows the magnitude of field intensity H (A/m) related to the mid of the MRF orifice

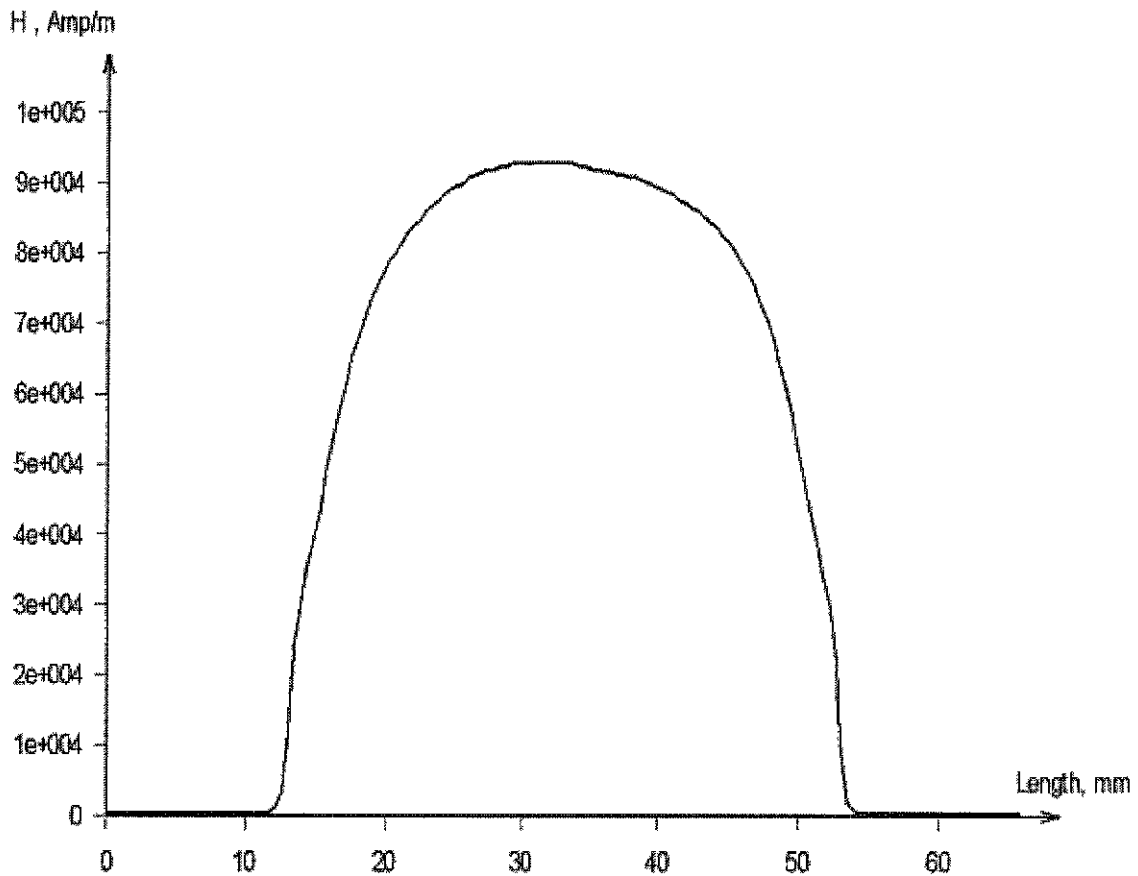


Fig. 106: FEMM Field intensity H (A/m) in the orifice

The orifice assembly is simpler than the preferred control valve assembly. The achievable performance would not be as good as the performance with preferred control valve assembly. An acceptable distribution of the magnetic field intensity along and across the MRF orifice has been achieved and the intensity level has been rated as acceptable for simpler device. The results of the magnetic field simulation have been used to set up the final design for experimental evaluation.

Chapter Six

Experimental evaluation

6.1 Experimental rig

To prove feasibility of the actuation principle experimental rig parts have been produced. The magnetostrictive actuator assembly, magneto-rheological control assemblies and load assembly has been prepared for experimental evaluation. The test results have been used to confirm the analytical calculations and the magnetic field simulation and to highlight the potential of performance optimization. The experimental rig parts of the magnetostrictive actuator are shown in Fig. 107.

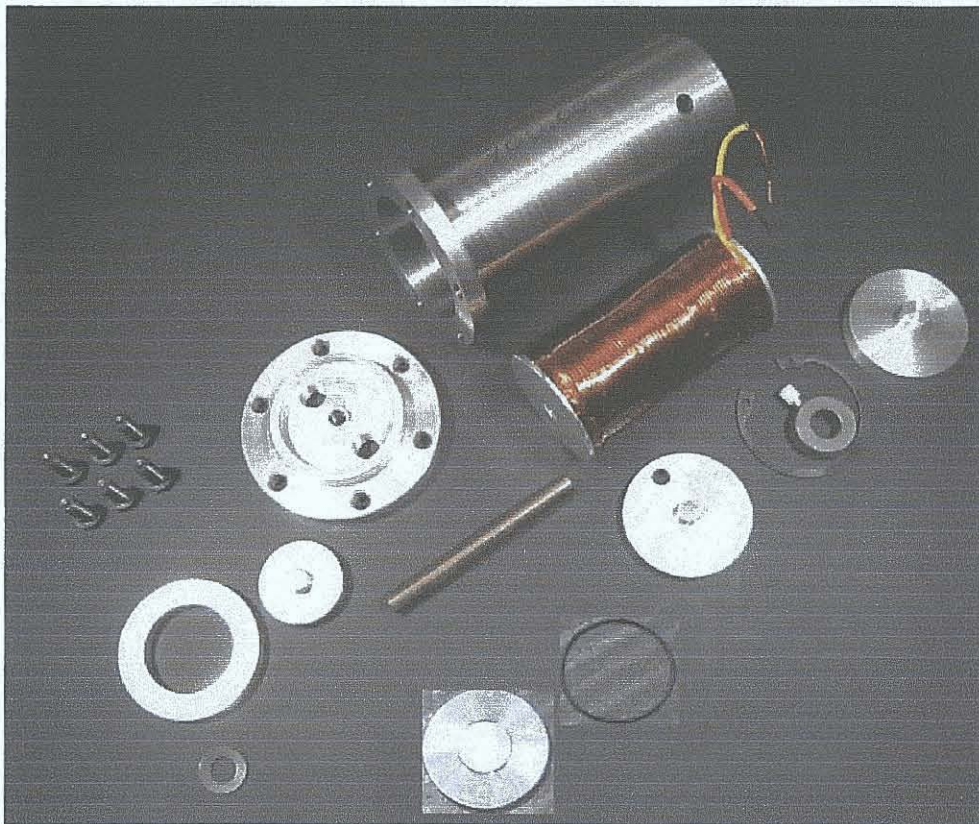


Fig.107: Picture from “MS”-actuator assembly

Details of the design are summarized in appendix A. Some experimental rig parts have been manufactured in DCU facilities, some has been ordered from external suppliers. The measured weight of the “MS”-actuator assembly is 1560 g and the volume is about 250 mm³.

The assembly of the control valve is presented in Fig. 108.



Fig. 108: Picture from “MR”-control valve assembly

The measured weight of the “MR”-valve assembly is 475 g and the volume is about 70 mm³.
The assembly of the “MR”-control orifice is shown in Fig. 109.

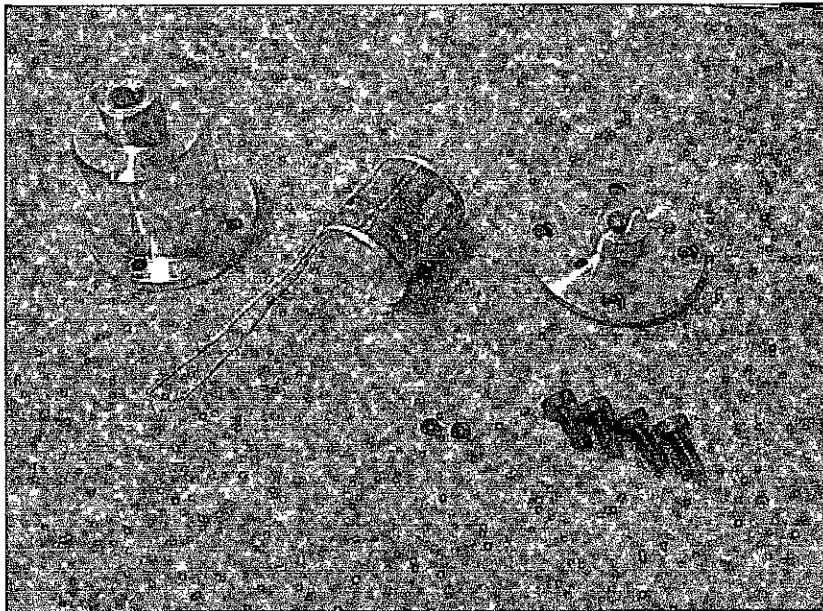


Fig. 109: Picture from control orifice assembly

The measured weight of the “MR”-orifice assembly is 530 g and the volume is about 75 mm³.

The assembly of the reference load, used for experimental evaluation, is presented in Fig. 110.

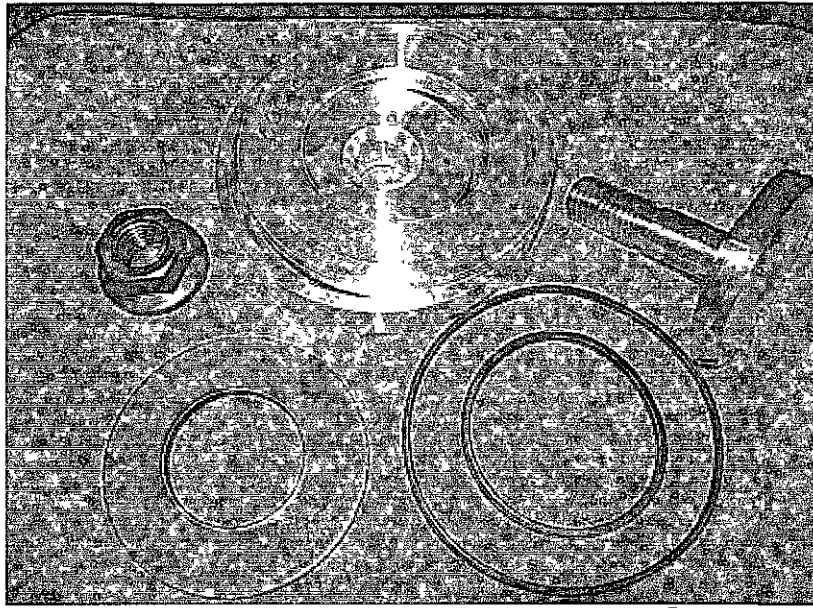


Fig. 110: Picture from load assembly

The housing has been prepared with M10x1 thread interface for a pressure transducer. The assembly of the MRF reservoir is depicted in Fig. 111.

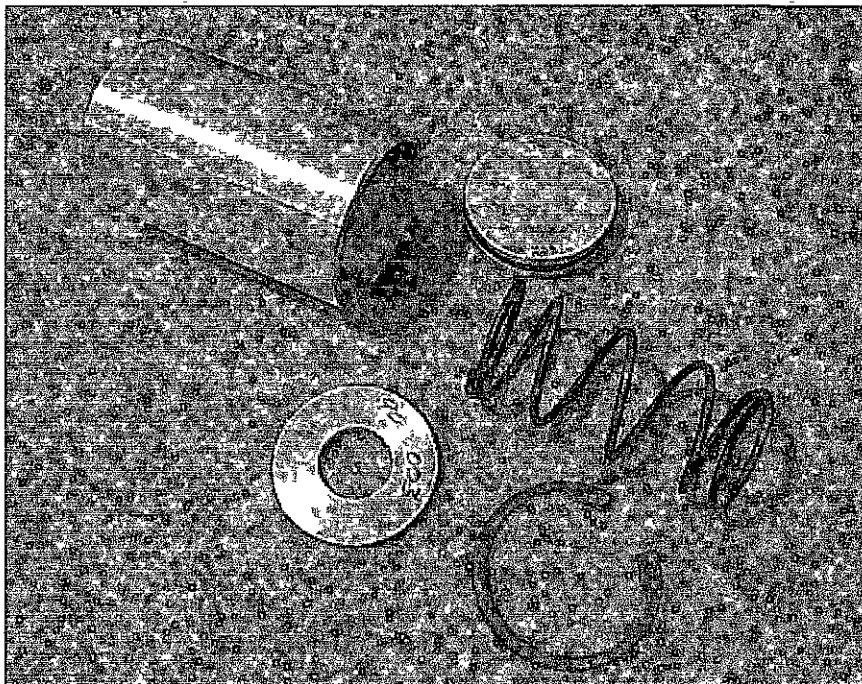


Fig. 111: Picture from assembly

An automotive “hydraulic-jack” has been used to bleed the system and for reference load measurements. All drawing from components and assemblies are summarized in the appendices A to F.

6.2 Rig test equipment and tools for experimental evaluation

The rig test equipment, power supply and data acquisition, has been prepared and the sensor calibration data have been checked by GKN Driveline test department. Table 11 shows the list of channels for data acquisition and used sensors with key performance data.

Tab. 11: Rig test data and sensors

Test rig equipment	Specification
Max. power from amplifier	1 x 40 A & 30 V, 2 x 5 A & 12 V
Input power frequencies	Option 1: variable from function generator Option 2: NI card with LabView 8.2 software interface
Input power type	sinusoidal, triangle & rectangular from PWM
Acquisition frequencies	>2000 Hz
Channel specification	Channel 1: Current from rig equipment Channel 2: Voltage from rig equipment Channel 3: Length from TR102/W1T3 = Sensor 1 Channel 4: Force from 9021A = Sensor 2 Channel 5: Pressure PE2000-5048 = Sensor 3 Channel 6: Force from 9051A = Sensor 4 Channel 7: Voltage from rig equipment Channel 8: Voltage from rig equipment
Measuring accuracies	Current: 7.3 A, 4.6 A, 4.6 A with +/- 0.2 A Voltage: 10.8 V, 1.3 V, 3.7 V with +/- 0.2 V Force 1: (9021A) 3 kN max, +/-100 N Force 2: (9051A) 20 kN max, +/-250 N Pressure: 4 MPa (40 bar) max, +/- 0.2 MPa (1 bar) Displacement: 0.1 mm max, +/- 0.005 mm
Sensors	Sensor 1: HBM TR102 / W1T3 Sensor 2: Kistler 9021A Sensor 3: Kavlico PE2000-5048 Sensor 4: Kistler 9051A

Power flow, current and voltage with various frequencies, have been checked with an oscilloscope. A function generator has been used for various actuator tests. A National Instruments I/O card with LabView8.2 has been used for the experimental tests with simultaneous power input for the magneto-rheological control device from the arrangement shown in Fig. 33. The recorded data have been investigated with MGraph 1.00, software tool for data acquisition. Fig. 112 depicts the rig test equipment with “MS”-actuator.

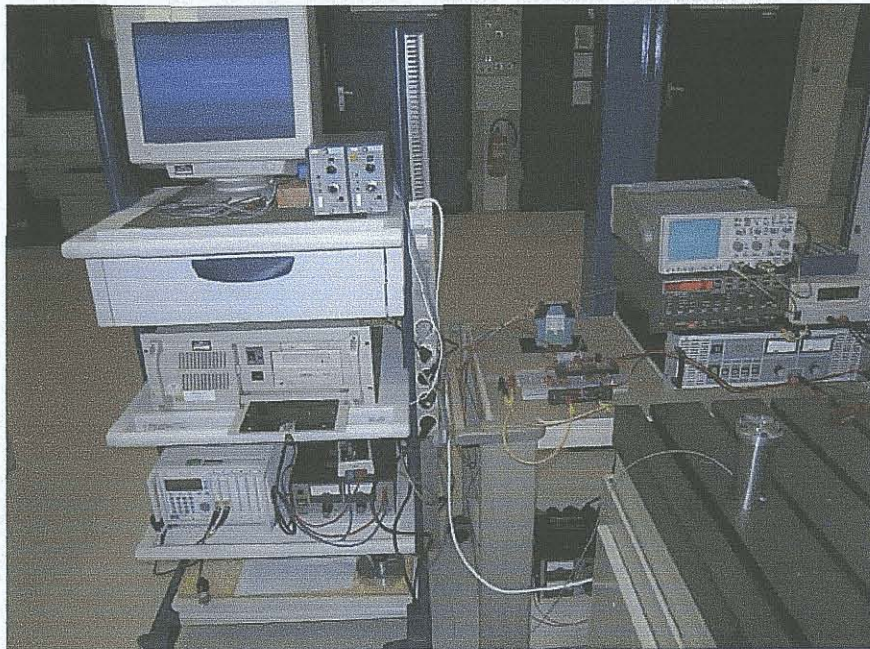


Fig. 112: Test rig equipment with “MS”-actuator prototype

Fig. 113 depicts the rig test equipment with function generator (left) and the rig test equipment with the NI I/O card device (right).



Fig. 113: Test rig equipment with function generator (left) and NI I/O card (right)

The set up with conventional function generator has been found to be sufficient for singular tests with magnetostrictive actuator or magneto-rheological control device. The NI I/O-card offers more flexibility for experimental evaluation with simultaneous power input for magnetostrictive actuator and the magneto-rheological control device. In some tests, up to three electrical coils had been powered with defined phase shift in current and voltage. The purpose of the experimental procedure was to confirm the analytical analysis, to prove the basic functionality of the actuator and to highlight the potential of possible improvements.

6.3 Experimental evaluation of magnetostrictive actuator

The actuator assembly has been completed and used to evaluate the performance (strain capability and blocked force level) of the magnetostrictive actuator. Fig. 114 depicts the test bench layout for force and for axial displacement measurements.

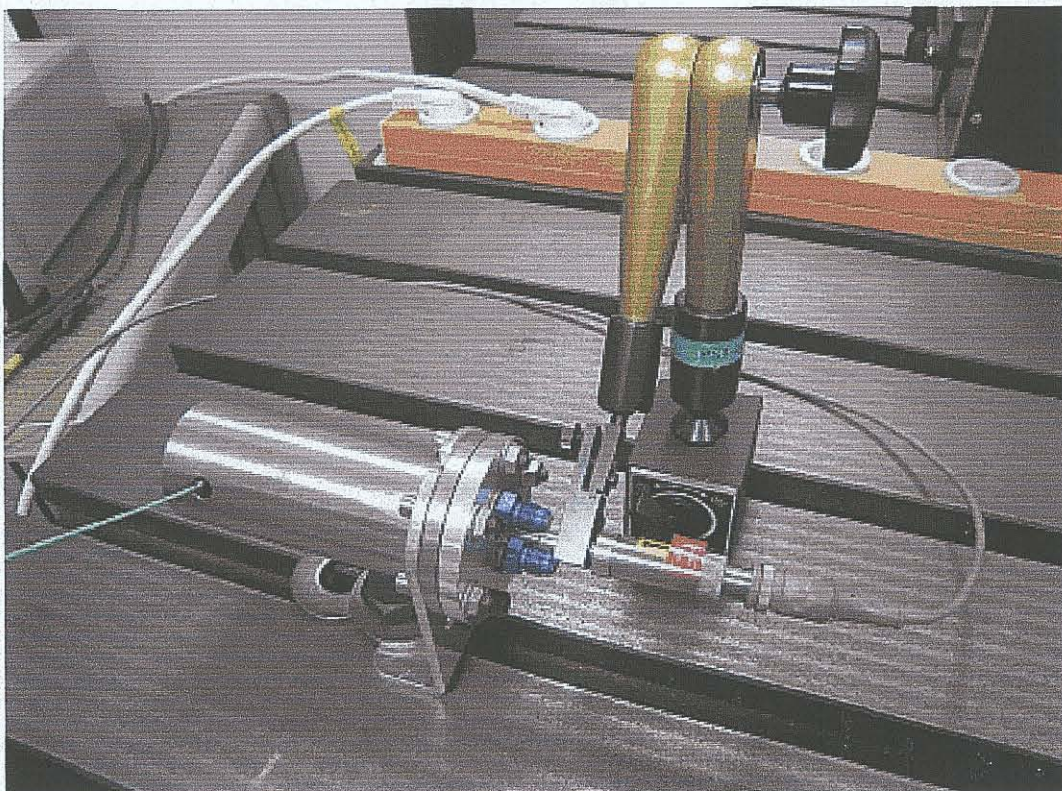


Fig. 114: Actuator assembly for performance measurements

Fig. 115 depicts the cross section of the tested assembly with force sensor and displacement sensor.

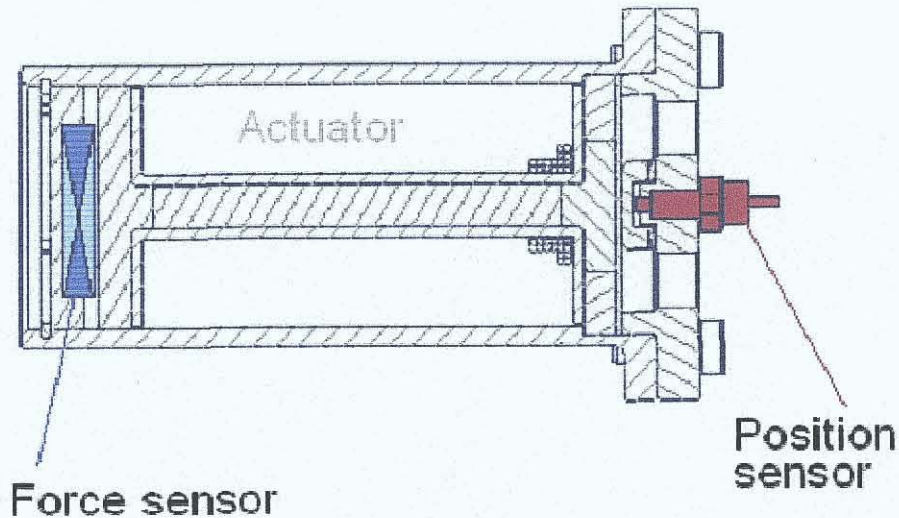


Fig. 115: Actuator assembly cross section for performance measurements

Using above shown assembly the specified performance of the actuator, based on magnetostrictive technology, has been proven on the rig test. Firstly, the effect of pre-stress has been evaluated. A piezo-sensor has been integrated into the assembly for accurate and dynamic force measurement. The details from used sensor are depicted in the appendix F of this thesis. Recorded data versus time were current, voltage, axial force and axial displacement. An evaluation of the displacement versus current has been used to define the optimal pre-stress of Terfenol-D shaft in the assembly. Pre-stress range of 6-34 MPa (300 N-1700 N pre-load) has been considered in this test session. Figures 116 to 131 show the results from experimental evaluation of the magnetostrictive actuator. In these figures on the left side: the time related data acquisition and on the right side: the displacement versus current.

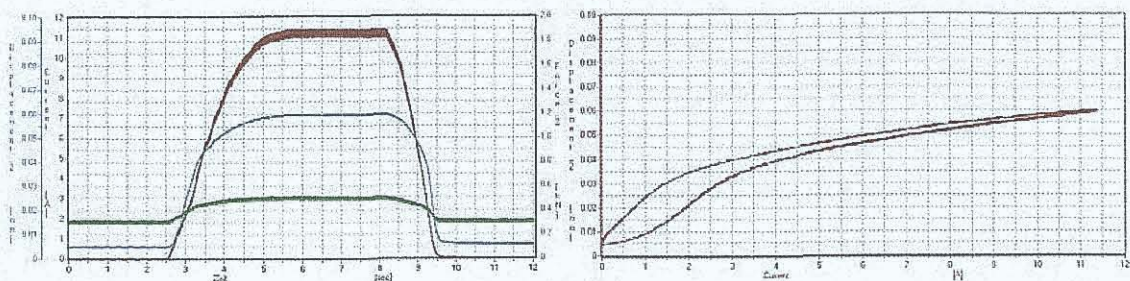


Fig. 116: "MS"-performance at pre-load with 300 N

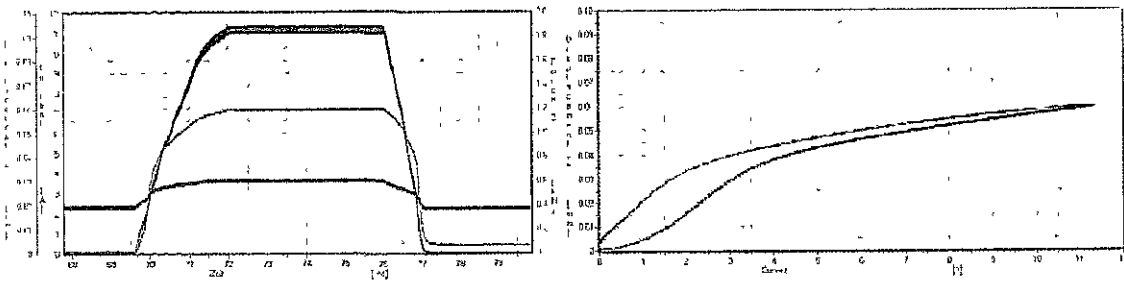


Fig. 117: "MS"-performance at pre-load with 400 N

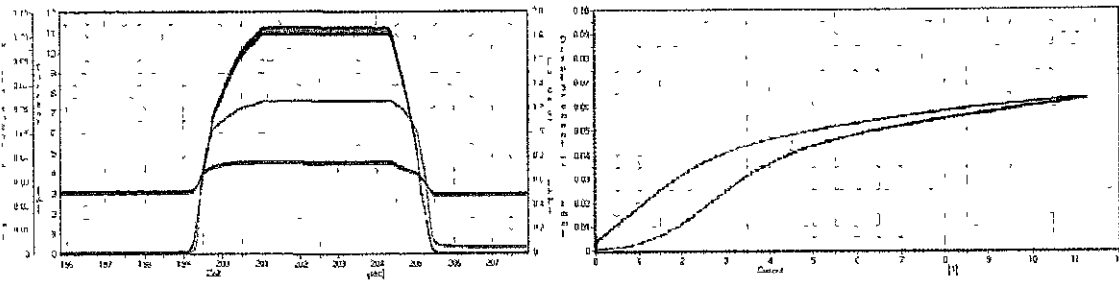


Fig. 118: "MS"-performance at pre-load with 500 N

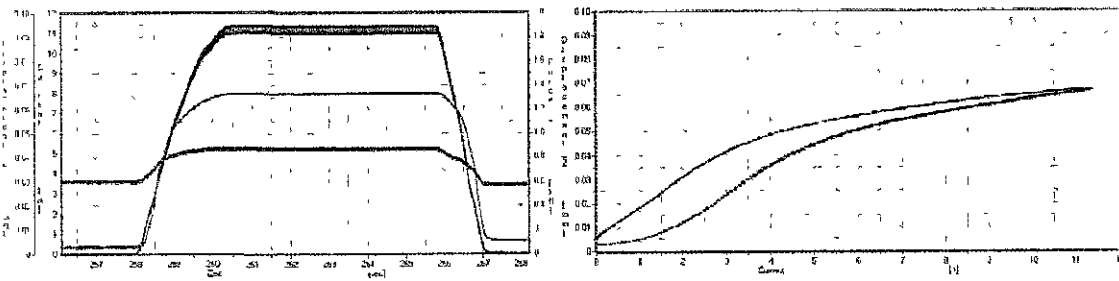


Fig. 119: "MS"-performance at pre-load with 600 N

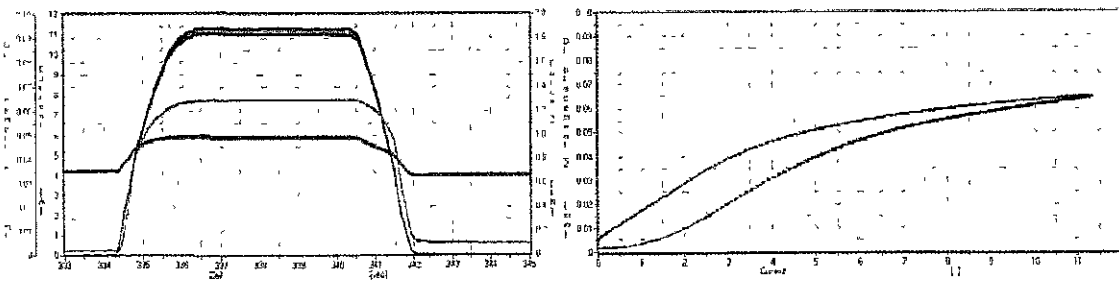


Fig. 120: "MS"-performance at pre-load with 650 N

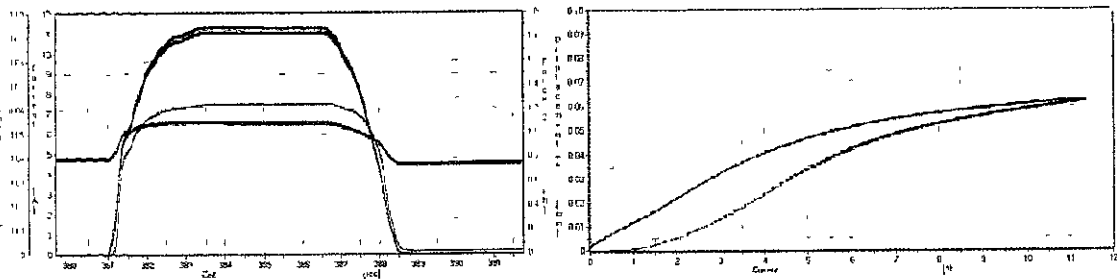


Fig. 121: "MS"-performance at pre-load with 750 N

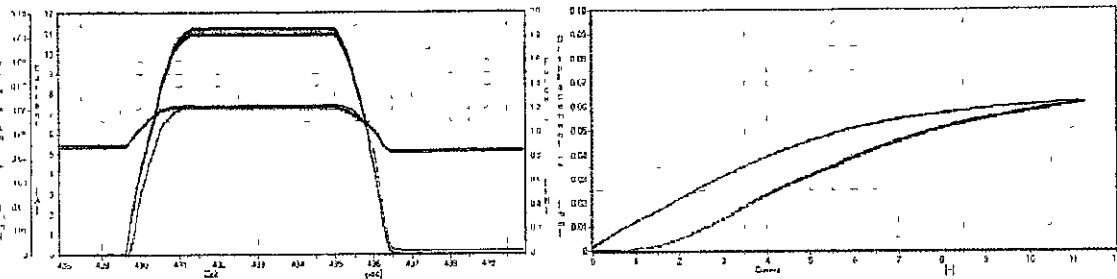


Fig. 122: "MS"-performance at pre-load with 850 N

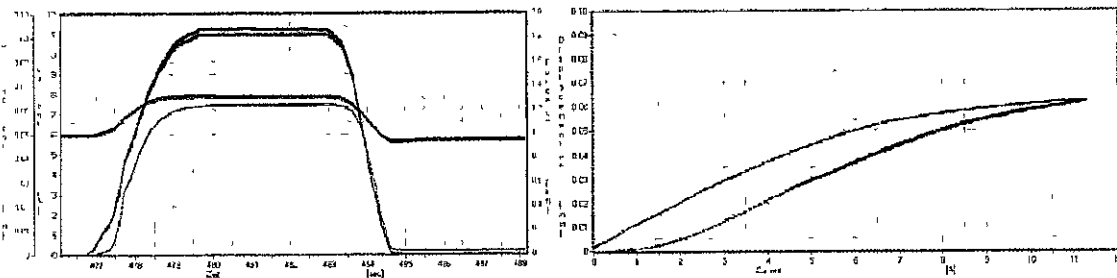


Fig. 123: "MS"-performance at pre-load with 950 N

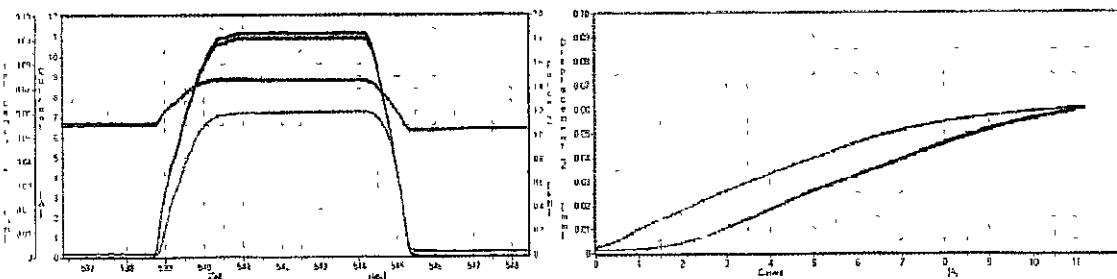


Fig. 124: "MS"-performance at pre-load with 1050 N

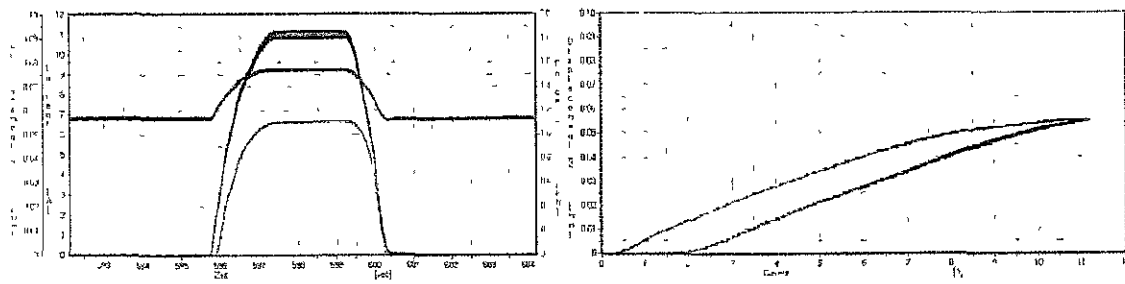


Fig. 125: "MS"-performance at pre-load with 1150 N

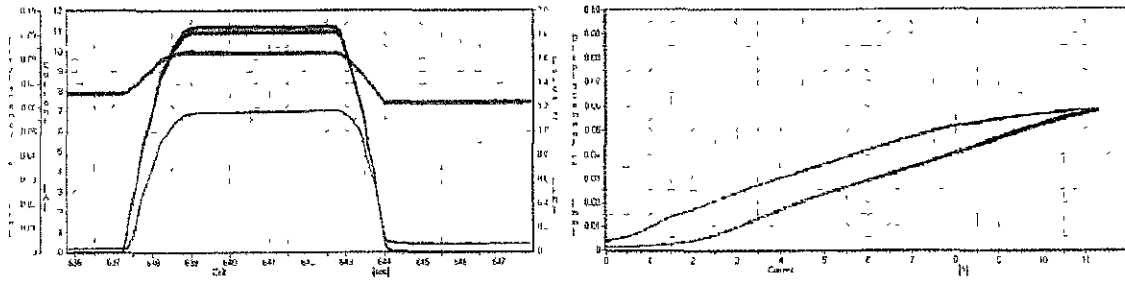


Fig. 126: "MS"-performance at pre-load with 1250 N

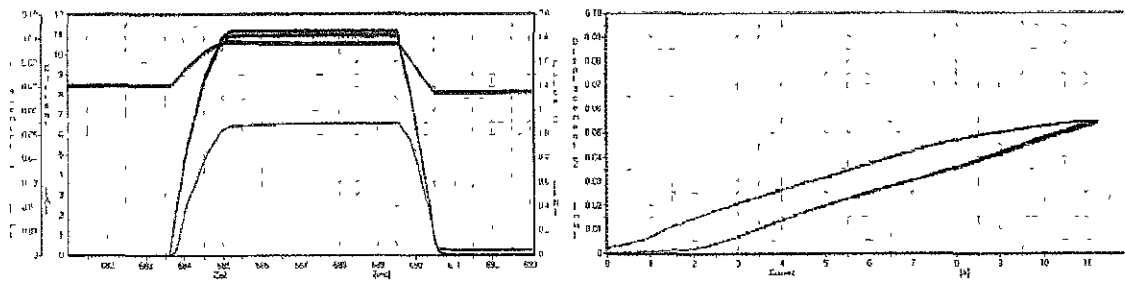


Fig. 127: "MS"-performance at pre-load with 1350 N

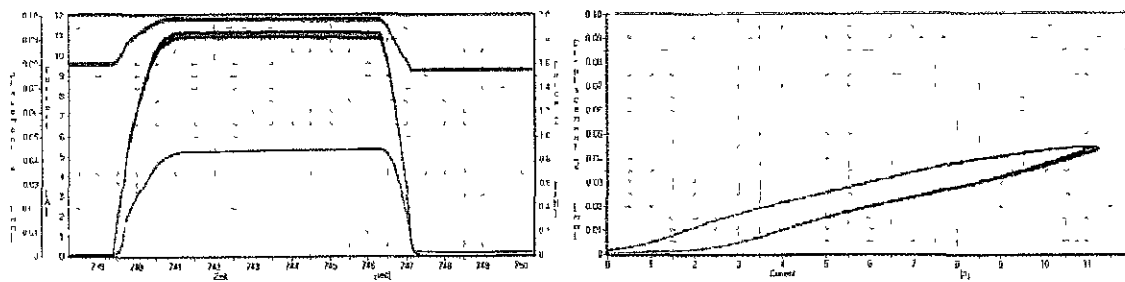


Fig. 128: "MS"-performance at pre-load with 1450 N

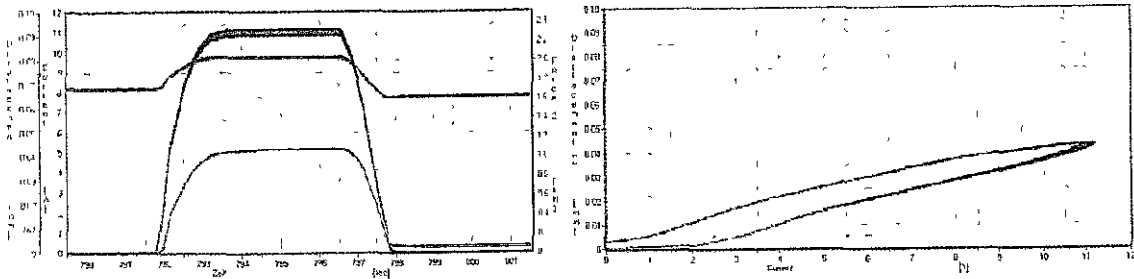


Fig. 129: "MS"-performance at pre-load with 1600 N

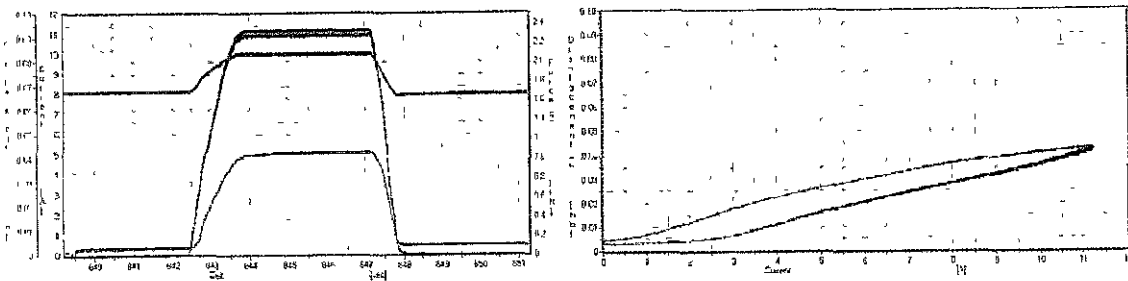


Fig. 130: "MS"-performance at pre-load with 1650 N

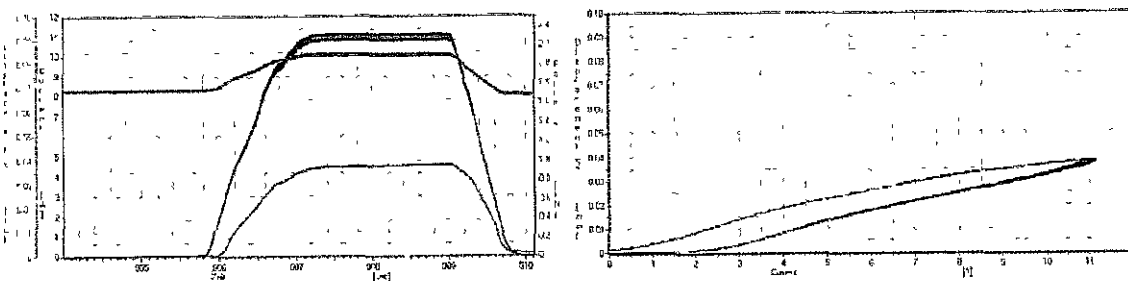


Fig. 131: "MS"-performance at pre-load with 1700 N

The effect of pre-stress has been evaluated experimentally. The level of achieved strain has been rated as sufficient and within the specified range. The optimal pre-stress has been set to the axial force of 500-600 N. At this axial force the Terfenol-D shaft is pre-stressed with 10-12MPa and the achievable displacement is about 0.065 mm. Related to the tested length of the Terfenol-D shaft, the strain was approximately 1000 ppm. This strain was within the specified strain range of the "MS"-shaft. The dependency of the achieved axial displacement versus electrical current is shown in Fig. 132. In Figure 132 the pre-load effect is shown as parameter.

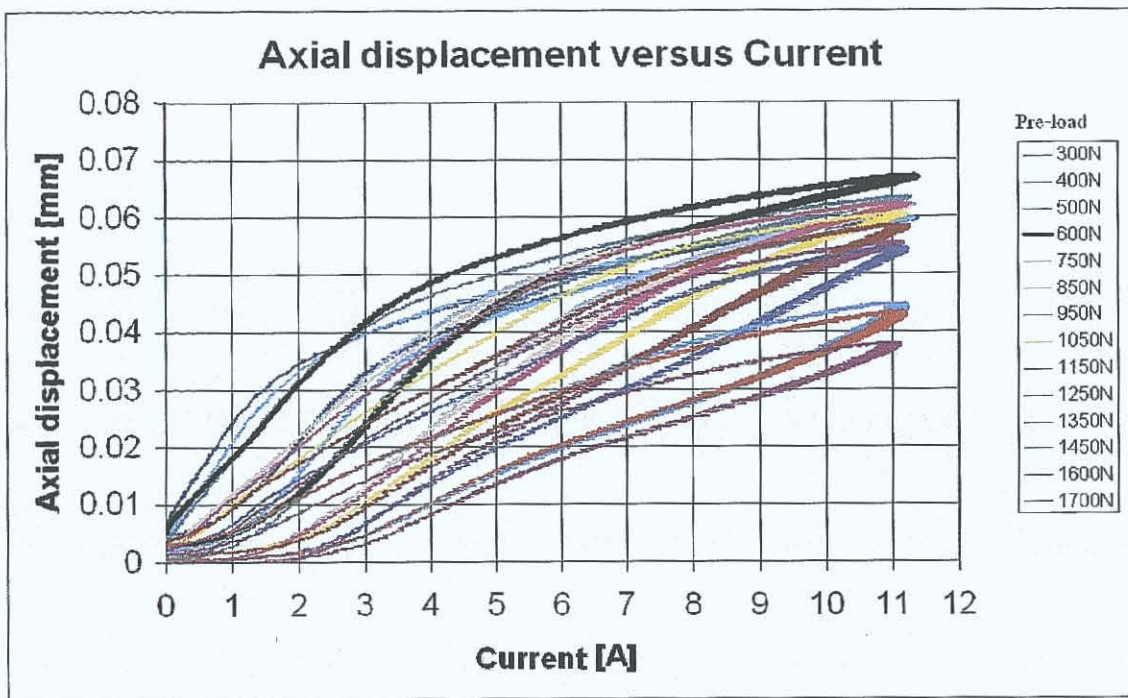


Fig. 132: Optimization of achievable strain with various pre-load

The evaluation of the frequency impact on the actuator performance strain capability has been carried out in the next test. Further, the butterfly-curves with sinusoidal power input have been measured to confirm symmetric behavior of the Terfenol-D. During this testing procedure the frequency dependency has been evaluated. In Fig. 133 to 138 on the left side: the displacement versus current, and on the right side: the time related data acquisition with force current and voltage.

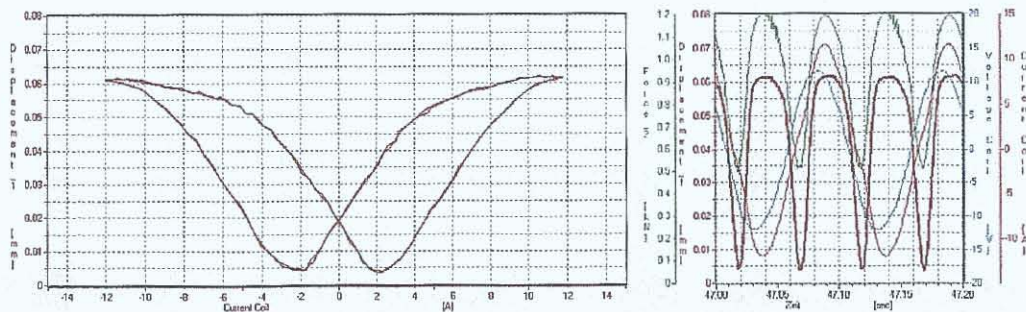


Fig. 133: Butterfly-curve at 550 N pre-load & 20 Hz sinusoidal power input

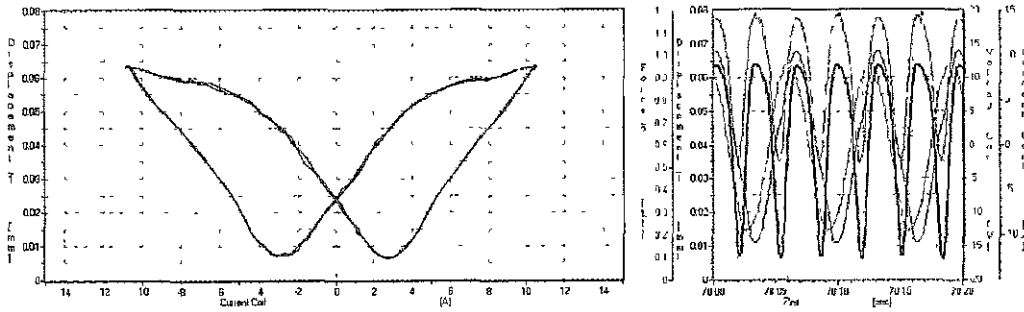


Fig. 134: Butterfly-curve at 550 N pre-load & at 30 Hz sinusoidal power input

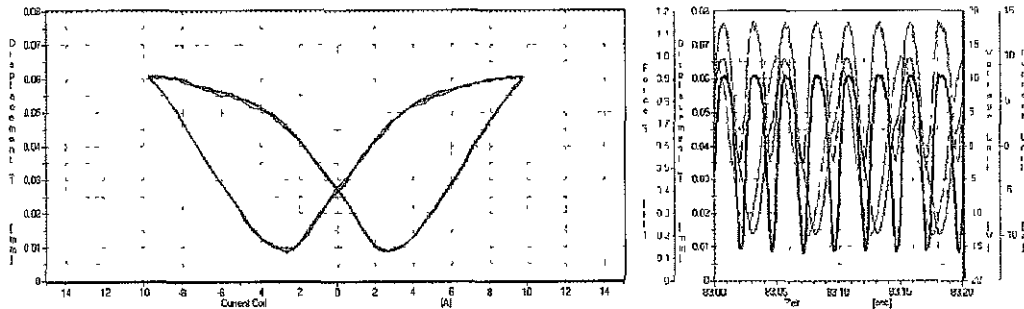


Fig. 135: Butterfly-curve at 550 N pre-load & at 40 Hz sinusoidal power input

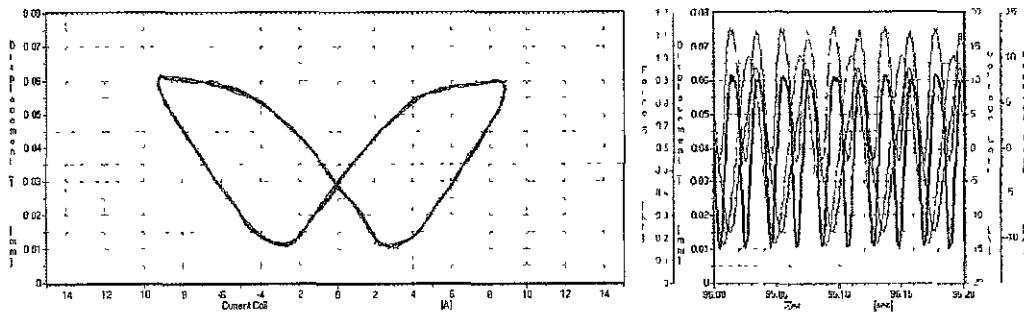


Fig. 136: Butterfly-curve at 550 N pre-load & at 50 Hz sinusoidal power input

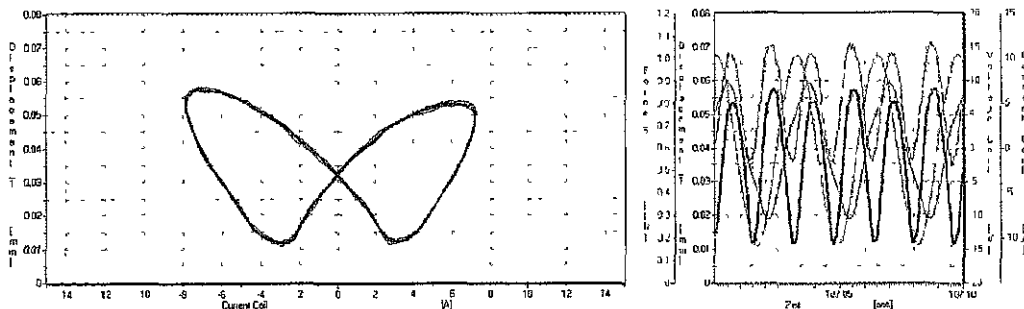


Fig. 137: Butterfly-curve at 550 N pre-load & at 60 Hz sinusoidal power input

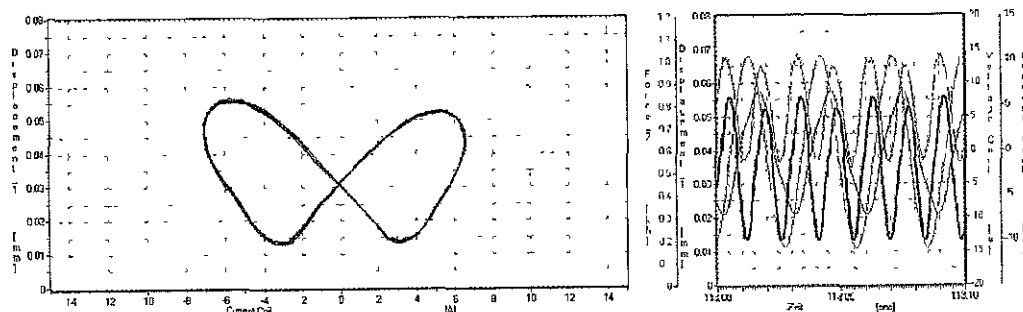


Fig. 138: Butterfly-curve at 550 N pre-load & at 70 Hz sinusoidal power input

Generally, butterfly-curves and the symmetric behavior of the Terfenol-D actuator have been confirmed. Some test equipment limitations (available power stage) and noise from the available displacement sensor has affected the symmetric behavior. To evaluate the Terfenol-D actuator capability regarding to the maximal axial force, the disc spring has been replaced by a washer. Considering the maximal compressive stress of the material two additional levels of pre-load have been tested. At the medium pre-load level of 1.7 kN, a clear butterfly curve can be observed and strain capability about 600 ppm (shaft elongation of 0.037 mm) has been measured. The measuring data are shown in Fig. 139.

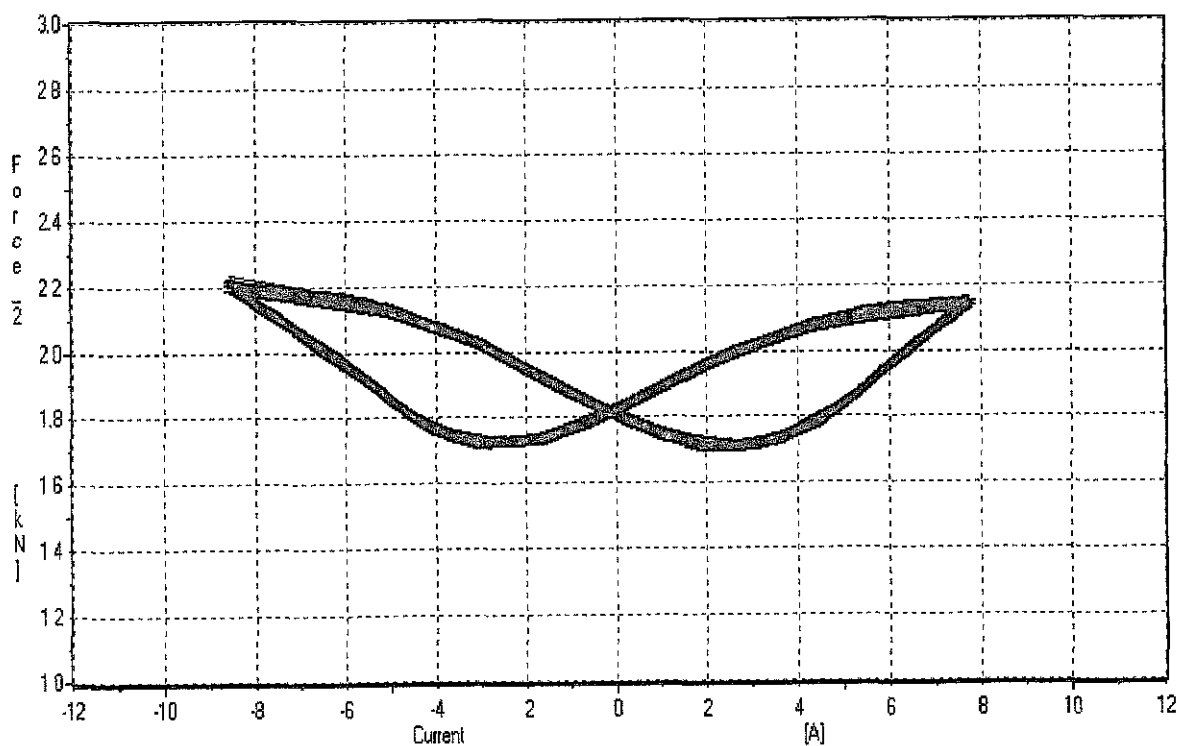


Fig. 139: Butterfly-curves, force versus current at medium level

With the increase of the pre-load force the actuator comes into the blocked force mode and the butterfly-curve is hardly visible. At the pre-load of approximately 4.5 kN the useable strain is very limited and could not be used any more as considerable displacement for a pump or other actuator principles. Fig. 140 depicts the hardly recognized butterfly-curves at blocked force level at which the strain capability is not significant any more.

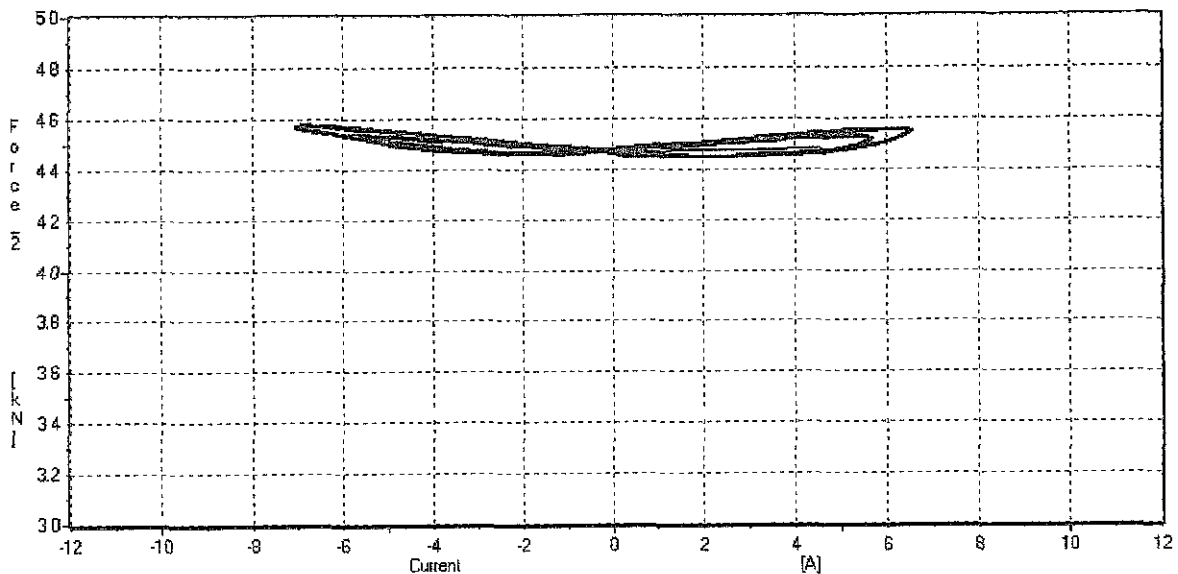


Fig. 140: Butterfly-curves, force versus current, at high level

The achieved results of the magnetostrictive actuator can be summarized as: acceptable displacement, good functionality at various frequencies and high blocked force level, which would be considered as sufficient and in line with theoretical performance calculations. Based on the achieved results, it can be stated that magnetostrictive technology offers big potential for various automotive applications.

6.4 Experimental evaluation of magneto-rheological control

Two different control devices, valve and orifice, with two different MR fluids have been evaluated experimentally. The static pressure capability versus applied current to the valve or orifice coil has been evaluated. The external pressure has been supplied from "hydraulic jack" after the coil from valve or orifice have been energized. Fig. 141 depicts arrangement with the cross section of tested structure for experimental tests of the "MR"-controlled valve assembly.

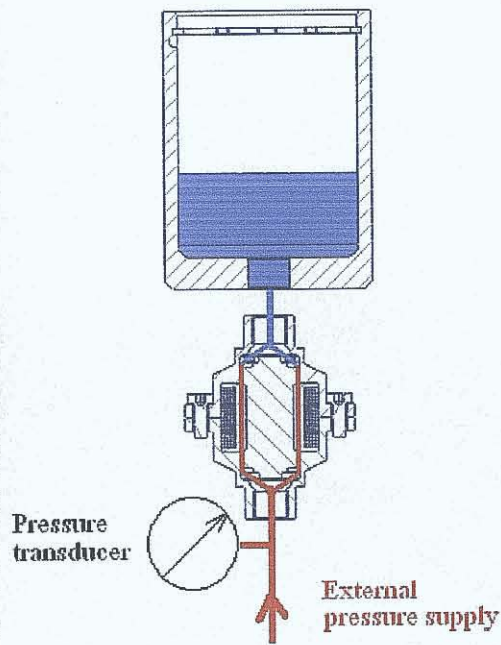
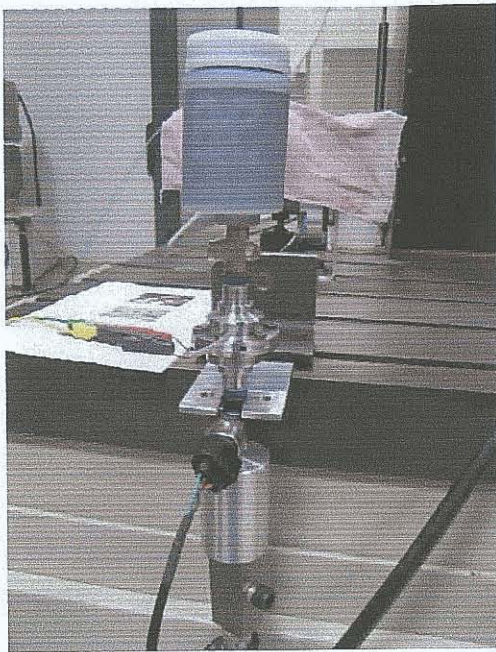


Fig. 141: Layout for experimental tests of the valve

Figure 142 presents arrangement for experimental tests of the alternative “MR”-controlled orifice assembly.

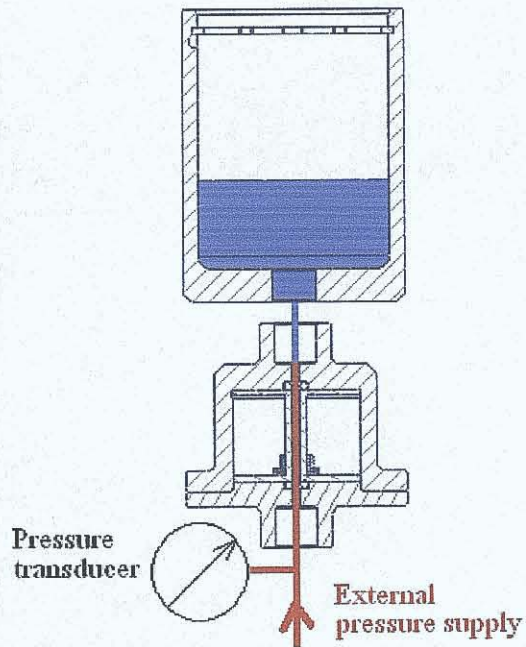
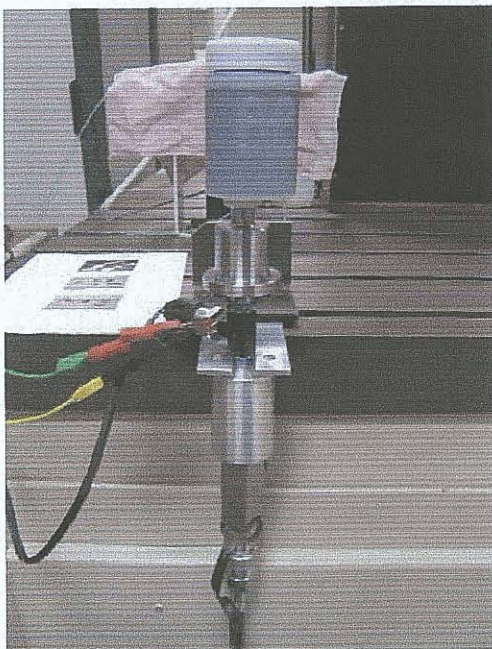


Fig. 142: Layout for experimental tests of the orifice

The above shown valve and orifice control assemblies, based on magneto-rheological fluid, have been evaluated experimentally. The position of the reservoir during the testing has been

chosen at the top to enable the self bleeding due to pump and suck operation. Both assemblies have been evaluated with MRF 132-AD and with MRF 336-AG. The data have been recorded for evaluation of achieved pressure performance. Fig. 143 depicts an example of the recorded data of the test procedure, where the valve filled with MRF 132-AD has been used.

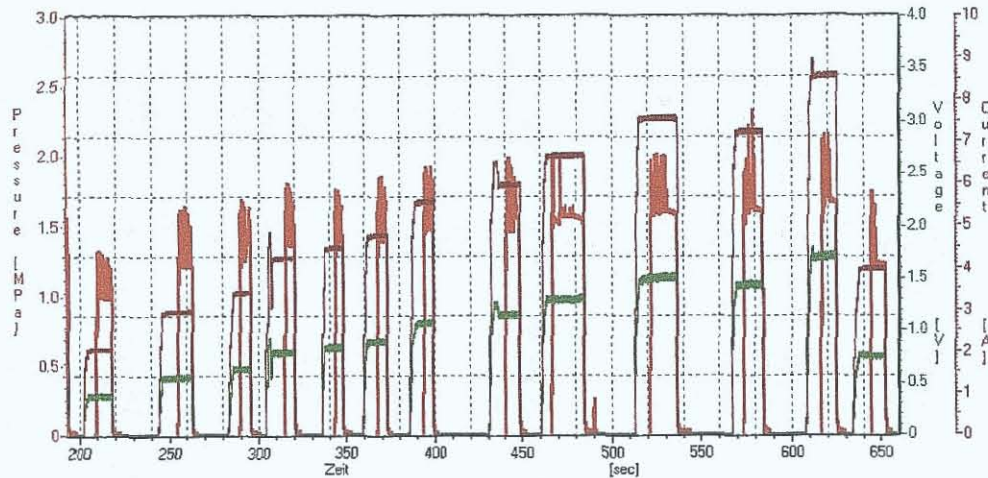


Fig. 143: Pressure capacity of valve with MRF 132-AD

As mentioned above, the external pressure has been supplied from the rig equipment. The maximal achievable external flow rate from the "hydraulic jack" is about $5 \times 10^{-6} \text{ m}^3/\text{s}$. The pumping through the valve without the electrically engaged control coil showed pressure drop of approximately 0.05 MPa. For evaluation of the pressure capacity, the stationary condition, static pressure has been evaluated. In this particular series of experimental trials, the delay in the build-up of the pressure is part of experimental arrangements, and does not indicate a delay in response time of the MRF. Figures 144 to 147 show examples of this static pressure capability from the valve with MRF 132-AD.

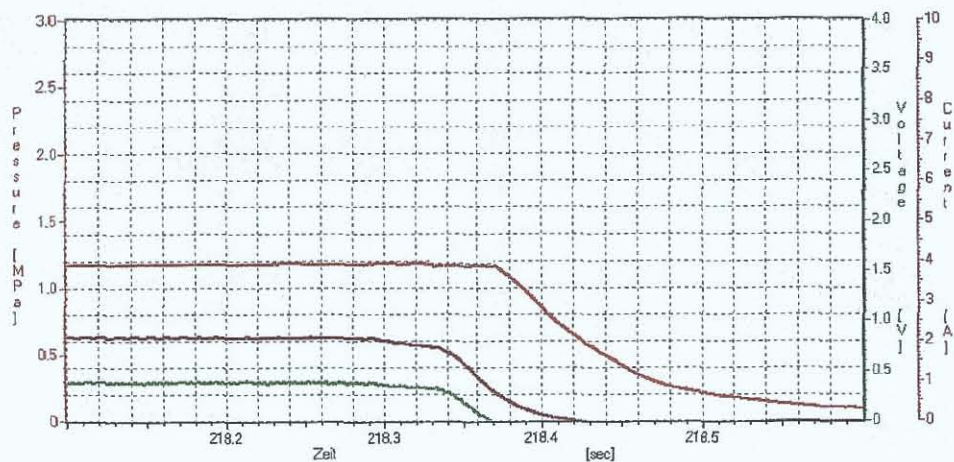


Fig. 144: Pressure capacity of the valve with MRF 132-AD (1.2 MPa @ 2A)

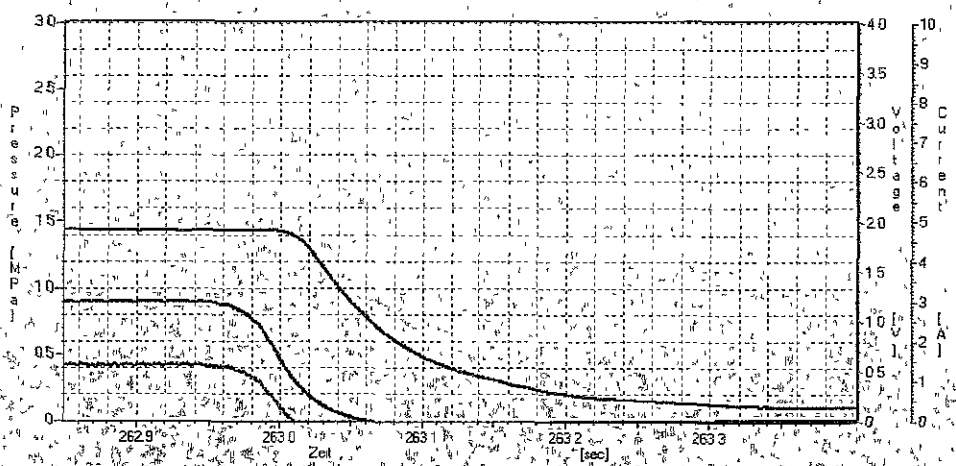


Fig. 145: Pressure capacity of the valve with MRF 132-AD (1.4 MPa @ 3A)

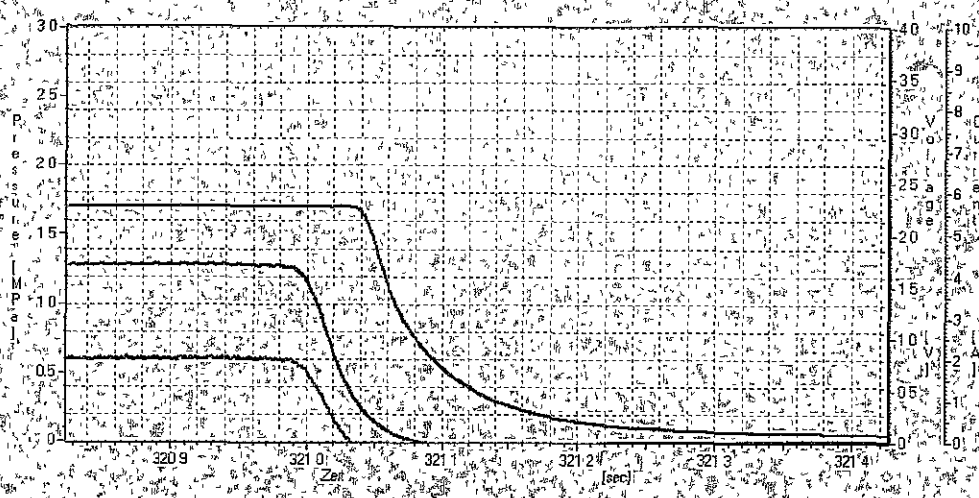


Fig. 146: Pressure capacity of the valve with MRF 132-AD (1.7 MPa @ 4.5A)

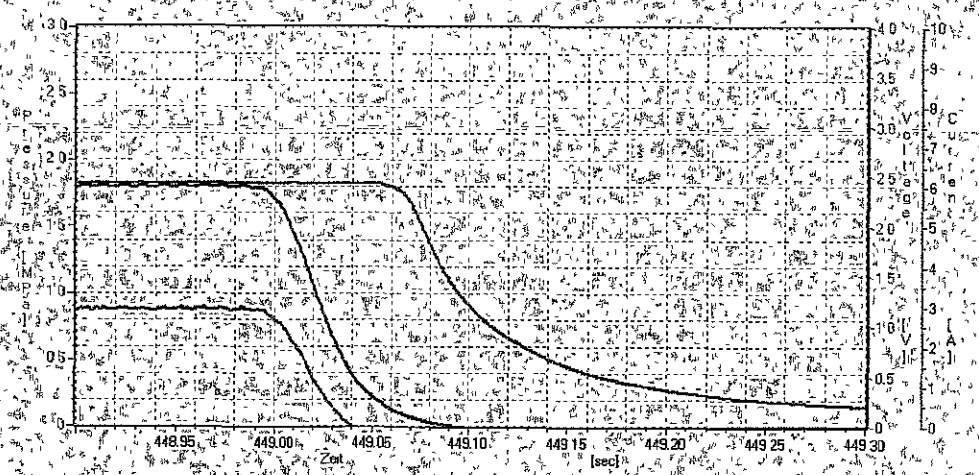


Fig. 147: Pressure capacity of the valve with MRF 132-AD (1.8 MPa @ 6A)

Tests have been repeated several times in order to get some statistical value of the pressure versus current capability and to prove the predictability. All testing has been carried out at ambient temperature of +20°C. The silicon based fluid has been found challenging for conventional bleeding and sealing devices. The MRF 336-AG fluid behavior in the orifice control arrangement, as well in the valve control arrangement, has been found as less than sufficient and predictable comparing with MRF 132-AD. Generally, silicon based MRF's are more difficult to seal and to bleed comparing with hydrocarbon based MRF's. On the other hand, silicon based MRF's are less sensitive to temperature variation. For support of the bleeding procedure the fluid has been heated up to about +60°C. The fluid performance and good bleeding is essential for the achievable pressure level. The recorded data from the experimental evaluation of the orifice assembly and the valve assembly, with MRF 132-AD and MRF 336-AG, are depicted in Fig. 148.

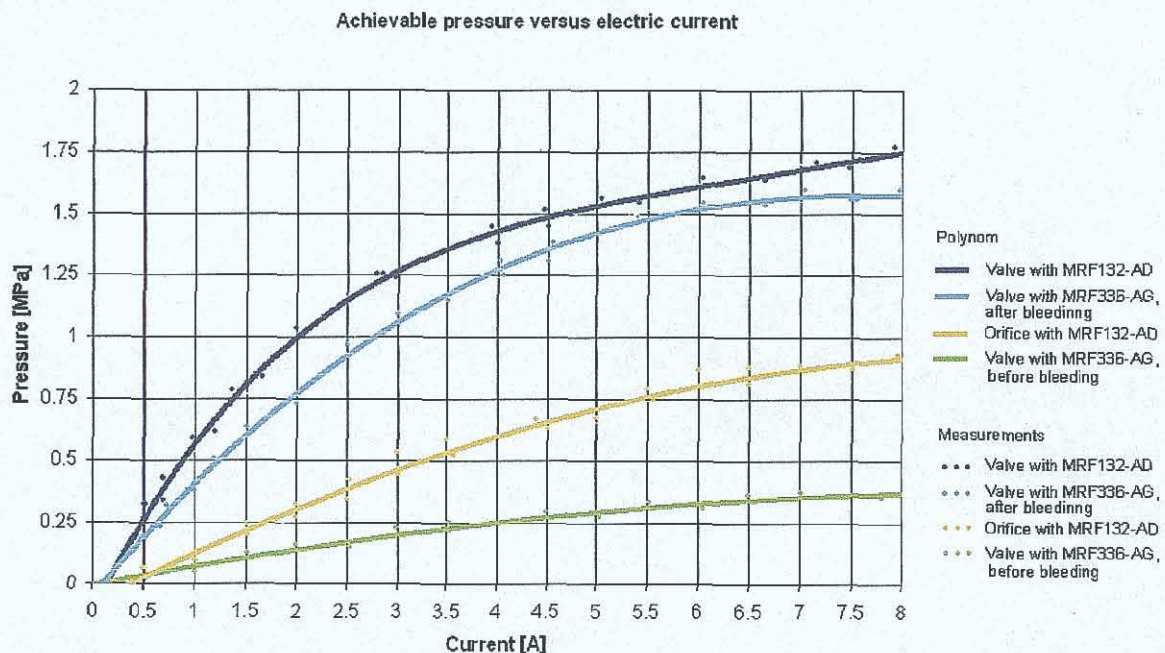


Fig. 148: Pressure capacity of MRF control assemblies

The pressure capacity of the “MR”-orifice depends mainly on the flow rate. Flow rate of 5 cm³/s was required to hold the pressure drop with the orifice. The “MR”-valve is capable to hold the pressure without a significant leakage. It was concluded from the above mentioned experimental results that the preferred control structure is the “MR”-valve, and the preferred fluid for the next test is MRF 132-AD. The combination of the valve control (orthogonal direction of magnetic field to the fluid motion) and the hydrocarbon based MRF 132-AD shows more acceptable and predictable performance. The achievable pressure level has been

predicted by calculation and simulation of magnetic field. The above showed results of the experimental evaluation (valve with MRF132-AD) have been found as sufficient and in line with specified performance. Based on the achieved results, it could be stated that, magneto-rheological technology offers big potential for various fluid applications.

6.5 Experimental evaluation of "MS"-pump

To prove the basic pump-functionality a layout with conventional check valve and hydraulic liquid (CHF 11S) has been prepared. Fig. 149 shows the layout on rig test with a representative cross section. Details on design can be viewed in the appendices A and D of this thesis.

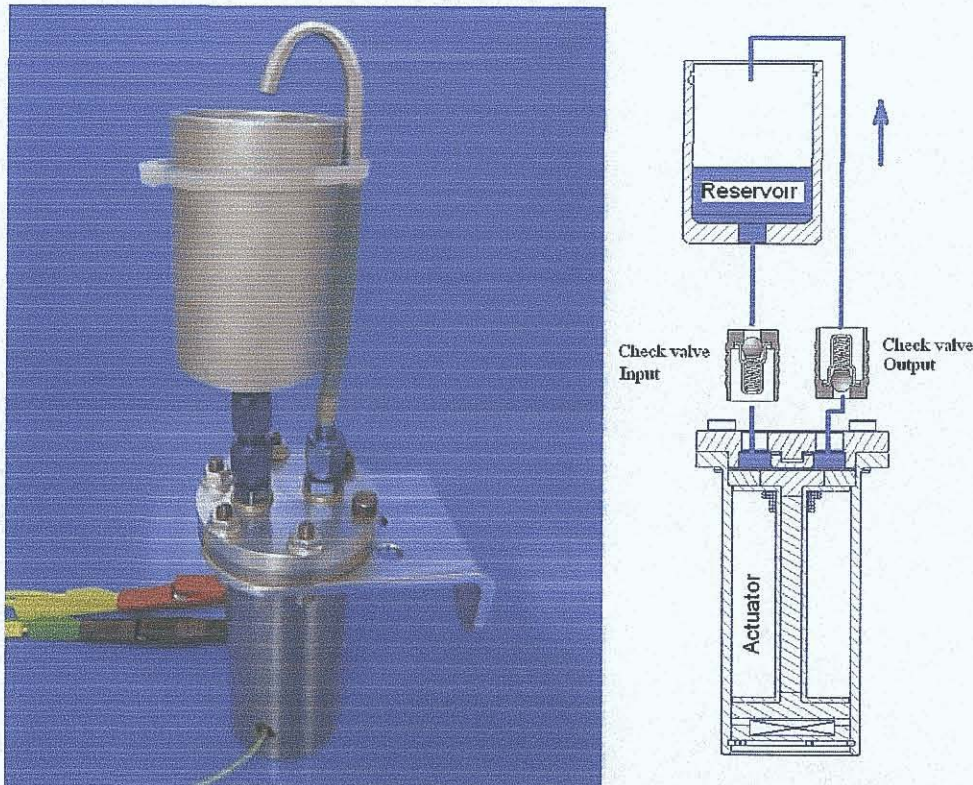


Fig. 149: "MS"-pump actuator assembly with check valves

Bleeding of the system was required to enable the pump functionality. The actuator coil has been powered with sinusoidal current. The axial force during the operation and the required time to pump 100 ml have been measured. Fig. 150 shows the result of the pumping performance with check valves and CHF 11S hydraulic fluid.

Achievable flow rate versus operational frequency

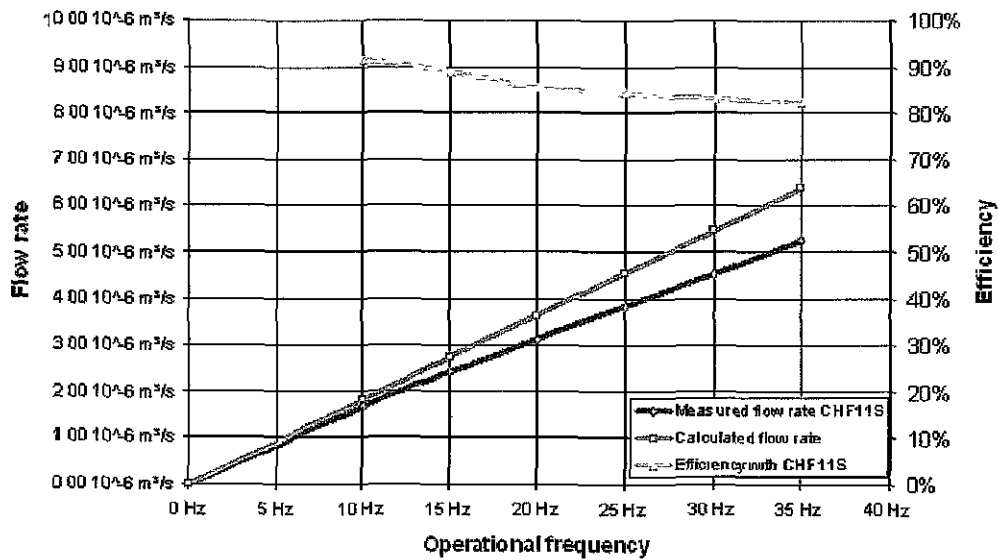


Fig. 150: "MS"-pump actuator assembly with check valves and CHF11S

In the next test session, the conventional fluid has been replaced with the MRF 132-AD. And, the same test procedure has been repeated to evaluate the basic pump functionality with magneto-rheological fluid. Fig. 151 shows the result of the pumping performance with conventional check valves and MRF 132-AD.

Achievable flow rate versus operational frequency

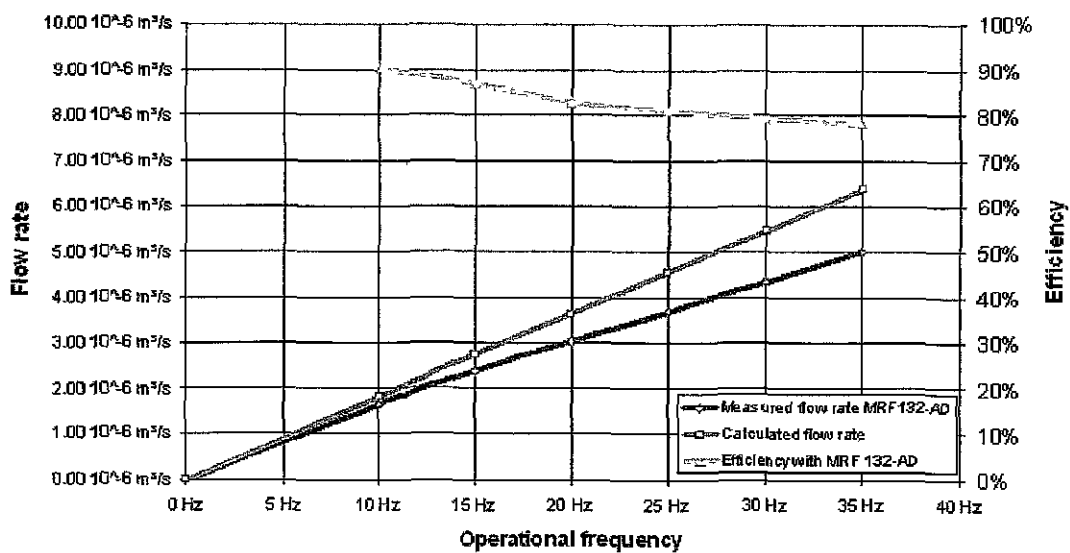


Fig. 151: "MS"-pump actuator assembly with check valves and MRF 132-AD

Some limitations from the available rig equipment (power electronic) regarding the achievable frequencies are accepted since the purpose of this study is to prove the basic functionality and to highlight the potential of the system. During the test, the axial force from the "MS"-shaft and the electric input, voltage and current, have been recorded. Fig. 152 shows a snap shut from the above tests.

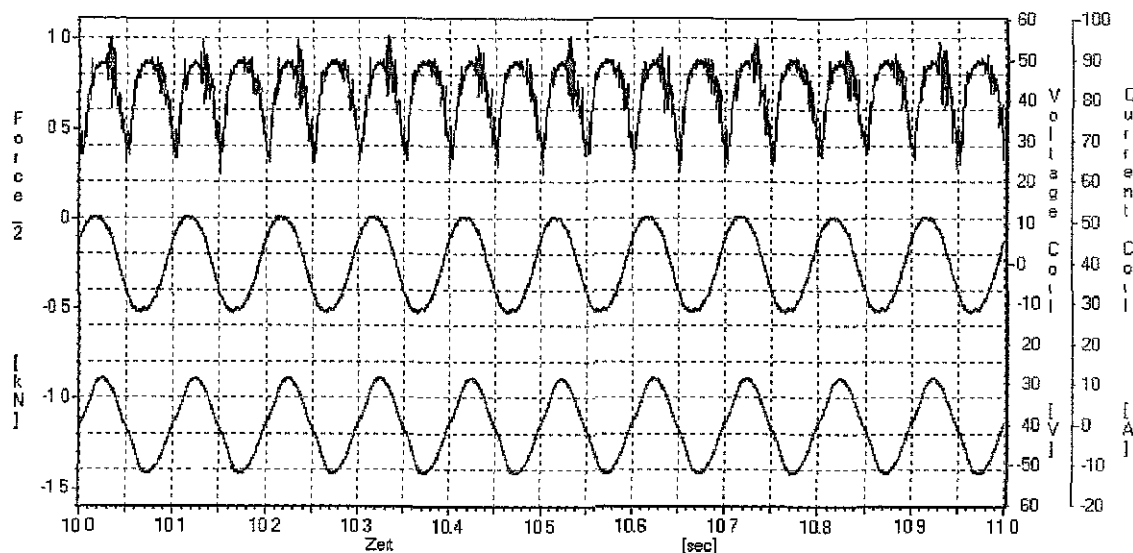


Fig. 152: "MS"-shaft force, voltage and current from pump actuator

The pump performance difference between two fluids, CHF11S and MRF132-AD, is not significant. The difference in efficiency is below 4%. Due to content of ferro-magnetic powder in MRF 132-AD the opening and closing of the one-way valve is less predictable comparing with conventional fluid. Some unpredictable behavior, due to metallic particles in the fluid, of the opening and closing of the check-valves has been observed. Generally, the basic functionality has been proven and could be predicted by analytical calculations. The tested structure could be extended to an "MS"-actuator with two conventional check valves, load and a controlled "MR"-valve as release valve. Further experimental testing will be carried out with the reference load assembly.

In the next step, the basic functionality of the "MS"-actuator with two "MR"-valves has been evaluated. The purpose of the testing is to understand whether a fully "MR"-controlled fluid flow could lead to better performance than above tested system with check valves. The additional electric power source has been adapted into the experimental test rig.

Simultaneously control of all three coils is required to enable the pump functionality. The control of the three coils with the defined phase shift has been realized with the LabView control panel and National Instruments I/O cards. The basic phase definition is defined as

following. The input valve is assembled between the reservoir and the pilot piston from “MS”-actuator. The output coil is assembled to the return line. Before the "MS" actuator is elongating, the input coil has to be powered, and the output coil is switched off. In this condition the elongation of the “MS”-shaft leads to pilot piston movement and this leads finally to the fluid flow. Before the pilot piston returns in the original position, the output coil should be powered to avoid the return of the fluid flow. Furthermore, after switching on of the output coil and before the disengagement of the MS-actuator coil, the input coil should be switched off. Opening the input coil in this moment leads to sucking of the oil from the reservoir for the next actuation loop. Fig. 153 depicts the user interface from prepared LabView control panel.

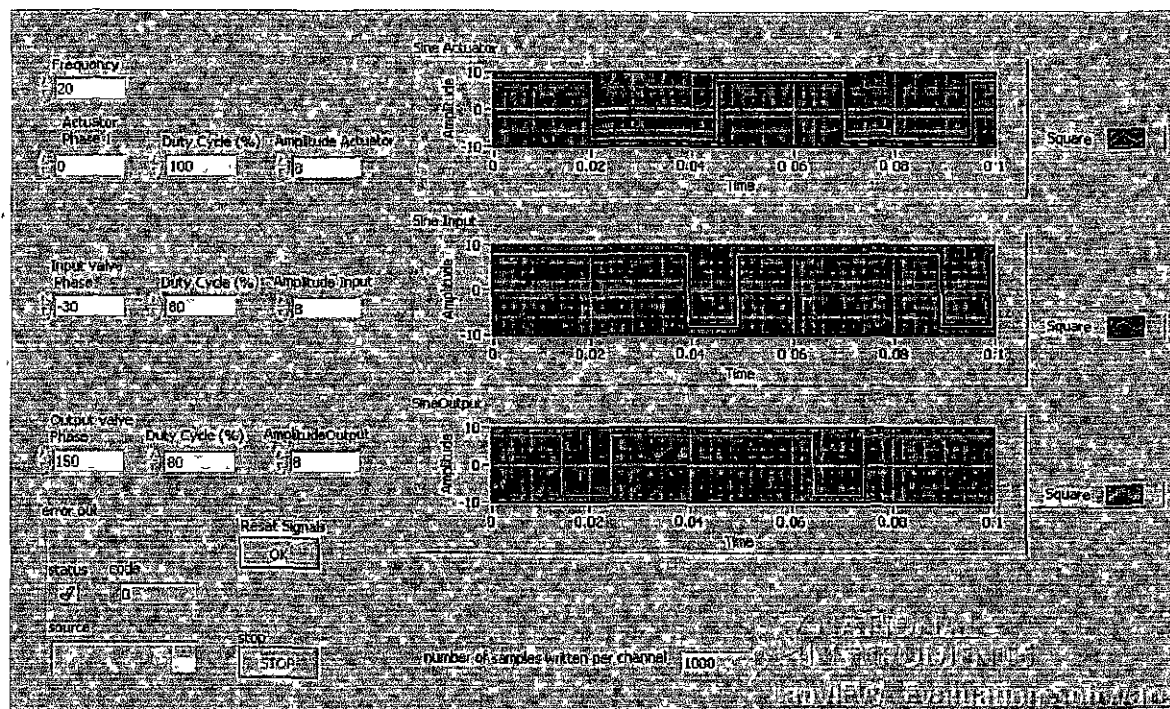


Fig. 153: NI interface for actuator with “MS” and “MR” control coils

During the test, the electric power flow has been recorded. Fig. 154 shows an example of the recorded data with the fully "MR"-controlled fluid flow.

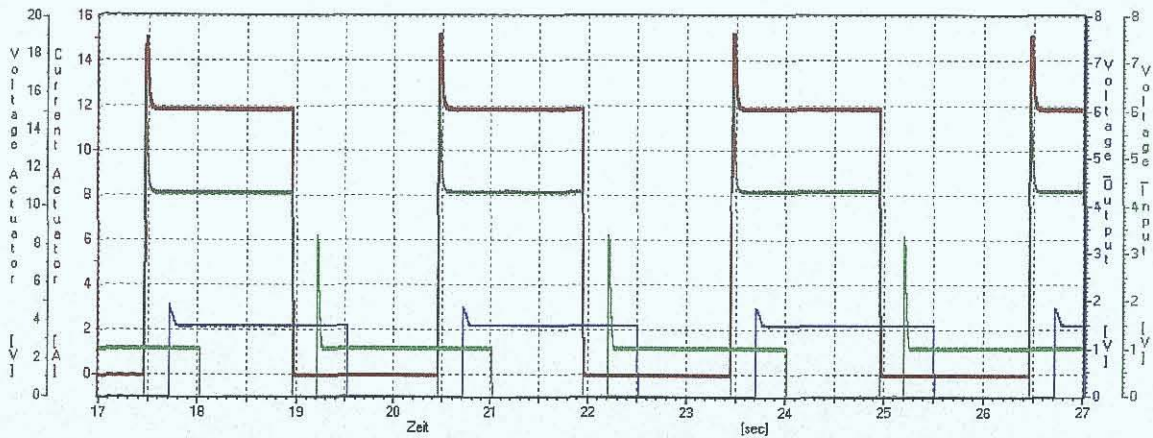


Fig. 154: Current and voltage flow during the testing as example

Fig. 155 presents the layout on rig test with a representative cross section. Details of the design could be seen in the appendixes A, B, and D of this thesis.

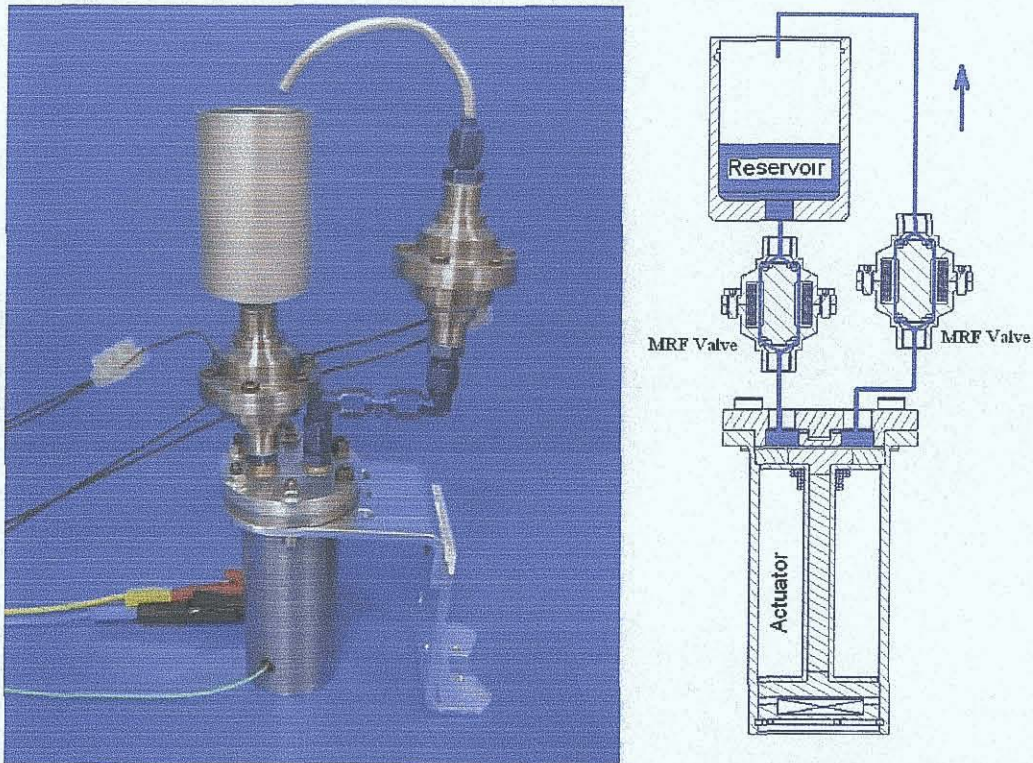


Fig. 155: "MS"-pump actuator assembly with "MR"-valves

Fig. 156 shows the result of the pumping performance fully "MR"-controlled fluid flow with MRF 132-AD. Proper bleeding and acceptable distribution of ferromagnetic particles in the "MR"-fluid was essential for pumping operation.

Achievable flow rate versus operational frequency

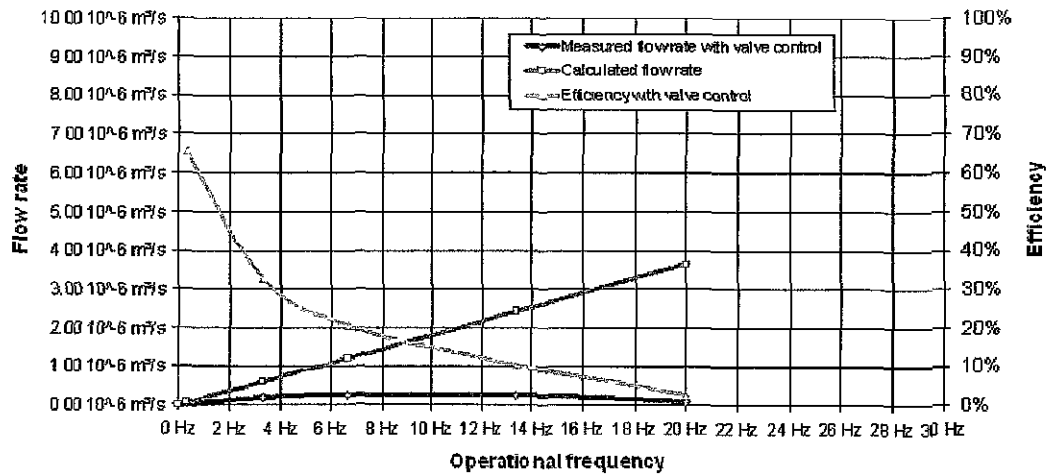


Fig. 156: "MS"-pump actuator assembly with two "MR" valves and MRF 132-AD

The achievable performance of the system based on two miniaturized check valves is significantly better than the performance from two active "MR"-valves. The lack of performance occurs due to delay in response time of the two "MR"-valves. The measured response time from the "MR"-valve is about 50 ms. Experimental results related to the response time are summarized in chapter 6.6. The delay in response time leads to parasitic fluid flow. The "MR"-fluid was moved forward and reverse, without a predictable fluid control. Advance power control of the current and voltage could help to improve the response time of the "MR"-valve. However, the drawback is the decreasing of the efficiency versus operational frequency. The "MR"-valve opening and closing at higher frequency, i.e. up to 5 Hz and higher, has been found as not sufficient. Basically, the decreasing of efficiency occurs in both valves, the "MR"-valve and the check valves. For the "MR"-valve is the response time, and for the check valve the leakage (return or parasitic flow) has to be taken into account. The above depicted results show clearly that, the performance limitations of the "MS"-pump is the control valve. The delay in response time is limiting the maximal operational frequency of the valve. Most of the problem is due to the difficulty in stabilizing the current for higher frequencies in the magnetic circuit with the particular inductance and reluctance. It was concluded from the above showed experimental result that the preferred control structure for the actuator should be based on check valves. However, to release the pressure an active valve will be required. The "MR"-valve assembly with the favored fluid for the MRF 132-AD is more suitable to be used as pressure release valve. Further experimental evaluation will be carried out with the complete actuator assembly including the reference load.

6.6 Experimental evaluation of complete actuator assembly

As the reference load for the study, the assembly with housing, piston and disc spring have been chosen. A modified "hydraulic jack" has been used to supply the required pressure for static performance measurement. The purpose of the test session is to evaluate the elasticity, to prove pressure and force capability, to fill and to bleed the pump assembly. The hydrocarbon fluid MRF 132-AD has been used as working fluid. Axial force from the magnetostrictive actuator, hydraulic pressure, axial force at the main piston and the axial displacement of the main piston against the disc spring have been recorded. Fig. 157 depicts the arrangement for experimental tests of the reference assembly.

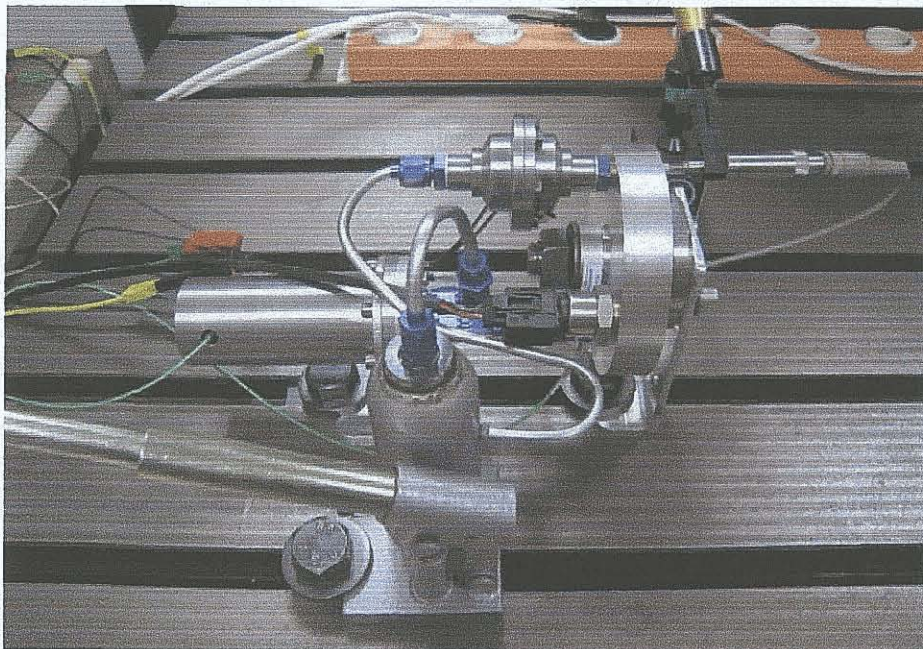


Fig.157: Reference assembly on test bench

Fig. 158 shows the cross section of the arrangement for experimental tests of the actuator, load assembly and the "MR" release valve.

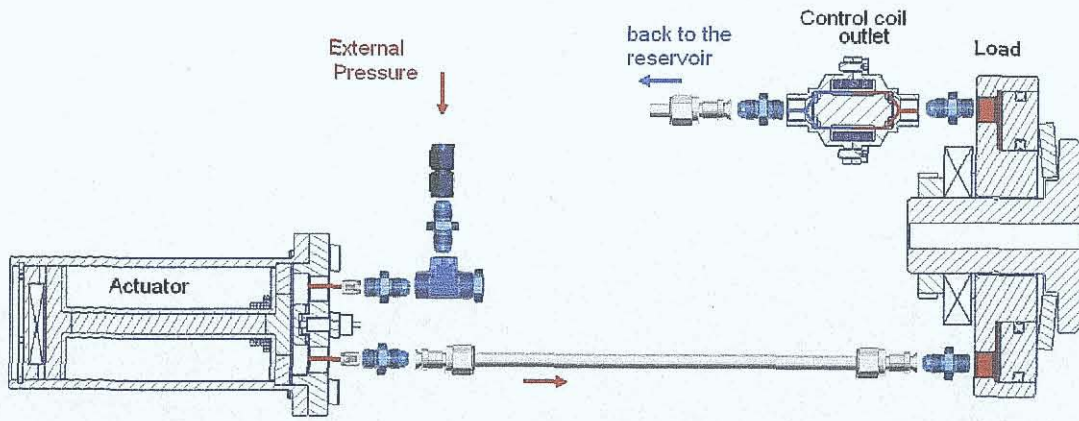


Fig.158: Experimental tests of the load arrangements

Fig. 159 shows the measurement results of the reference assembly. The shown data have been recorded versus time.

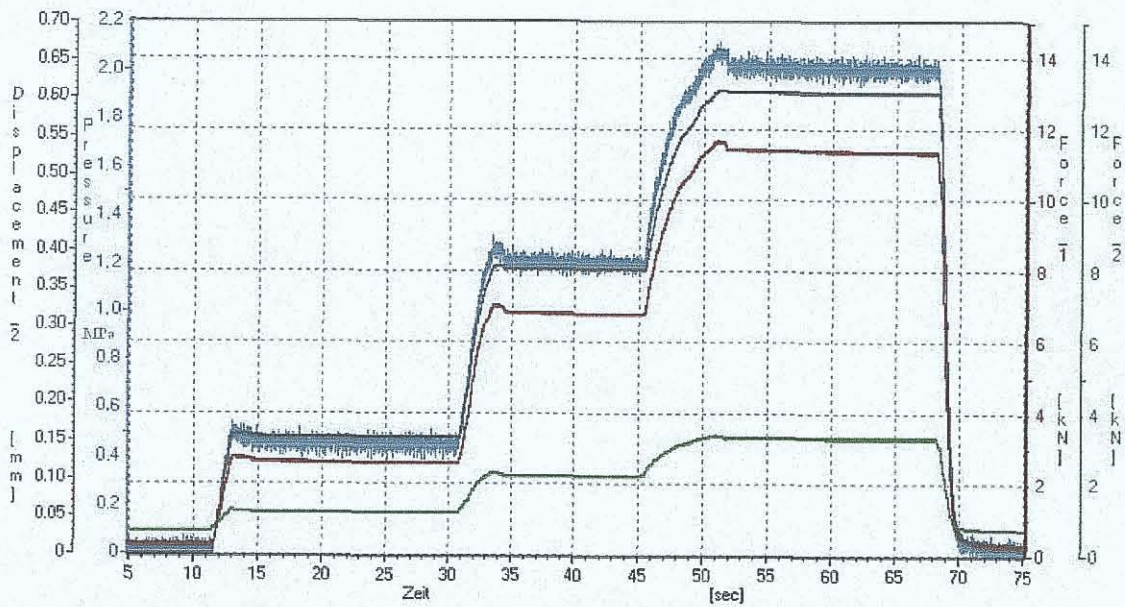


Fig. 159: Measurement of the reference assembly

As an extract of above diagram the new diagrams "axial force and displacement versus pressure" have been created. MRF control coils have not been used during this test. Fig. 160 shows the performance characteristic of the reference assembly.

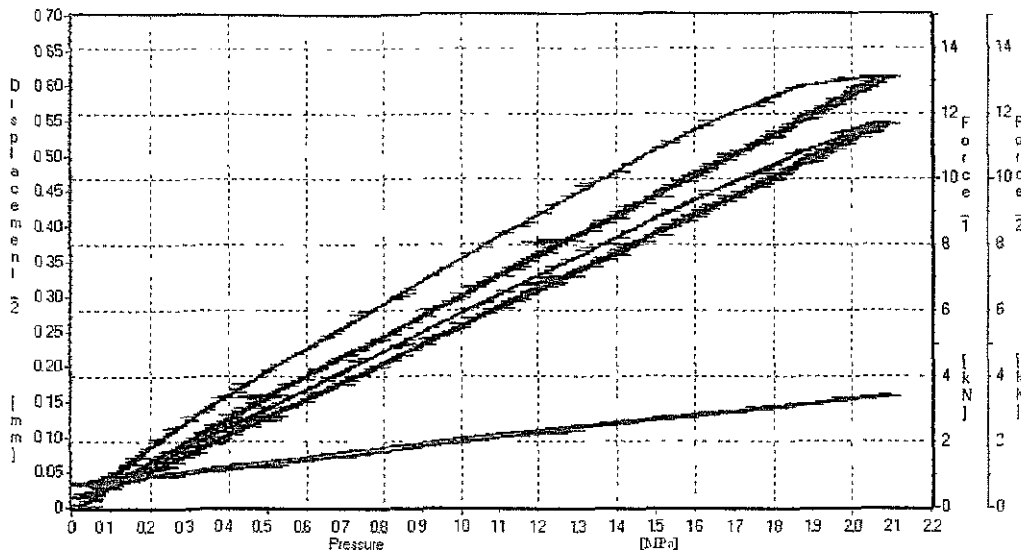


Fig. 160: Axial force and displacement versus pressure

The axial force depicted in Fig. 160 as Force_1 is measured at the main piston and the Force_2 is measured at the magnetostrictive actuator. The hysteresis (counter clockwise) of displacement and the axial force from the main piston is caused by friction (piston sealing) and could be improved by appropriate coating of the housing surfaces.

In the following test the "MR"-valve pressure capability and the pressure performance of the complete assembly, have been evaluated. The pressure was applied externally with "hydraulic jack" after the release valve was energized. By switching off the electric power from release valve the disengagement behavior has been recorded. Figures 161 to 168 show the pressure release performance of the control in the complete assembly at various pressure levels.

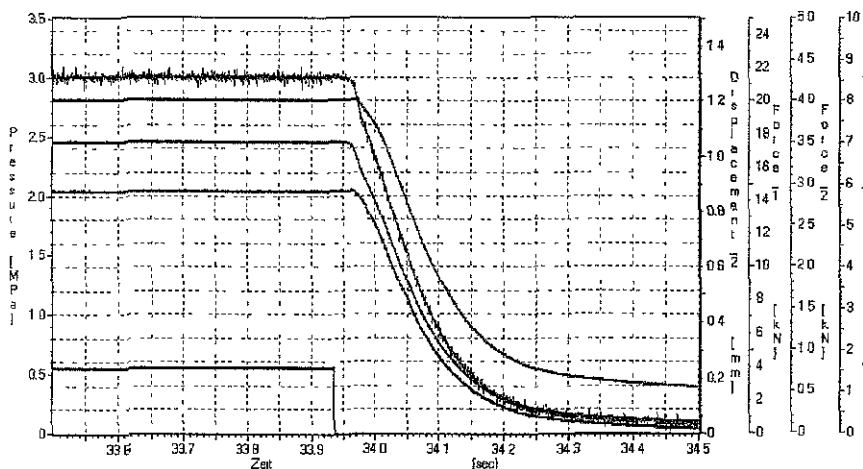


Fig. 161: Disengagement performance from 3 MPa

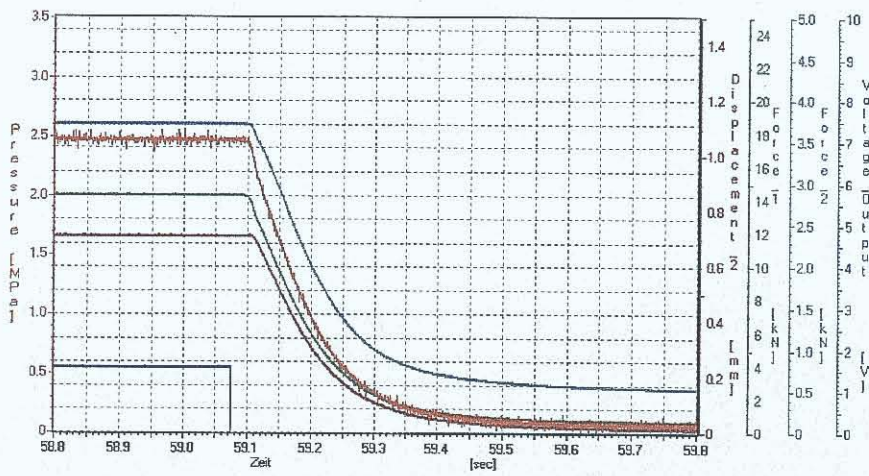


Fig. 162: Disengagement performance from 2.5 MPa

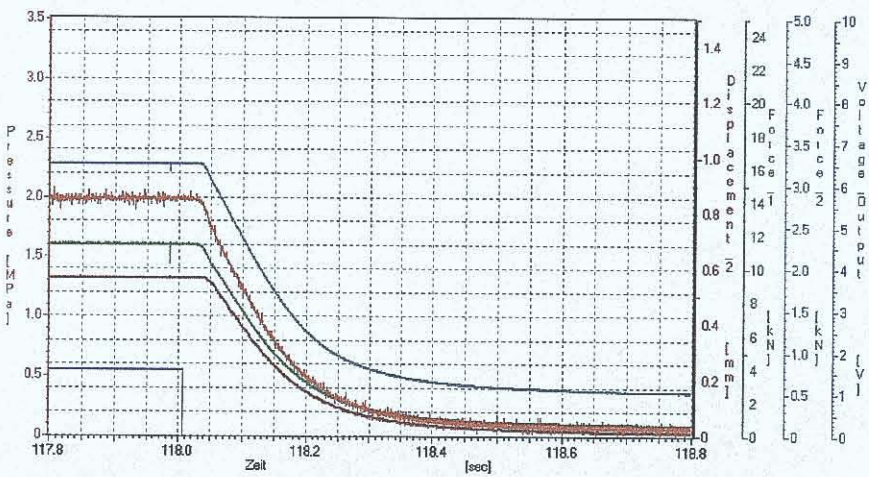


Fig. 163: Disengagement performance from 2.0 MPa

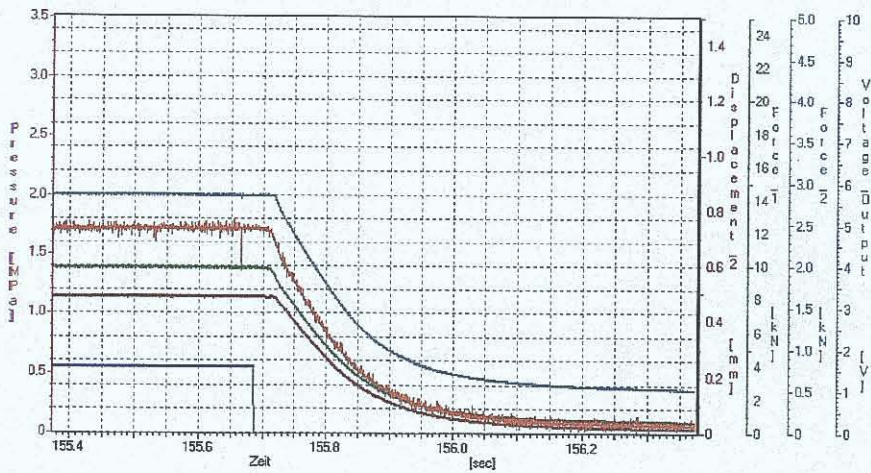


Fig. 164: Disengagement performance from 1.7 MPa

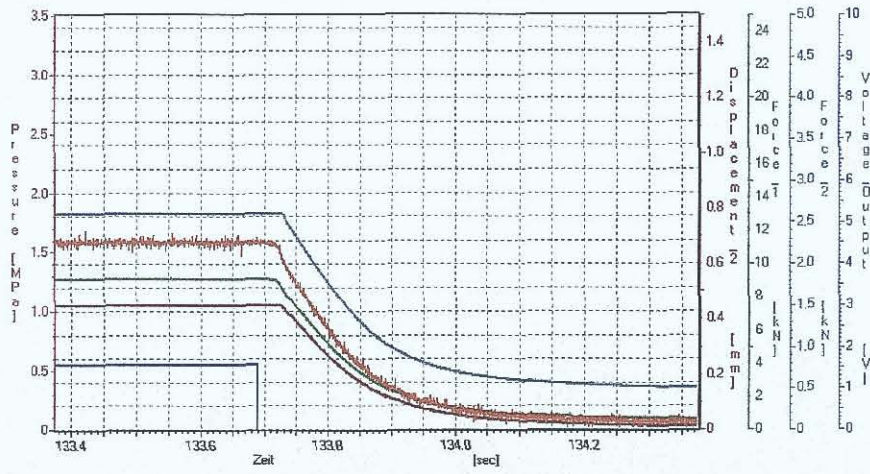


Fig. 165: Disengagement performance from 1.6 MPa

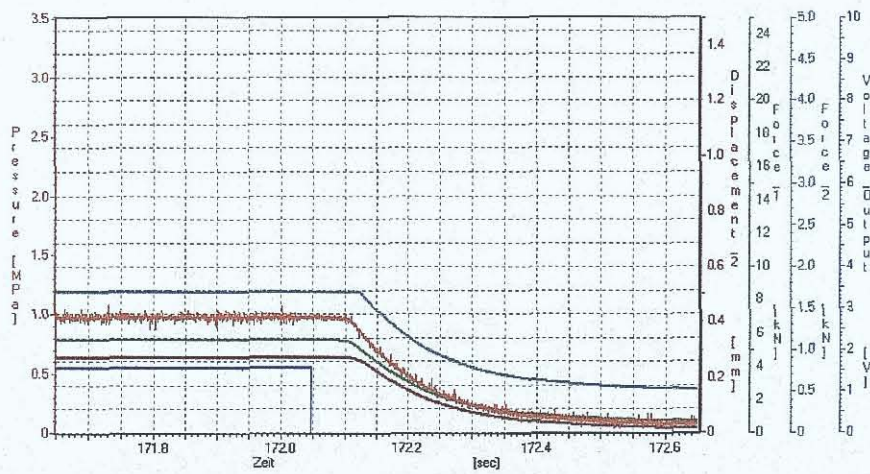


Fig. 166: Disengagement performance from 1.0 MPa

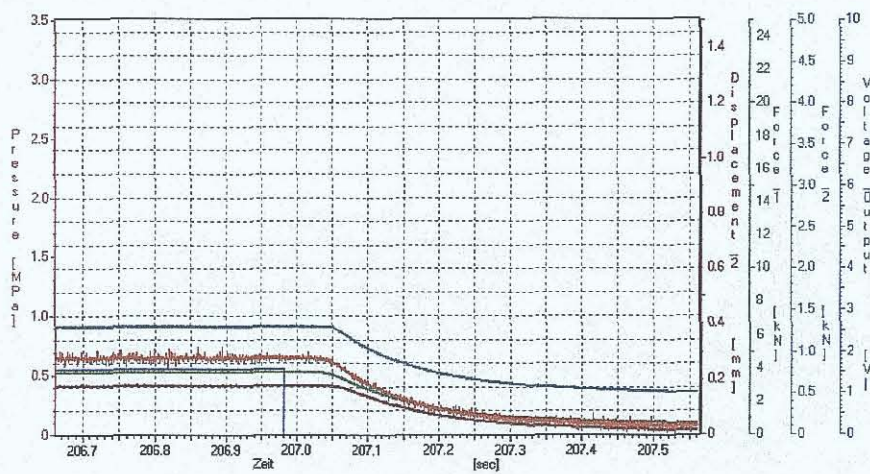


Fig. 167: Disengagement performance from 0.7 MPa

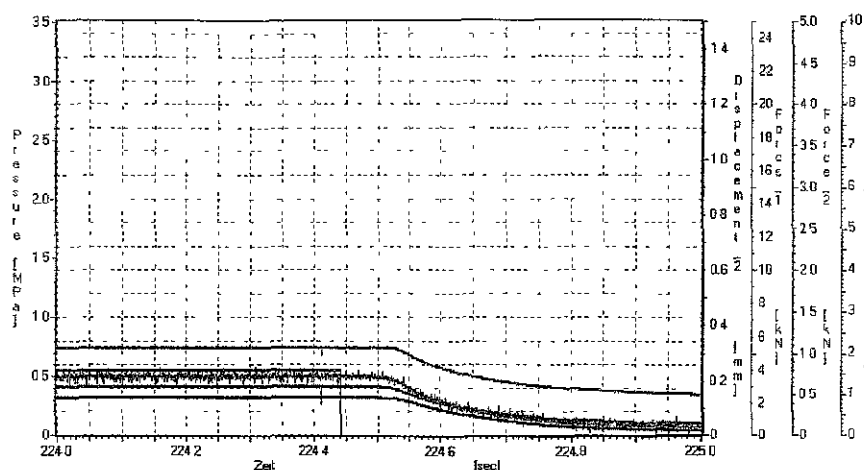


Fig. 168: Disengagement performance from 0.5 MPa

Based on above depicted results it has been concluded to continue the basic functionality tests with proposed load assembly. Less than 150 ms were required to decrease the pressure from 1.0 MPa to 0.25 MPa, and about 200 ms were required to decrease the pressure from 1.7 MPa to 0.25 MPa. Some delay, up to 25 ms, is caused by translation from the digital to the analog signal. The delay in response could be overcome by further optimization of the valve assembly and the advanced control strategy. Especially at low pressure level, due to the hysteresis of the load system and the resistance from viscous medium some delay in disengagement occurs. Pressure of up to 3 MPa has been measured with the "MR"-valve assembly. In this valve assembly the MRF gap was 0.5 mm. Generally, the performance of the load assembly has been rated as acceptable for further testing.

6.7 Experimental evaluation of the "MS"-pump actuator

To confirm the expected performance of the fully "MR"-controlled structure actuation tests have been performed. The complete assembly is depicted in Fig. 169

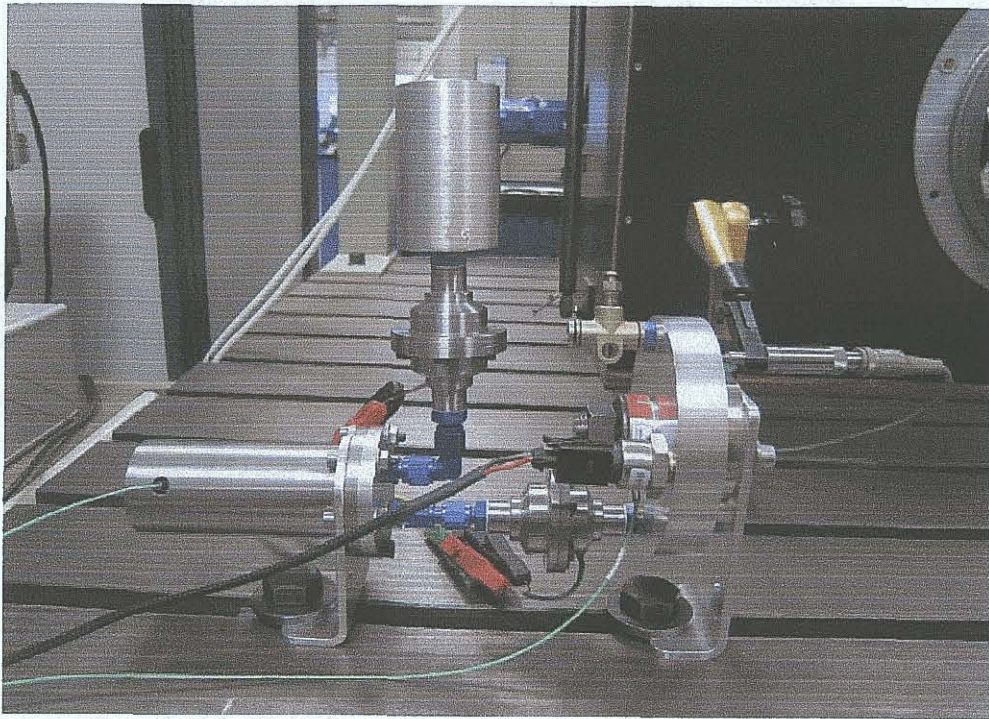


Fig. 169: MS actuator with full MRF control

Fig. 170 shows the cross section from the assembly. MRF 132-AD has been used for the basic functionality test. The purpose of the test is to confirm the functionality and to evaluate whether better bleeding and pre-load of the reservoir will significantly change the performance. Based on discussed results in 6.6, the fully "MR" controlled system is not the preferred system. However, the basic functionality will be checked.

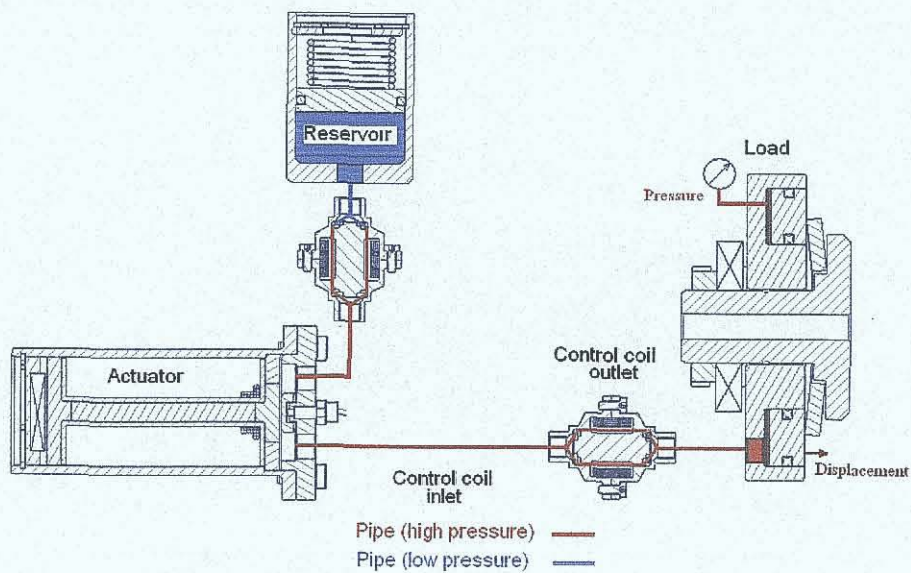


Fig. 170: Cross section of "MS"-actuator with full MRF control

Fig. 171 presents the basic functionality of "MS"-actuator with full MRF control at low frequency. It could be observed that the reverse pilot piston movement creates some leakage through the valve.

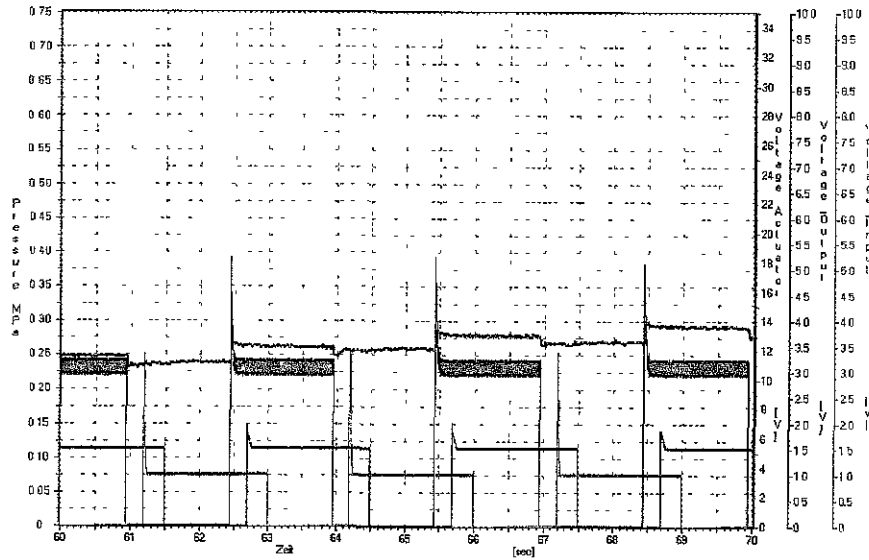


Fig. 171: Micro-pumping at low frequency (<1 Hz)

Fig. 172 shows the example of the function at higher frequency. Maximal achievable pressure is about 0.35 MPa. Further increase of operational frequency, higher than 15 Hz, leads to loss of micro-pumping due to delay in response from the valves.

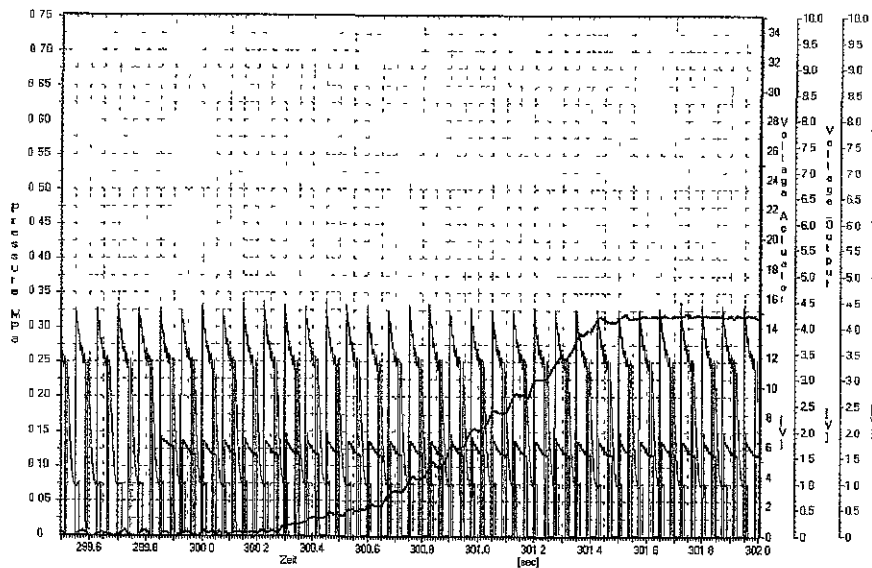


Fig. 172: Micro-pumping at medium frequency (<15 Hz)

As expected, further increase of the operational frequency stops the micro-pumping due to response time delay from the "MR"-valves. Furthermore, the fully "MR"-controlled fluid flow requires to control three coils simultaneously. The structure of the electronic control unit becomes more complex and expensive in the application. Based on measurement results it has been concluded to prefer the simpler structure where "MR"-valve is used to release the pressure. Fig. 173 presents the structure of "MS"-pump actuator with two check valves and "MR"-valve in the return line to release the pressure.

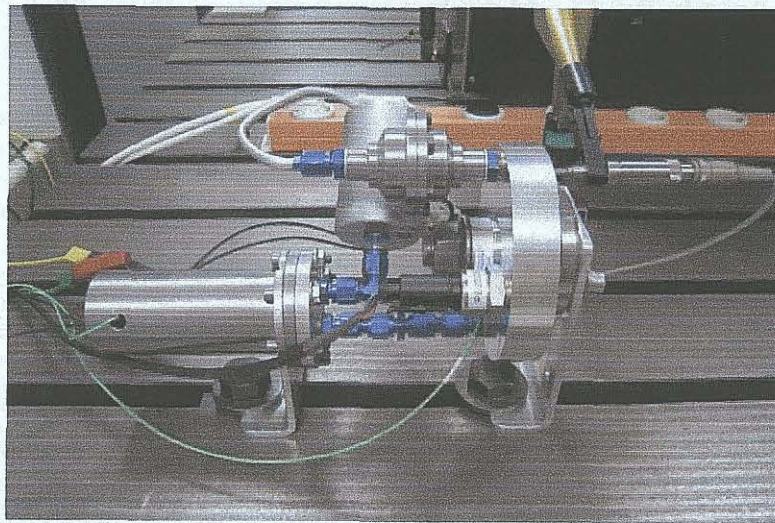


Fig. 173: "MS" pump actuator with "MR" release valve

Fig. 174 depicts the cross section of the "MS"-pump actuator with two check valves and "MR"-valve. "MR"-valve is used as pressure release valve.

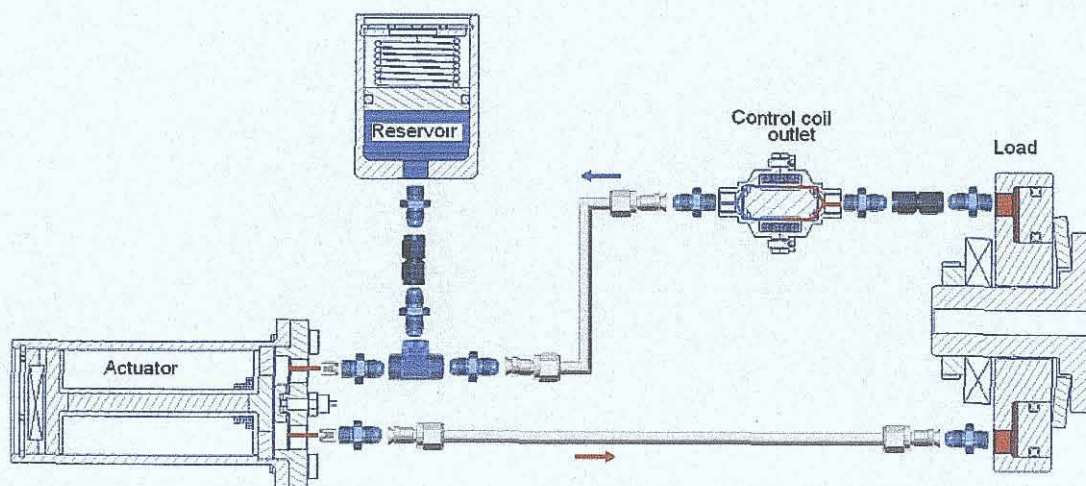


Fig. 174: Cross section of "MS" pump actuator with "MR" release valve

The basic functionality of the pump mechanism has been already proven in chapter 6.5. The purpose of this test is to evaluate whether the combination of "MS" and "MR" technologies could be used in one actuator. The check valves enable the fluid flow through the pipes. Then the "MR" release valve has been energized and the pressure increases. Fig. 175 depicts an example of performed testing at 1 Hz micro-pumping.

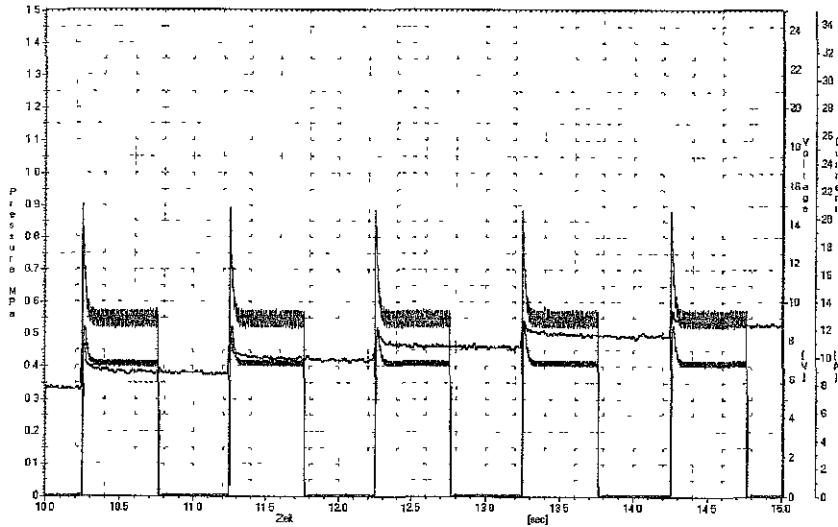


Fig. 175: Basic performance of pump actuator at 1 Hz

Fig. 176 shows recorded data at 10 Hz micro-pumping in the dead-lined main piston.

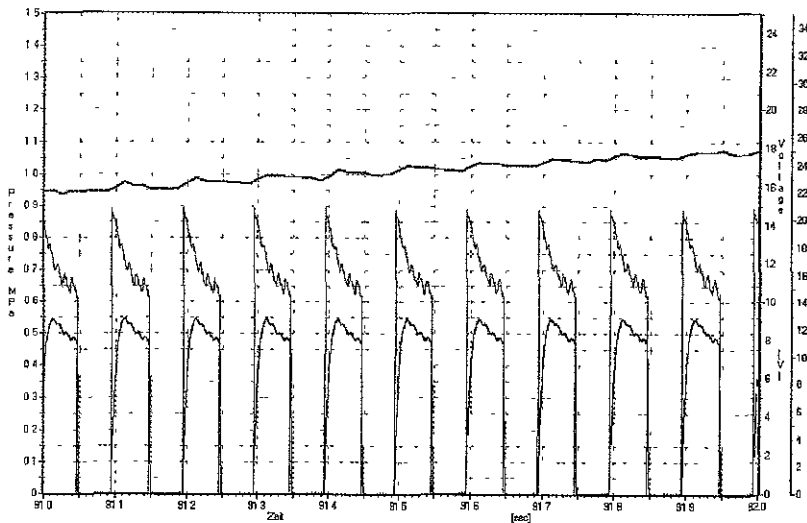


Fig. 176: Basic performance at 10 Hz

Fig. 177 depicts one example of achieved performance with “MR”-valve. All data have been recorded versus time.

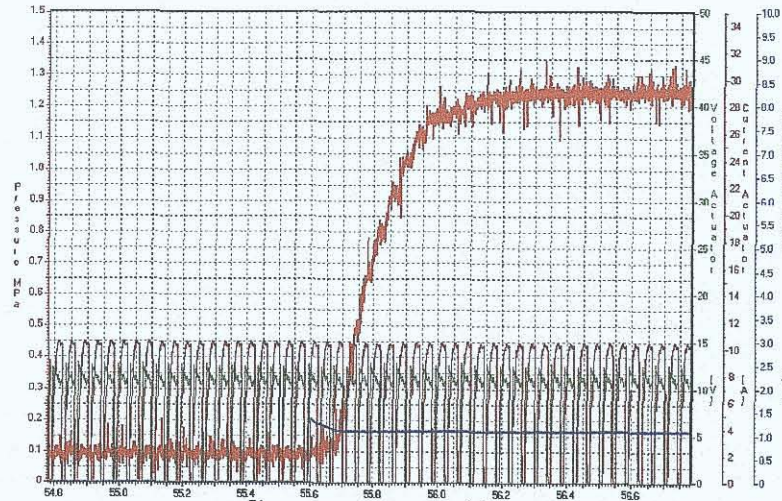


Fig. 177: Engagement performance at 25 Hz

It could be observed that from the time where the release valve is energized the pressure could be increased. At about 1.2MPa the axial displacement of the “MS”-shaft is not sufficient to increase further the operational pressure. The pressure remains nearly constant; despite continuing power to the “MS”-actuator at this frequency. The pressure release performance, disengagement performance, are shown in Fig. 178.

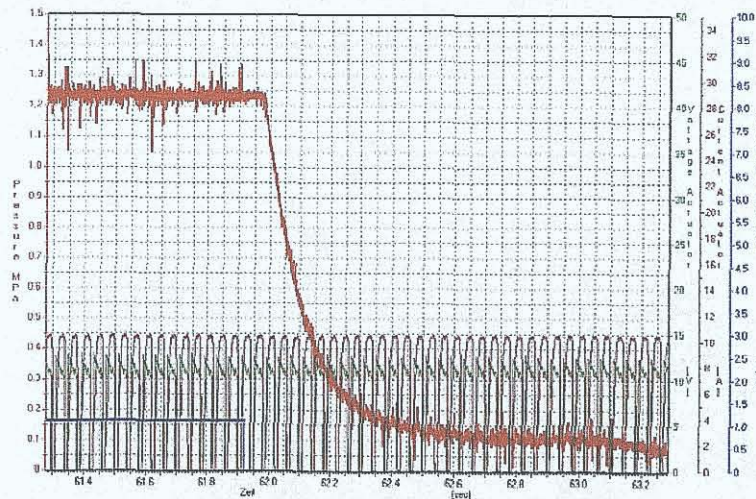


Fig. 178: Pressure release performance

After the “MR”-release valve has been switched off, the pressure starts to decrease. Fig. 179 presents the achievable pressure versus operational frequencies.

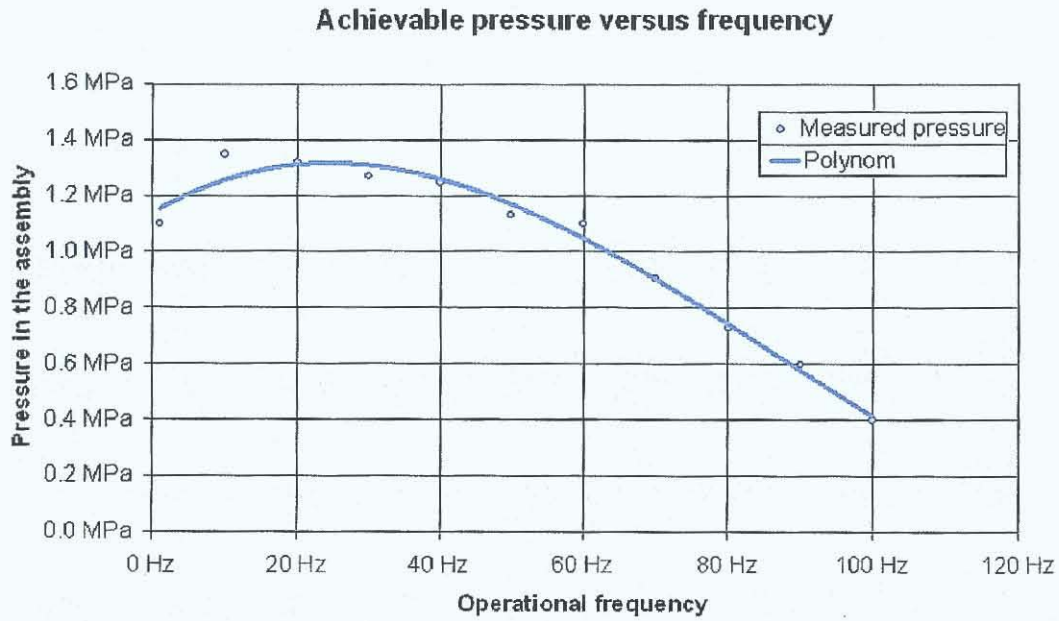


Fig. 179: Achievable pressure versus operational frequency

Above depicted results are confirming the expected performance which has been evaluated in chapter 6.5. The limitation of the actuator system is the valve structure. As well, the influence of bleeding and settling of the “MR”-fluid has been observed several times during the experimental testing.

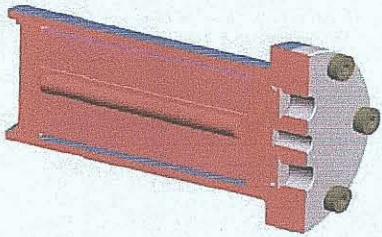
Chapter Seven

Conclusions and recommendation

7.1 Conclusions

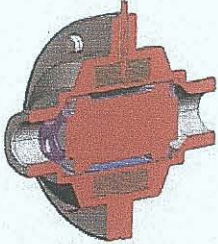
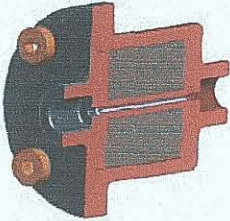
High power density and simple design of the magnetostrictive actuator has been evaluated and optimized. A literature survey for “MS”-technology has been extended with analytical calculations, magnetic field simulations and experimental evaluation. Based on calculations and simulation results, the design of an “MS”-actuator has been proposed. An experimental rig has been built and the specified performance has been proven with experimental results. Acceptable magnetostrictive strain a high blocked force has been achieved. The key experimental results, related to “MS”-actuator, are summarized in Table 12.

Tab. 12: “MS”-actuator key data

“MS”-actuator	Actuator key data	Experimental results
Actuator 	Actuator coil: -950 turns, 1.5 ohm -wire diameter of 1.12 mm Terfenol-D shaft: -shaft diameter of 8 mm -shaft length 67.5 mm	Optimized pre-stress: 12 MPa (600 N pre-load) Strain capability: 0.065 mm @10 A (1000 ppm @ 108 kA/m) Blocked force: > 4500 N

Furthermore, this thesis is the introduction of an actuator based on MS technology and possible control arrangement which is based on MRF technology. A literature survey for “MR”-technology, extended with analytical calculations, magnetic field simulations and experimental evaluation has been carried out to enable the actuator principle. Based on calculations and simulation results a design of the actuator with “MR”-control has been proposed. Experimental rig assemblies of two different control arrangements have been built and the performance has been evaluated experimentally. The key experimental results, related to “MR”-valve and orifice, are summarized in Table 13.

Tab. 13: "MR"-valve and orifice

"MR"-device, 3D CAD	Actuator key data	Experimental results
Valve 	Valve coil: -120 turns, 0.3 ohm -wire diameter of 0.9 mm MRF gap size: -gap of 0.5 mm and -gap length of 12 mm	Used fluid: -MRF132-AD Pressure drop at 5 cm ³ /s: -less than 0.05 MPa Achieved pressure: 1.5 MPa @ 4.5 A & 0 cm ³ /s
Orifice 	Orifice coil: -490 turns, 0.84 ohm -wire diameter of 0.9 mm MRF orifice size: -diameter of 1.5 mm -length of 40 mm	Used fluid: -MRF132-AD Pressure drop at 5 cm ³ /s: -less than 0.2 MPa Achieved pressure: 0.6 MPa @ 4.5A & 5 cm ³ /s

An actuator based on MS technology and a control arrangement based on MRF technology has been combined in one possible application. The basic functionality of proposed pump actuator systems, one with full MRF control and another with check valves, have been proven. The performance limitation, namely the valve structure, has been identified. Valve leakage and dependency on the operational frequency are the limiting the performance of the actuation system. However, a pressure of 1.2MPa with check valves and 0.35MPa with two "MR"-valves has been achieved in the actuation system. Higher pressure capacity could be achievable using a valve structure with faster control response and less leakage.

Presented calculations, magnetic field simulations and experimental evaluation results for both technologies, "MS"-actuator and "MR"-control device, can be used as basis for future development work. An important milestone in combination of smart technologies has been achieved and enables further development of new applications based on MS and MRF technologies, in combination and separately.

7.2 Recommendations for future work

Based on calculations, simulations and experimental results the performance of the "MS"-actuator could be predicted now more accurately. It is recommended for the final application to enlarge the Terfenol-D shaft and the pilot piston to achieve higher pressure level and to

increase the flow rate. However, the potential of "MS"-technology is very attractive for various actuator applications.

Related to the "MR"-technology, it can be stated that the contactless nature of fluid control is attractive for various control device. Settling behavior, especially under micro pump operational conditions, should be evaluated. Achieved performance of "MR"-valve is desirable for a pressure release valve application. Significant improvement of response time and reduction of leakage are required in order to improve the micro-pump performance. Advanced integration of the "MR"-valve with reservoir into the "MS"-actuator is recommended for the future development work. Fig.180 presents cross section of the actuator with integrated valve.

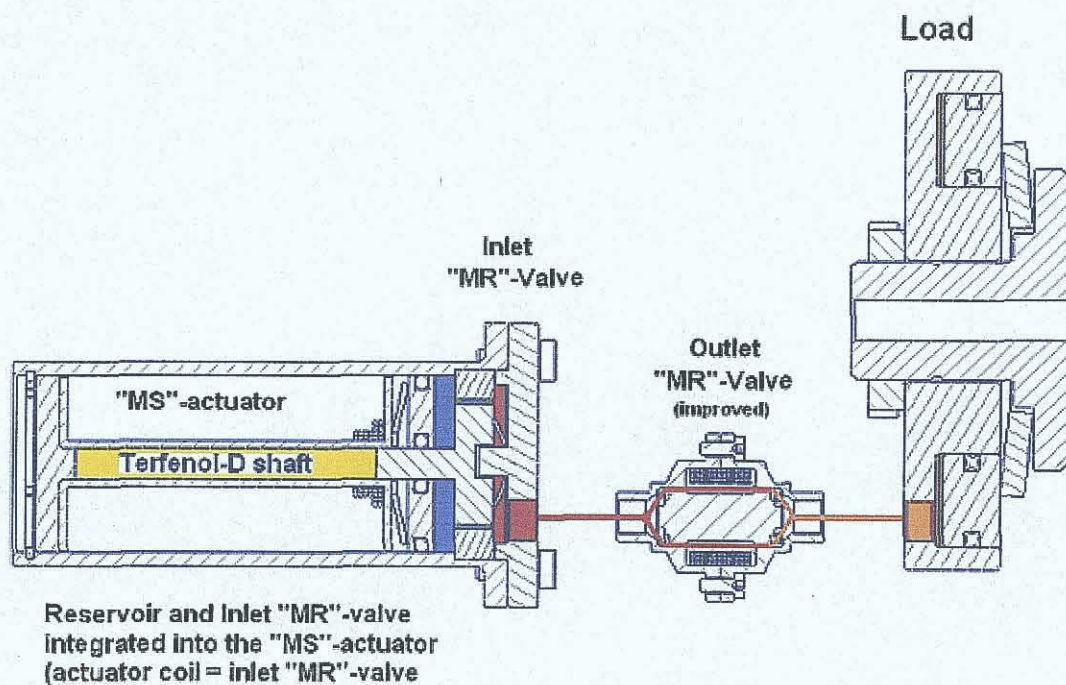


Fig. 180, Actuator layout with integrated inlet valve

The proposed integration leads to a concept with only two electric coils, and offers automatic synchronization of the shaft elongation and with pressure control for the inlet valve. The magnetic field from the "MS"-actuator is used simultaneously for the "MR"-inlet valve. A bias DC could be used to activate the inlet valve, before the full elongation of the shaft introduces the pumping of the fluid to the main piston. The presented structure should lead to simpler control structure and offers potential to improve the performance of the "MS"-actuator and "MR"-control arrangement. Nevertheless, for micro pump actuation other smart valve structure with less leakage, less frequency dependency and faster response might be

considered too. An alternative structure for the actuator using “MR”-control is a simple pump, which could be driven by e-motor. Fig. 181 presents a schematic layout of a simple electro-hydraulic actuator with “MR”-release valve.

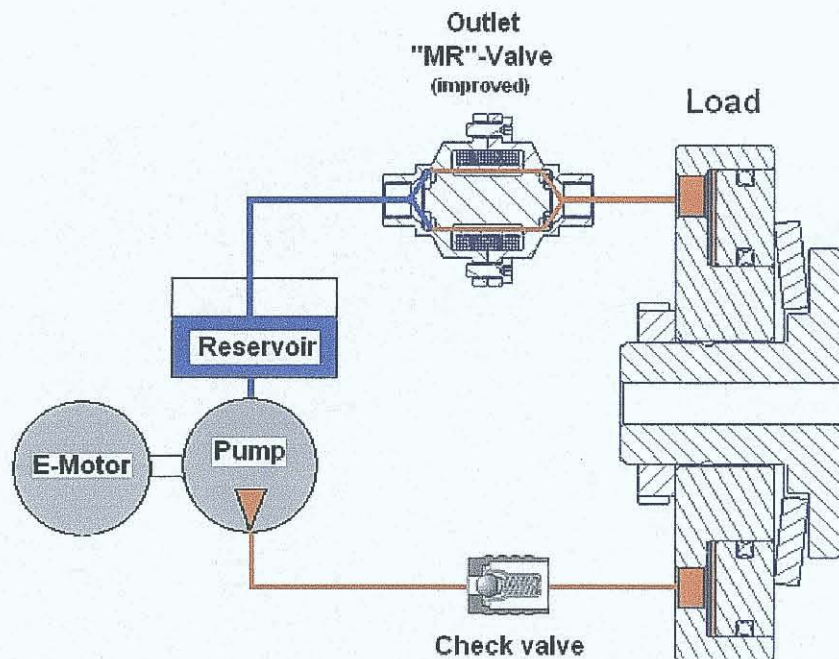


Fig. 181, Actuator layout with conventional pump

In this arrangement a conventional pump could be used to supply the pressure to the load. “MR”-valve is used to release the pressure. Durability of the pump components and “MR” fluid in a realistic duty cycle should be the topic of the future work. However, further improvement of the response time from the “MR”-valve should be evaluated in collaboration with fluid supplier in the near future.

Summarizing it can be stated that both technologies, “MS” and “MR”, with their smart materials like Terfenol-D and Magneto-Rheological Fluids, offer very attractive and valuable features. The contact-less nature of fluid control from “MR”-technology is attractive for automotive applications, where fluid motion is controlled. The precise small motions with high energy density and fast control response could be applied as well in some automotive and aerospace applications. Further extension of the “know-how” related to smart technologies, like “MR” and “MS”, will enable researchers and engineers to create and to establish new products in various industries.

Reference list

- [1] H. Janocha (ed.), F. Claeysen, **Adaptronics and Smart Structures**, Springer Verlag, ISBN 3-540-61484-2, Germany 1999, pp. 124-143
- [2] H. Janocha (ed.), **Actuators**, Springer Verlag, ISBN 3-540-61564-4, Germany 2004, pp 277-292
- [3] C. MacWilliam, **Design of a Magnetostrictive Actuator**, School Of Engineering and Industrial Design, University of Western Sydney, March 2004, Thesis, pp.1-86
- [4] Y. Yamamoto, Tokai University Hiratsuka, Japan; H. Eda, J. Shimizu, Department of Systems Engineering, Ibaraki University, Hitachi, Japan, **Application of Giant Magnetostrictive Materials to Positioning Actuators**, Conference paper, 1999 IEEE /ASME International Conference on Advanced Mechatronics, Atlanta USA 1999, pp. 215-220
- [5] Y. Yamamoto, Tokai University Hiratsuka, Japan; T. Makino, Hiro Matsui, Institute of Advanced Technology, Moritex Corporation, Yokohama, Japan; **Micro Positioning and Actuation Devices Using Giant Magnetostriction Materials**, Conference, 2000 IEEE International Conference on Robotics and Automation, San Francisco CA USA 2000, Conference paper pp. 3635-3640
- [6] M.J. Dapino, Department of Mechanical Engineering, The Ohio State University 2091 Robinson Laboratory Columbus, OH 43210-1107, USA, **On magnetostrictive materials and their use in smart material transducer**, Structural Engineering and Mechanics Journal, USA 2002, pp. 1-28
- [7] A.B. Flatau, M. J. Dapino, Aerospace Engr. & Engr, Mechanics, Iowa State University; F. T. Calkins, Boeing Information Space and Defense Systems, **High bandwidth tuneability in smart vibration absorber**, 1998 SPIE Smart Structures and Materials Conference, Paper #3329-19/3327-42
- [8] M. Zupan, M F. Ashby, N.A. Fleck, Cambridge University Engineering Department, **Actuator Classifications and Selection, The development of a Database**, Advanced Engineering Materials, Weinheim 2002, 4, No. 12, pp. 933-940
- [9] Z. Houqing, L. Jianguo, W. Xiurong, X. Yanhoung, Institute of Acoustics, Academia Sinica, Beijing 100080, China, Z. Hongping, Central Iron and Steel Research Institute, Beijing 100081, China, **Application of Terfenol-D in China**, Journal of Alloys and Compounds 258, 1997, pp. 49-52
- [10] MIDE, **Active Materials**, Comparison of active materials, www.mide.com, www.mide.com/active_materials.html

- [11] Fraunhofer Institute for Machine Tools and Forming Technology IWU, Adaptronic Applications, **Integration of smart materials into intelligent components of production systems**, www.iwu.fraunhofer.de
- [12] F. Claeysen, N. Lhermet, R. Le Letty, Cedrat Recherche, Zirst, F38246 Meylan Cedex, France and P. Bouchiloux, Magsoft Corporation, NY 12180, USA, **Actuators, transducers and motors based on giant magnetostrictive materials**, Journal of Alloys and Component 258 (1997), pp. 61-73
- [13] M.G. Aston, Magnetostrictive Technology Systems Ltd, Unit 17, Newlands House, Newlands Science Park, Inglemire, Hull, HU6 7TQ, UK, R.D. Greenough, A.G.I. Jenner, W.J. Metheringham, K. Prajapati, Department of Applied Physics, The University Of Hull, Cottingham Road, Hull, HU6 7RX, UK, **Controlled high power actuation utilizing Terfenol-D**, Journal of Alloys and Compounds 258, 1997, pp. 97-100
- [14] ETREMA Products Inc., **Terfenol-D Magnetostrictive Actuator Information**, Specifications, Public domain information, www.terfenoltruth.com, www.etrema.com
- [15] C.H. Joshi, Energen Inc. Billerica MA USA, **Compact Magnetostrictive Actuators and Linear Motors**, Conference Actuator 2000, Bremen, Germany June 2000, Conference handout paper
- [16] F. Claeysen, Cedrat Recherche, France; Ph. Bouchilloux, Magsoft Corporation, USA, **Design and construction of a new resonant Magnetostrictive Motor**, IEE Transactions of Magnetics, September 1996, Vol. 32, No. 5
- [17] J D Snodgrass, O.D. McMasters, Eterma Products, Inc. 2500 N. Loop Drive, Ames, Iowa 50010, USA, **Optimized Terfenol-D manufacturing processes**, Journal of Alloys and Compounds 258, 1997, pp. 24-29
- [18] M.J. Dapino, F.T. Calkins, B. Flatau, Aerospace Engr. & Engr, Mechanics, Iowa State University, IA5001; D.L. Hall, Iomega Inc. Roy USA , **Measured Terfenol-D material properties under varied applied magnetic field levels**, 1996 SPIE's Symposium on Smart Structures and Materials, paper # 2717-66
- [19] A.G.I. Jenner, R.J E. Smith, R.D. Greenough, Department of Physics, University of Hull, Hull HU6 7RX, UK; A.J. Wilkinson, School of Engineering, University of Hull , **Actuation and transduction by giant magnetostrictive alloys**, Mechatronics 10, Journal 2000, pp. 457-466
- [20] W.J. Park, Z.H. Lee, Department of Materials Science and Engineering, Korea Advanced Institute of Science and Technology, 373-1 Kusong-dong, Yusong-gu, Taejon 305-701, South Korea, D.R. Son, Department of Physics, Hannam University, 133 Ojeng-dong, Daedeok-gu, Taejon 306-791, South Korea, **Modeling of magnetostriction in grain aligned Terfenol-D and preferred orientation change of Terfenol-D dendrites**, Journal of

- Magnetism and Magnetic Materials 248 (2002), pp. 223-229
- [21] F. Claeysen, D. Colombani, Cedrat Recherche, France; A. Tessereau, B. Ducros, Ets Degreane, France, **Giant dynamic magnetostrain in rare earth-iron magnetostrictive materials**, IEEE Transaction on Magnetics Vol. 27, No. 6, 11/1991, pp 5343-5345
- [22] HyperPhysics, **Electricity and Magnetism**, Basic calculations and physical background, Georgia State University, 2005, www.hyperphysics.phy-astr.gsu.edu
- [23] D.L. Hall, A.B. Flatau, Aerospace Engr. & Engr, Mechanics, Iowa State University, IA5001, **Broadband Performance of a Magnetostrictive Shaker**, Journal of Intelligent Material Systems and Structures, August 1994, pp. 1-16
- [24] F.T. Calkins, M. J. Dapino, A.B. Flatau, Aerospace Eng. & Eng Mechanics, Iowa State University, IA50011, **Effect of prestress on the dynamic performance of a Terfenol-D transducer**, 1997 SPIE's Symposium on Smart Structures and Materials, paper # 3041-23
- [25] R. Kellog, A. Flatau, Aerospace Eng. & Eng., Mechanics, Iowa State University, IA50011, **Blocked force investigation of a Terfenol-D transducer**, 1999 SPIE's Symposium on Smart Structures and Materials, paper # 3668-19
- [26] W.J. Park, Z.H. Lee, Department of Materials Science and Engineering, Korea Advanced Institute of Science and Technology, 373-1 Kusong-dong, Yusong-gu, Taejon 305-701, South Korea, J.C. Kim, B.J. Ye, Department of Metallurgical Engineering, Kyungpook National University, Teagu 305-701, South Korea, **Marcrosegation in Bridgman growth of Terfenol-D and effects of annealing**, Journal of Crystal Growth 212 (2000), pp. 283-290
- [27] B. Jones, ETREMA products, Inc; Ch. Liang, San Diego State University; **Magnetostriction: Revealing the Unknown**, IEEE AES Systems Magazine, March 1996, Journal paper
- [28] J. M. Vranish, D.P. Naik, NASA Coddard Space Flight Center, Greenbelt; J.B. Restorff, J.P. Teter, R43, Naval Surface Warfare Center, Silver Spring; **Magnetostrictive direct drive rotary motor development**, IEEE Transaction on Magnetics Vol. 27, No. 6, November 1991, pp. 5355-5357
- [29] D.A. Bushko and J H. Goldie, SatCon Technology Corporation, Cambridge, MA, **High Performance Magnetostrictive Actuators**, IEEE AES Systems Magazine, Nov 1991, Journal pp. 21-25
- [30] E. Qandt, K. Seemann, Forschungszentrum Karlsruhe, Institute of Materials Research I, D-76021 Karlsruhe, Germany, **Fabrication and Simulation of magnetostrictive thin-film actuators**, Sensors and Actuators Journal, A50 (1995), Journal pp. 105-109
- [31] A. Ludwig, M. Tewes, S. Glasmachers, M. Löhndorf, E. Quandt, Centre of Advanced European Studies and Research (Caesar), Friedensplatz 16, D-53111 Bonn, Germany, **High-frequency magnetoelastic materials for remote-interrogated stress sensors**, Journal of

Magnetism and Magnetic Materials 242-245, 2002, pp. 1126-1131

- [32] H. Janocha, **Neue Aktorprinzipien im Kraftfahrzeug**, Universität des Saarlandes Saarbrücken, Handout Paper, 2002, pp. 1-18
- [33] A.E. Fitzgerald, Ch. Kingsley, St. D. Umans, **Electric Machinery**, Mc Graw Hill, 2003, ISBN 007366009-4, pp. 1-30
- [34] T. Fukuda, **GMA applications to micromobile robot as microactuator without power supply cables**. IEEE Micro-electro-mechanical Systems proc. 1991, pp. 210-215
- [35] K. Prajapati, R.D. Greenough and A. Wharton Department of Applied Physics, University of Hull, Hull, England **Effect of Cyclic Stress on Terfenol – D**, Journal: IEEE Transactions on Magnetics Vol. 32 No 5 September 1996
- [36] R. D. Greenough, M.P. Schulze, A.G.L. Jenner and A.J. Wilkinson, Department of Applied Physics, University of Hull, Hull, UK, **Actuation with Terfenol – D**, Journal. IEEE Transactions on Magnetics, Vol. 27, No. 6, Nov 1991.
- [37] D.L. Hall, A. Flatau, **Nonlinearities, harmonics and trends in dynamic applications of Terfenol-D**, Aerospace Engr & Engr, Mechanics, Iowa State University, IA50011
- [38] A.B. Flatau, F.T. Calkins, M.J. Dapino, Aerospace Engr. & Engr, Mechanics, Iowa State University, IA5001, **Transducer based Terfenol-D Property Measurement**, SPIE 1996, Proceedings on Smart Structures and Integrated Systems, paper #67, Vol. 2717, 2/96
- [39] L. E. Faidley, B.J. Lund, A. Flatau, F.T. Calkins, Aerospace Engr. & Engr, Mechanics, Iowa State University, IA5001, **Terfenol-D elasto-magnetic properties under varied operating conditions using hysteresis loop analysis**, 1998 SPIE's Symposium on Smart Structures and Materials # 3329-92
- [40] F.T. Calkins, A.B. Flatau, Aerospace Engr. & Engr, Mechanics, Iowa State University, IA5001, **Transducer based on measurements of Terfenol-D material properties**, 1996 SPIE's Symposium on Smart Structures and Materials # 2717-67
- [41] K. Kondo, Mechanical Engineering Laboratory, AIST, MITI, Namiki 1-2, Tsukuba, Ibaraki, Japan, **Dynamic behavior of Terfenol-D**, Journal of Alloys and Component 258 (1997), pp. 56-60
- [42] D. Davino, C. Visone, Univers. Piazza, Roma, Benevento 82100, Italy, C. Natale, S. Pirozzi, Seconda Univers. di Napoli, Roma 27, Aversa 81031, Italy, **Rate-dependent losses modeling for magnetostrictive actuators**, Journal of Magnetism and Magnetic Materials 272-276 (2004) e1781-e1782
- [43] E. du T. de Lacheisserie, K. Mackay, J. Betz, J.C. Peuzin, Laboratoire Louis Neel, CNRS, B.P. 166 38042 Grenoble Cedex, France, **From bulk to film magnetostrictive actuators**, Journal of Alloys and Component 275-277 (1998), pp. 685-691
- [44] R.D. Greenough, M.P. Schulze, D. Pollard, Department of Applied Physics, The

- University of Hull, Cottingham Road, Hull HU6 7RX, UK, **Non-destructive testing of Terfenol-D**, *Journal of Alloys and Component* 258 (1997), pp. 118-122
- [45] J. Schäfer, H. Janocha, Laboratory for Process Automation, University of the Saarland, PO Box 151150, D-66041 Saarbrücken, Germany, **Compensation of Hysteresis in solid-state actuators**, *Sensors and Actuators A49* (1995), pp. 97-102
- [46] G. Engdahl, F. Stillesjö, Electric Power Engineering, Royal Institute of Technology, S-100 44 Stockholm, Sweden, **Estimation of the intrinsic magnetomechanical response of magnetostrictive actuators by dynamic simulations**, *Journal of Alloys and Component* 258 (1997), pp. 79-82
- [47] E. Quandt, A. Ludwig, Forschungszentrum Karlsruhe, Institute of Materials Research I, P.O. Box 3640, D-76021 Karlsruhe, Germany, **Magnetostrictive actuation in microsystems**, *Sensors and Actuators* 81 (2000), pp. 275-280
- [48] S. Guruswamy, N. Srisukhumbowornachai, Metallurgical Engineering, University of Utah, 135 S 1460 E, RM412, Salt Lake City, UT 84112, A.E. Clark, Clark Associates, J.B. Restroff, M. Wun-Fogle, Naval Surface Warfare Centre, **Strong, Ductile and Low-Field-Magnetostrictive Alloys Based on Fe-Ga**, *Scripta mater.* 43 (2000), pp. 239-244
- [49] J. Hudson, S.C. Busbridge, A.R. Piercy, Department of Mechanical and Manufacturing Engineering, University of Brighton, Moulsecoomb, Brighton, BN2 4GJ UK, **Dynamic magneto-mechanical properties of epoxy-bonded Terfenol-D composites**, *Sensors and Actuators* 81 (2000), pp. 294-296
- [50] P.A. Bartlett, S.J. Eaton, J. Gore, Defense Evaluation and Research Agency, Farnborough, Hants, GU140LX, UK, W J. Metheringham, A.G. Jenner, Newlands Technology Limited, Hull, E. Yorkshire, UK, **High-power, low frequency magnetostrictive actuation for anti-vibration applications**, *Sensors and Actuators A91* (2001), pp. 133-136
- [51] Z.D. Zhang, B.W. Wang, International Centre for Material Physics, Institute of Metals Research, Academia Sinica, Wenhua Road 72, Shenyang 110015, China, Z.J. Guo, S.C. Busbridge, A.R. Piercy, Department of Mechanical and Manufacturing Engineering, University of Brighton, Moulsecoomb, Brighton, BN2 4GJ UK, **Dynamic magnetic and magnetoelastic properties of epoxy-TbFe₂ composites**, *Journal of Magnetism and Magnetic Materials* 239 (2002), pp. 554-556
- [52] G. Ausanio, V. Iannotti, L. Lanotte, C. Luponio, INFN-UdR Napoli, Dipartimento di Scienze Fisiche, Università "Federico II", P.le.V. Tecchio 80, 80125 Napoli, Italy, E. Bonetti, L. Pasquini, INFN-UdR Bologna, Dipartimento di Fisica, viale B. Pichat, 40127 Bologna, Italy, **Time dependence of magnetization and strain in Terfenol**, *Journal of Magnetism and Magnetic Materials* 242-245 (2002), pp. 1453-1456
- [53] Young-Woo Park, Department of Mechanics Engineering, Chungnam National

- University, 220 Kung-Dong, Yusong-Gu, Daejeon 305-764, SouthKorea, Do-Youn Kim, LG Chemical Ltd., Battery Research and Development, P.O. Box 61, Yusong-Gu, Science Town, Daejeon, South Korea, **Development of magnetostrictive microactuator**, Journal of Magnetism and Magnetic Materials 272-276 (2004), e1765-e1766
- [54] L. Wu, Department of Modern Applied Physics, Tsinghua University, Beijing 100084, China, W.Zhan, X. Chen, State Key Laboratory of Magnetism, Institute of Physics, Chinese Academy of Sciences, Beijing 100080, China, **Directional growth of single crystal Terfenol-D by the electron beam zoning method**, Journal of Magnetism and Magnetic Materials 164, 1996, pp. 367-370
- [55] R.D. Greenough, A.D. Wharton, The Department of Applied Physics, The university of Hull, Cottigham Road, Hull HU6 7RX, UK, **Methods and techniques to characterize Terfenol-D**, Journal of Alloys and Compounds 258, 1997, 114-117
- [56] H. Janocha, **Application Potential of Magnetic Field Driven Actuators**, LPA, Universität des Saarlandes, Saarbrücken, EMSA 2000, Hand out paper, pp. 1-14
- [57] Ken-ichi Yamamoto, Hironobu Nakano, Yasumasa Yamashiro, Faculty of Engineering, University of the Ryukyus, 1 Senbaru, Nishihara, Okinawa 903-0213, Japan, **Effect of compressive stress on hysteresis loss of Terfenol-D**, Journal of Magnetism and Magnetic Materials 254-255 (2003), pp. 222-224
- [58] Inventables LLC, **New Materials & Technology Resource** for Innovative Design, www.inventables.com
- [59] P. Czimmek, Siemens VDO, Virginia, US, **Characterization of Magnetic Shape Material**, Engineering Report, May 2004, pp 1-12
- [60] R. Fletcher, MIT Media Laboratory 20, Ames Street, Cambridge, Massachusetts 02139-4307, **Force Transduction materials for human-technology interface**, IBM System Journal, Vol. 35, NOS3&4, 1996, pp. 630-638
- [61] Energen Inc., 650 Suffolk Street, Lowell, MA 01854, USA, **Magnetic “Smart” Materials**, Company, information available on <http://www.EnergenInc.com>
- [62] H.P.R. Frederikse, **Properties of magnetic materials**, [www.nmsl.chem.ccu.edu.tw.pdf](http://www.nmsl.chem.ccu.edu.tw/pdf), CRC Press LLC, 2000
- [63] G. Engdahl (ed.), **Handbook of Giant Magnetostrictive Materials**, Royal Institute of Technology, Stockholm, Sweden, ISBN 012238640, pp. 1-373
- [64] G. H. Hitchcock, F. Gordaninejad, X. Wang, Composite and Intelligent Materials Laboratory, University of Nevada, Reno, NV 89557, USA, **A new By-Pass, Failsafe, Magneto-Rheological Fluid Damper**, Proceedings of SPIE Conference on Smart Materials and Structures, San Diego, March 2002, pp. 1-7
- [65] Phillips, R.W., **Engineering Applications of Fluids with a Variable Yield Stress**,

Ph.D. Thesis, University of California, Berkeley, 1969

[66] J.D. Carlson, **What Makes A Good MR Fluid**, 8th International Conference on Electrorheological (ER) and Magnetorheological (MR) Suspensions, Nice, July 2001 and Journal of Intelligent Material Systems and Structures, 2002, No. 13, pp. 431-435

[67] J.D. Carlson, D.M. Catanzarite and K A.St. Clair, Lord Corporation, Cary, NC 27511 USA, **Commercial Magneto-Rheological Fluid Devices**, Proceedings of the 5th International Conference on ER Fluids, MR Fluids and Associated Technology, U. Sheffield, UK, 1995, pp. 20-28 and on www.literature.lord.com/root/other/rheonetic/

[68] M.R. Jolly, J W. Bender and J.D. Carlson, **Properties and Applications of Commercial Magnetorheological Fluids**, SPIE 5th Annual Int. Symposium on Smart Structures and Materials, San Diego, CA, March 15, 1998 and on www.literature.lord.com/root/other/rheonetic/

[69] Lord Corporation, **Dr. Dave's Do-It-Yourself MR Fluid, Designing with MR Fluid, Magnetic Circuit Design, FAQs, Fluid specifications**, 2004, www.lord.com

[70] J. Huang, J.Q. Zhang, Y. Yang, Y.Q. Wei, **Analysis and design of a cylindrical magnetorheological fluid brake**, Journal of Materials Processing Technology, Vol. 129, No. 1, 2002, P 559-562

[71] P.L. Wong, W.A. Bullough, C. Feng, S. Lingard, **Tribological performance of magnetorheological suspensions**, Wear 247, 2001, Page 33-40

[72] D. Lampe, **Untersuchungen zum Einsatz von Magnetorheologischen Fluiden in Kupplungen**, TU Dresden, 2000, PhD Thesis

[73] D. Lampe, **Anwendungen von Magnetorheologischen Fluiden in Kupplungen**, Institut für Luft- und Raumfahrttechnik der TU Dresden, www.donnerflug.de/publikationen/antrieb.pdf

[74] Dr. V. Rabitsch, **Einführung in die Rheologie, Kurs1 und Kurs2**, University of Graz, www.copuserve.de/ctmatlke/Kurs1.html, ... [Kurs2.html](#)

[75] A. Milecki, **Investigation and control of magneto-rheological fluid damper**, International Journal of Machine and Manufacture 41 (2001), Page 379-391

[76] J. Rabinow , **Magnetic fluid clutch**, Technical News Bulletin, National Bureau of Standards, 32/4, 1948, Page 54-60

[77] W. Wislow, **Field Responsive Fluid Couplings**, US Pat. No. 2.886.151, (1959)

[78] X.Z.Zhang, X.L.Gong, P.Q.Zhang and Q.M. Wang, **Study on the mechanism of the squeeze-strengthen effect in magnetorheological fluids**, Journal of Applied Physics, 2004, Vol. 96, Issue 4, pp. 2359-2364

[79] J.D. Carlson, Lord Corporation, Cary, NC 27511 USA, MRF Workshop in Carry, North Caroline 2004, workshop hand outs

- [80] F D. Goncalves, J.-H. Koo, M Ahmadian, **A Review of the State of Art in Magnetorheological Fluid Technologies**, The Shock and Vibration Digest, Vol. 38, No 3, May 2006, pp. 203-219
- [81] J.D. Carlson, **Magnetorheological Fluid Actuators**, Adaptronics and Smart Structures, Editor H. Janocha Springer Berlin 1999, Page 180-195, ISBN 3-540-61484-2
- [82] P. Kulkarni, C. Ciocanel, S.L Vieira, N. Naganathan, M.I.M.E. Department, Nitschke Hall 4005, University of Toledo, OH 43606, USA, **Study of Behaviour of MR Fluids in Squeeze, Torsional and Valve Modes**, Journal of Intelegent Material Systems and Structures, Vol. 14-February 2003, pp. 99-104
- [83] B.M.Kavlicoglu, F. Gordaninejad, C A. Evrensel, N. Cobanoglu, Y. Lui, A. Fuchs, Composite and Intelegent Materials Laboratory, University of Nevada, Reno, NV 89557, USA and G. Korol, Visteon Automotive Systems, Dearborne, MI 48126, USA, **A High-Torque Magneto-Rheological Fluid Clutch**, Proceedings of SPIE Conference on Smart Materials and Structures, San Diego, March 2002, pp. 1-8
- [84] D. Meeker, FEMM-Software Manual, **Finite Elements Method Magnetics User's Manual and Tutorial**, 2004, www.feem.com
- [85] Introduction to Computational Electromagnetics, **Opera Software for Electromagnetic design**, Vector Fields Software manual and tutorials, 2005
- [86] M.E.H. Benbouzid, **Artificial Neural Networks for Finite Element Modeling of GM devices**, Journal: IEEE transactions on Magnetics, Vol. 34, No. 6 Nov 1998, pp 3853-3856
- [87] C. Body, G. Reyne, G. Meunier, **Non linear finite element modeling of magneto-mechanical phenomenon in giant magnetostrictive thin films**, IEEE Transactions on Magnetics, Vol. 33, No.2, March 1997, pp. 1620-1623
- [88] R.S. Weston, T. Cedell, Department of Production and Materials Engineering, Ole Römors V.1, Box 118, 221 00 Lund, Sweden, **Finite elements solutions to magnetostriction**, Finite Elements in Analysis and Design 30 (1998), pp. 187-196
- [89] X. Tan, J.S. Baras, Institute of Systems Research, University of Maryland, College Park, MD 20742, USA, **Modeling and control of hysteresis in magnetostrictive actuators**, Automatica 40 (2004), pp. 1469-1480
- [90] G. Liu, C.W Nan, N. Cai, Y. Lin, Department of Materials Science and Engineering, State Key Laboratory of New Ceramics and fine Processing, Tsinghua University, Tsinghua Park, Beijing 100084, China, **Calculations of giant magnetoelectric effect in multiferroic composites of rare-earth-iron alloys and PZT by finite element method**, International Journal of Solids and Structures 41 (2004), pp. 4423-4434
- [91] L.Sun, X. Zheng, Department of Mechanics, Lanzhou University, 222 ThainShui South Road, Lanzhou 730000, China, **Numerical simulation on coupling behavior of Terfenol-D**

rods, International Journal of Solids and Structures (2005), pp. 1-9

[92] D. Kinderlehrer, L. Ma, Center for Nonlinear Analysis, Department of Mathematical Sciences, Carnegie Mellon University, Pittsburgh, PA 15213-3890, USA, **The simulation of magnetoelastic configurations**, Physica B 233 (1997), pp. 376-380

[93] The Lee Company, **Technical Hydraulic book**, Catalogue, Lee Hydraulische Miniaturkomponenten GmbH, Frankfurt am Main, Germany, 2005, p. 8-9

Appendices

The content of the appendix has been discussed in several chapters of this thesis. The main content of the appendix are drawings of experimental rig parts, specifications and some additional rig test results.

The appendix is structured as follows:

- Appendix A contains detailed drawings of the “MS”-actuator
- Appendix B contains detailed drawings of the “MR”-valve
- Appendix C contains detailed drawings of the “MR”-orifice
- Appendix D contains detailed drawings of the reservoir
- Appendix E contains detailed drawings of the load and some additional results from experimental evaluation
- Appendix F contains additional specifications for experimental evaluation
- Appendix G contains additional magnetic field simulation results for the actuator assembly with experimental measurements of flux density.
- Appendix H contains additional list of various publications related to the thesis

Fig. A1: Actuator assembly 700.000

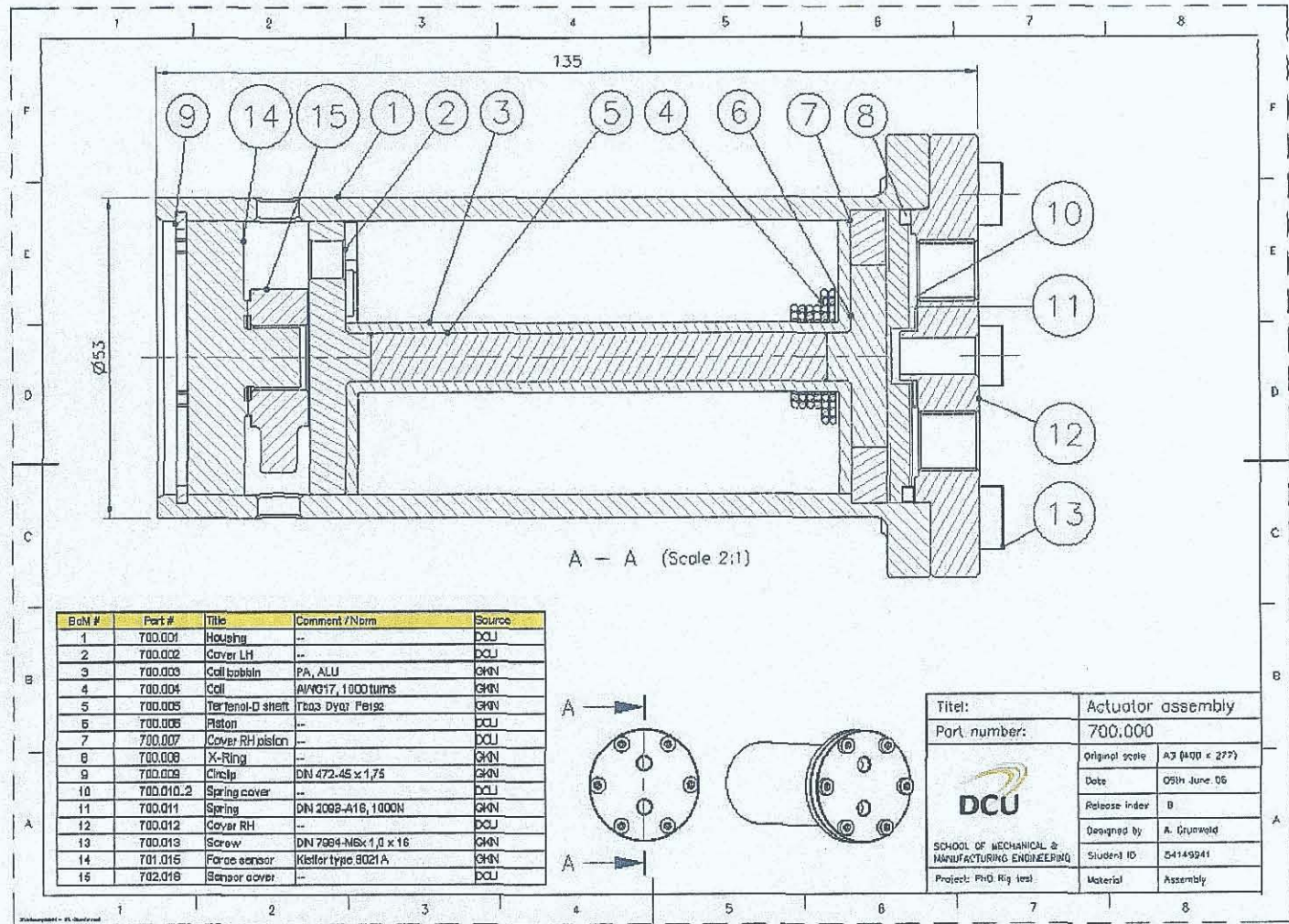


Fig. A2: Actuator assembly 700.000 with membrane and small piston

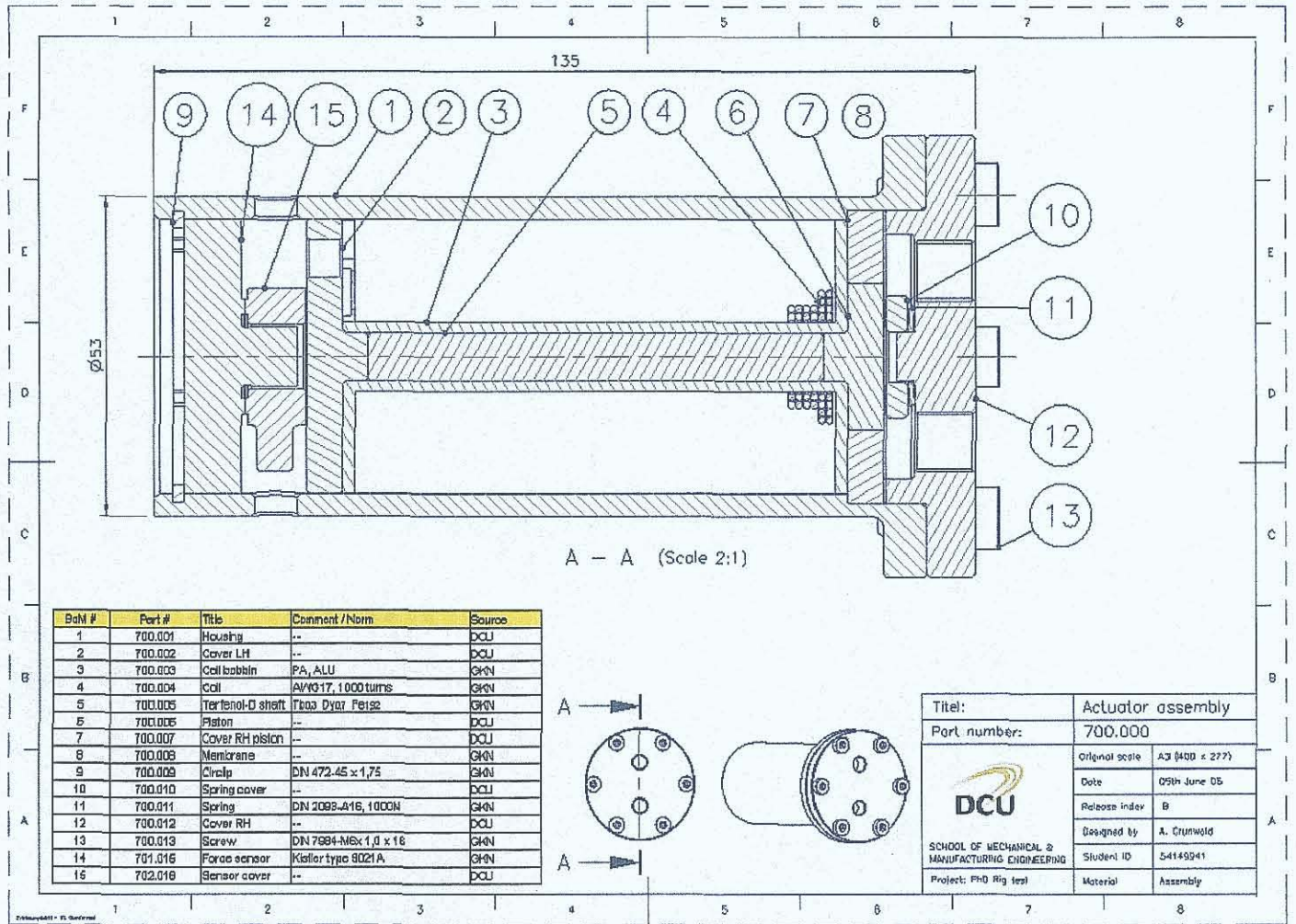


Fig. A3 shows a picture from prototypes of the alternative actuator assembly with small pilot piston with 24mm outer diameter and membrane.



Fig. A3: Actuator assembly 700.000_o

Fig. A4-Housing-700.001

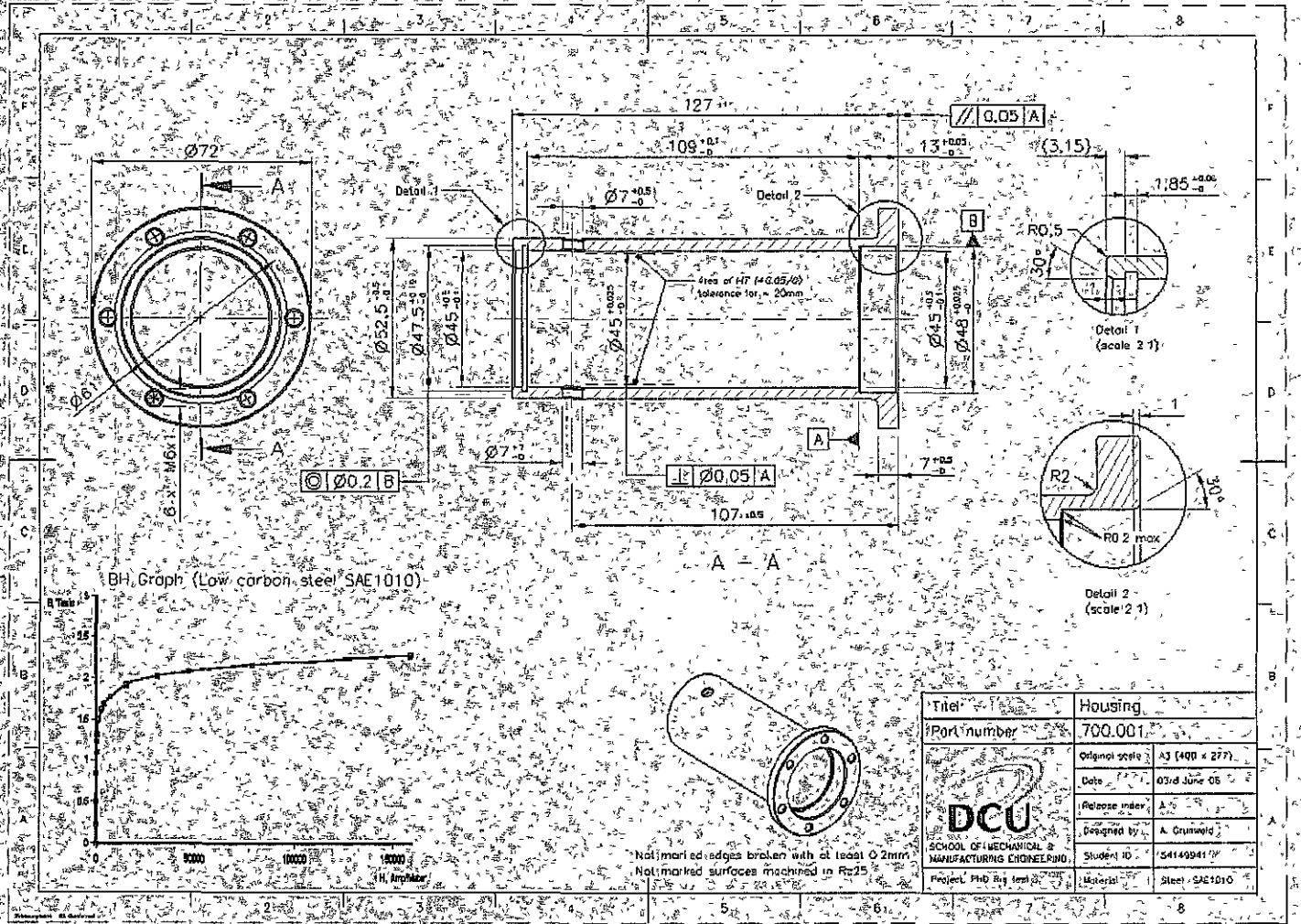
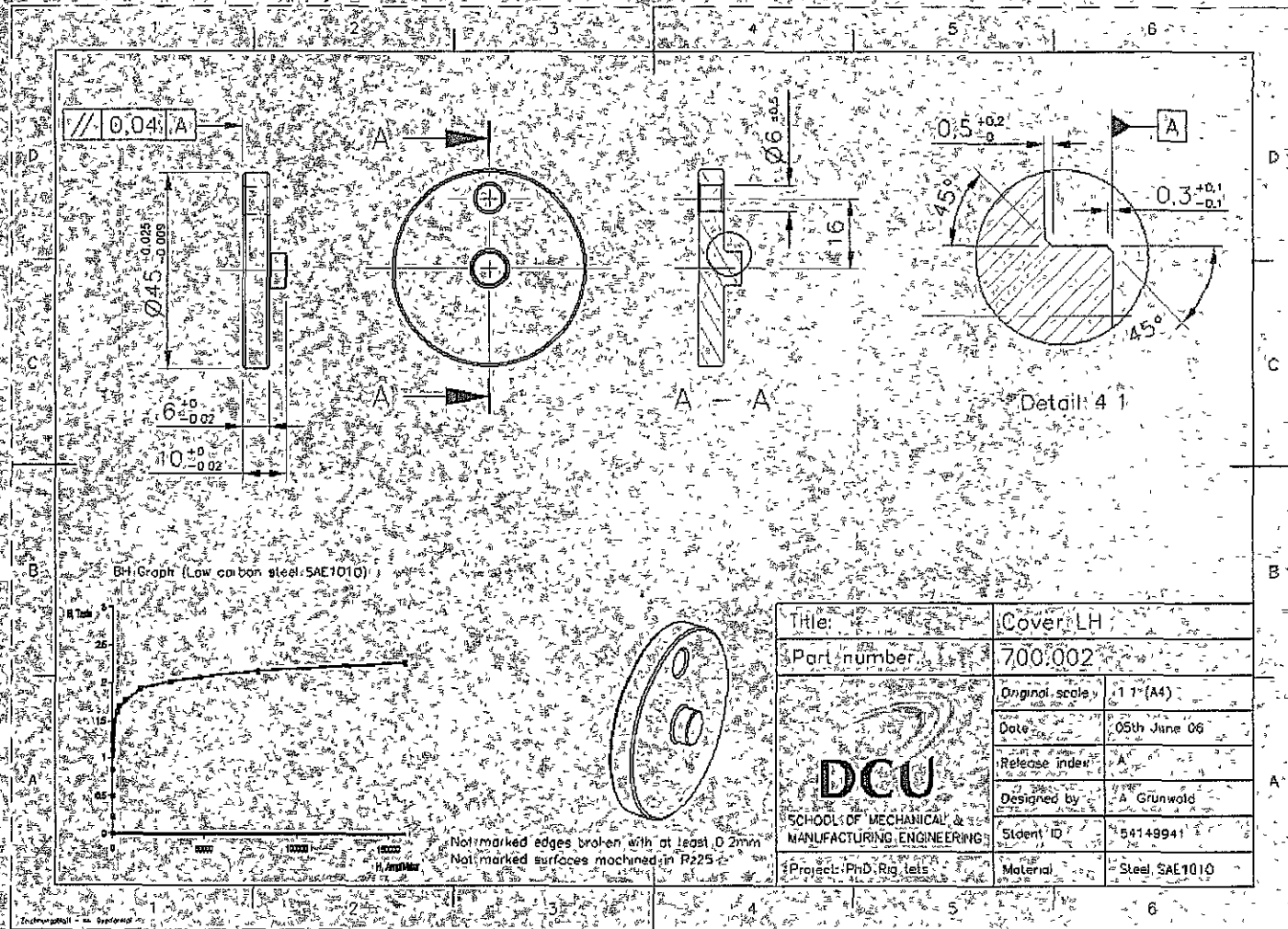


Fig. A5: Cover LH 700.002




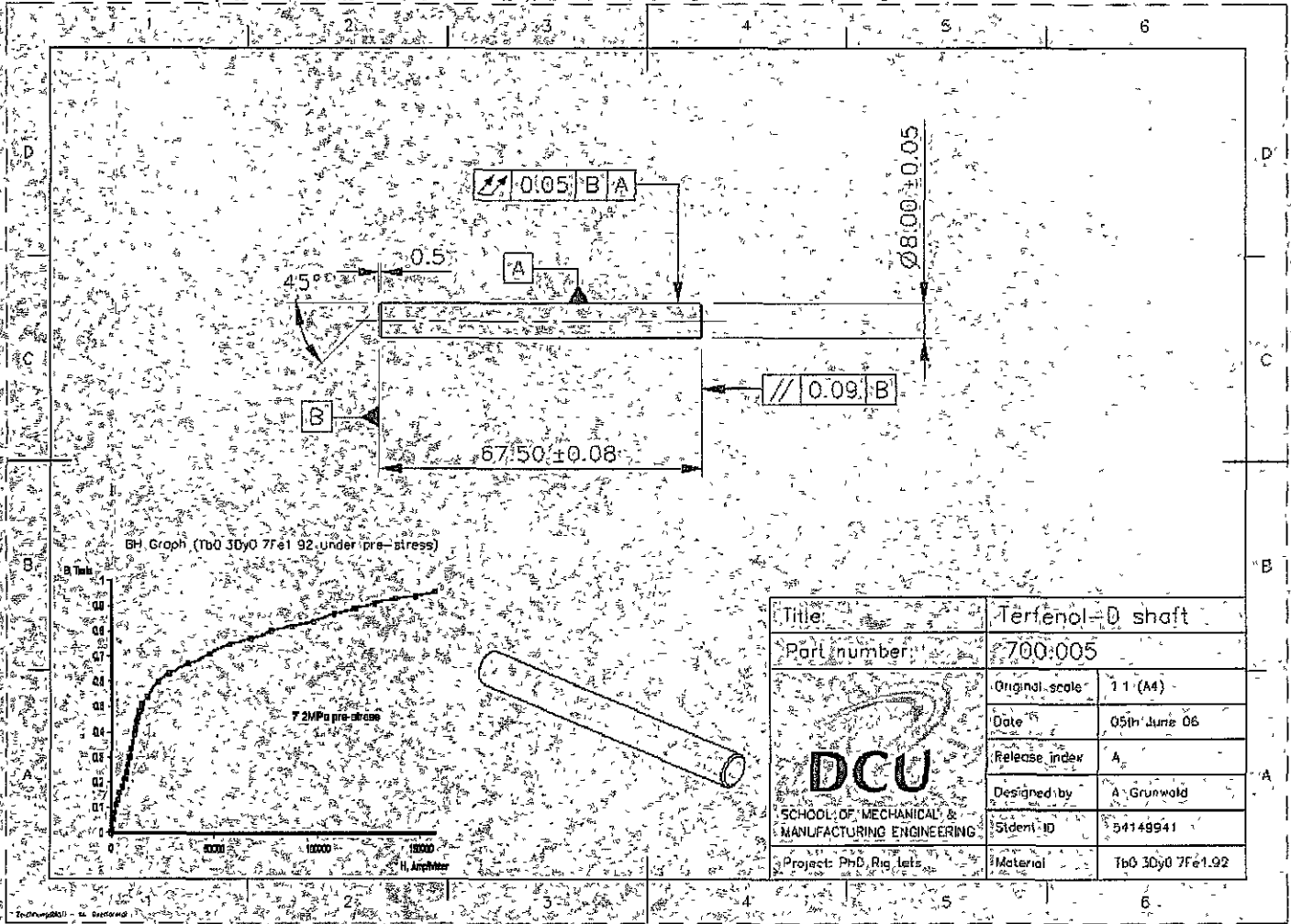

Title:	Cover LH	
Part number:	700.002	
 SCHOOL OF MECHANICAL & MANUFACTURING ENGINEERING	Original scale:	1:1 (A4)
	Date:	05th June 06
	Release index:	A
	Designed by:	A Grünwald
	Student ID:	54149941
Project: Ph.D. Rig tests	Material:	Steel SAE1010

Fig. A6: Terfenol-D shaft 700-005



Title	Terfenol-D shaft	
Part number	700-005	
 SCHOOL OF MECHANICAL & MANUFACTURING ENGINEERING	Original scale	1:1 (A4)
	Date	05th June 06
	Release index	A
	Designed by	A. Grunwald
	Student ID	54149941
Project: PhD, Rig lets	Material	Tb0 3Dy0 7Fe1.92

Pictures from Terfenol-D shaft (Diameter 8mm)

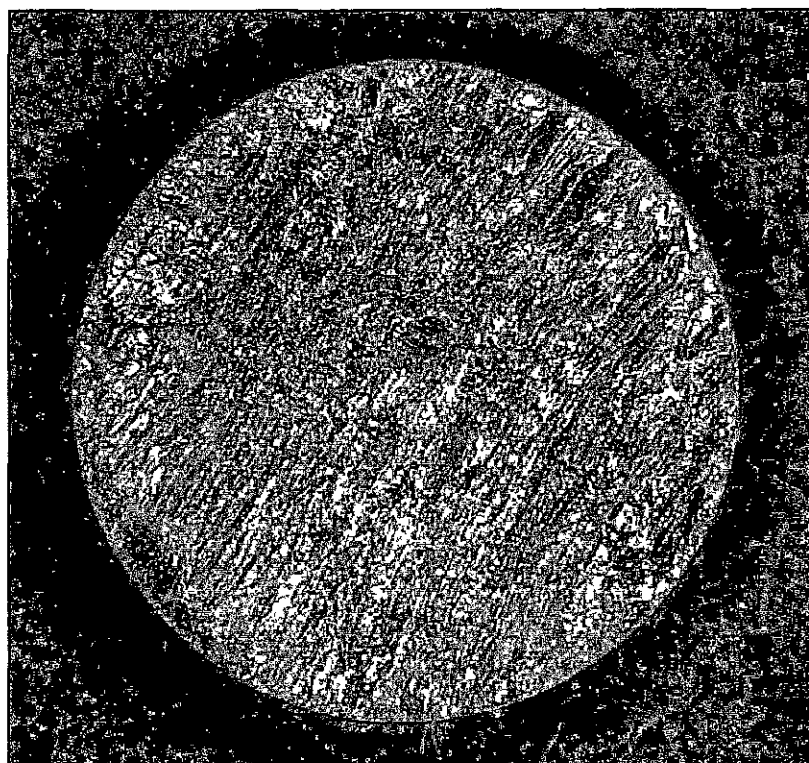


Fig. A7: Terfenol-D shaft 700.005

Pictures from Terfenol-D shaft (Diameter 8mm, zoom)

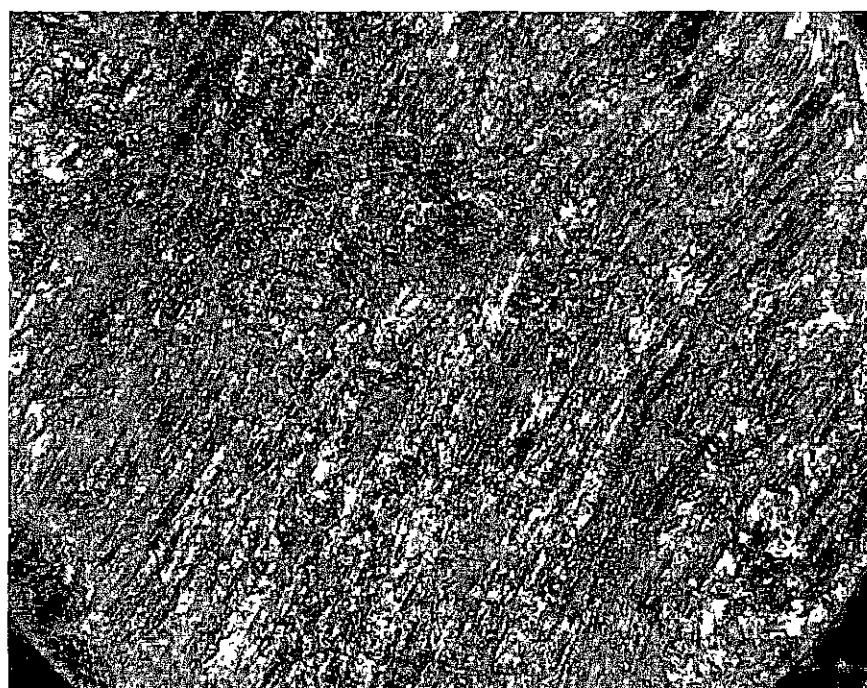


Fig. A8: Terfenol-D shaft 700.005 (zoom)

Fig. A9: Piston 700.006

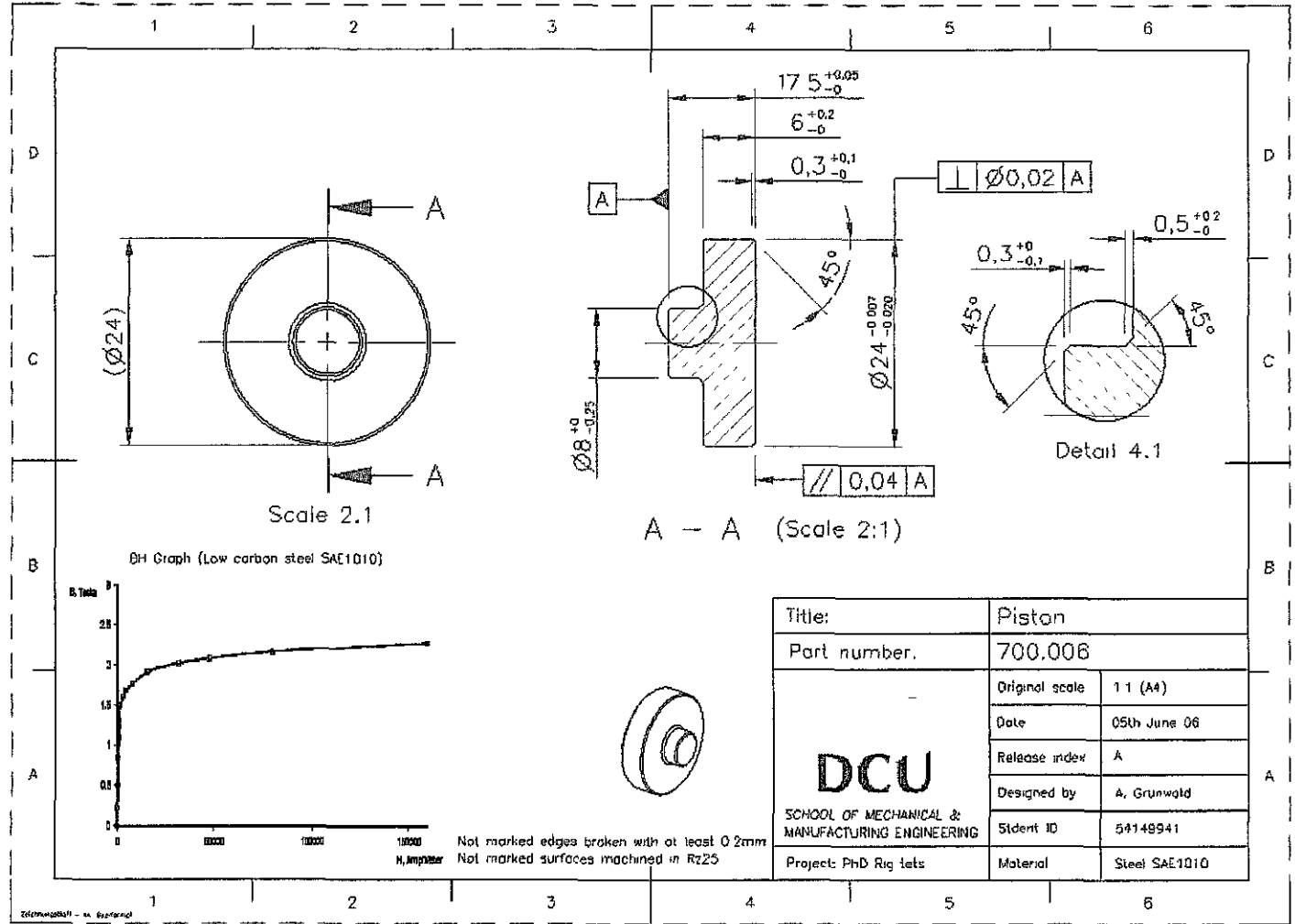


Fig. A10: Cover RH piston 700-007

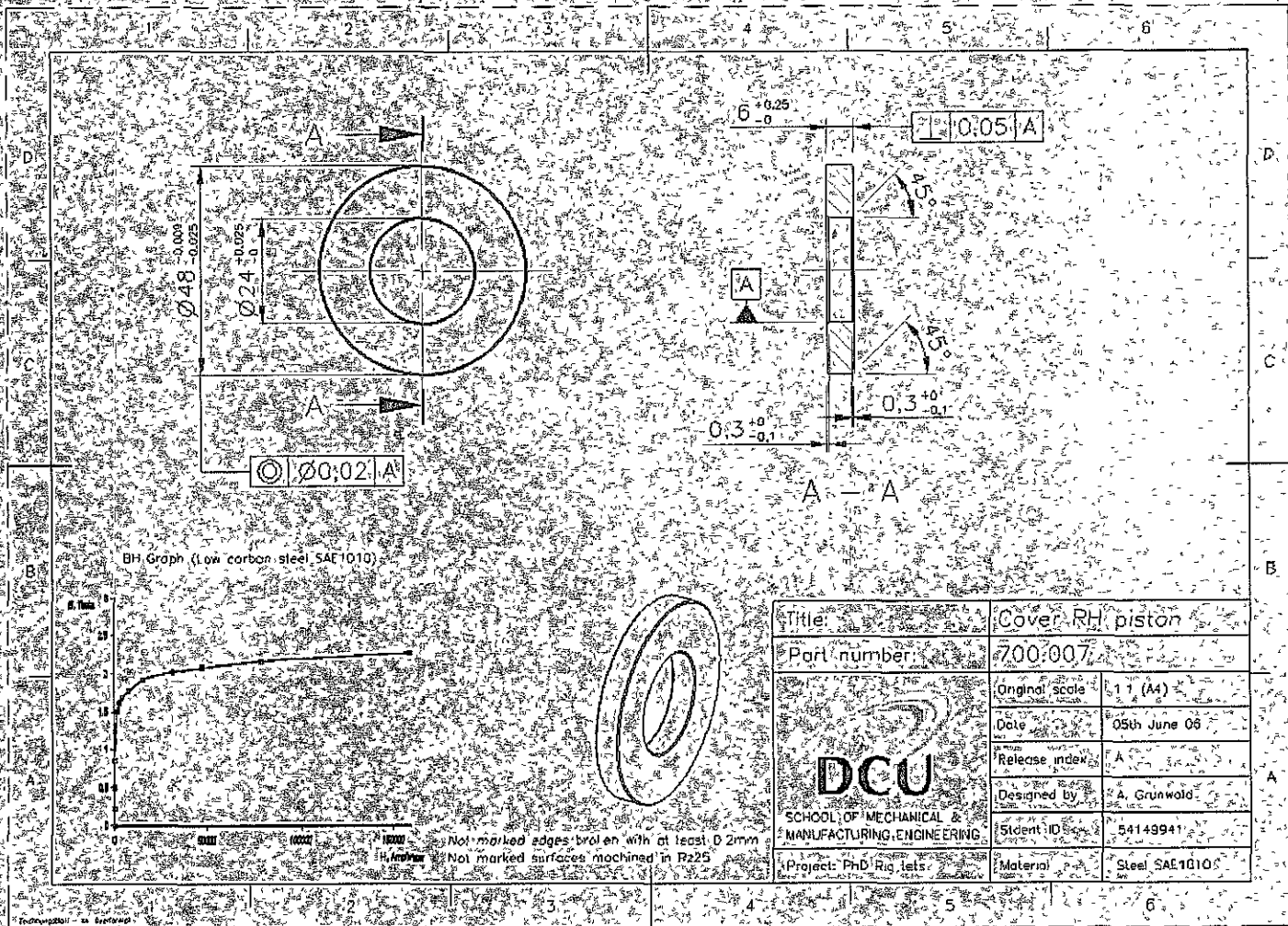


Fig. A11: Spring cover 700.010.2

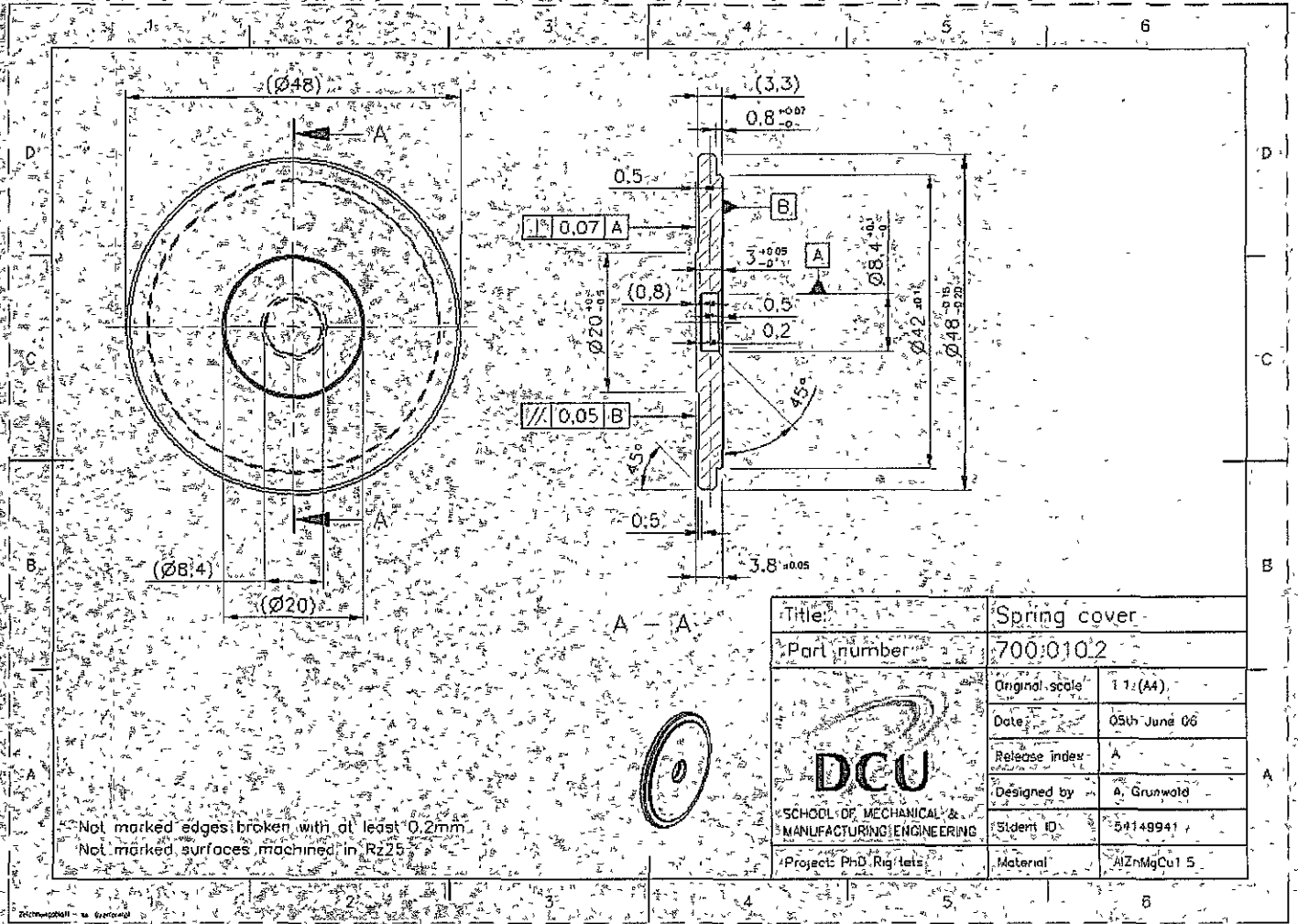


Fig. A12: Disc spring 700.011

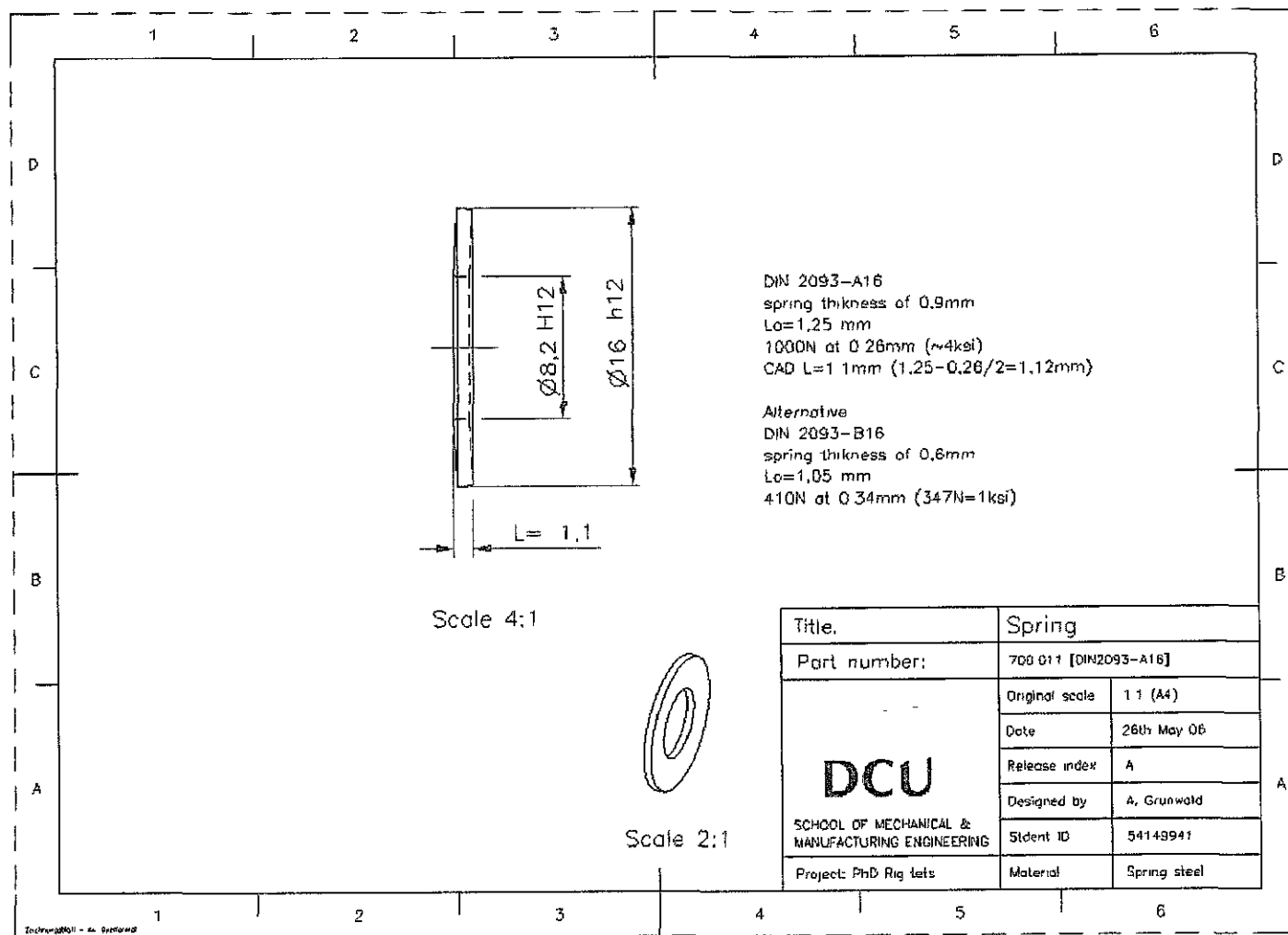
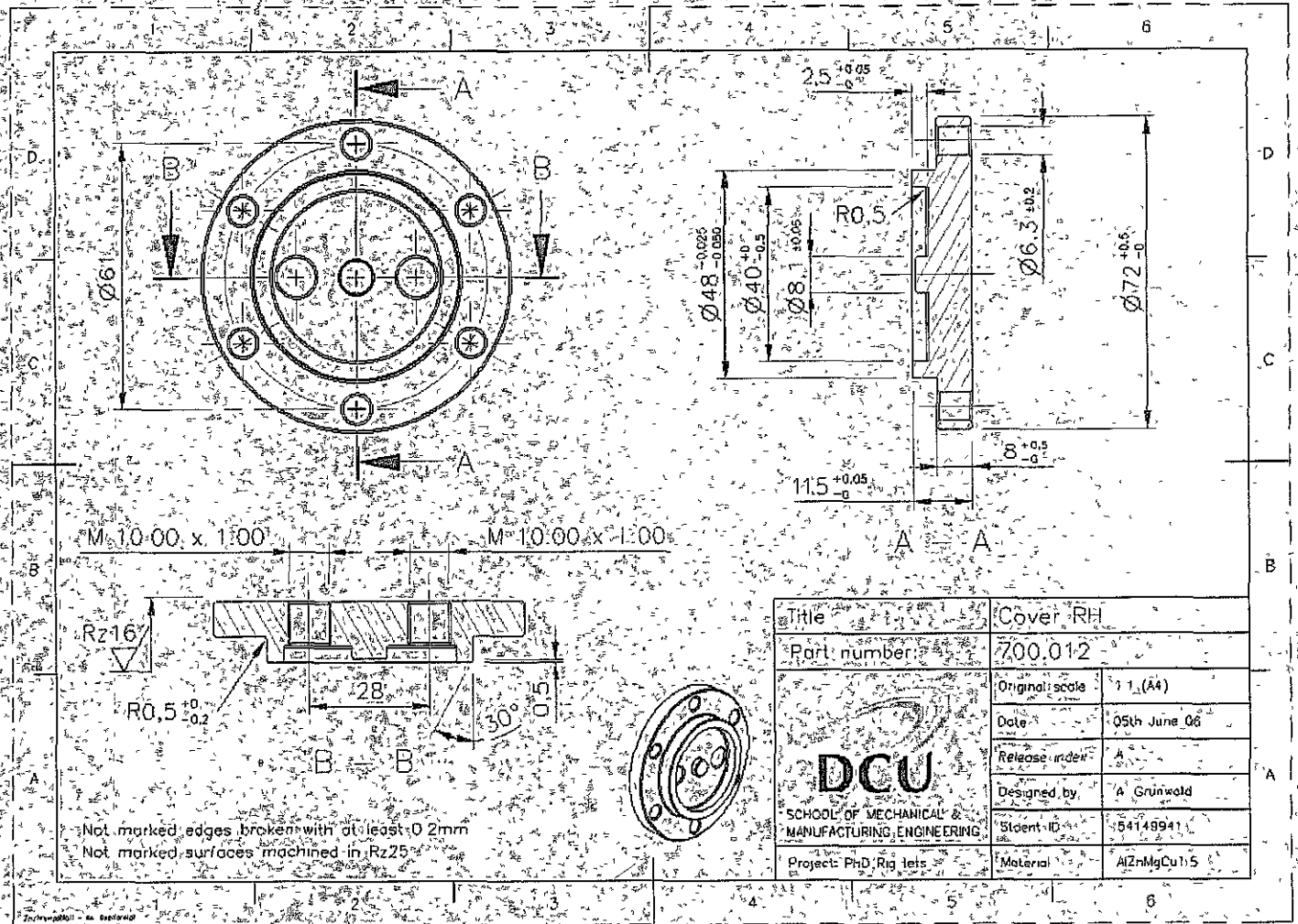


Fig. A13: Cover RH 700.012



Title	Cover RH
Part number	700.012
Original scale	1:1 (A4)
Date	05th June 06
Release index	A
Designed by	A Grünwald
Ident. ID	54148941
Material	AlZnMgCu1:5

Fig. A14: Actuator coil 700 014

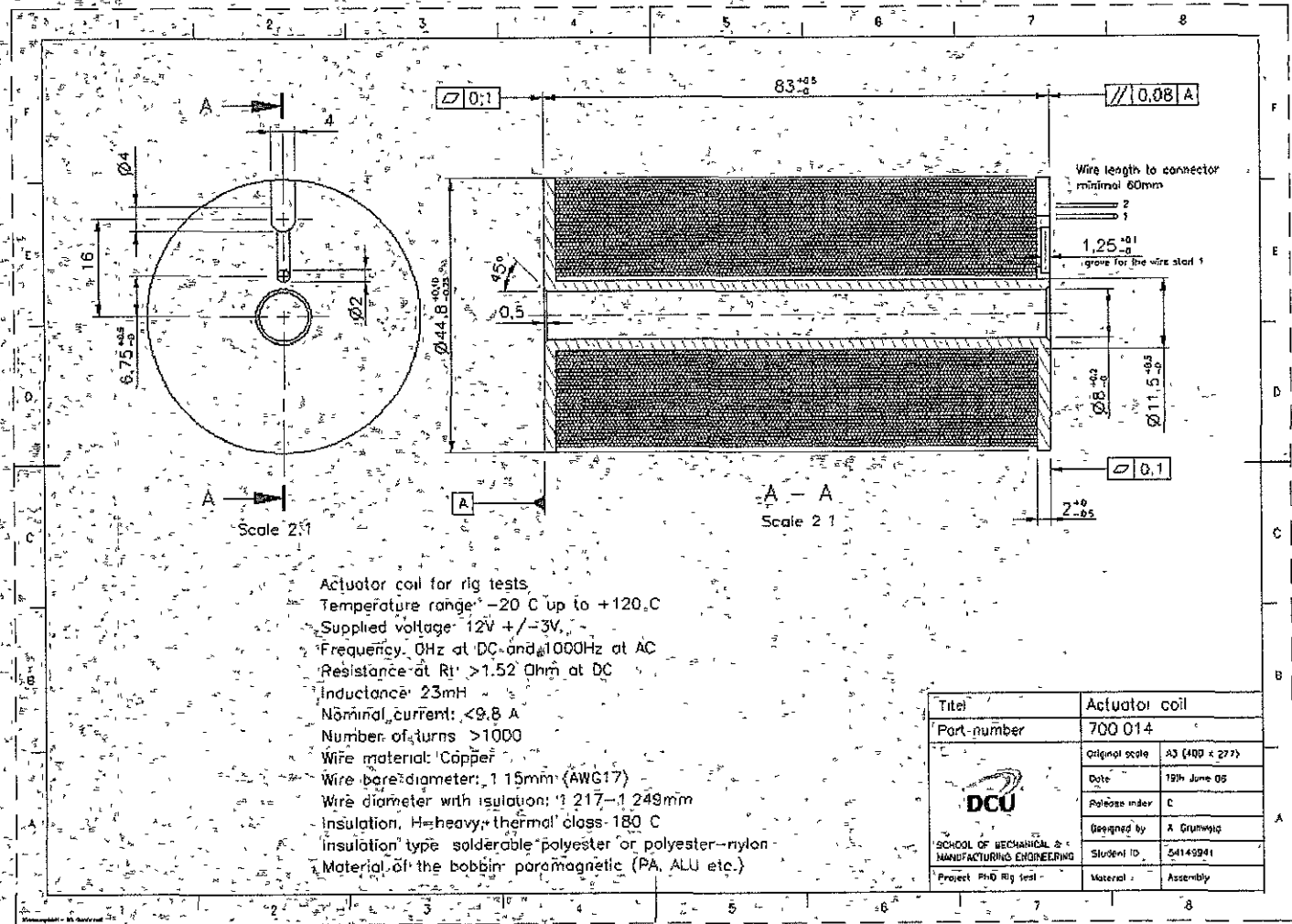
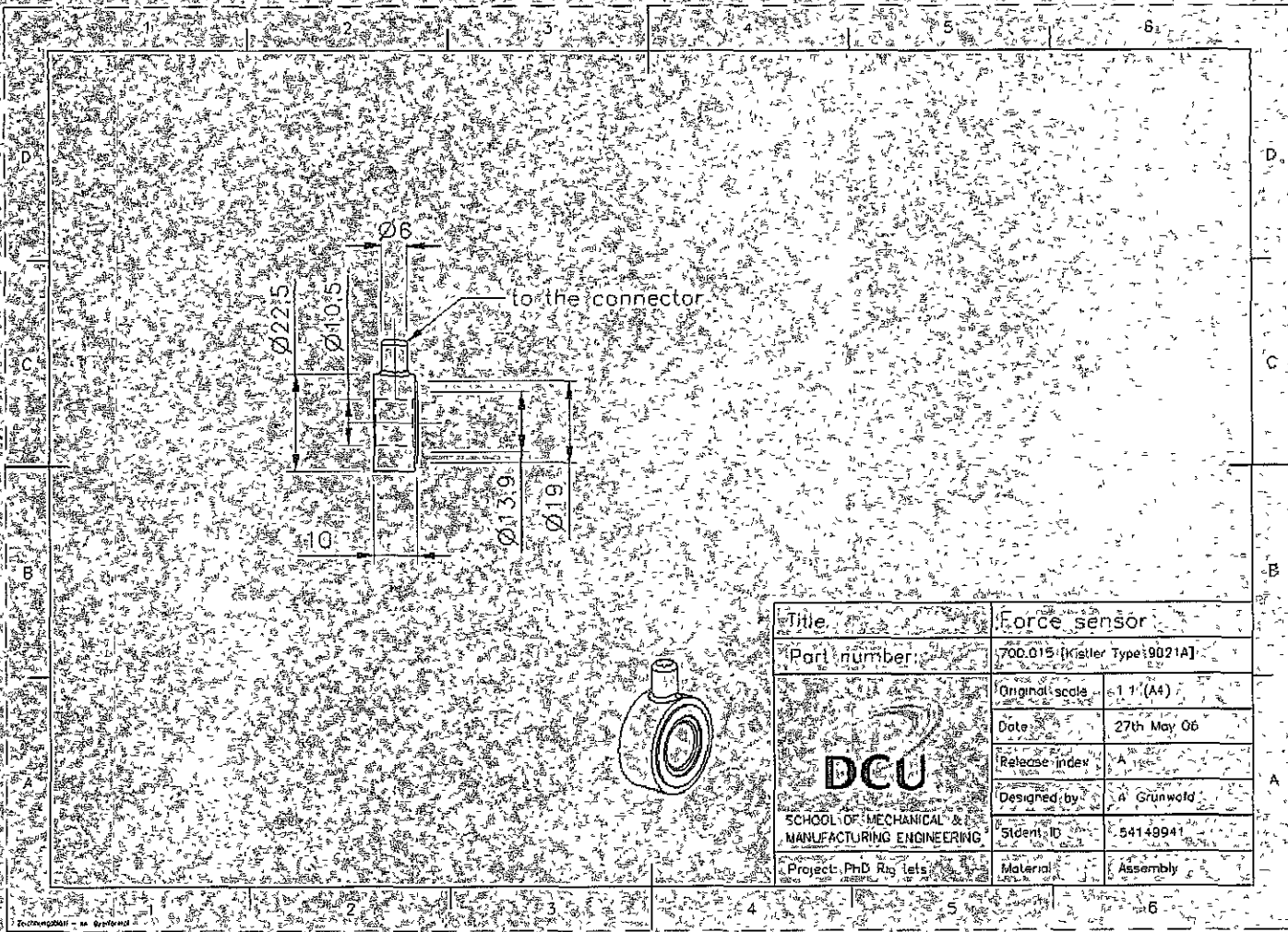


Fig. A15: Force sensor 700-015




Title	Force sensor	
Part number	700-015 (Kistler Type: 9021A)	
 DCU SCHOOL OF MECHANICAL & MANUFACTURING ENGINEERING	Original scale	1:1 (A4)
	Date	27th May 06
	Release index	A
	Designed by	A. Grünwald
	Student ID	54149941
	Project: Ph.D. Thesis	Material: Assembly

Fig. A16: Sensor cover 700.016

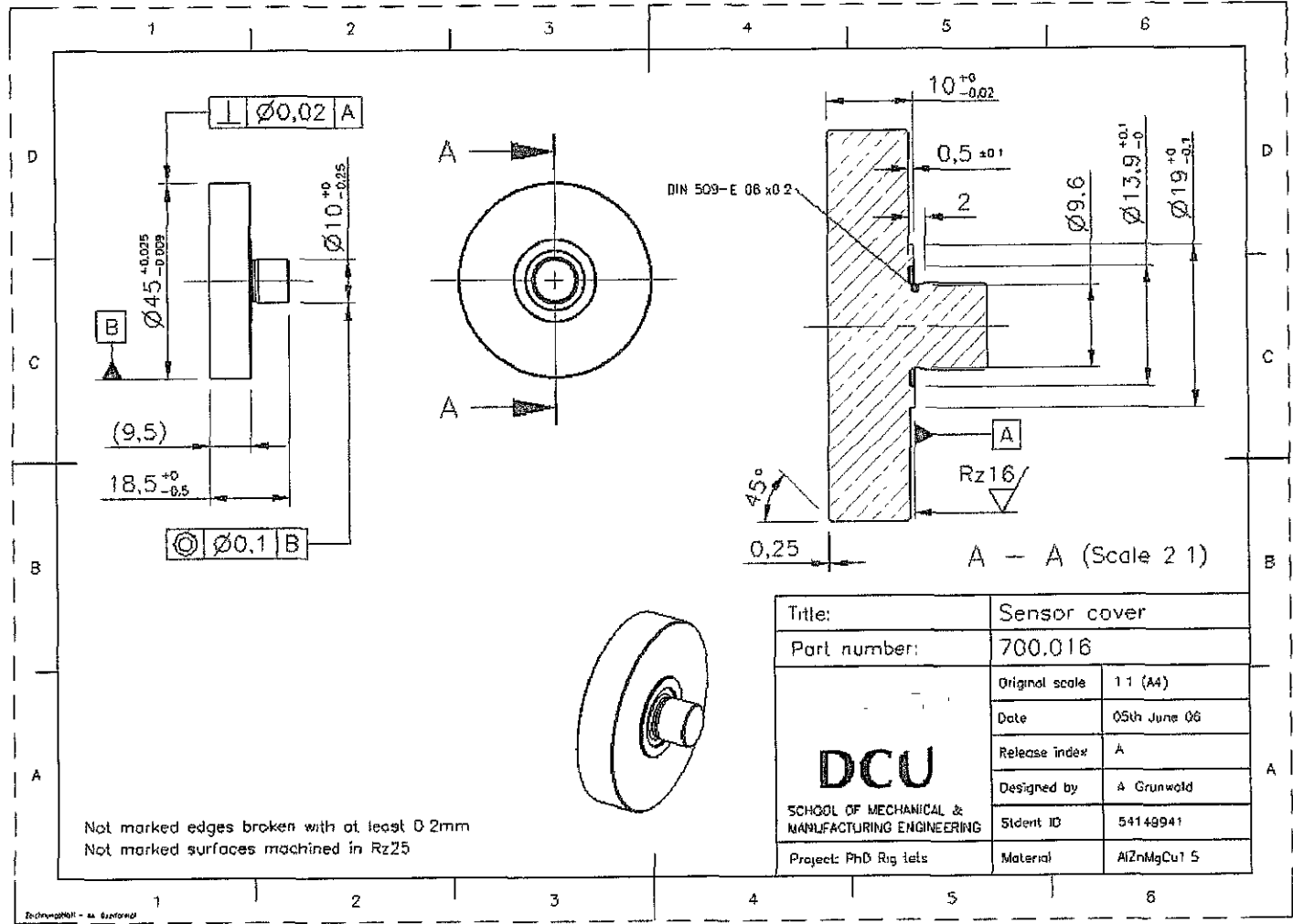


Fig. B1: Control valve assembly 802.000

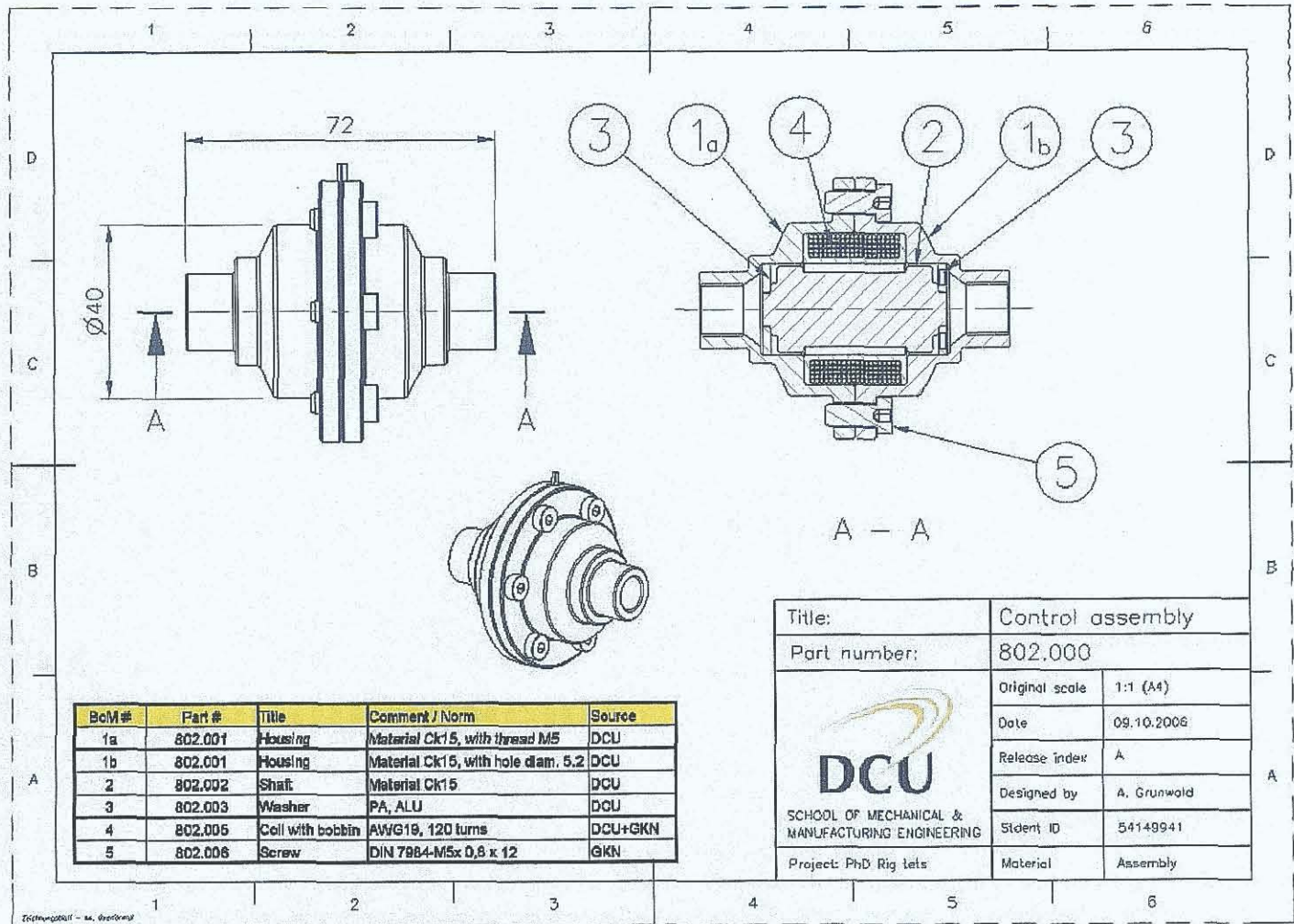


Fig. B2: Housing 802.001

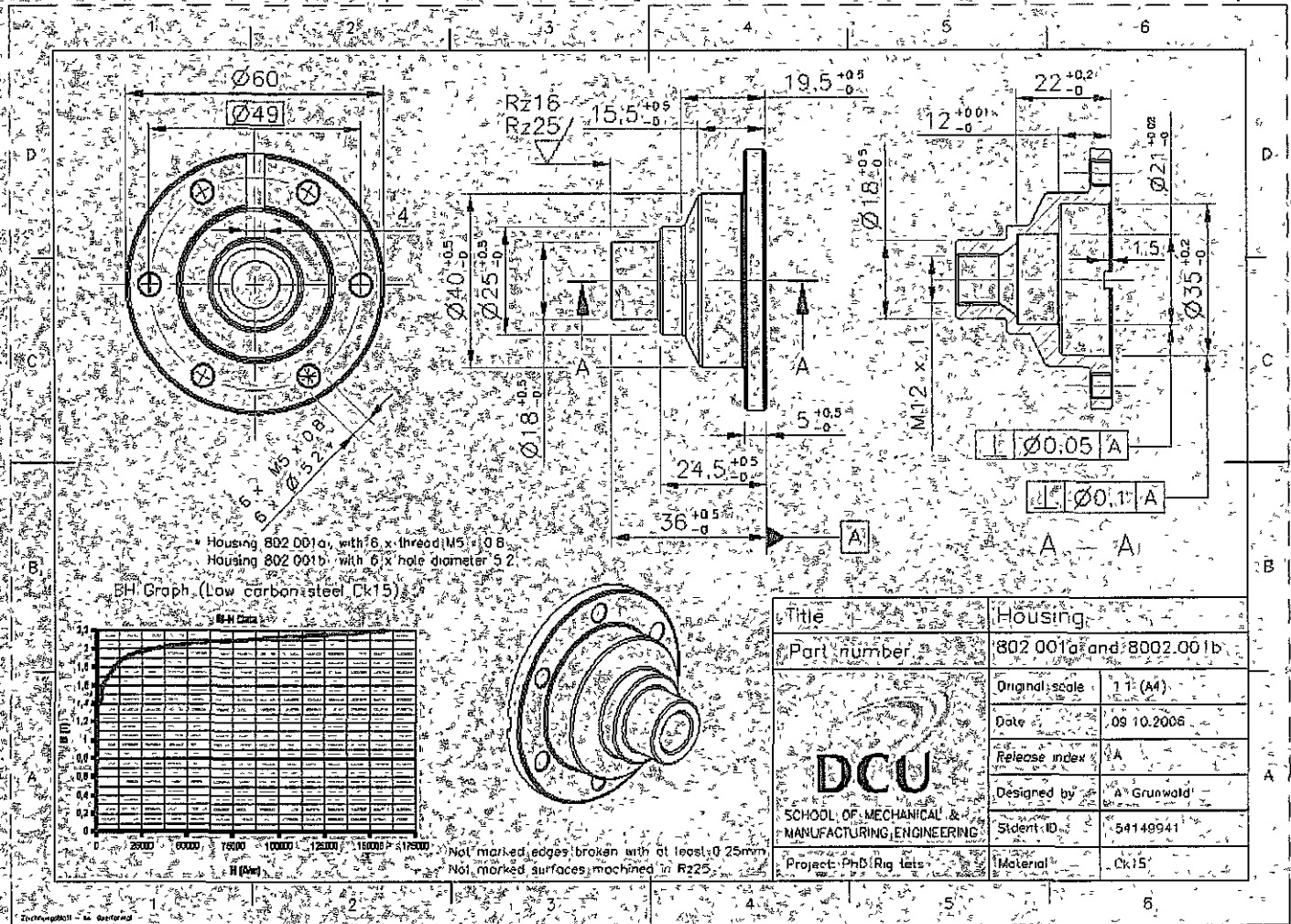


Fig.B3: Shaft 802.002

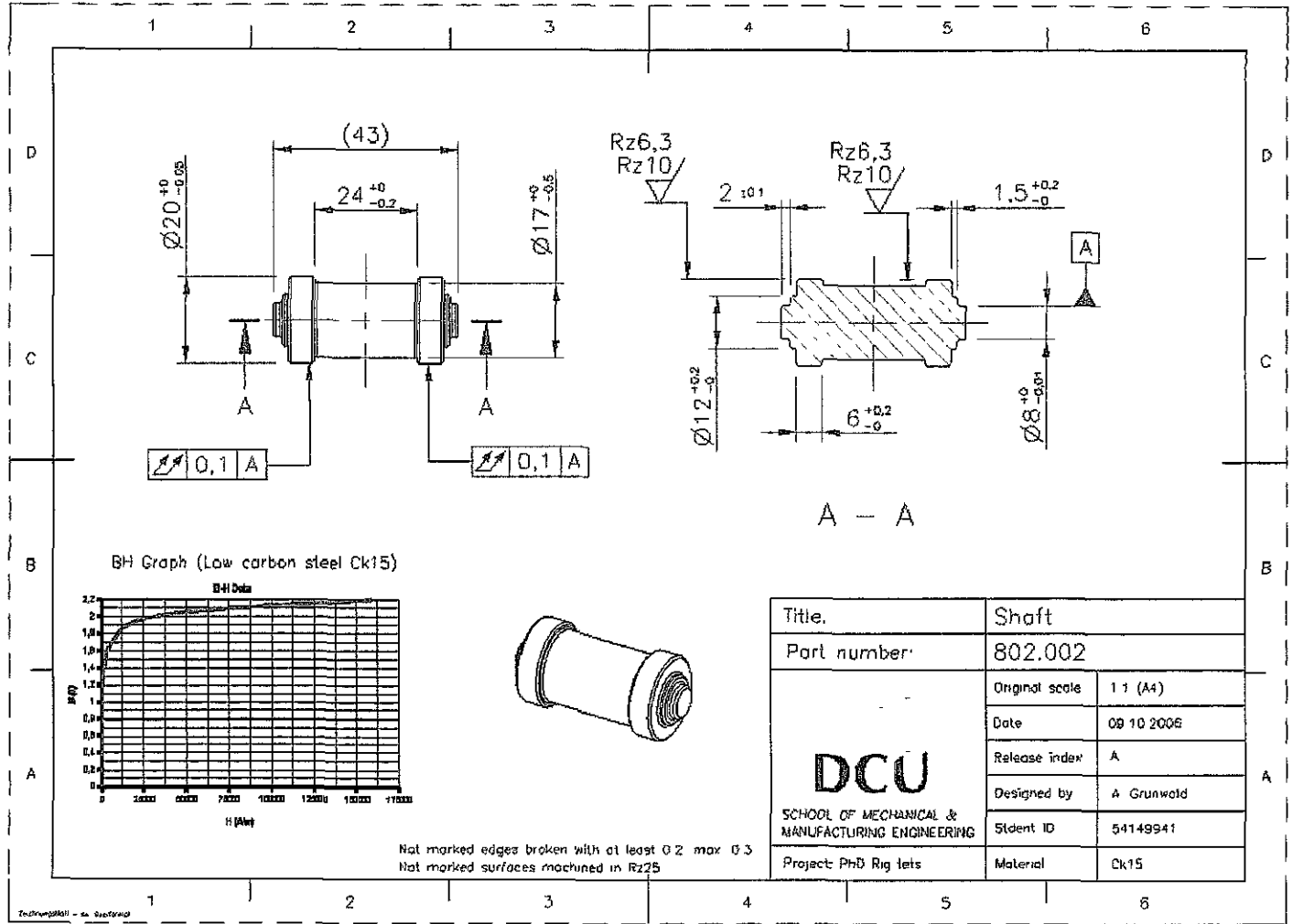


Fig.B4: Washer 802.003

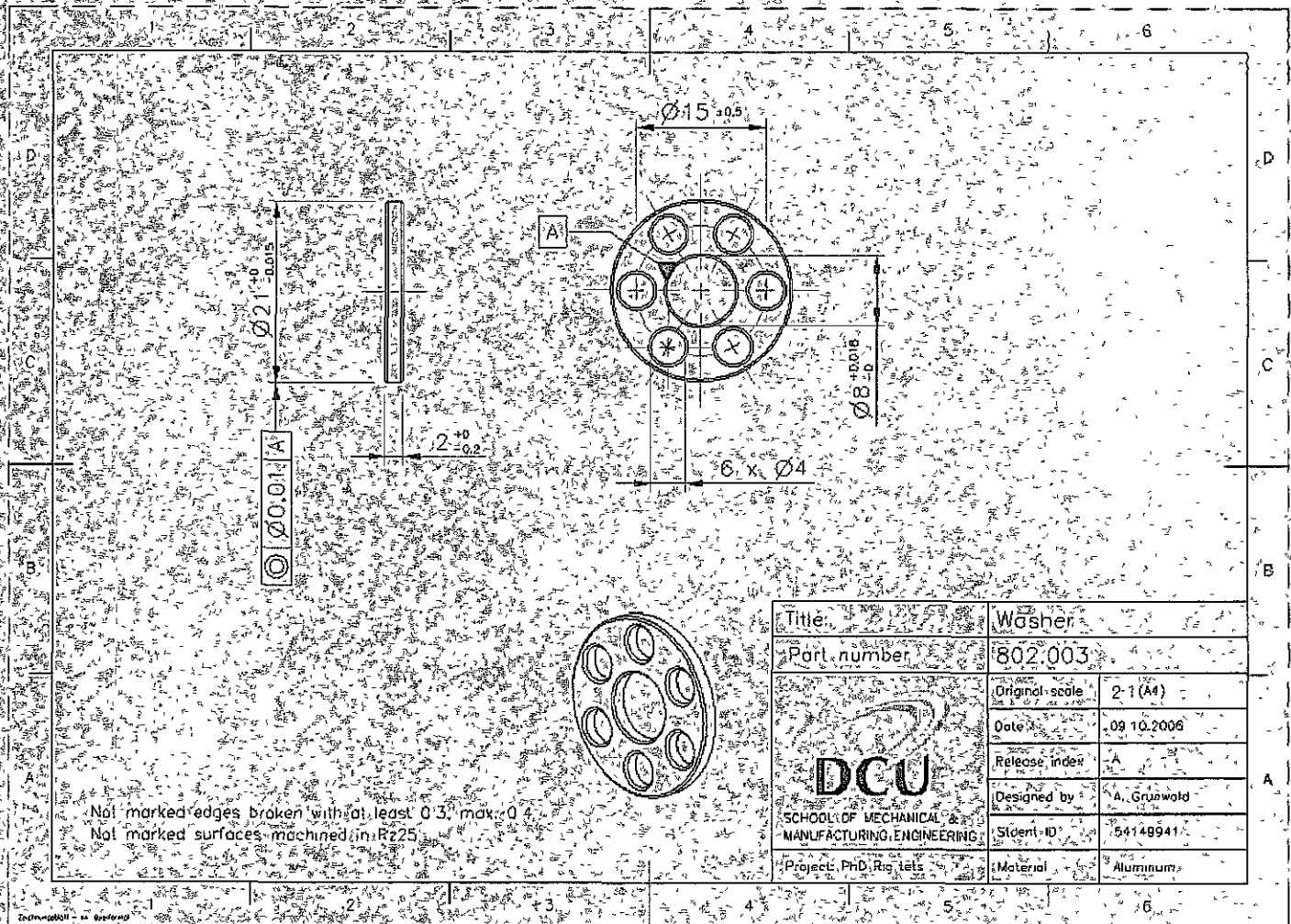


Fig.B5: Coil bobbin 802.004

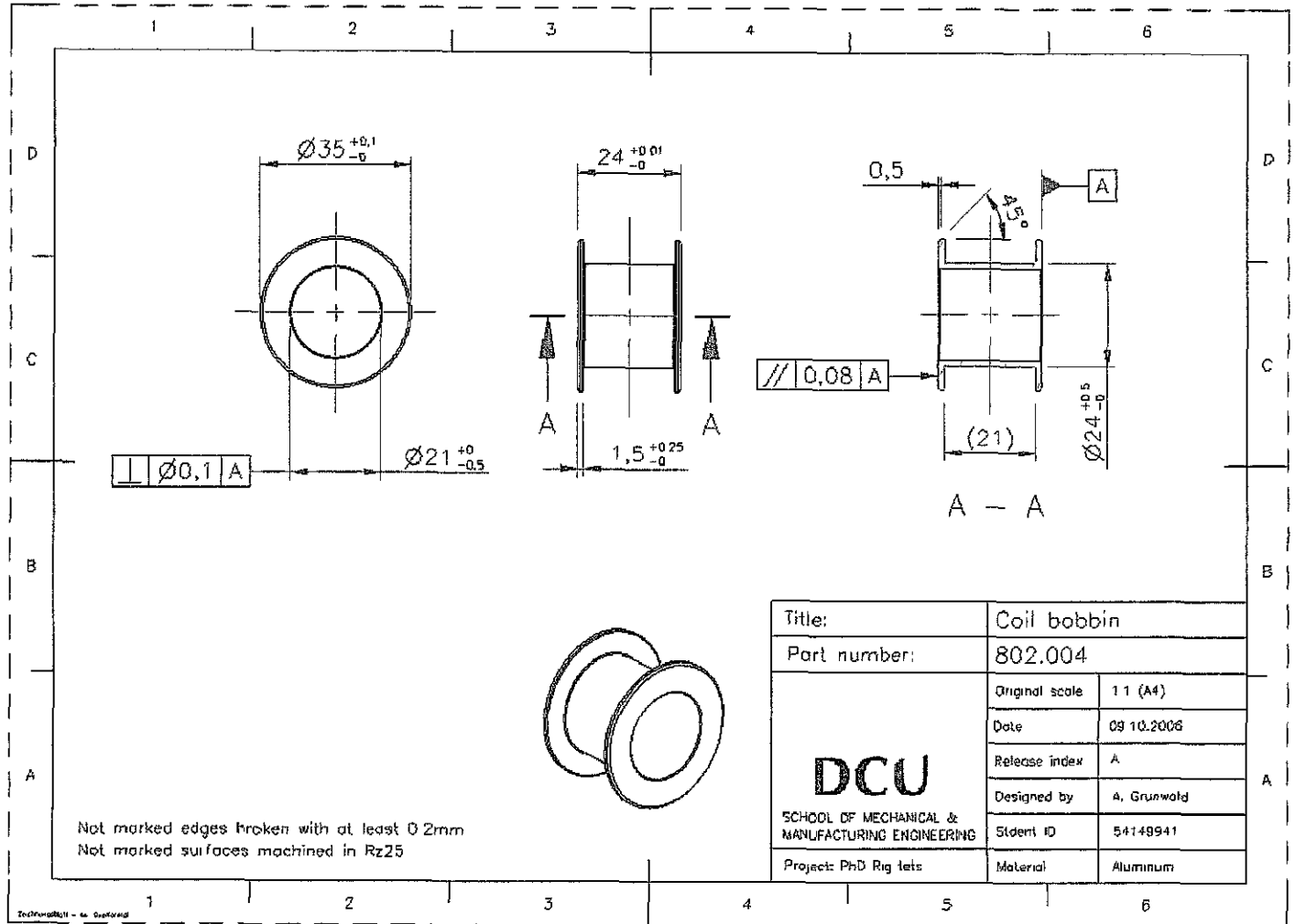


Fig.B6: Coil 802.005

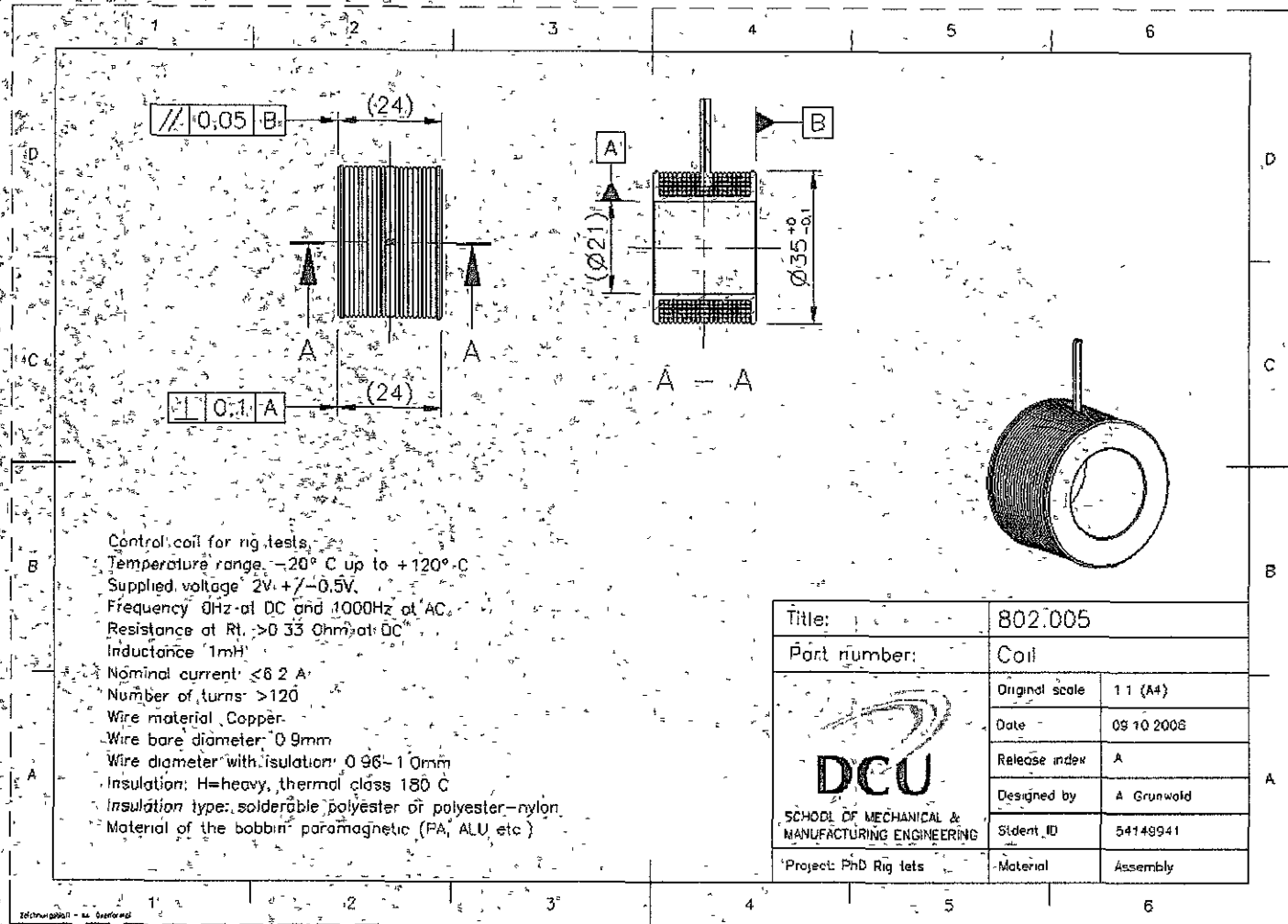


Fig.C1: Control assembly 800.000

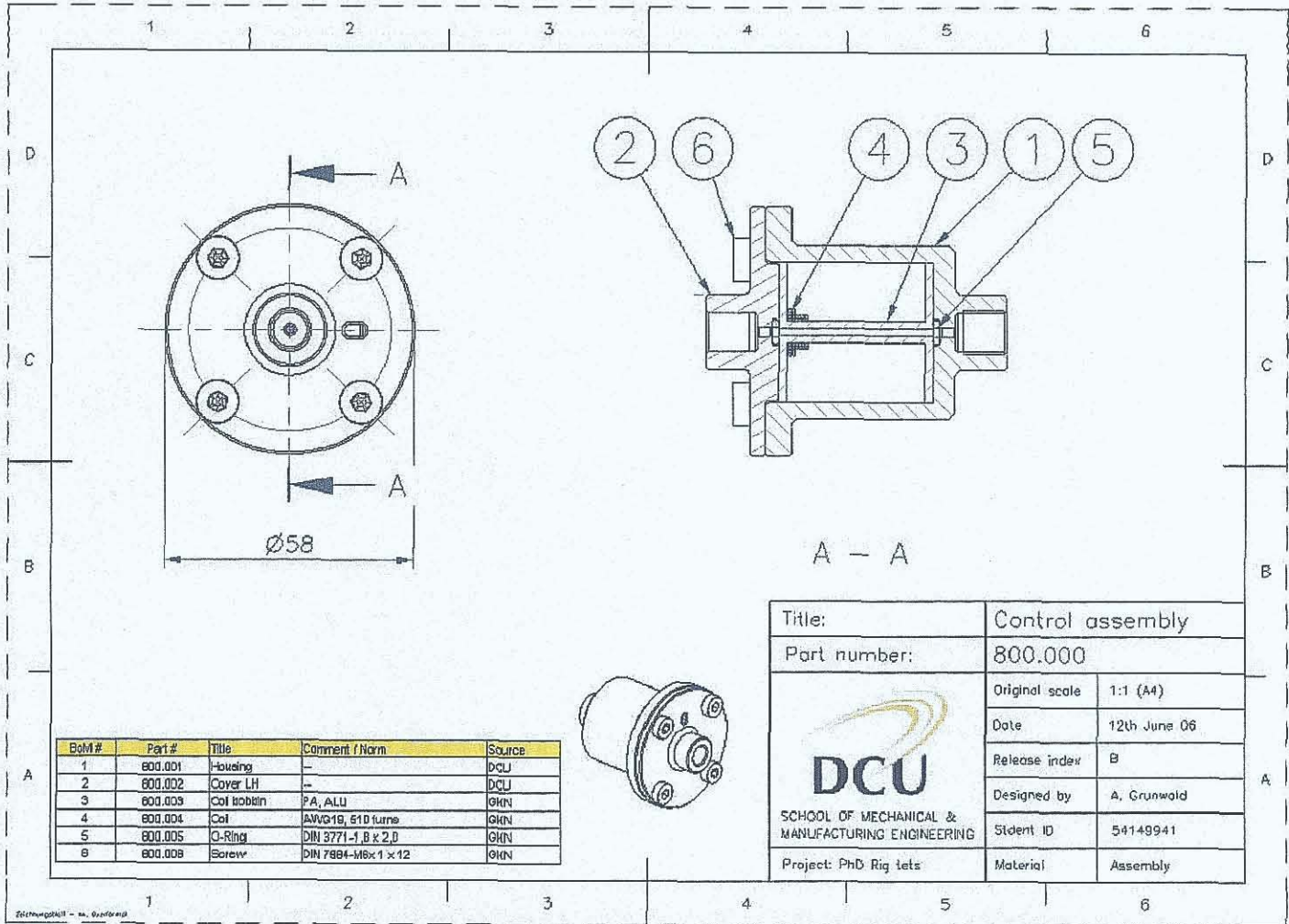


Fig. Q2: Housing 800.001

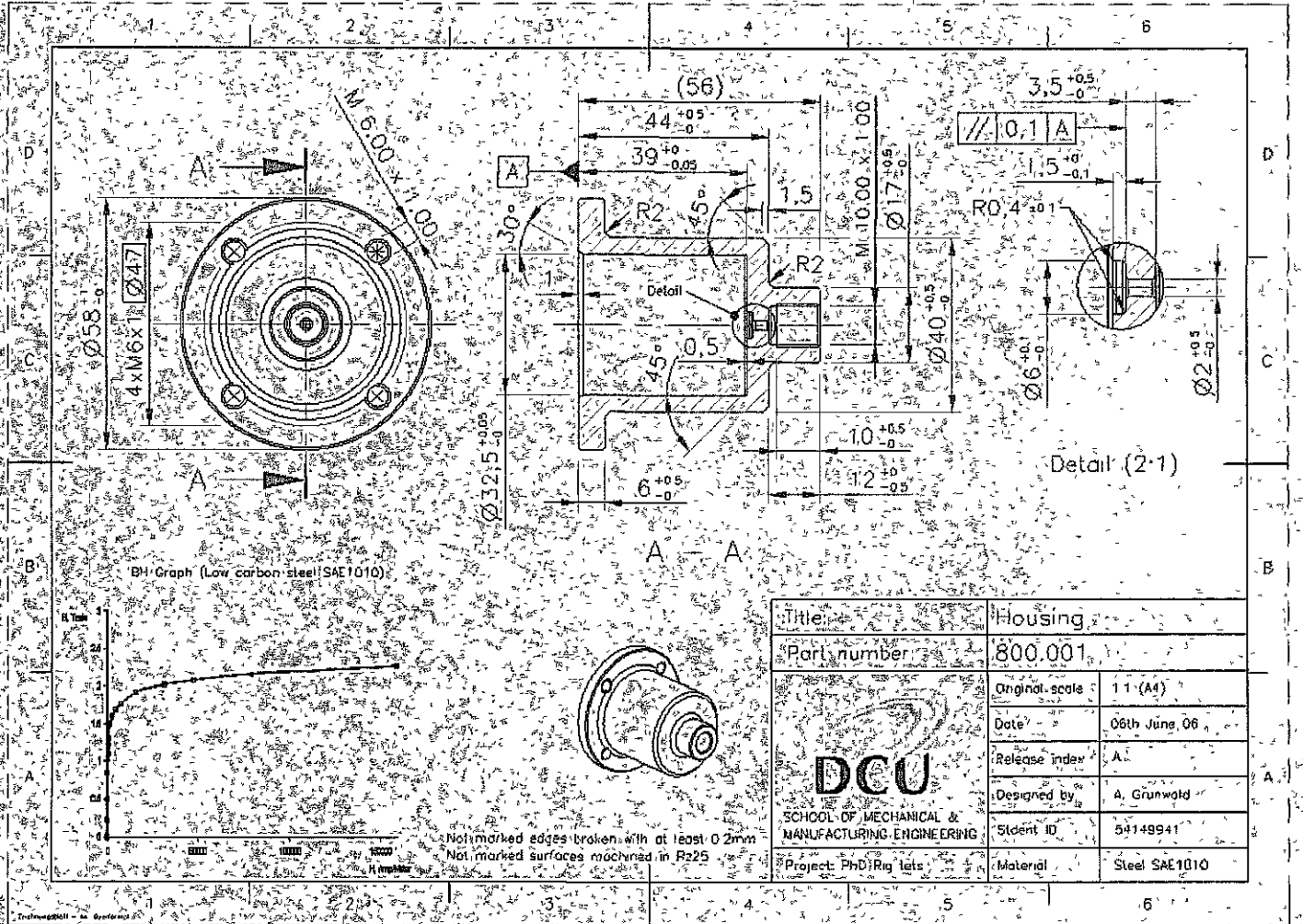


Fig.C3: Cover_LH 800.002

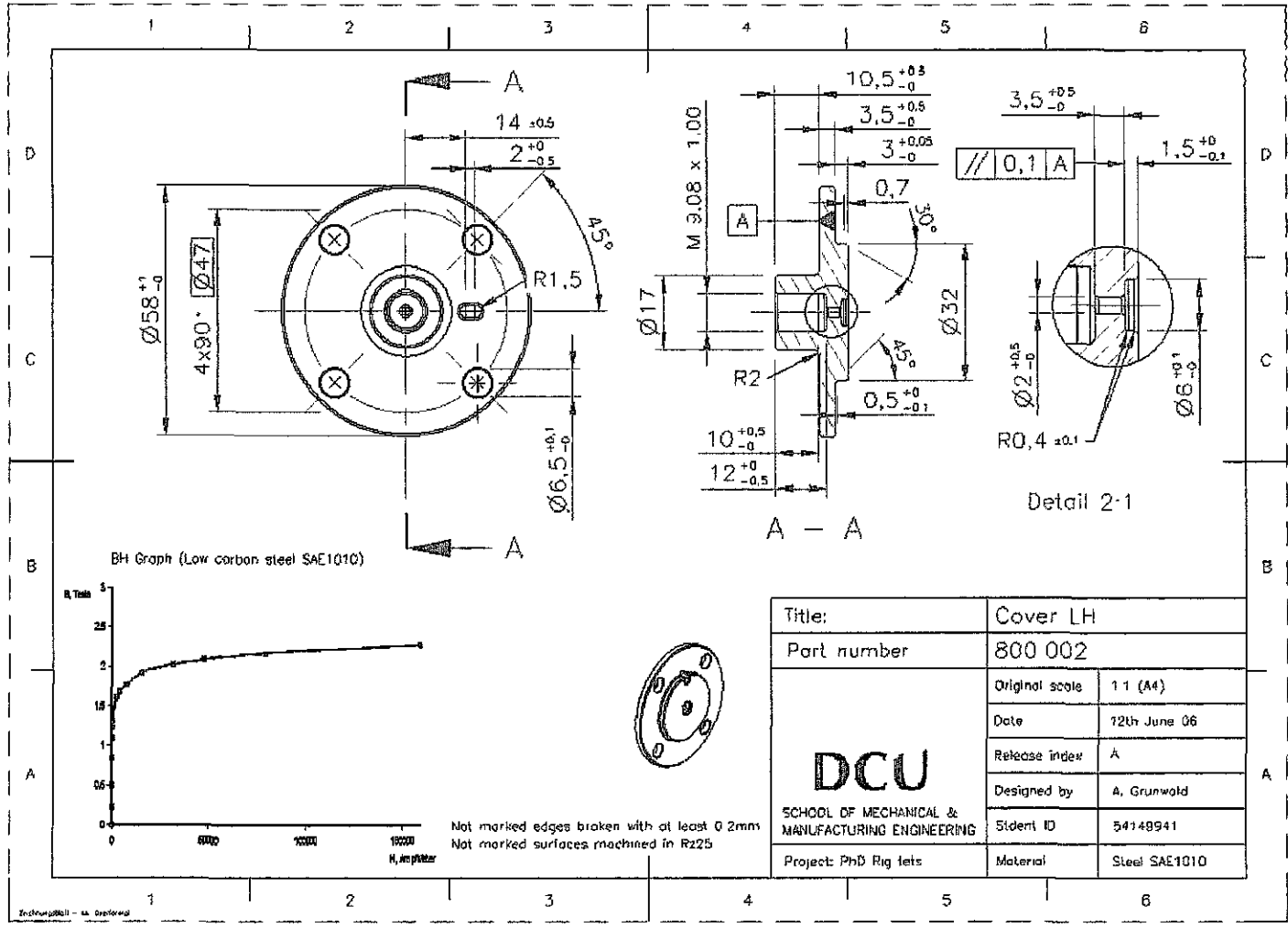


Fig.C4: Control coil 800.007

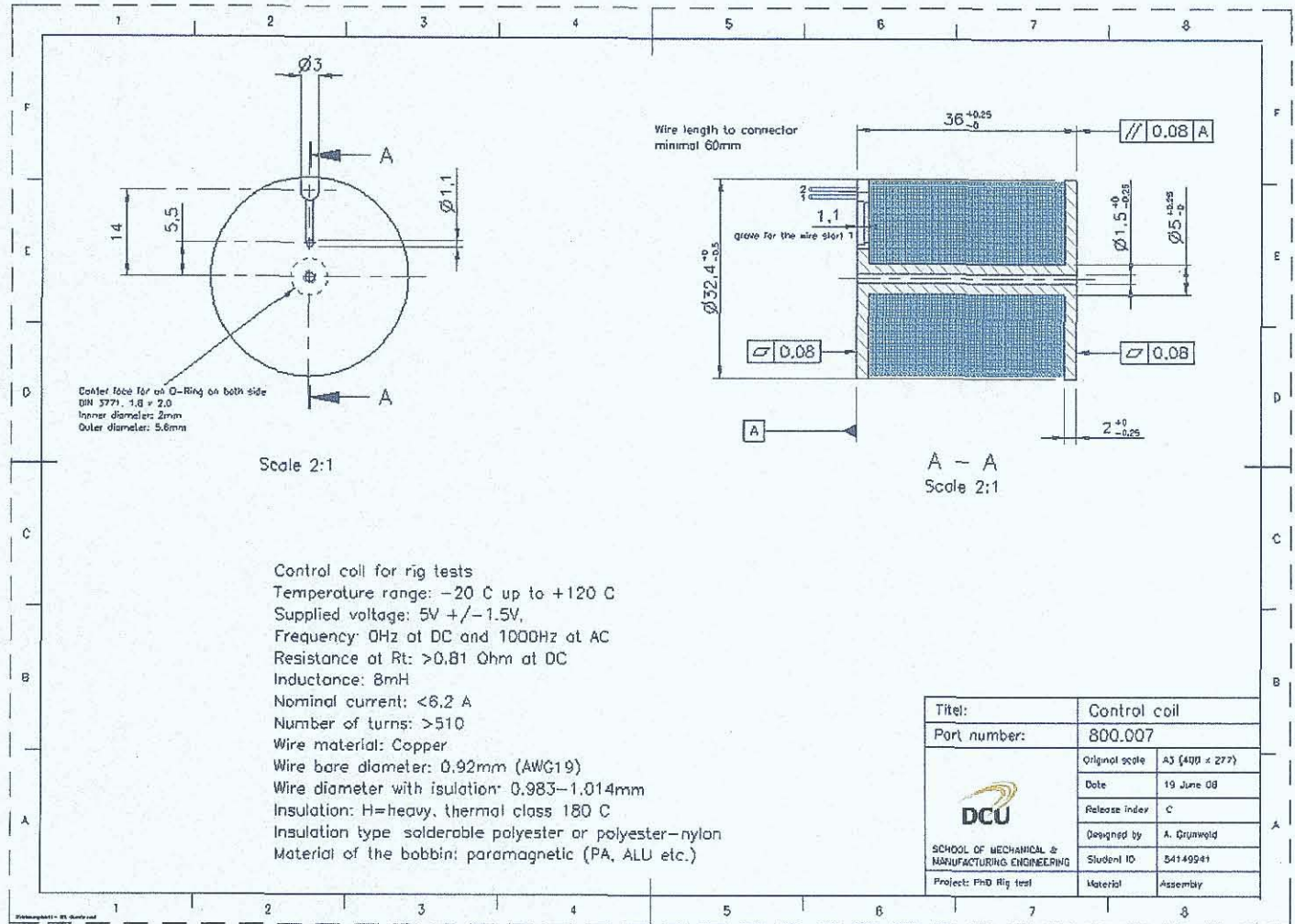


Fig. D1: Reservoir assembly 900.000

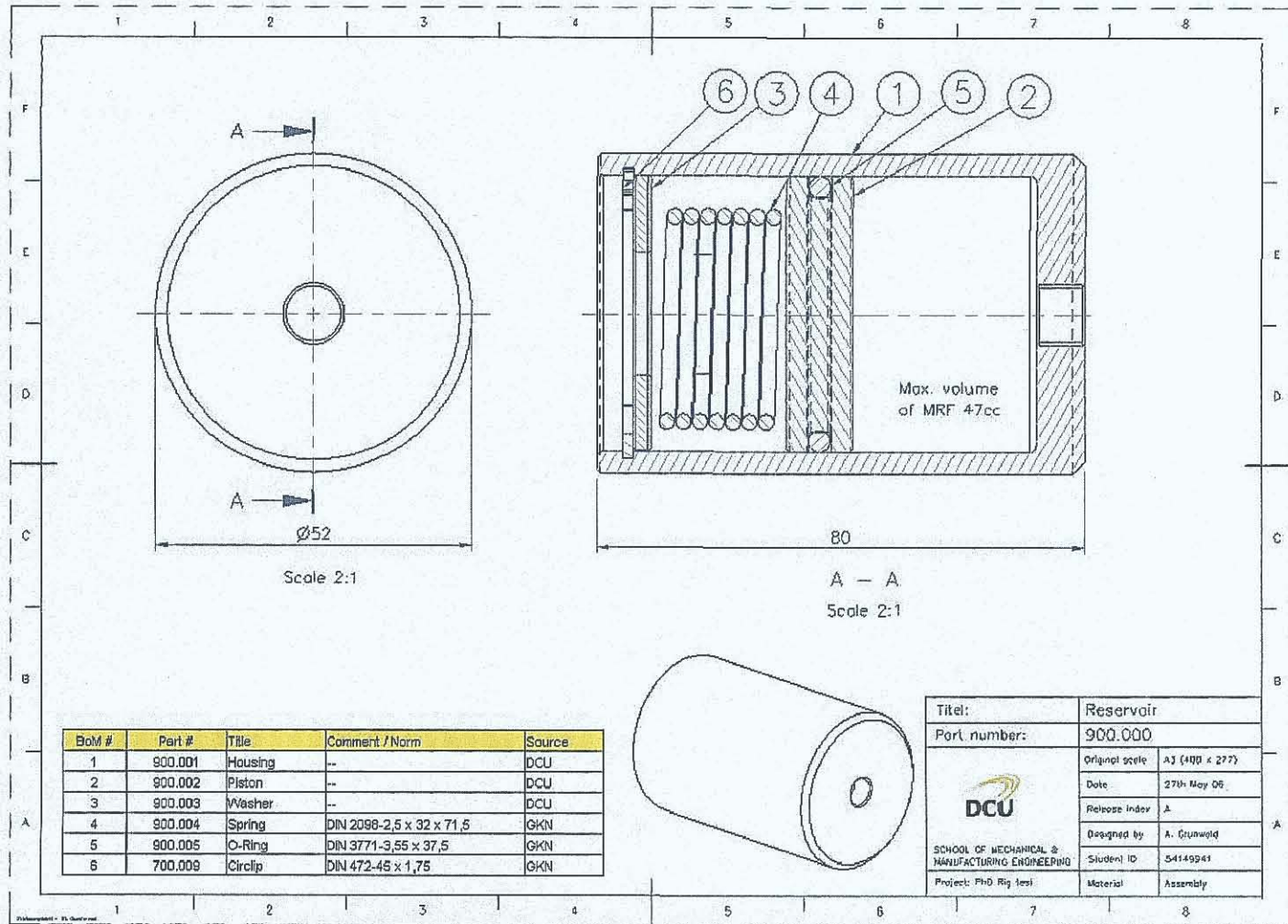
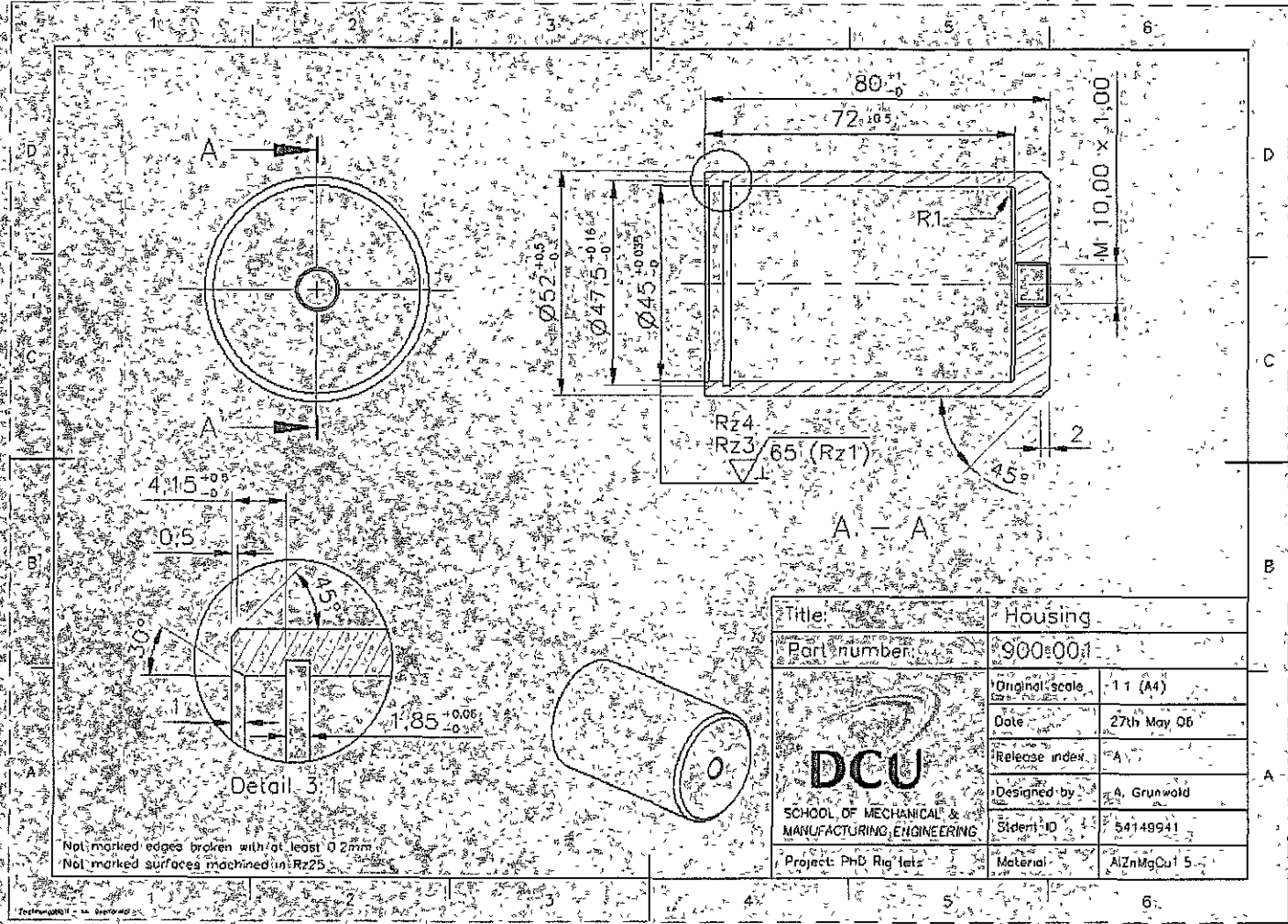


Fig.D2: Housing 900:001




Title:	Housing		
Part number:	900:001		
 <p>DCU SCHOOL OF MECHANICAL & MANUFACTURING ENGINEERING</p>	Original scale:	1:1 (A4)	
	Date:	27th May 06	
	Release index:	A	
	Designed by:	A. Grunwald	
Project: PhD Rig lets	System ID:	54148941	
	Material:	AlZnMgCu15	

Fig.D3: Piston 900.002

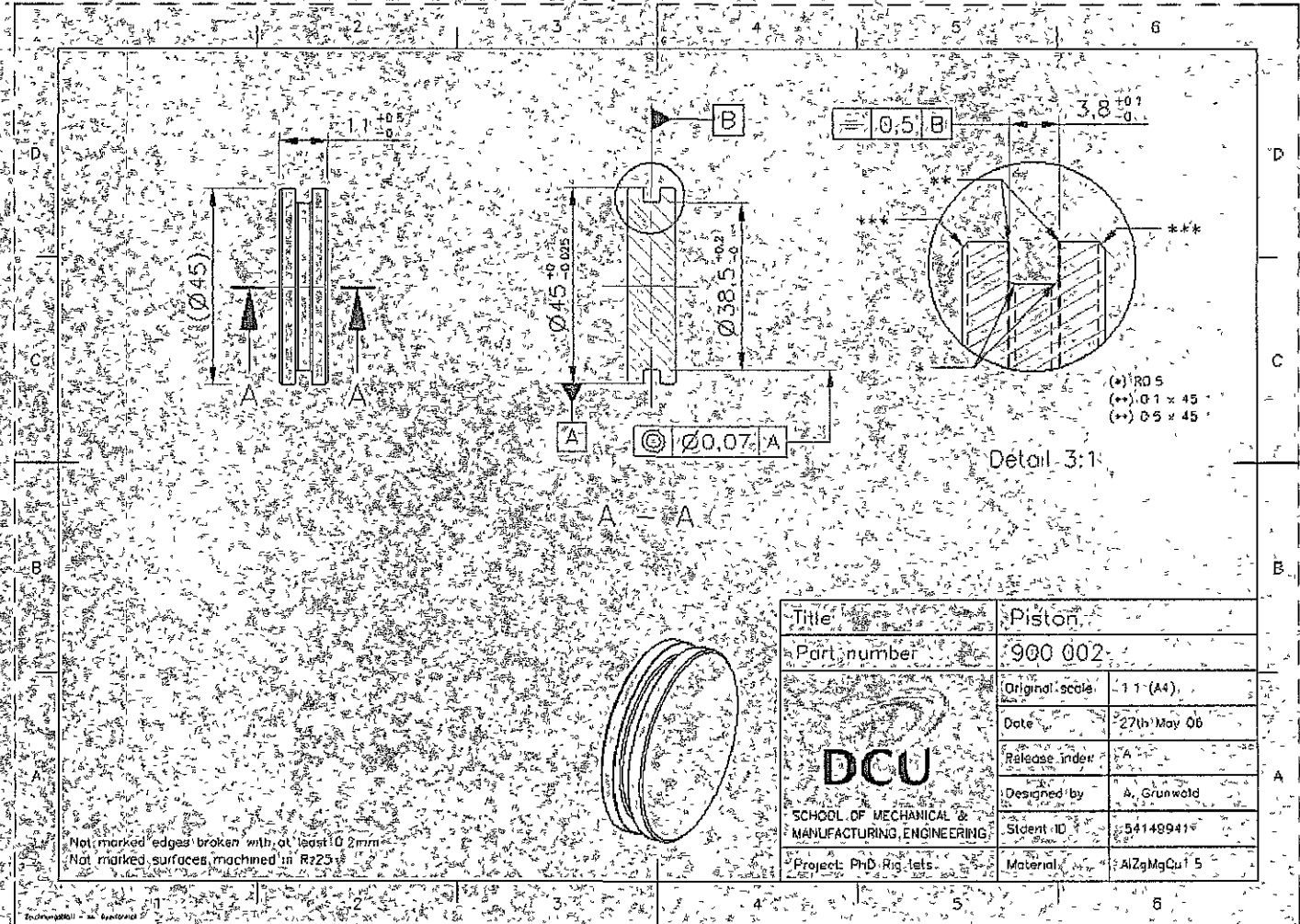


Fig.D4 - Washer 900.003

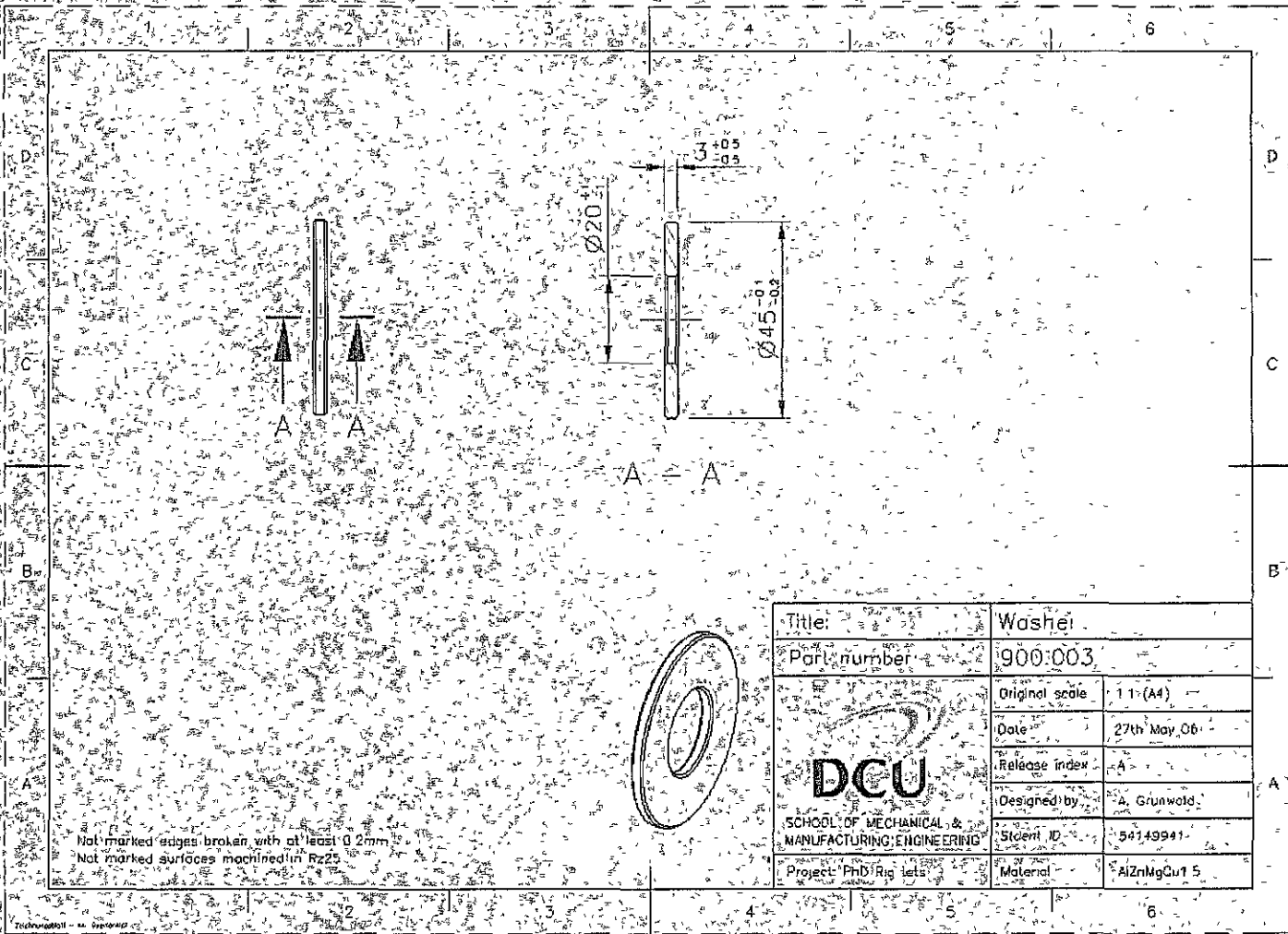


Fig. E1: Load assembly 600.000

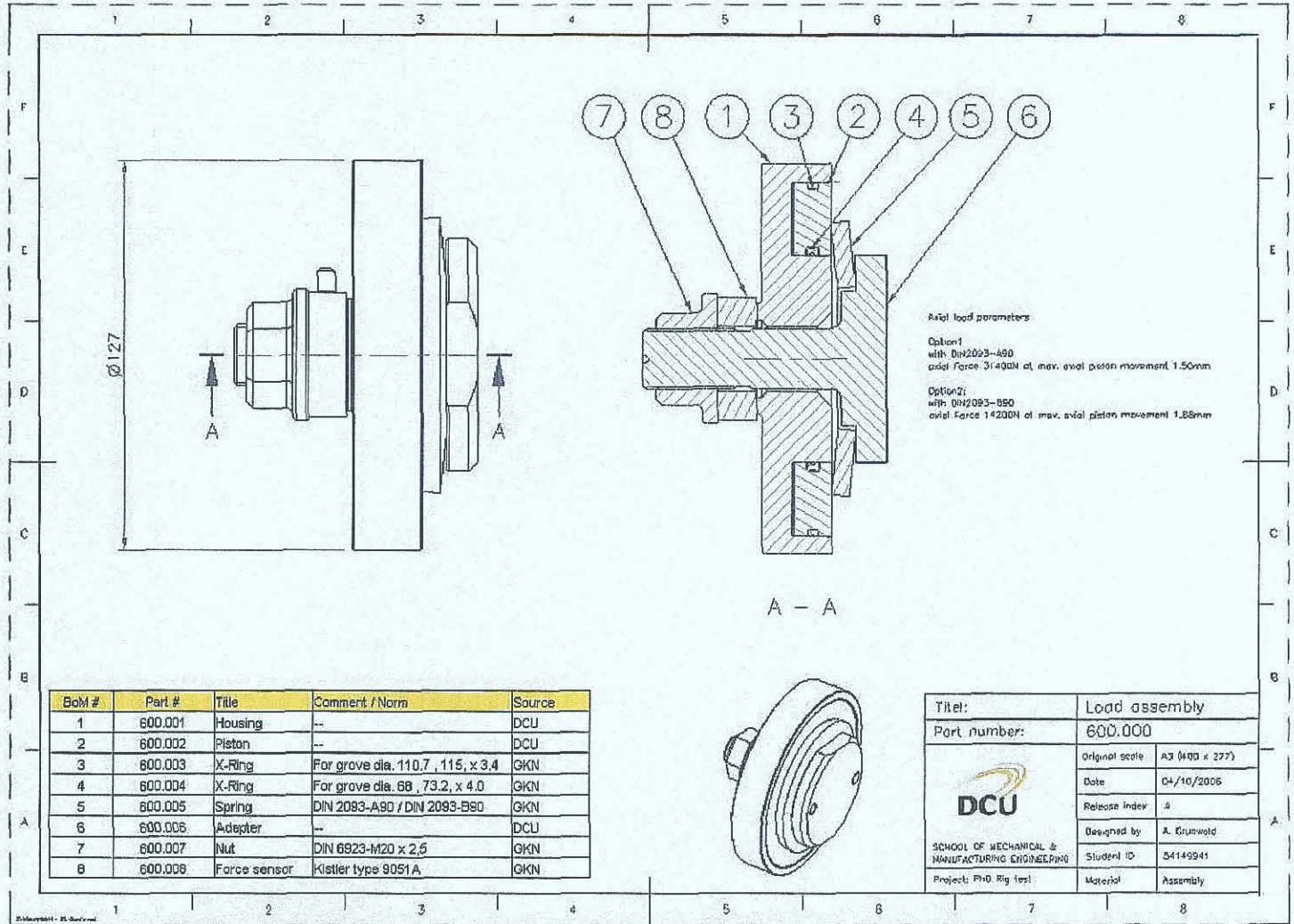


Fig. E2: Housing 600.001

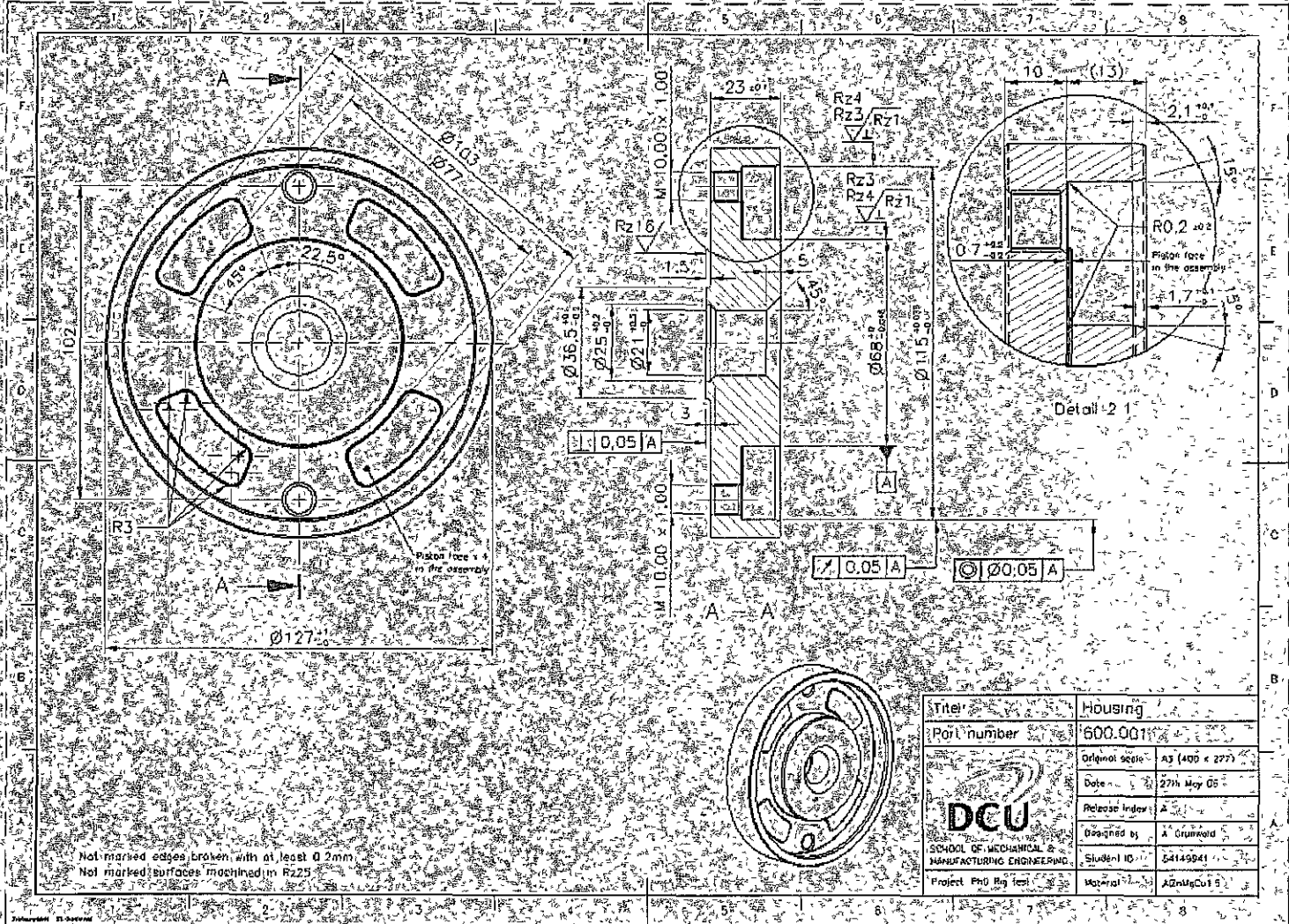


Fig. E3: Piston 600.002

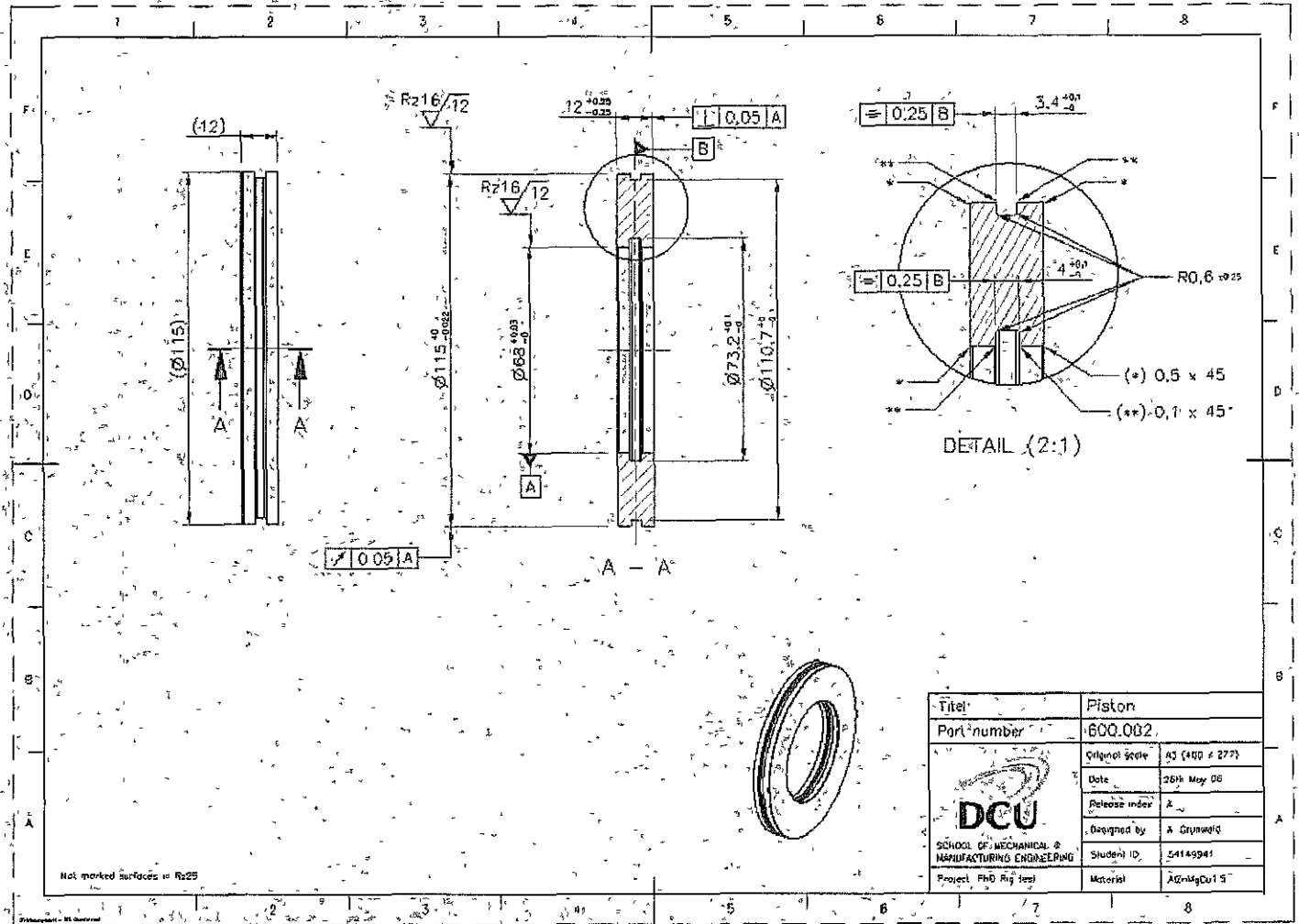
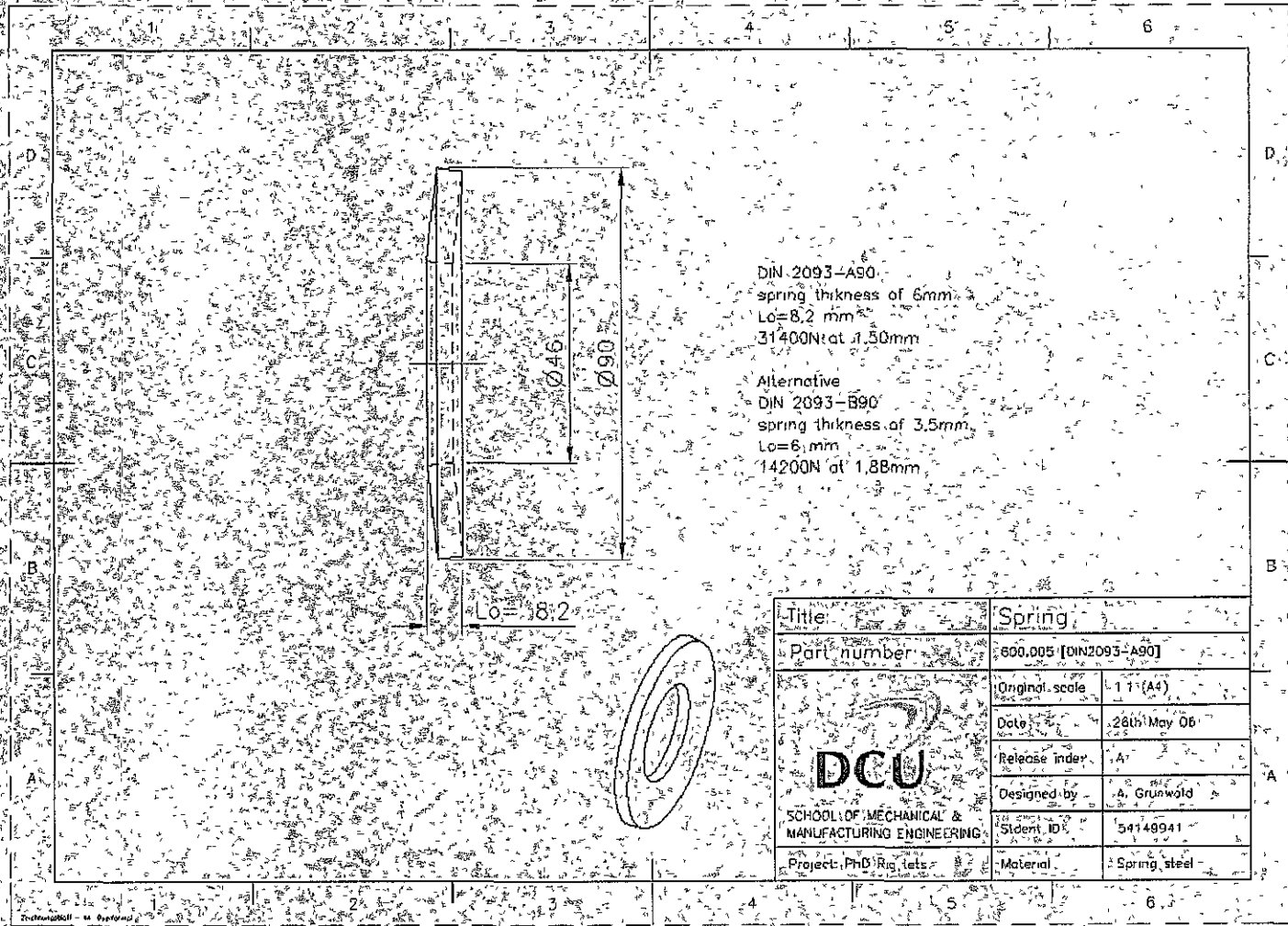


Fig. E4: Spring 600.005



DIN 2093-A90
 spring thickness of 6mm
 $L_o = 8.2$ mm
 31400N at 1.50mm

Alternative
 DIN 2093-B90
 spring thickness of 3.5mm
 $L_o = 6$ mm
 14200N at 1.88mm


Title	Spring	
Part number	600.005 [DIN2093-A90]	
 DCU SCHOOL OF MECHANICAL & MANUFACTURING ENGINEERING	Original scale	1:1 (A4)
	Date	28th May 06
	Release index	A
	Designed by	A. Grunwald
	Student ID	54149941
Project: PhD Rig tests	Material	Spring steel

Fig. E5: Adapter 600.006

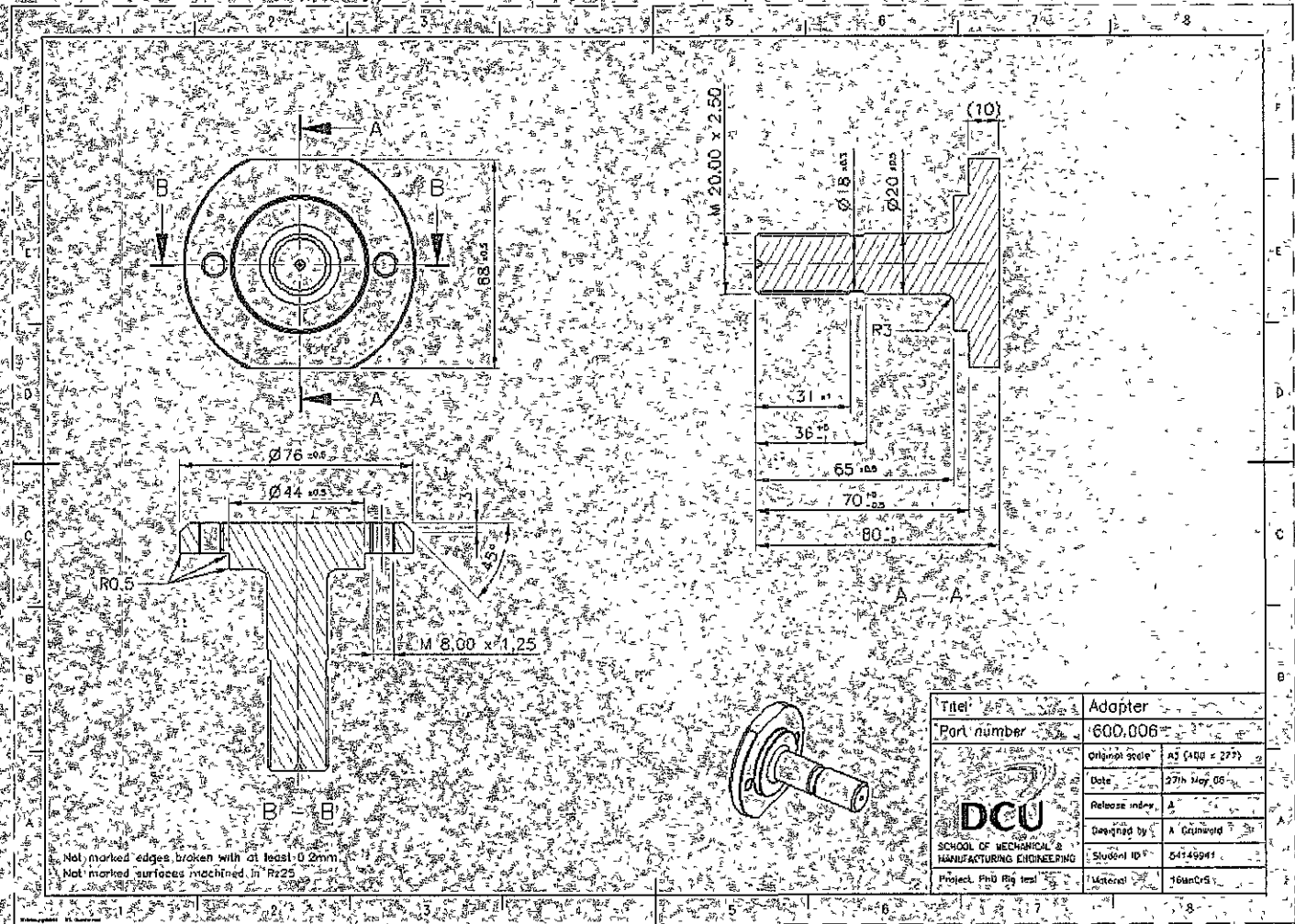


Fig. E6: Nut 600/007

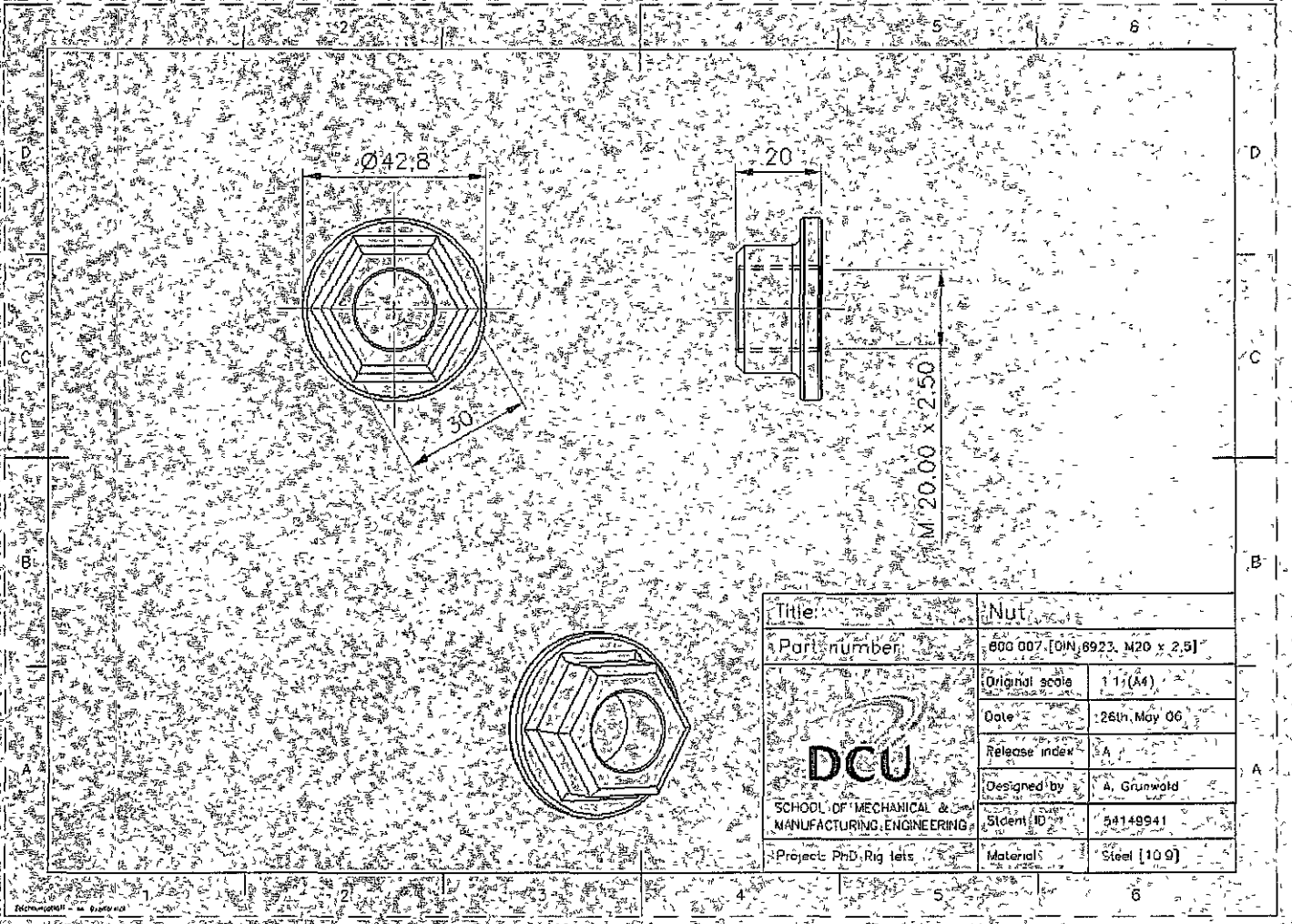
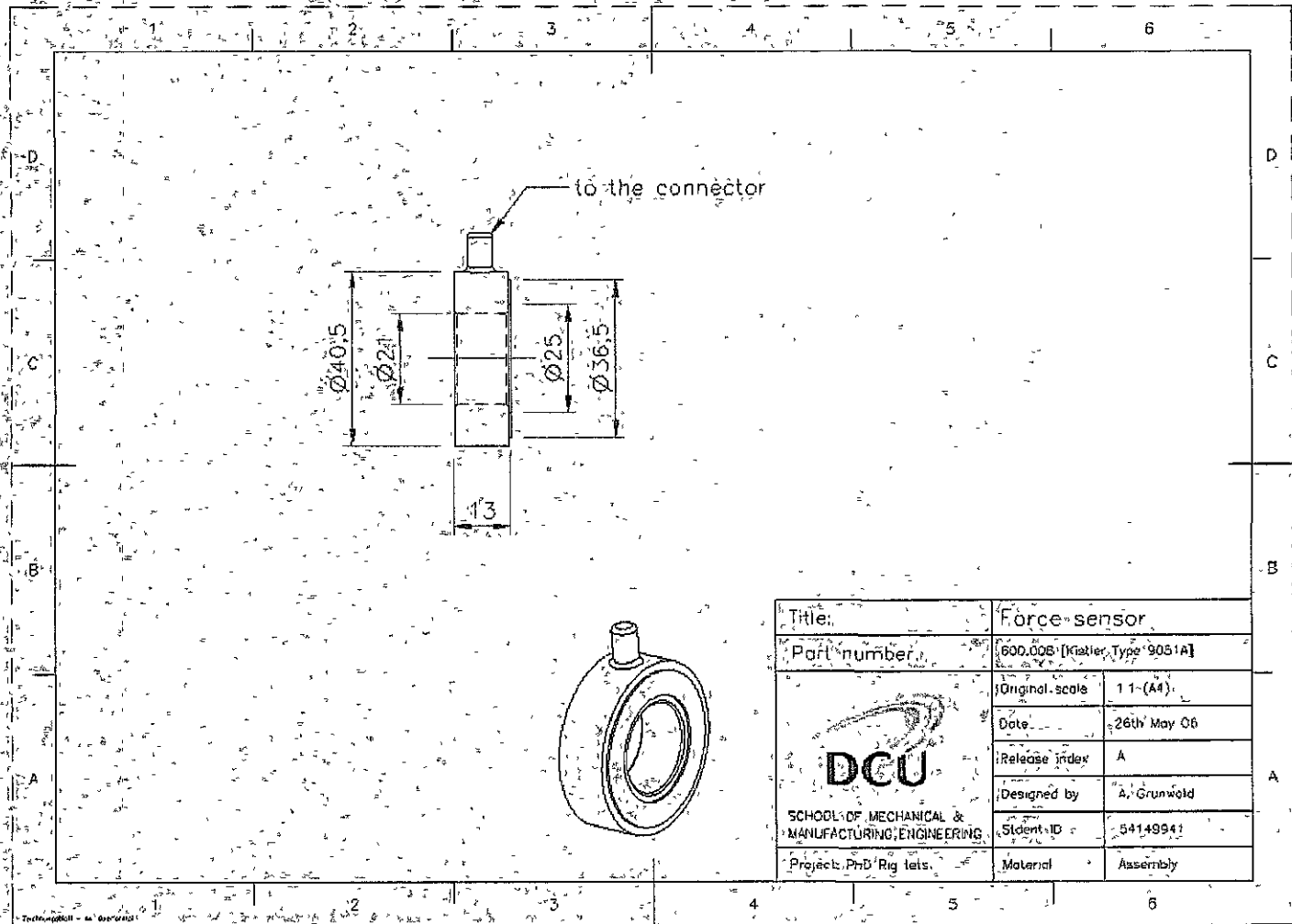


Fig. E7: Force sensor 600.008




Title:	Force sensor	
Part number:	600.008 [Grater, Type 9051A]	
 SCHOOL OF MECHANICAL & MANUFACTURING ENGINEERING	Original scale	1:1-(A4)
	Date	26th May 06
	Release index	A
	Designed by	A. Grunwald
	Student ID	54149941
Project: PhD Rig tests	Material	Assembly

Figure E8 depicts the test proceeding of the reference load. External pressure supply has been used to evaluate the elasticity and to prove the sealing concept.



Fig. E8: Reference load on test bench

Figure E9 depicts the cross section of the arrangement for experimental tests of the load assembly.

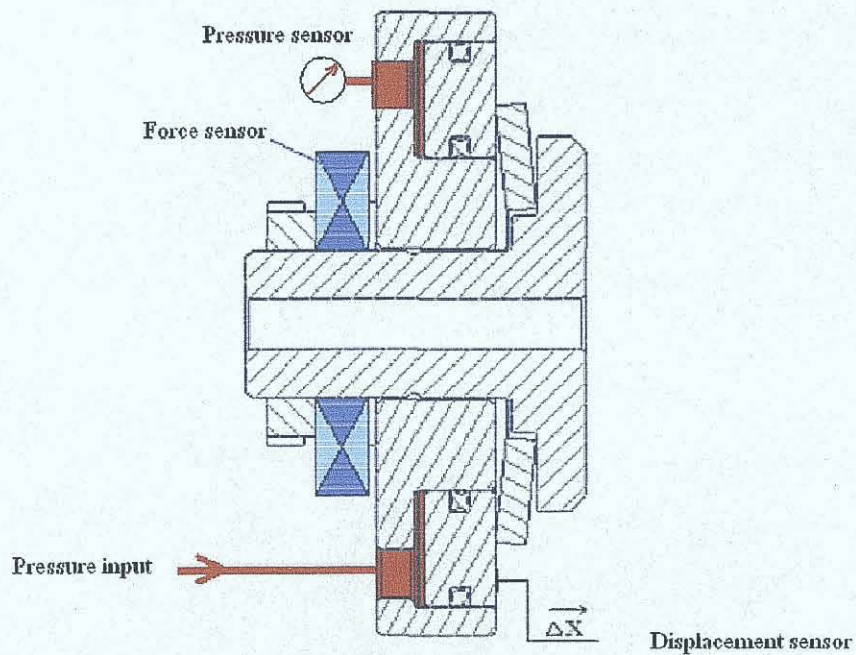


Fig. E9: Experimental tests of the load arrangements 600.000

Load assembly with different disc spring specifications has been applied with external pressure using a conventional fluid (CHF11S). The force, axial displacement and the pressure has been recorded. Fig. E10 shows the measurements result of the load assembly.

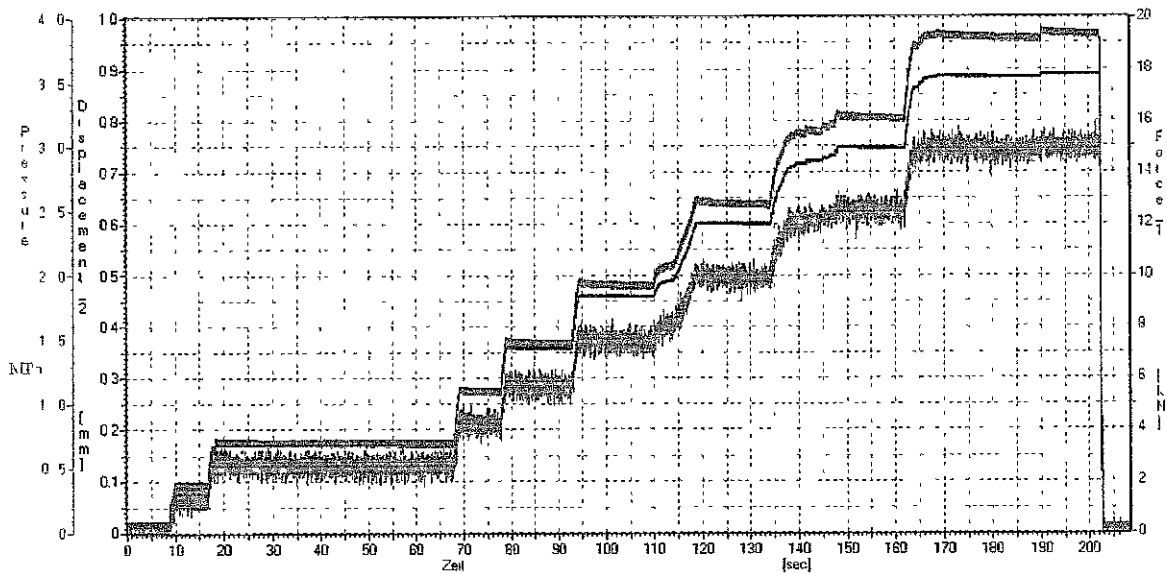


Fig. E10: Measurement of assembly 600.000 with disc spring DIN2093-A90

As an extract of above diagram the new diagrams "pressure and axial force versus axial displacement" have been created. The axial displacement has been measured on the hydraulic piston. The linear relationship between pressure and axial force and low pressure drop versus time is confirming low hysteresis and good sealing of reference assemblies.

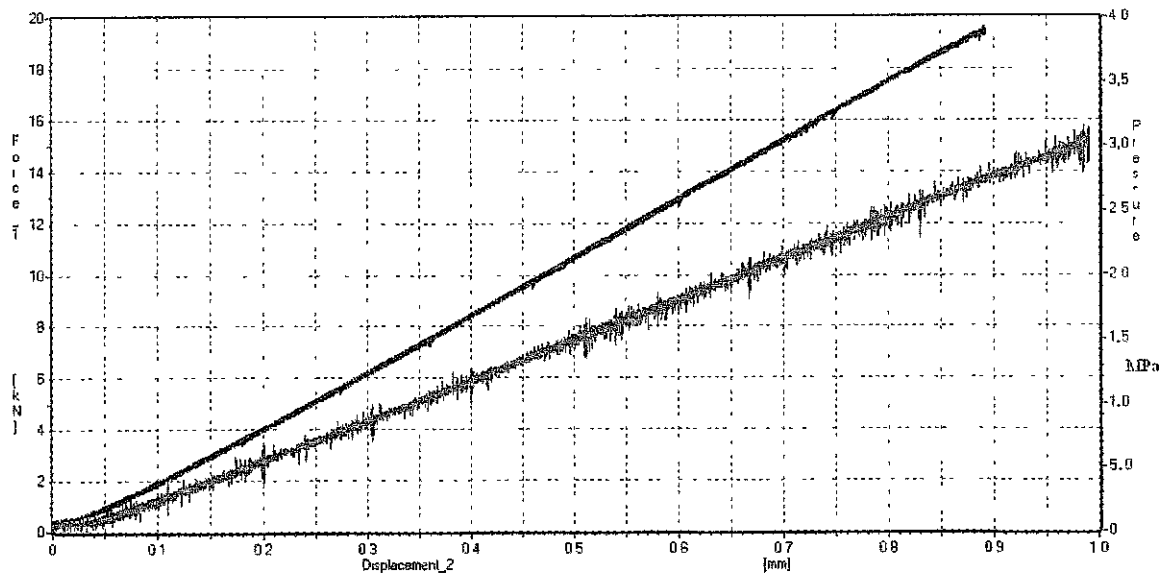
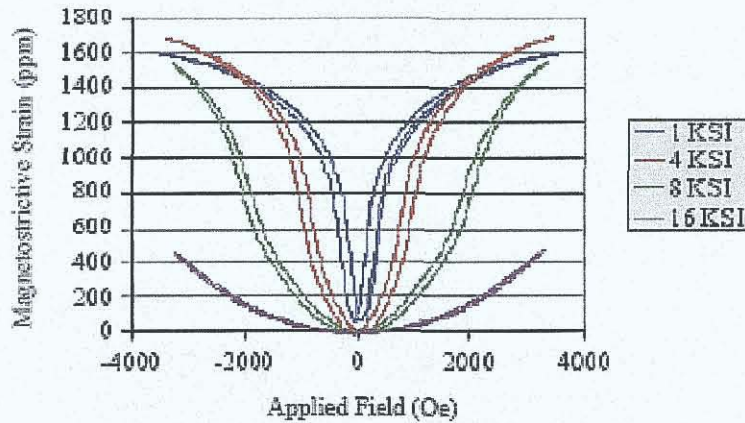
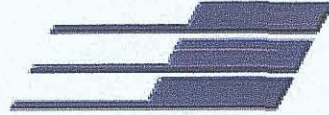


Fig. E11: Measured load assembly performance (with DIN2093-A90)

Etrema Products, Inc.
 2500 N. Loop Dr.
 Ames, IA 50010
 (515) 296-8030
 (515) 268-4540 Fax
 (800) 327-7291 Toll-Free
 www.etrema-usa.com



TERFENOL-D versus field at various preloads

TERFENOL-D PHYSICAL PROPERTIES	
Nominal Composition	Tb _{0.3} Dy _{0.7} Fe _{1.99}
Mechanical Properties	
Young's Modulus	25-35 GPA
Sound Speed	1640-1940 m/s
Tensile Strength	28 Mpa
Compressive Strength	700 Mpa
Thermal Properties	
Coefficient of Thermal Expansion	12ppm/°C
Specific Heat	0.35kJ/kg-K
Thermal Conductivity	13.5 W/m-k
Electrical Properties	
Resistivity	58 x 10 ⁻⁸ Ohm
Curie Temperature	380 °C
Magnetostrictive Properties	
Strain (estimated linear)	800-1200ppm
Energy Density	14-25 kJ/ m ³
Magnetomechanical Properties	
Relative Permeability	3-10
Coupling Factor	0.75

Fig. F1: Terfenol-D specification from supplier [Etrema Inc.]

Pentosin CHF 11S

All-Purpose High Performance-Hydraulic Fluid for Application both in Automotive Comfort- and Safety Devices

Description

Pentosin CHF 11S is a synthetic high performance hydraulic fluid for life-time application in modern vehicle aggregates. It is suitable for all extreme ambient temperatures and guarantees full performance from -40°C to over 130°C system temperature.

Pentosin CHF 11S is especially designed for hydraulics in the automotive industry with highest technical requirements. Due to its excellent features it is used in following devices (extract): power steering, level control, shock absorber, hydro-pneumatic suspension, stability- and traction control, hydraulics for convertible tops, central lock systems.

Quality Level

DIN 51 524T3 and ISO 7308

Approvals

Worldwide approved by leading car manufacturers, e.g.:

Bentley
BMW
Fendt
Ford
DaimlerChrysler
GM/Opel
MAN
Porsche
Saab
Volvo

Product Classification

The product is not classified as dangerous.

Pentosin CHF 11S	Typical Data		
	Unit	Result	Method
Appearance		green	visual
Density at 15 °C	kg/m ³	830	DIN EN ISO 12185
Flash point	°C	156	ISO 2592
Kinematic Viscosity at 100 °C	mm ² /s	6,0	DIN 51 562 part 1
Kinematic Viscosity at 40 °C	mm ² /s	19,0	DIN 51 562 part 1
Kinematic Viscosity at -40 °C	mm ² /s	1100	DIN 51 562 part 1
Pourpoint	°C	-57	ISO 3016
FZG wear test (A/8.3/90)	Failure Load Stage	11	DIN 51354 part 2

While handling lubricants the relevant safety rules have to be taken into account. For more detailed information please see the current safety data sheet for this product.

This product may not be available at all locations. For more information, please call us at +49 4103-9134-0 or visit us at www.pentosin.com. Due to continual product research and development, the information contained herein is subject to change without notification. Typical data may vary slightly.

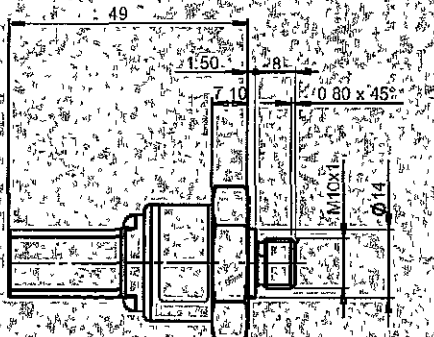
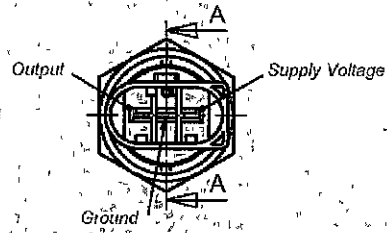
© 2006 Deutsche Pentosin-Werke GmbH. All rights reserved. (V3 GB SEP06 glu)

Fig. F2: CHF11S specification from fluid supplier [Pentosin Werke]

Used sensors for the rig test

Pressure transducer

Input pressure range	0 - 60 barS
Proof pressure	80 barS max.
Burst pressure	130 barS min
Operating supply voltage range V_s	5.0 ± 0.25 VDC
Excitation voltage polarity	5 MINUTEN / minutes
Over voltage	14.5 VDC max.
None of output voltage	0.500 VDC @ 0 barS -- 1.500 VDC @ 60 barS ($V_s = 5.0$ VDC)
Accuracy	Including offset, nonlinearity, hysteresis and repeatability at a temperature range of -40°C to 135°C See figure 1
Temperature error	See figure 2
Saturation voltages	0.3 + 0.07 / 0.05 V -4.65 - 0.07 V
Excitation current	< 15 mA
Output impedance	< 100 Ω
Response time	5 ms max.
Current sink / Current source	1 mA sink and 0.1 mA source min
Operating temperature range	-40°C bis + 135°C



(Port in accordance to DIN 3852-A M10x1)

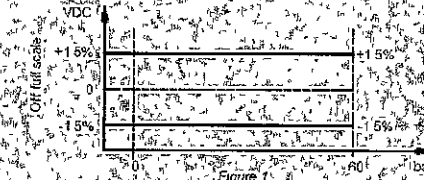


Figure 1 Accuracy error allowed

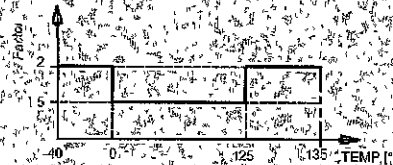
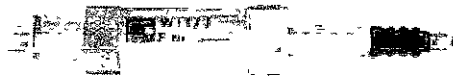


Figure 2 Error multiplier factor over temperature range °C

Fig. F3: Pressure transducer specification from

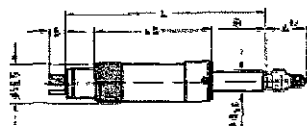
W1T3, W5TK

Inductive displacement probes

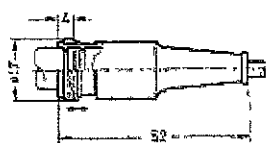


W1T3

W1T3 with ball guide



HK 315-G



Special features

- Wear-resistant inductive measurement system
- Clamping according to dial gauge standard, M2.5 measurement inserts (to DIN 878)
- Interchangeability error < 1 %
- Insignificant friction of sliding (W5TK) or ball guide (W1T3)
- W1T3 with outward-travel adjustment as standard
- Summation and subtraction by parallel or antiparallel circuit possible
- Explosion-proof versions [Ex] available

Dimensional variation to DIN 7165 coarse

Displacement probe Type	Nominal displacement mm	Weight in g		Dimensions in mm				Stroke in mm			
		Transducer ⁽²⁾ , approx.	Probe, approx.	L	A ⁽¹⁾	B	a _{min}	b	a _{max}	d _{min}	d _{max}
W1T3	± 1	50	7	78.5	15	20 24	±	± 1	± 5	5 5	

Technical Data

Transducer type		W1T3	W5TK
Nominal displacement (Nominal displacement span)	mm	± 1 (2)	± 5 (10)
Nominal sensitivity (nominal output-signal at nominal displacement, output not loaded)	mV/V	± 81	
Sensitivity tolerance (deviation of sensitivity from nominal sensitivity)	%	± 1	
Nominal output-signal range	mV/V	± 80	
Temperature effect per 1°C in the nominal temperature range			
on the sensitivity (rel. to the actual value)	%/10K	± 0.2	
on the zero signal (rel. to the nominal sensitivity)	%/10K	± 0.05	
Linearity deviation, (incl. hysteresis rel. to the nominal output-signal range)	%	0.2	
Nominal excitation voltage (rms value)	V	2.5 ± 5%	
Service range of the excitation voltage (rms value)	V	1.6	
Carrier frequency	KHz	4.5	
Amount of the input impedance	Ω	= 1000	
Protection to EN 61529		IP 20	
Nominal temperature range (Service temp. range)	°C (°F)	-20 -40 [-4, +176]	

Transducer type	Permissible acceleration in m/s ²		Initial spring tension ⁽¹⁾ at dimension A in N approx.	Spring constant in N/mm, approx.
	transducer body	Probe tip		
W1T3	50	25	0.3	0.05
W5TK	50	200	1.50	0.10

Fig. F4: Displacement sensor specification [HBM]

Contactless Displacement Transducers

Berührungslöse Wegaufnehmer

Tr12x1; Tr18x1; Tr30x1,5

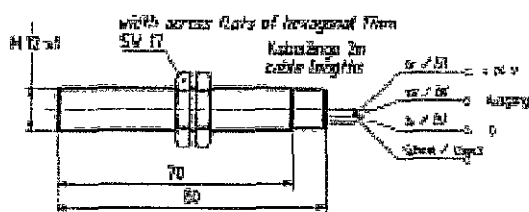
Contactless eddy current displacement transmitter able to detect distances on metallic objects such as copper aluminium, ferritic and austenitic steel.

Berührungslöse Wirbelstrom Wegmeßumformer zur Erfassung von Wegänderungen an metallischen Objekten wie Kupfer, Aluminium, ferritischer und austenitischer Stahl.

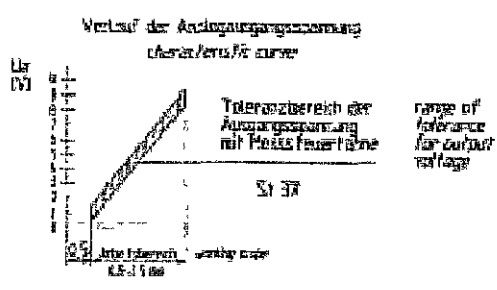
- Transmitter with integral amplifier.
- Strokes of ± 1 ; $\pm 1,5$; $\pm 3,5$ mm
- Nominal operating temperature range -25 ... $+70$ °C.
- Small space requirement.
- Entirely free from reactions on the measured object

- Eingebauter Maßverstärker
- Meßwege ± 1 ; $\pm 1,5$; $\pm 3,5$ mm
- Nenntemperaturbereich -25 ... $+70$ °C
- geringer Platzbedarf
- völlige Rückwirkungsfreiheit a.d. Meßobjekt

Order number	Bestell Nummer	1-TR 12X1	1-TR 18X1	1-TR 30X1,5
Drawing number	Zeichnungs Nummer	364 11-1001 d	364 11-1001 d	364 12-1001 d
Linear stroke	Linearer Maßweg	0,5 - 2,5 mm	1 - 4 mm	7 - 14 mm
Initial air gap	Ausgangsluftspalt	0,9 mm	1 mm	7 mm
Output voltage in centre position	Ausgangsspannung in Mitteneinstellung	± 5 V		
Sensitivity with nominal load-resistor	Empfindlichkeit mit Nennbelastungswiderstand	± 5 V/mm	± 3,3 V/mm	± 1,4 V/mm
Nominal load-resistor	Nennbelastungswiderstand	5 kΩ		
Oscillator frequency	Oszillatorfrequenz	500 kHz		
Measurement frequency range	Meßfrequenzbereich	0...100 Hz		0...30 Hz
Excitation voltage	Speisespannung	24 V ± 25 %		
Current consumption	Stromaufnahme	± 12 mA		
Temperature dependant output deviation in the operating temp. range between $+20$ °C ... $+50$ °C	Temperaturabhängige Abw. des Meßwertes im Gebrauchstemperaturbereich zwischen $+20$ °C ... $+50$ °C	± 3 % ± 1,5 µm/K ± 0,7 µm/K	± 2 % ± 2,25 µm/K ± 1,5 µm/K	± 2 % ± 5,25 µm/K ± 3,0 µm/K
Temperature dependant zero deviation per 10K	Temperaturabhängige Abw. des Nullsignals pro 10K	50 µm	50 µm	50 µm
Nominal temperature range	Nenntemperaturbereich	-25 ... $+70$ °C		
Operating temperature range	Gebrauchstemperaturbereich	-25 ... $+70$ °C		
Protection class (acc. to EN 60 529)	Schutzart nach DIN 40 050	IP67		
Maximum permissible acceleration	Maximale Beschleunigung IEC88-2-6	300 m/s ²		
Cable length	Anschlußkabelänge	2 m		
Weight	Gewicht	± 50 g	± 100 g	± 200 g



Tr12x1



Versorgungsspannung	24 V ± 25%	supply voltage
Ausgangsspannung	± 5 V	output voltage
Max. Laststrom	12 mA	current load

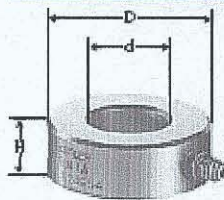
Fig. F5: Displacement sensor specification [HBM]

KISTLER

measure. analyze. innovate.

Messunterlagscheibe, kalibriert

Messunterlagscheiben Typ 9001A ... 9071A



Typ kalibriert	Mess- bereich kN	Empfind- lichkeit pC/N	Steifheit kN/ μ m	Betriebs- temperatur °C	d mm	D mm	H mm	Gewicht g
9001A	0 ... 7,5	-4,3	-1	-196 ... 200	4,1	10,3	6,5	3
9011A	0 ... 15	-4,3	-1,8	-196 ... 200	6,5	14,5	8	7
9021A	0 ... 35	-4,3	-3,5	-196 ... 200	10,5	22,5	10	20
9031A	0 ... 60	-4,3	-6	-196 ... 200	13	28,5	11	36
9041A	0 ... 90	-4,3	-7,5	-196 ... 200	17	34,5	12	53
9051A	0 ... 120	-4,3	-9	-196 ... 200	21	40,5	13	78
9061A	0 ... 200	-4,3	-14	-196 ... 200	26,5	52,5	15	160
9071A	0 ... 400	-4,3	-26	-196 ... 200	40,5	73,5	17	366



Anschluss
10-32 neg.

Eigenschaften
grosser Messbereich, hohe
Steifheit, kompakte Bauform,
Einbaubehälter

Anwendung
Materialprüfung, Maschinen-
prüfung, Messen von Aufprall-,
Lagereaktions-, Schrauben-,
Klemm- oder Stempelkräften

Zubehör
Anschlusskabel Typ 1631C ...
Vorpannelemente Typ 9420A ...
Einbaubehälter Typ 9505 ... 9579

Datenblatt
000-105

Fig. F5: Force sensor specification [Kistler]

Ein-/Dreikomponenten- und Drehmomentsensoren

Kistler offeriert drei grundsätzlich verschiedene Arten von piezoelektrischen Kraftsensoren:

Ein-Komponenten-Kraftsensoren

In diesen meist ringförmigen Sensoren befinden sich druckempfindliche Quarzscheiben zwischen zwei Stahlringen.

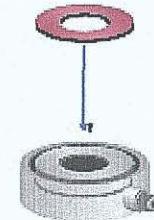
Dreikomponenten-Kraftsensoren

Schubempfindliche Quarzscheiben (F_x , F_y) werden zusammen mit druckempfindlichen Quarzscheiben (F_z) zu einem sehr kompakten Dreikomponenten-Kraftsensor verbaut.

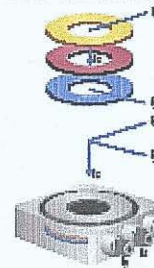
Drehmomentsensoren

Schubempfindliche Quarzscheiben werden kreisförmig so angeordnet, dass ihre empfindlichen Achsen tangential ausgerichtet sind. Unter Vorspannung eingebaut, können so Drehmomente gemessen werden.

Ein-Komponenten-
Kraftsensoren: druck-
empfindliche Quarz-
scheiben zwischen
zwei Stahlringen.



Dreikomponenten-
Kraftsensoren: Schub-
empfindliche und
druckempfindliche
Quarzscheiben.



Drehmoment-
Sensoren:
schubempfindliche
Quarzscheiben, kreis-
förmig angeordnet.



FEMM verification

In order to verify the simulated model of actuator, the experimental rig assembly has been prepared for measurements of flux density with Tesla Meter.

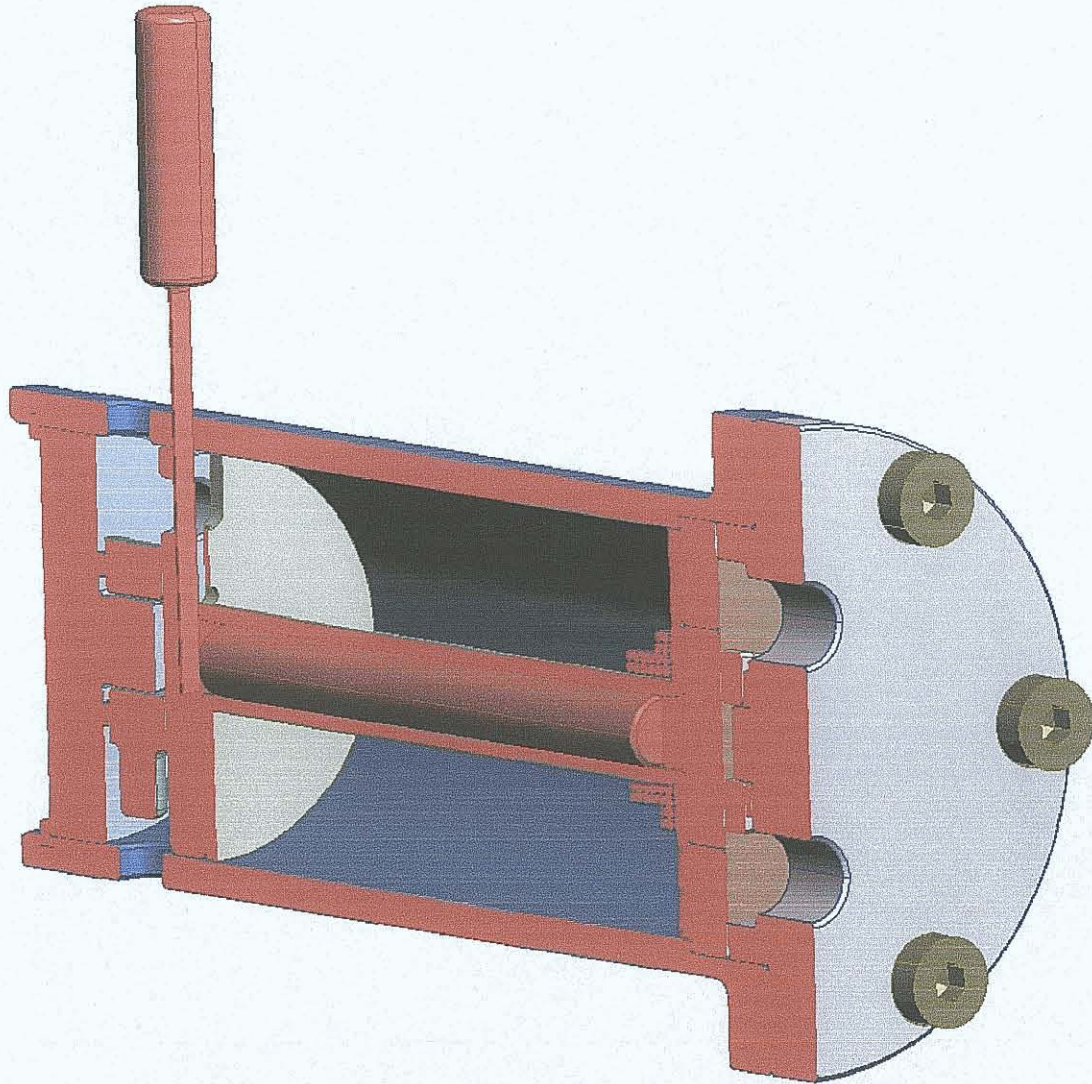
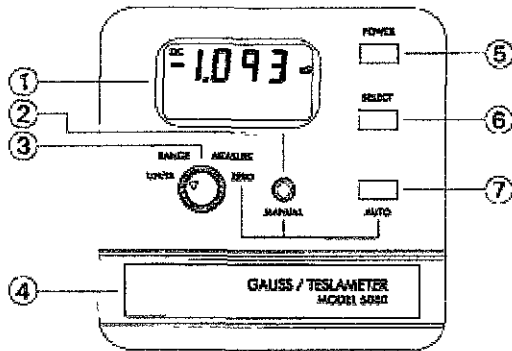
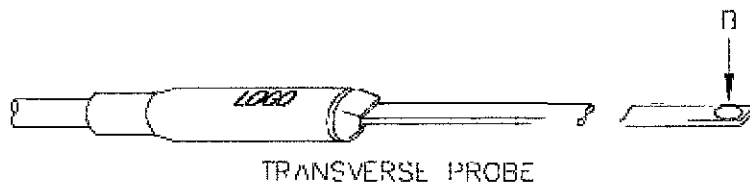


Fig. G1: Actuator with Tesla-Meter probe (Model 5080)



ACCURACY (analog output, including probe)

dc mode: $\pm 1\%$ of reading, ± 5 mV.



Model 5080

GAUSS / TESLA METER

Fig. G2: Tesla-Meter Model 5080 [Instruction Manual, F.W. Bell]

Following simulation model has been used to verify the simulated flux density with the measured flux density:

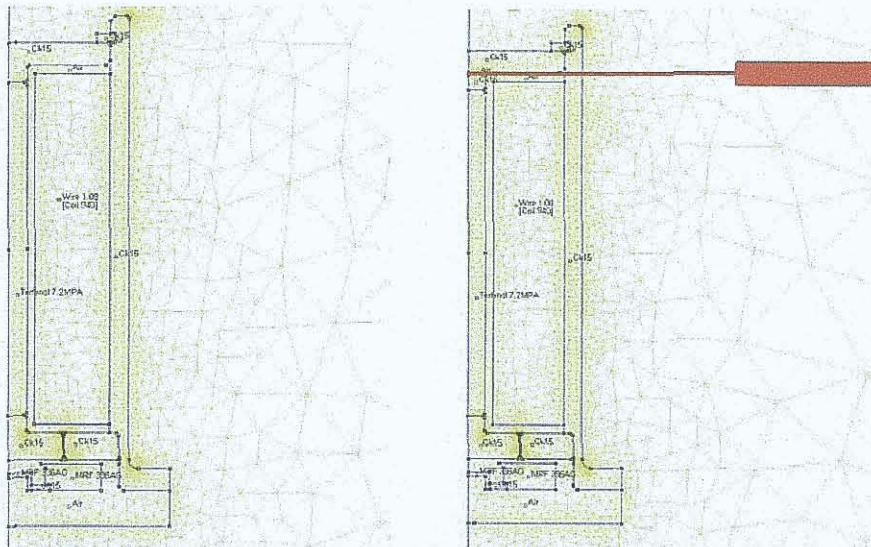


Fig. G3: Actuator model without (left) and with (right) Tesla-Meter probe

Fig. G4 presents the simulation results of flux density B (T) obtained with FEMM at nominal electrical current. On the left side: the original actuator assembly; on the right side: the modified assembly for Tesla-Meter probe. Top-to-bottom reference centre line has been used as reference.

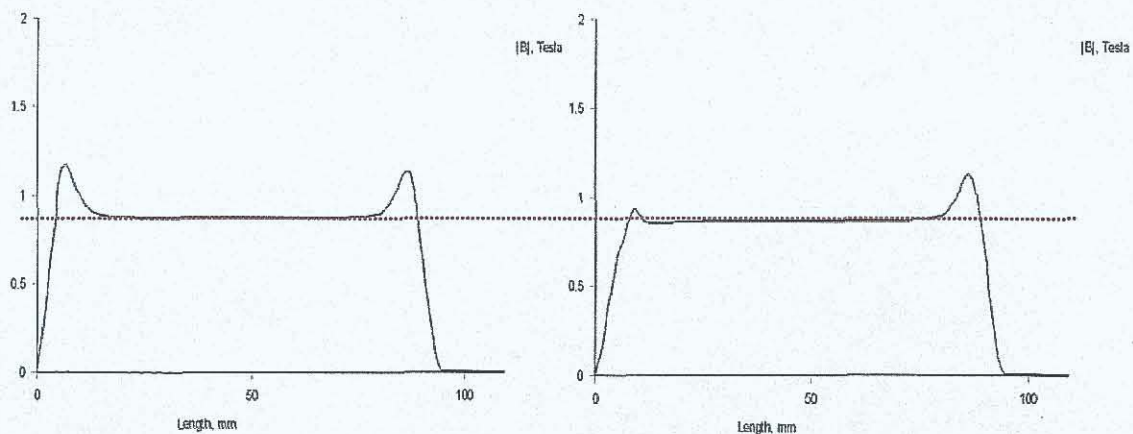


Fig. G4: Flux density without (left) and with (right) Tesla-Meter probe

The difference between the two above showed results has been found as acceptable for verification of the magnetic field simulation results. Figures G5 to G19 show the simulation results of flux density B (T) and field intensity H (kA/m) at various current levels.

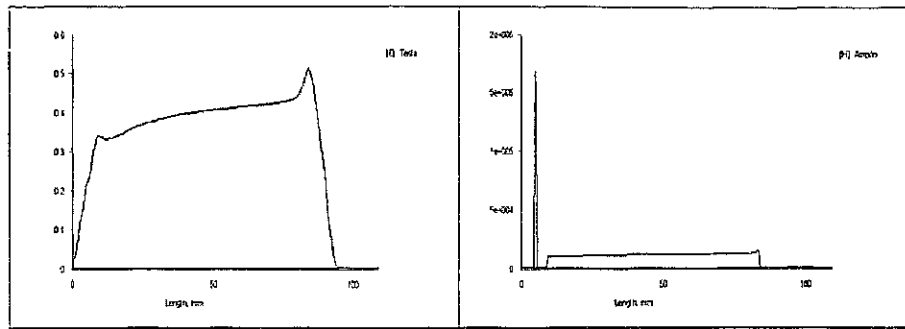


Fig. G5: FEMM flux density B (left) and field intensity H (right) at 1 A

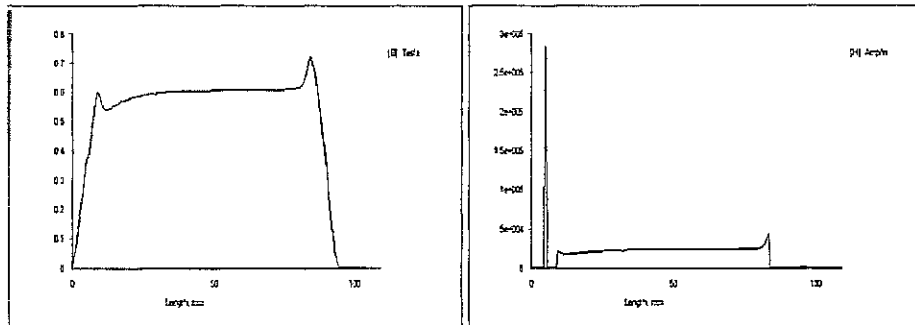


Fig. G6: FEMM flux density B (left) and field intensity H (right) at 2 A

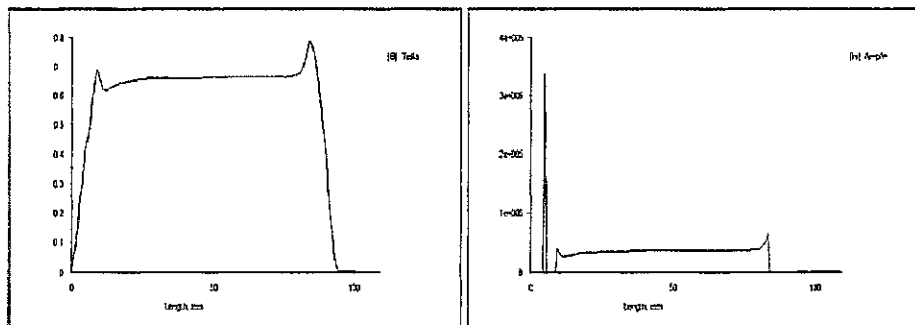


Fig. G7: FEMM flux density B (left) and field intensity H (right) at 3 A

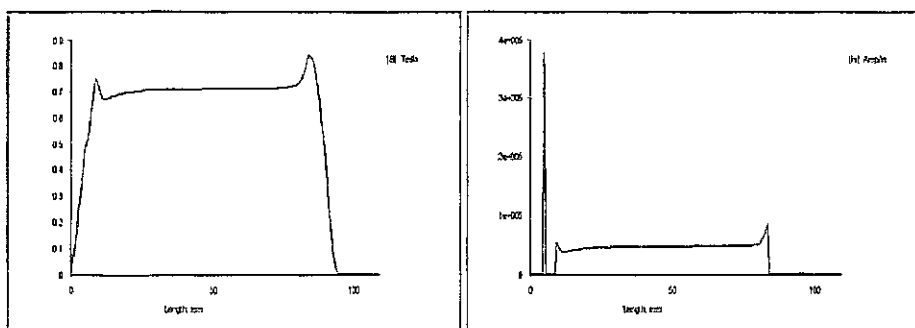


Fig. G8: FEMM flux density B (left) and field intensity H (right) at 4 A

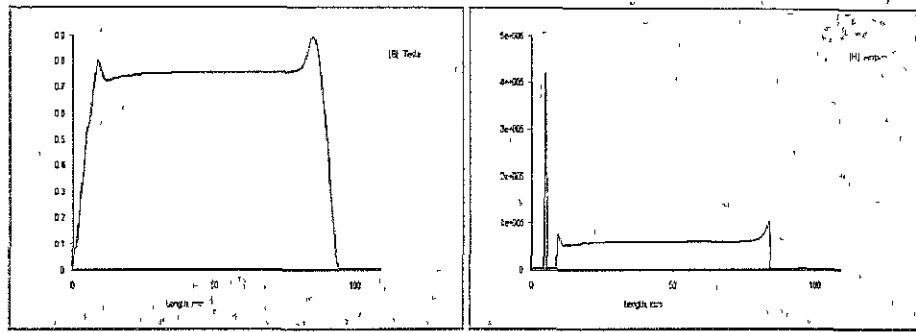


Fig. G9: FEMM flux density B (left) and field intensity H (right) at 5 A

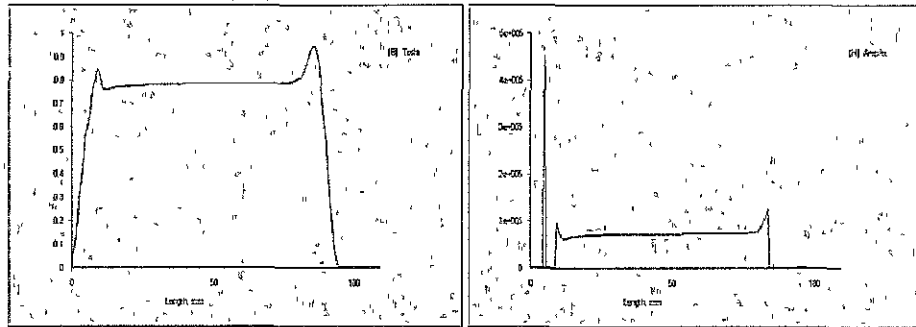


Fig. G10: FEMM flux density B (left) and field intensity H (right) at 6 A

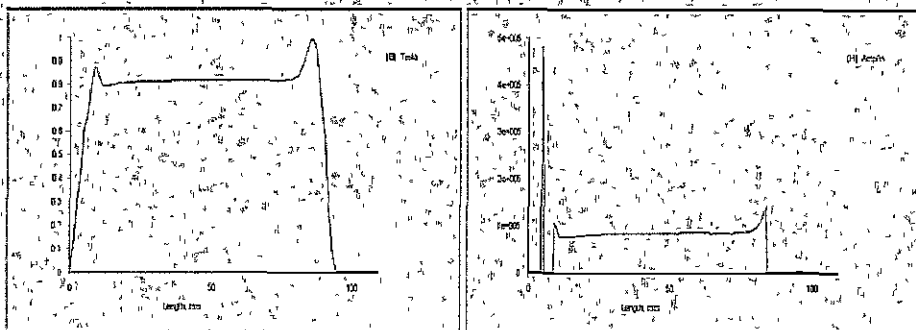


Fig. G11: FEMM flux density B (left) and field intensity H (right) at 7 A

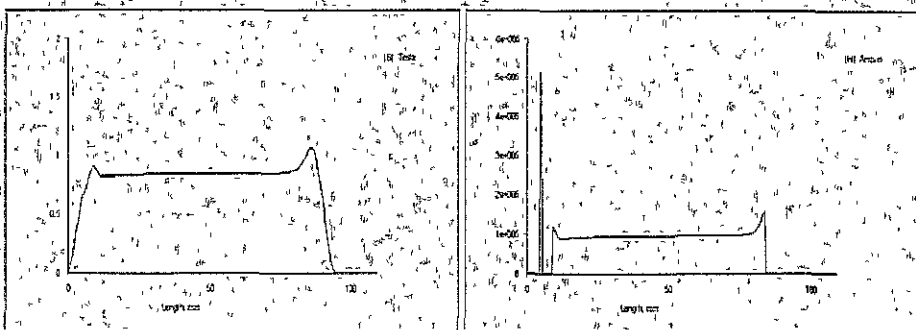


Fig. G12: FEMM flux density B (left) and field intensity H (right) at 8 A

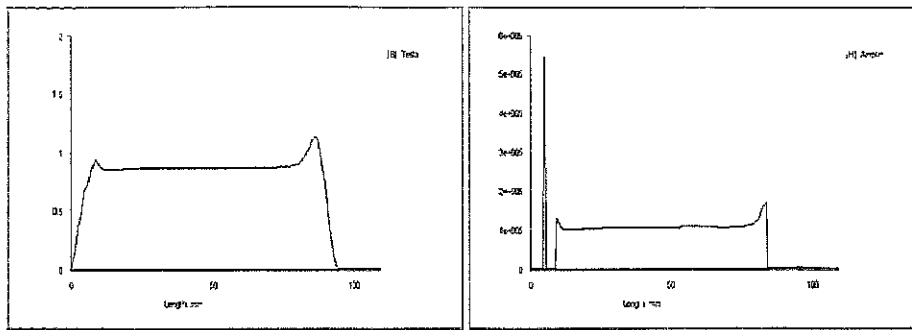


Fig. G13: FEMM flux density B (left) and field intensity H (right) at 9 A

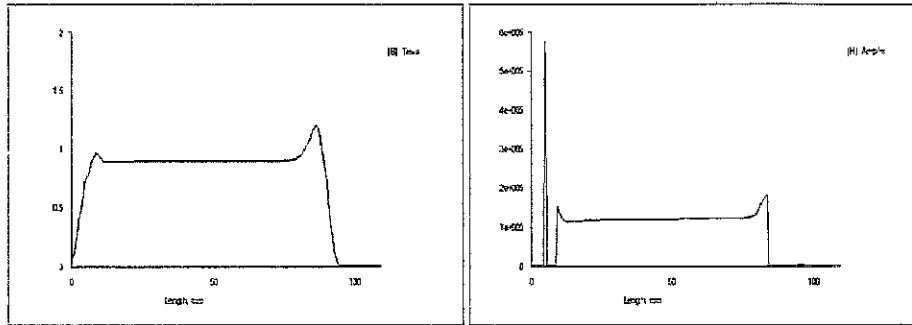


Fig. G14: FEMM flux density B (left) and field intensity H (right) at 10 A

Table G1 presents the results from FEMM magnetic field simulation and the measurement results of flux density at the top of the Terfenol-D shaft.

Table G1: Simulation and measurement result for comparison

Electric current I (Amp)	FEMM flux density in the gap B (Tesla)	Measured flux density in the gap B (Tesla)	FEMM flux density in Terfenol-D B (Tesla)	Expected field intensity in Terfenol-D H (A/m) at 7.2MPa
0.0	0.000	0.000	0.000	0
1.0	0.200	0.220	0.400	11800
2.0	0.330	0.300	0.600	23000
3.0	0.400	0.342	0.660	37000
4.0	0.450	0.382	0.710	47800
5.0	0.500	0.417	0.750	58000
6.0	0.540	0.450	0.775	67800
7.0	0.580	0.480	0.810	87000
8.0	0.620	0.520	0.830	93000
9.0	0.640	0.560	0.870	108000
10.0	0.660	0.580	0.890	118000

A power supply unit (up to 10A, DC), a Multi-Meter for current measurements and the Tesla-Meter Model 5080 have been used for the measurements. The flat Tesla-probe has been adapted in to the actuator assembly according Fig. G1. The difference in the simulated results and the measured flux density is predictable and was caused by accepted variations of the housing material and measurement tolerances.

Figure G15 depicts the measured flux density at the top of the Terfenol-D shaft with simulated results, obtained with FEMM.

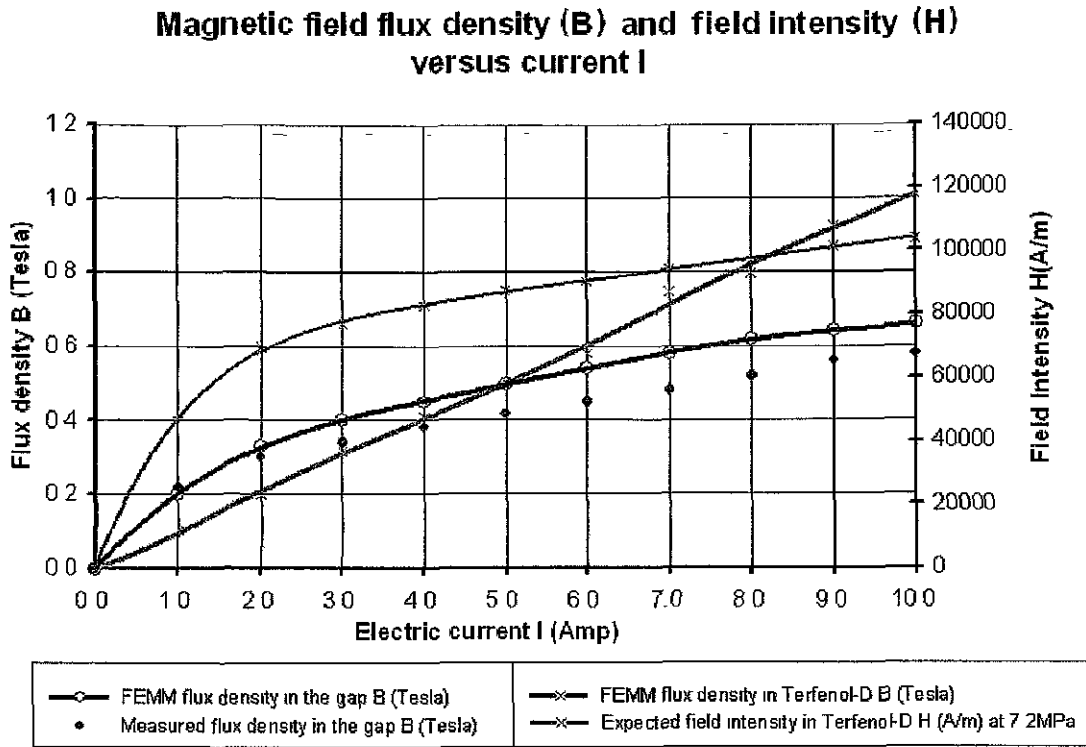


Fig. G15: FEMM flux density B (T) versus electrical current

Summarizing the results from simulation and the flux density measurement with the Tesla-Meter Model 5080 can be stated, that the results are within the specified range and in good consistence.

List of publications

Following articles, related to this thesis, have been published:

[a1] A. G. Olabi, A. Grunwald, **Design and application of magneto-rheological fluid**, Dublin City University, Materials & Design 28 (2007), pp. 2658-2664

[a2] A. G. Olabi, A. Grunwald, **Design and application of magnetostrictive materials**, Dublin City University, Materials & Design (2007), available on www.science-direct.com

Following articles, related to this thesis, are under review:

[a3] A. G. Olabi, A. Grunwald, **Design of magneto-rheological (“MR”) fluid device**, Dublin City University, Materials & Design, submitted to science direct in August 2007

[a4] A. G. Olabi, A. Grunwald, **Design of magnetostrictive (“MS”) actuator**, Dublin City University, Materials & Design, submitted to science direct in August 2007